# Numerical and experimental studies in development of polymer injection micro molding.

## Citation

Angelov, Aleksandar Kolev - Lehigh University. *Numerical and Experimental Studies in Development of Polymer Injection Micro Molding*. 2008, https://preserve.lehigh.edu/lehigh-scholarship/graduate-publications-theses-dissertations/theses-dissertatio
numerical-28.

# Numerical and Experimental Studies in Development of Polymer Injection Micro Molding

by

Aleksandar Kolev Angelov

Presented to the Graduate and Research Committee
of Lehigh University
in Candidacy for the Degree of
Doctor of Philosophy

in

Department of Mechanical Engineering and Mechanics

Lehigh University

December 2007

ProQuest LLC
789 E. Eisenhower Parkway
PO Box 1346
Ann Arbor, MI 48106-1346

# Certificate of approval

This dissertation is accepted and approved in partial fulfillment of the requirements for the degree of Doctor of Philosophy

December 7, 2007
Date

John P. Coulter
Dr. John P. Coulter
Committee Chairman and Dissertation Advisor

December 7, 2007
Accepted Date

Committee Members:

Dr. Herman F. Nied
Committee member

Dr. Raymond A. Pearson
Committee member

Dr. Richard P. Vinci
Committee member

# Acknowledgments

First, I would like to give my sincere thanks to my parents, my brother-in-law and my sister for their never ending support.

Second, I would like to thank my adviser Dr. John P. Coulter for his guidance, discussions, supports and encouragements throughout my years of graduate studies at Lehigh University.

Third, I would like to acknowledge Dr. Herman F. Nied, Dr. Raymond A. Pearson, and Dr. Richard P. Vinci for being my Ph.D. committee members and for supporting the research effort. I would like to thank Dr. Pearson and Dr. Vinci for their technical support.

I would like to thank also Dr. Floyd C. Miller, Dr. Alfred C. Miller, Dr. Wenyong Lin, Dr. Volkmar Dierolf, Dr. Boon S. Ooi and his graduate students of Lehigh University; Dr. Gary P. Wiederrecht of The Argonne National Lab, Dr. Timothy J. Bunning of The Air Force Research Laboratory at The Wright-Patterson Air Force Base, and Dr. Tom Krupenkin and Dr. Ashley Taylor of Bell Labs at Alcatel-Lucent for their scientific discussions and technical support without which the completion of this effort would not have been possible.

Finally, I would to acknowledge all the fellow graduate students in our lab with whom I have worked and in particular Mr. Gregory S. Layser. I also would like to give my thanks to Mr. Richard E. Towne and Mr. Herman C. Baader for their help on the machining work.

## Table of Contents

## List of Figures

# List of Tables

## Abstract

The present research focused on the investigation of the Injection Micro-Molding process for replication of nano- and micro-patterned polymer surfaces. The major objective of the research was to develop the scientific understanding of the injection micro-molding process both by experimental and numerical studies, and to develop and employ experimental protocols that enable the manufacture of polymer replicated features at the nano- and micro-scale.

This work presents a method for the replication of ordered polymeric arrays from silicon molds treated with plasma polymerized (PP) ultra-thin anti-adhesive organic coating. Silicon molds were fabricated with e-beam lithography and deep reactive ion etching (DRIE) in the Bosch® process mode. An inductively coupled plasma reactor was utilized to deposit PP coating from $C_4F_8$ (octafluorocyclobutane) precursor gas. Characterization of the PP film was performed via X-ray Photoelectron (XPS) and Fourier Infrared Spectroscopes. Surface analysis revealed excellent chemical composition of the film. Nano-features with different shapes and sizes, as small as 25 nm, were successfully replicated via injection molding with Cyclo Olefin Copolymer (COC) and were imaged with scanning electron and atomic force microscopes. High aspect ratio (AR~8) submicron-sized pillars were also achieved. Fluorine diffusion from the PP film to the melt processed polymer, detected with XPS as well, decreased with the subsequent molding cycles.

In a different set of experiments, successfully injection molded nano-patterned COC substrates were tested as templates for generation of surface

plasmon-polariton excitations. Two very distinct modes of light transmission were observed and their behavior was found to depend on the wavelength influenced scattering from the sub-wavelength-sized pattern.

In addition, experimental protocols were also developed suitable to perform replication of passive optical components, e.g. polymer diffraction gratings, and others which resulted in the manufacture of micron-sized alphanumeric characters.

Static parametric stress-strain structural finite element (FE) analysis revealed that molds made out of Si can keep their structural integrity at the range of pressures and mold temperatures commonly used during polymer injection micro-molding. High principle stresses with values above $\sigma_{yield}$ were found to arise only at very high pressures which are unlikely to be used in injection micro-molding applications. Therefore, brittle failure of the Si molds with the considered geometry is not expected to occur during injection micro-molding.

Flow simulations by employing non-elastic Non-Newtonian governing equations describing the behavior of a polymer melt flow under isothermal conditions were considered to simulate the flow in micro-sized cavities as well. In this continuum based FE scheme approach, the expression for the melt viscosity was given with Cross model incorporating Eringen-Okada's term valid for micro-flows. In addition, the flow was considered in the presence of a wall slip. The results were in good agreement with previously reported experimental data. It was shown that the slip velocity introduces a shift in the viscosity vs. shear rate dependence.

# CHAPTER 1

# INTRODUCTION

*“One of the symptoms of an approaching nervous breakdown is the belief that one's work is terribly important." - Bertrand Russell*

## 1.1 Introduction

The development of plastics technology with the associated manufacturing science has been one of the most important industrial advancements of the last half century. On the other hand, it is believed that the ability to control matter deliberately and create structures by design that possess unique engineered functionality at the nano- and micro-scale would enable the commercialization of ingenious functional devices having superior or unmet performance. Therefore, in recent years, a promising significant expansion of the realm of polymer product application has evolved through the introduction of polymer micro-components and nano- and micro-patterned surfaces for a wide range of applications ranging from biomedical devices to miniaturized electronic and optoelectronic components for automotive and communication applications. Although such polymer components have so far played only a subordinate role in the multibillion-dollar microsystems industry, they have begun to show great commercial potential. It has been estimated by the NEXUS-The Product Technology Roadmap for Microsystems/MEMS III, 2005-2009, that this industry will grow from the $12 billion market in 2004 to a $25 billion market in 2009.

At present, one way to manufacture patterned structures utilized in MST/MEMS devices is by the top down approach in which polymers are shaped via transferring topographic features from soft or hard masters, e.g. molds. As a result, the major goal of this comprehensive work was to advance the science related to such manufacture performed by utilizing polymer injection micro-

-molding process.

## 1.2 Challenges Related to the Injection Micro-Molding Applications

### 1.2.1 Mold Fabrication

The fabrication cost of polymer-based devices is barely affected by the level of complexity of the design. Once the mold insert is made, hundreds and thousands of components could be manufactured. The cost of the engineered polymers, that are usually used, is not a significant factor in the formation of the final price of a given component, because only small material quantities are used in a well optimized molding process. On the other hand, the cost to make the mold inserts could be substantial. Their manufacture always requires the use of complicated, expensive equipment and very well trained personnel. Unfortunately, a well manufactured mold insert does not always guarantee that the processed polymers will flawlessly replicate its structure.

The progress in the fabrication of polymer-based microsystems has been made mainly due to three major factors: availability of engineered polymers with suitable properties for small-scale molding, development of machines suitable for precision molding, and development of techniques for production of the nano- and micro-structured mold inserts. Consequently, the future progress of polymer-based microsystems will depend upon the advancement of any of those fields. During the years, several methods for mold insert microfabrication have been developed and established as the workhorse techniques of choice. In this

Chapter, a brief review of the current progress and ongoing research related to the manufacture of nano- and micro-structured mold inserts is presented. First, LIGA and related methods are discussed. Second, the other major trend in mold insert fabrication, e.g. silicon based processing, is also reviewed. Third, the so called shop methods, EDM and metal cutting, are also discussed. Last, several not so popular unconventional methods are introduced as well.

### *1.2.1.1 LIGA and Related Techniques*

Interestingly, one of the first documented studies in implementing micro replication with thermoplastic polymer was long ago in 1970. The objective of the work, done in RCA laboratories in Princeton, was to develop a low-cost reproduction technique of hologram motion pictures for television playback [1, 2]. Later on, work was done on production of diffraction grating by hot embossing of Polyvinyl Chloride (PVC) in Zurich, Switzerland. The development of micromolding as a manufacturing process started in Karlsruhe, Germany in the middle of 80's as a replication follow-up process for LIGA process. Initially, the acronym LIGA meant "*Lit*ografie and *Gal*vanic" which stands for "lithography and electroplating". Later on micromolding was introduced and the acronym was expounded as "*Lit*ografie, *Gal*vanic and *A*bformung" which means "lithography, electroplating, and molding" [3]. A typical process sequence of standard LIGA process starts with transferring two dimensional pattern of an X-ray mask into a positive poly(methyl methacrylate) (PMMA) or negative (SU-8) [4, 5] resist by exposing it with highly collimated X-ray synchrotron radiation, as seen in Figure 1-1. The resist is usually several hundred microns thick usually, up to 1.4 mm for PMMA [4] and up to 2 mm for SU-8 [6], which has been solvent cast or glued onto various substrates which most of the cases are Si, $SiO_2$, ceramic, or anodized aluminum [4]. The substrate is previously deposited with electrically conductive layer of gold, but other materials as titanium oxide, aluminum, copper and copper oxide, are used as well [4]. The X-ray mask is one of the most important and most expensive components in LIGA technology. It is usually made of X-ray adsorbent gold patterns deposited on a polycrystalline carbon (graphite). Initially, the designed patterns are created on a photomask and are subsequently transferred on the graphite by UV-lithography. The last steps to form a working X-ray mask are gold electro-deposition and resist, usually a high molecular weight PMMA, stripping which most of the times is a difficult procedure. The gold should be thick enough so that it creates reliable contrast during exposure with the synchrotron radiation [7]. The type of the resist used for mold manufacturing depends strongly on the application. For example, PMMA has a high resolution but low sensitivity, which increases the irradiation time and the related cost with the mold insert production [4]. After irradiation and resist development, the process proceeds with a metallization step. A variety of metals and metal alloys are used, such as Ni, Ni-Co, Ni-W, Co-W, Cu-Zn, Ni-PTFE (PTFE, Poly(tetrafluoroethylene)) to name a few [4]. In such a way one may control the surface properties of the mold, such as hardness and wear by friction. After electrodeposition the metal replica is lifted-off and the rest of the resist is stripped. Later-on, the replica is used for molding. Not until recently, it was widely accepted that LIGA has failed to become broadly approved method for master fabrication because of hurdles in making appropriate X-ray masks, the cost and limited availability of the exposure equipment. This led to development of alternative LIGA processes known as UV-LIGA and Laser-LIGA. In UV-LIGA, the source used for irradiation of the resist is ultraviolet light. The resist used is a chemically amplified SU-8 but there is a thickness limitation due to the adsorption of the UV-energy by the resist [6]. On the other hand, Laser-LIGA uses excimer laser ablation to ablate the resist. It utilizes intense pulses of UV-radiation at 248 nm or 193 nm wavelengths. The process allows production of complex 3D structures in the resist, ablating of various types of resists. In addition, there is no depth limitation [8]. All the other steps are kept the same as those in the standard LIGA process.

Recently, a lot of research has been done on the effort to make LIGA more cost efficient. The ongoing research is related to the development of better scientific understanding of X-ray mask manufacturing, metal and metal-alloys for electrodeposition, and substrate material properties. The latter is crucial since it is a source of backscattered electrons and accompanying photons which expose the resist from the bottom. Actually, this is one of the fundamental limitations inhibiting irradiation of smaller feature sizes than the theoretical minimum stated by x-ray physics [9]. The overexposure leads to formation of undercuts on the resist profiles and deterioration of the interface between the resist and the substrate. Interestingly, nowadays LIGA could be done *in-situ* since a portable monochromator synchrotron radiation unit is already commercially available and could be coupled with an x-ray scanner. The energy range of the radiation coming out of the chamber is between 90 and 1800 eV and is ideal for LIGA process. Unfortunately, even with utilizing such equipment, the process is still expensive.

Nevertheless, LIGA and related techniques are still the best processes for manufacturing of high quality mold inserts and must be used for manufacturing of high aspect ratio micron-sized mold inserts whenever possible. LIGA offers a number of advantages compared with other techniques, such us very high precision <1 µm, low surface roughness Ra <20 nm, and high aspect ratios [10].

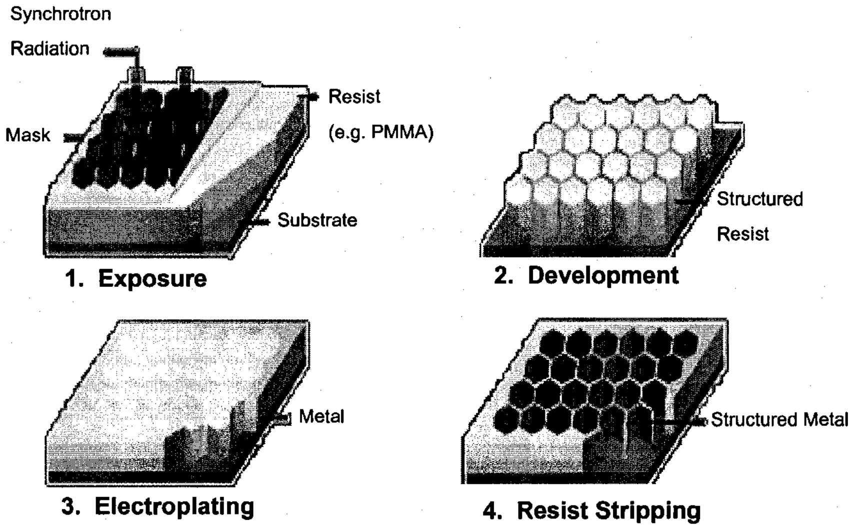

**Figure 1-1.** Schematic representation of LIGA process sequence.

### *1.2.1.2 Silicon based processing*

The high purity and crystalline perfection of single-crystal silicon makes it a material with excellent electronic and mechanical properties. Silicon has been the workhorse material for the Integrated Circuit (IC) industry ever since its inception. The microsystems industry, or the idea of building microstructures in the vertical z-direction, evolved naturally from the Very Large Scale Integration (VLSI) industry when there was a need to accommodate the large amount of components on a single chip [11, 12]. Thus Si became the favorite material of choice because most of processes were especially designed for working with that material. Naturally, during the years, it was also accepted as a structural material for production of mold inserts. Silicon molds have many advantages such as fast and low-cost production, optically flat surfaces, admissible hardness, strength, and thermal conductivity. In this subchapter, several techniques commonly used for production of inserts, are briefly discussed.

At present, mainly two silicon based processes are widely employed for fabrication of Si molds, e.g. wet bulk etching and dry etching. The latter techniques can also be divided in the following groups Deep Reactive Ion Etching (DRIE) and DRIE related techniques, e.g. DEEMO.

Wet bulk etching is a chemical anisotropic etching which mostly uses potassium hydroxide (KOH), sodium hydroxide (NaOH), lithium hydroxide (LiOH), cesium hidroxyde and ammonium hydroxide ($NH_4OH$) solutions [12, 13]. The mask used for etching is usually $SiO_2$. It utilizes directionally dependant-etching rate, which is used to get microstructures defined by the slow etching planes as seen on Figure 1-2. This process is cheap since it does not require use of expensive equipment. Unfortunately, the roughening of Si surfaces caused by the etching and the limitations of produced final profiles rendered that technique of a little use [14].

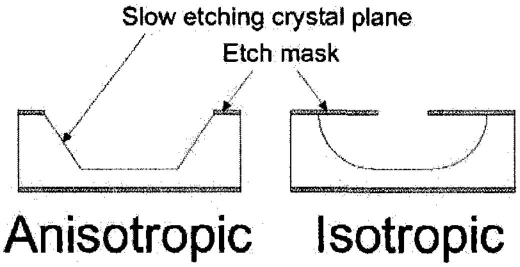

**Figure 1-2**. Schematic representation of profiles achieved by wet bulk etching of Si.

On the other hand, DRIE and related techniques offer a robust way of Si etching. DRIE employs a type of high-density plasma reactor with inductively coupled plasma reactor. In this type of reactor, a fluorinated gas – sulfur hexafluoride ($SF_6$) is pumped into a chamber and the plasma is generated by applying an RF power to a coil around the ceramic walls of the chamber. The power source produces magnetic field, which in turn induces an electric field, which accelerates the electrons to higher energies and confines them to the plasma. This increases the ionization rates, i.e. the collisions between the electrons and the gas molecules. Thus, high concentrations of fluorine atoms and other highly reactive radicals are formed from the inert gas ($SF_6$). The substrate in the chamber is bombarded by high density flux of reactive radicals, which damage the lattice and etch away substrate atoms in the form of volatile $SiF_x$ or $SiF_x$ + $CF_x$ compounds depending on the substrate (Si or SiC). The etch rates are usually around 3-4 μm/min. Besides $SF_6$, octafluorocyclobutane ($C_4F_8$)

gas is also used for sidewall passivation (BOSCH® process mode). The two gases are pumped independently one at a time, which enables etching of the very deep structures into the Si substrate [15, 16]. Before using the DRIE process, a protective layer (masking material) is spin coated right on top of the Si wafer and imaged by UV-lithography or Electron beam lithography. In another embodiment, DRIE is employed as the first step followed by electroplating and molding (DEEMO-*D*ry *E*tching, *E*lectroplating, and *M*olding). DEEMO process is a fast and amenable technique for polymer microstructuring. It competes with LIGA and LIGA alike processes in which the X-ray lithography step is substituted with a dry etching process. The mold inserts that are manufactured from Si could be used and are used for micro hot embossing and micro injection molding applications [14, 16-19]. In DEEMO process, the Si wafers must be conductive to assure electron transfer to the Ni ions, which are moving towards the cathode (the wafer). For example, this can be achieved by doping the wafer with boron from diboron hexahydride ($B_2H_6$) for 1 h at 1100 $^0$C through a diffusion process [19] and pre-doped wafers with prescribed surface resistivity are readily available as well.

The ongoing research in the field of Si based processing is mainly in the area of optimization of the dry etch step for providing profiles with a desired taper, controlling the aspect-ration dependent etching, and regulating the uniformity of the plasma etch [19]. DRIE and DEEMO processes are cost efficient and could provide very high quality, high aspect ratio structures with surface roughness comparable to LIGA and LIGA related process. The bare Si made molds have suitable hardness and mechanical strength. They are also suitable for rapid prototyping, and yield flat, planar surfaces in comparison with the Ni molds, which exhibit bowing resulted from stress concentration during plating [14]. Those techniques provide cheap and fast access to the manufacture of nano-and micro-structured inserts.

### *1.2.1.3. EDM and Metal Cutting*

Electro Discharge Machining (EDM) or spark machining is a process, which utilizes high frequency electrical sparks formed between a cathode tool and a conductive anode substrate (the mold). The anode and cathode are immersed in a dielectric fluid which most of the time is DI water, silicon oils, or triethylene, which washes away the resolidifying metal particles. When the two electrodes are moved to close distance around 25 μm, the dielectric liquid suddenly becomes conductive and electric discharge is formed. There are two major methods of EDM - sinker EDM and wire EDM. In sinker EDM, the cathode tool, which could be made from copper, graphite, or silver, is shaped in the form of the desired cavity form. The higher the DC pulse frequency, the smoother the resulting surface after erosion is. The frequency range is between 180 Hz to 300-400 kHz. The tolerances achieved with sinker EDM are typically around 20 - 30 μm but could be smaller depending on the machine levels of control.

In wire EDM, also called wire electrode discharge grinding (WEDG) complex shapes are cut from thick conductive metals. In this technique a copper, brass, or molybdenum-steel wire with thickness from 0.15 to 0.3 mm is continuously drawn between two reels, one above and one below the substrates. This approach is also used for machining the electrodes for sinker EDM. The electrodes could also be made by LIGA processing [20]. The tolerances achieved with wire EDM are typically around 1 μm. The removal rate of EDM machining is between 0.001 and 0.1 $cm^3/h$. In some embodiments [21], attempts to hybridize the sinker and wire EDM with short duration pulses have been made. In others [22], magnetic field has been introduced to improve removal of the resolidification material away from the eroded cavities, thus lowering the surface roughness.

The ongoing research in the area of EDM machining embroils the optimization of the process so that smoother profiles could be attained by reducing the short pulse duration and peak currents; development of methods for fabrication of electrodes with different cross-sectional shapes. EDM methods provide rapid access to manufacture of metal mold insert with admissible quality and could be used virtually with any conductive materials. The utilization of this relatively cheap mold insert manufacturing method depends solely on the design requirements of the particular application.

Another shop technique which has recently started gaining momentum is the micro-end milling process. It is a pure macro scale machining operation, which is scaled down and is still in its infancy. In spite of this, it is gaining popularity and could be considered as rival technique of EDM. The tool sizes range from several hundred micrometers to about 25 μm. In doing micro-milling cutting one should take into account the change of the metallurgical phases when the tool moves along its tool-path, which leads to force variations in the tool, increased level of vibrations and tool breakage. Numerical models are also available that predict the feed rate and tool rpm required for flawless machining [23]. The achieved dimensional error is no larger than 2 μm. In some cases, the cooling during micro-machining is achieved by controlling the oxygen concentration around the tool. This enables heat absorption by the oxidized chips since the oxidation is endotropic reaction [23]. Mold inserts, fabricated with micro-endmilling, were used for polymer replication of polymer micro-cantilevers [24].

#### 1.2.1.4 Other Techniques

Besides the above-discussed major processes, there are other techniques, which did not get much popularity for production of mold inserts, but generally are used as direct methods for microfabrication and could complement the standard mold insert fabrication methods. Such methods include - pulsed electrochemical machining as a follow-up step after EDM, which is used to improve the surface finish of the spark eroded cavities [25], micro-stereo-lithography for fabrication of ceramic microstructures suitable for mold inserts [26], focused-ion beam etching for production microstructures in glassy carbon molds [27], metal deposition methods for constructing MEMS type heater with short time response on a standard type metal master and MEMS type resistance temperature gage [28].

### 1.2.2 Modeling of Polymer Melt Flow at the Micro-scale

While in recent years research has been carried out in an attempt to understand the process dynamics of micro injection molding using computerized flow analysis software - used for standard injection molding processes, much of the work has been concentrated on two-dimensional analysis. Recent studies [29-33] reveal that, for extremely small dimensions of micro components, existing flow simulation software packages are no longer sufficient to describe all the three-dimensional effects in micro molding. The inadequacy could be attributed to the usage of conventional polymer rheological data, and the elimination of effects such as wall-slip and surface tension. First, the rheological data used in current packages is obtained from macroscopic experiments. This macroscopic data would not be suitable for modeling micro-scale flows, where the polymeric fluid would be subjected to extraordinary levels of shear stresses. Second, the polymer has a strong tendency to slip in micro channels. When the classical 'no-slip' boundary is utilized in current packages, the consequence of wall slip cannot be predicted. Third, micro-scale surface effects could either boost or hinder the flow depending on the mold wall surface condition. These surface effects are not accounted for in existing simulation packages. In this regard, it is desirable to investigate the surface effects of the filling flow into micro-channel, since surface effects become more dominant as the characteristic length is smaller.

Commercial CAE packages such as Moldflow have become an accepted part of mold design. The Hele-Shaw model neglects the inertia and the gap-wise velocity component for polymer melt flow in the thin cavities. The three-dimensional flow regions i.e. flow around corners, the thickness-change regions, or the fountain flow effect of melt fronts cannot be represented in Hele-Shaw model.

Studies by Ho and Tai [34] indicated that surface effects dominate the fluid flowing through miniature mechanical devices because of the large surface-to-volume ratio on micro-scale configurations. In a related study, Kim and Whitesides [35] carried out an experimental study of flow of liquids into rectangular capillaries having micrometer dimensions, and analyzed filling flow by a concept of dynamic contact angle between the flow and the wall. They showed that the rates of filling flow into capillary are linearly correlated to the cosine of the static advancing contact angle.

Many experimental and numerical studies of micro-channel flow have been performed in attempts to understand the micro-scale fluid flow in microfludic devices [36-39]. However, these studies are mostly directed to obtaining relationships between flow variables for the case of completely filled flow in micro-channels. Tseng *et al*, [40] investigated fluid filling into micro-reservoirs. They used the “volume-of-liquid” method as a numerical scheme, and considered surface tension, whose physical basis is not well known, as a volumetric force.

Kim *et al*, [41] performed flow visualization experiments of micro-channel filling flow to observe the characteristics of filling flow into micro-channels considering the relations between inlet pressure, viscous force and surface tension effects. They also completed numerical simulations incorporating surface tension effects to predict the filling flow into micro-channels, using water as the working fluid. Their study indicates that the inertia force dominates for higher inlet pressure, while viscous forces dominate in the case of lower inlet pressure.

In another recent study, Yao and Kim [29] investigated a micro filling simulation scheme for polymeric materials including micro-scale viscosity and wall slip. Their study suggests that due to the high heat diffusion rate in the micro-scale, micro cavities are filled almost isothermally. In addition, they claimed that surface tension effects were not important in micro molding. Based on their experiments using polystyrene (PS) as a model fluid, they showed the importance in employing micro-scale viscosity and wall slip in micro filling simulations [42-44].

The possibility of the occurrence of slip in a polymer flow has been studied [45, 46] and is particularly relevant to polymer processing events that occur near the wall [44, 47]. In particular, at very high shear stresses a polymer melt flow can violate the classical no-slip hydrodynamic boundary condition at solid surfaces by exhibiting flow instabilities and complex non-linear dynamics [48, 49]. A study by Awati *et al*, [50] experimentally demonstrated that for mono-disperse polystyrene melt, two distinct regimes of slip are seen: (i) a low shear rate regime in which the slip velocity increases slowly with shear rate (weak slip) and (ii) a high shear rate regime in which the increase is dramatic (strong slip). They also showed that through scaling of stress/shear rate data that the crossover between the two regimes occurs when the bulk polymer chains are effectively disentangled.

Rosenbaum *et al* [44] for simplicity modeled the local slip velocity by a modified Power-law expression, with no pressure and temperature dependence. In another study Lee *et al*, [51] modeled the wall slip boundary condition using a generalized Navier slip law with a power law tangential velocity dependence of the shear force. Recently, Joshi *et al* [52] proposed a unified network model to explain the temperature dependence of critical stress for wall slip by debonding. Their experimental studies also revealed that the dependence of critical stress for instability (slip) is inversely dependent on temperature.

Considering viscosity change in micro-channels, there are a number of reports that indicate that flows in the micro-channels are different from those at the macro-scale [42, 53-57]. Experiments with Newtonian fluids, such as water, and with dilute polymer solutions indicate that the viscosity close to the wall is 50-80% higher that the bulk viscosity of the fluid [42, 53, 58]. This increase is believed to be either due to collective molecular motion effects or to the immobility of the layer of molecules in contact with the solid surface [58]. Due to this fact, the classical Navier-Stokes theory along with a size independent viscosity relation cannot be used to explain the flow behavior. To remedy this failure, Eringen and Okada [42] proposed a non-local continuum theory of viscous fluids by taking into account consideration the molecular orientation effects.

## 1.4 Objectives of the Dissertation

The overall objective of this study was to develop scientific understanding of the injection micro-molding process both by experimental and numerical studies, and to develop and employ experimental protocols that enable the manufacture of structured polymer replicated features at nano- and micro-scale.

Experimental procedures were initiated and implemented that made possible the manufacture of structured silicon molds suitable for injection micro-molding applications. The approach taken during those studies relied heavily on the utilization of micro-fabrication and micro-characterization equipment which involved exploitation of scanning electron and atomic force microscopy, e-beam lithography, deep reactive ion etching, oxygen plasma etching, ellipsometry, x-ray photoelectron spectroscopy, Fourier transform infrared and Raman spectroscopy, near and far field optical microscopy. During the present investigation limitations and processing conditions of some of the micro-fabrication tools were investigated as relevant to the manufacture of structured silicon molds. Cyclo Olefin Copolymer (COC) was extensively utilized as a polymer of choice during the molding trials due to its optical, thermal, and physical properties and its stability in harsh environments, e.g. high vacuum, e-beam radiation, and x-ray radiation.

Numerical procedures for both structural and polymer melt flow types of simulations were implemented by utilizing COMSOL Multiphysics finite element libraries. Structural analysis was carried out to investigate the structural integrity of mold made out of silicon (Si) subjected to pressure and temperature in ranges commonly found during injection micro-molding. Flow analysis was performed to simulate the flow of polymer melt in micro-channels with continuum-based finite element methodology. For this purpose a suitable physical model describing the flow at micro-scale was created and successfully modeled with COMSOL.

## 1.5 Structure of the Dissertation

The general structure of the dissertation is compiled to present first an overview of the related scientific and engineering developments in the filed of patterning of surfaces which follows with experimental and numerical studies developed to advance the science related to the polymer injection micro-molding. A more detailed description of each chapter follows.

Chapter 1 serves as an introductory part of the dissertation and presents the current progress in mold insert fabrication and various approaches used in simulation of flow in micro-cavities.

Chapter 2 reviews the current state-of-the-art related to the nano- and-micro-structuring of polymeric surfaces by various techniques. Different manufacturing approaches are briefly presented.

In Chapter 3, the experimental procedure and results of molding of passive optical components, e.g. ruled diffraction gratings are presented. This chapter details both the mechanical and optical types of approaches that were utilized to characterize the components. The effect of the mold temperature is studied to improve the fidelity of polymer replication. Various characterization equipment suitable for component testing are validated and digital imaging processing techniques are also shown as a way to further expand the information obtained analyzing the raw data obtained from the characterization tools.

In Chapter 4, experimental protocols are established for the manufacture of micron- and submicron-sized polymer replicated features. E-beam lithography and deep reactive ion etching are implemented for the manufacture of silicon based molds and tools specific processing conditions are discussed. In addition, static parametric structural stress-strain analysis is performed to investigate the structural integrity of a prototype of an etched silicon mold.

Chapter 5 details the results from an experimental procedure developed to investigate the feasibility of using injection molding for the replication of polymeric sub-100 nm sized patterned surfaces from Si molds treated with plasma polymerized (PP) anti-adhesive ultra-thin fluorocarbon coating. In this study, surface characterization schemes are employed to examine the chemical composition of the coating as well. Theoretical predictions of the mechanical stability of successfully molded high aspect ratio pillars are also implemented.

Chapter 6 presents the finding of preliminary investigative work on utilizing successfully manufactured polymer nano-patterned surfaces as cost-effective and novel platforms for generation of surface plasmon-polariton (SPP) excitations. For this purpose, near-field optical microscopy is utilized to provide direct evidence for the SPP excitations. Explanation of the findings is also presented.

Chapter 7 discusses the conceptual mathematical description of a physical model describing polymer flow in micro-channels during injection micro-molding. This model is later utilized to numerically simulate the flow during various boundary and molding conditions by employing finite element schemes through COMSOL libraries. In addition, Moldflow simulations are also initiated and the results from both types of simulations are compared and analyzed.

Chapter 8 presents the conclusion of the dissertation, which includes both a summary of the conducted research and brief description of the envisioned future recommended studies, considered as possible continuation of the presented research work.

# CHAPTER 2

# RELATED TECHNOLOGY TO POLYMER MOLDING OF PATTERNED SURFACES

Nanomanufacturing includes *"all means that have the capability to reproducibly transform matter-from a* bulk *form or from individual atoms, molecules, and supramolecular structures-into nanoscale or* nanostructured *materials, devices, or systems with desired properties and performance characteristics, typically in large quantities. Additionally, nanomanufacturing is the capability to integrate such nanoscale materials and devices into systems spanning nanoscale to macroscale dimensions."*- www.nano.gov

## 2.1 Introduction

Polymer molding is a key technology for the replication of devices with nano-structured surfaces. With the increasing demand for polymer based nano- and micro-patterns on large area substrates, the development of such technology has become a priority. During the years this technology became well established in the sub-micron regime, e.g. compact disk (CD) molding and with current digital versatile disk (DVD) technology, structures with lateral dimensions of 400 nm and a depth of 100 nm are now replicated [59]. In recent years there has been a great need to develop low-cost technologies for mass-production of sub-100 nm structures since it is believed that such technology can bring enormous impact to many areas of engineering [60]. Many efforts have been done in structuring of surfaces utilized in sub-wavelength quarter-wave plates and antireflective polarizers [61], polymer micro-ring filters and resonant modulators [62, 63], substrates for cell-substratum interaction studies, important for cellular engineering applications [64, 65], discrete track recording (DTR) media for high capacity data storage magnetic hard disks [66, 67], and for the new generation of optical near field optical data storage systems to name a few. The drive towards obtaining low-cost masters has led the research community to rather unique approaches as well. Successful attempts were made to produce features from molds with nano-sized features directly from transferring the topography of insect wings [68], plant leaves [69], or type I bovine collagen-coated silicon wafers [70]. Technology developments in master fabrication are presented in Chapter 1.

Since a major part of the experimental work presented in this comprehensive study deals with nano- and micro-structuring of polymer surfaces, in this Chapter a brief overview describing currently available technologies utilized for the manufacture of patterned surfaces is presented.

## 2.2 Nano-imprint Lithography and Related Techniques

Nanoimprint lithography (NIL), Figure 2-1 or Step and Flash Imprint Lithography (S-FIL), Figure 2-2 are parallel process lithography techniques which can offer sub-100 nm resolution. In imprint lithography, a mold with nanometer-scale features is pressed into a thin resist, which most of the times is poly(methyl methacrylate) (PMMA), that is cast on a substrate. This step creates a thickness contrast pattern in the resist. After mold removing and UV curing, if liquid UV curable resist is used, an isotropic etching is utilized to transfer the pattern into the entire resist thickness by removing the remaining resist in the compressed area. In general the resist is a thermoplastic polymer that is heated during pattern transfer to soften the polymer relative to the mold. If the temperature is above the $T_g$ of the polymer, the polymer behaves as a viscous fluid and can flow into the mold cavities, therefore conforming to the mold [71, 72]. Nielsen e*t al* reported on utilizing cyclo olefin copolymer (COC) as a material suitable for nanoimprint lithography as well. The mold can be made of different substrates, such as metals, dielectrics, or semiconductors [72] and pattern transferring process can be performed by reactive ion etching and halogen etching in most of the cases or wet etching. Reports in scientific journals also demonstrate that NIL can be used for imprinting features below 50 nm [59, 71-74].

(a) Substrate coating with a resist.

(b) Resist heating and Mold pressing.

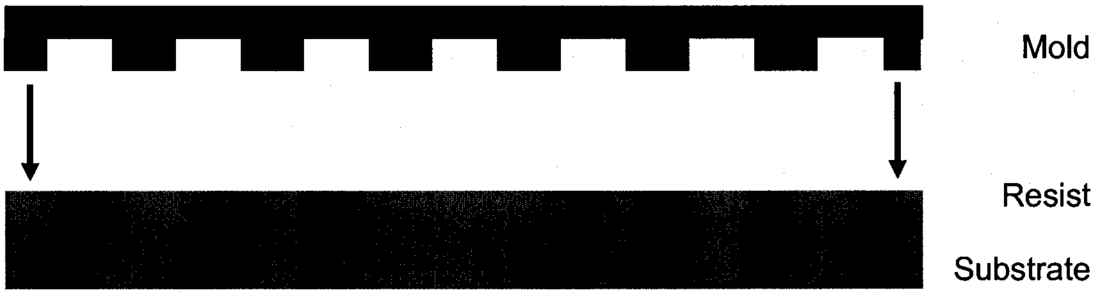

(c) Mold release.

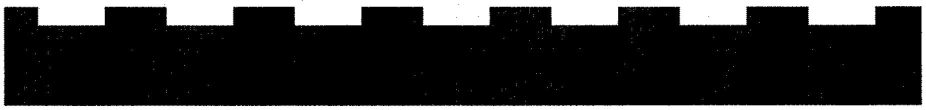

(d) Reactive Ion Etching (RIE).

**Figure 2-1.** Schematic representation of the nanoimprint lithography (NIL) process flow. Compression molding is used to create a thickness contrast in a resist, followed by anisotropic etching which exposes the surface of the underlying substrate.

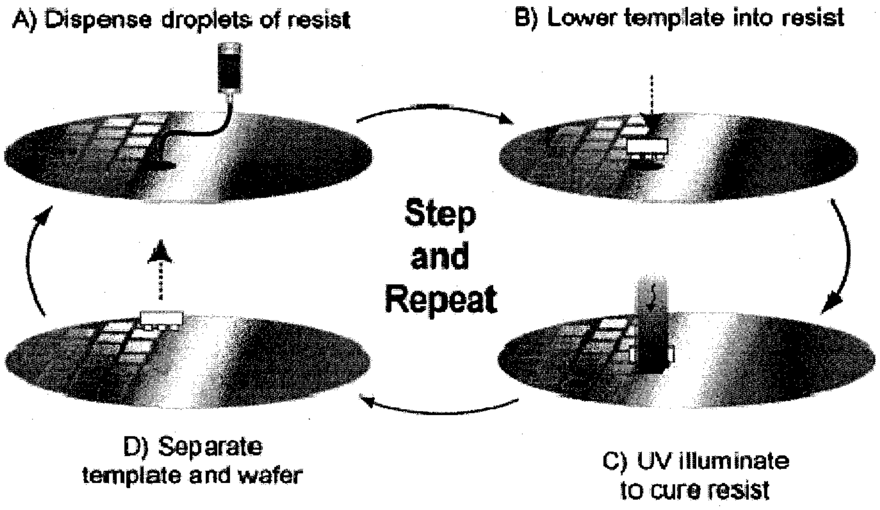

**Figure 2-2.** S-FIL process flow. *Adapted from www.molecularimprints.com.*

As a result, the International Roadmap for Semiconductors (ITRS) announced the inclusion of imprint lithography onto their roadmap to begin in production in 2013 at the 32 nm node [75]. It is expected that NIL and S-FIL would play a significant and important role in the manufacture of devices having sub-100 nm patterned features. Hot embossing is another similar technique to NIL which uses a pre-heated mold in which micro-structured mold insert, situated in an evacuated chamber, is brought into contact with a thermoplastic polymer, Figure 2-3. After melting the polymer the whole complex of cooled down and the part is demolded. A major process limitation is considered the long cycle time which can reach 30 min but this process uses slow velocities and pressures which leads to low internal stress in the final components [76]. The hot embossing is a convenient way for replicating high aspect ratio structures and is used for the replication of optical components.

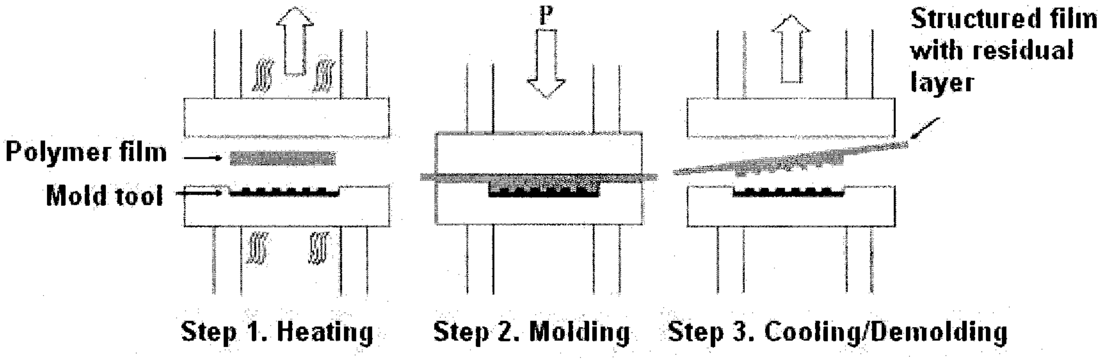

**Figure 2-3.** Schematic drawing of the hot embossing process flow. *Adapted from [76].*

### 2.3 Injection Micro-molding and Related Techniques

Injection micro-molding is a manufacturing technique which stems from the standard injection molding process. In general, in a standard injection molding process melting of the polymer is done in a plasticization unit, followed by injecting it into a mold which is nano- or micro-structured, as seen in Figure 2-4. In injection micro-molding polymer degradation and waste are reduced either by employing machines with small screw diameters (smaller that 20 mm) or by utilizing two stage units, e.g. one employed in plasticization unit and the other one employed in the metering/injection unit. There is a number of injection molding processes which also attracts the attention of both the industry and academia such as reaction injection molding, thermoforming and compression injection molding [3]. The latter process is considered to represent a mixture between hot embossing and injection molding processes. One major difference between conventional and micro molding is the use of a mold temperature which is close to the melt temperature ($T_m$) or to the glass transition temperature ($T_g$) for amorphous polymers. In order to decrease the cycle time which increases with the utilization of high mold temperatures, a variotherm process has been proposed [76]. The advantages of utilizing such approach are that this process allows for polymer degradation decrease, lower internal stresses, limiting of short shots among others.

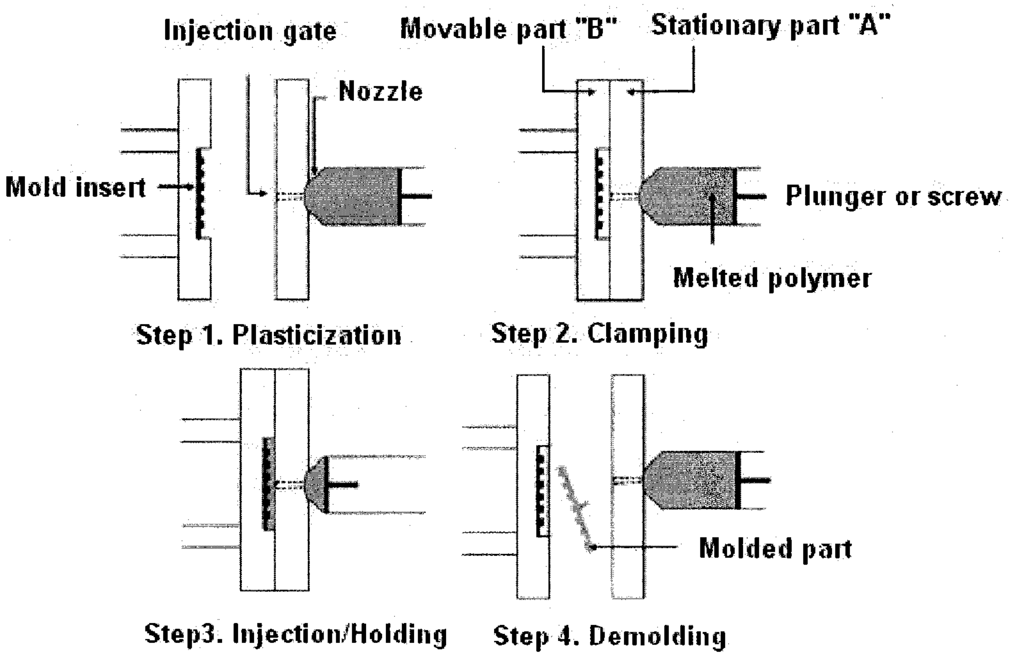

**Figure 2-4.** Schematic representation of injection micro-molding process flow. *Adapted from [76].*

The microinjection molding of thermoplastic polymers is a promising method for the large scale replication of patterned surfaces and is related to the development of MST/MEMS polymer based systems or parts. Injection molding should always be used in cases where large scale production is required. This manufacturing process was extensively utilized in all experiments reported in this comprehensive work.

## 2.4. Other Unconventional Techniques

Besides NIL, injection micro-molding and related techniques there are a number of unconventional methodos utilized for patterning of organic surfaces but the scaling up of manufacture has not been shown to be technically feasible. During the years, considerable attention gained the use of scanning probe lithography and soft lithography and its related techniques micromolding in capillaries, microtransfer molding, and solvent assisted micromolding [77, 78] for fabrication methods that can lead to sub-100 nm structuring of surfaces and functionalization of substrates by deposition of clusters of molecules. Among them, soft lithography is the best studied fabrication method, therefore its description follows.

Soft lithography is indispensable methodology for prototyping applications of test structures due to its simplicity and ease of use. Most commonly poly(dymethylsiloxane) (PDMS) is utilized as a soft mold or a template for the replication of polymer compositions with replication performed manually. PDMS molds are used since they exhibit low surface energy, flexibility, optically transparent and thermally stable. Disadvantages of this fabrication technique include lack of control reducing the deformation and distortion of the polymeric features and ability to optimize processing conditions.

In conclusion it is believed, that conventional techniques, e.g. NIL, S-FIL, and injection molding would continue to dominate the field of nano- and micro-structuring of polymer substrates. Therefore, in this work injection micro-molding was extensively utilized as a manufacturing technique of choice.

# CHAPTER 3

# INJECTION MOLDING OF PASSIVE OPTICAL COMPONENTS

*"Curiosity inspires Research."*

## 3.1 Introduction

A diffraction grating (DG) is a passive optical component which diffracts polychromatic light into its component wavelengths or monochromatic light into surfaces of constant phase, Figure 3-1(a). There are several types of diffraction gratings with different profile geometries that determine their properties. In most cases, after obtaining a master by various techniques the gratings are manufactured by UV curing of epoxy compositions. A typical grating consists of a thick piece of float glass, having a layer of patterned UV curable epoxy overlaid with a reflective coating, Figure 3-1(b) or a refractive index-matched epoxy, in the case of transmission type gratings. Since the manufacturing sequence is tedious and makes use of various equipment, and the final components contain a number of different materials, there have been attempts to eliminate some of the manufacturing expenses. Furthermore, the current manufacturing sequence is not suitable for applications in which DG spectroscopy capability is an integral part of the device [79]. Different techniques and materials have been investigated. Poly(methyl methacrylate) (PMMA), poly(carbonate) (PC), styrene-butadiene block copolymer (SBS), cyclo olefin copolymer (COC) and other polymers have been processed by injection molding or hot embossing to fabricate such gratings [80-83].

Among all polymers suitable for optical applications COCs are preferred since they are amorphous polymers made by a catalytic reaction of ethylene and randomly distributed 2-norbornene. The latter bulky group prevents forming of crystalline sites in the bulk volume and stiffens and strengthens the polymer chain. COC has high heat resistance, is a good moisture barrier, as seen in Table 3-1, is resistant to polar solvents, has low dissipation and dielectric loss, is highly transparent in the visible and near UV regions, and has low optical birefringence. These properties imply that COCs are excellent candidates for optical, electronic, and pharmaceutical applications [84]. Detailed information about the physical properties of TOPAS® COC 5013 S can be found in [84].

| property | unit | COC | PMMA | PC | epoxy [a] |
|---|---|---|---|---|---|
| heat deflection temp. | $^0$C | 130 | 92 | 142 | 72 |
| water absorbance | % | 0.01 | 0.1 | 0.04 | 0.07 |
| stress optical coeff. | $10^{-12}$, Pa$^{-1}$ | 4 | -4.6 | 68 | depends on the curing agent |

[a] The epoxy utilized in the commercial gratings used in the study is EPON 815.

**Table 3-1.** Physical properties of COC and other polymeric materials used for manufacturing of diffractive components.

### 3.2 Gratings Physics

The principle of a constructive interference imposes that a diffracted wavefront with rays in phase is formed only if the geometrical path difference between two adjacent grooves and given by:

$$d \sin \alpha - d \sin \beta, (\beta < 0) \tag{3-1}$$

equals an integer number of wavelengths, Figure 3-1. These relationships are expressed by the grating equation:

$$m\lambda = d(\sin \alpha - \sin \beta) \tag{3-2}$$

where $d$ is the groove spacing, and $\lambda$ is the wavelength. When the spectral order $m = 0$, the grating acts as a mirror, and the wavelengths are not separated. The last equation implies that light of wavelength $\lambda$ diffracted by a diffraction grating along direction $\beta$ should superimpose by integral fraction of $\lambda/2$, $\lambda/3$, $\lambda/4$ and so forth. This phenomenon is termed overlapping of the diffracted spectra and is intrinsic to every grating. Upon differentiation of eqn. (3-2) with respect to change of the wavelength, and assuming a constant value of $\alpha$, the angular spread $\Delta\beta$ of a spectrum of order $m$ between $\lambda$ and $\lambda + \Delta\lambda$ is found to be:

$$D = \frac{d\beta}{d\lambda} = \frac{m}{d\cos\beta} = \frac{m}{d}\sec\beta = Gm\sec\beta \tag{3-3}$$

where $G = 1/d$. The quantity $D$ is termed angular dispersion and is a measure of the separation between the diffracted light of different wavelengths. The resolving power $R$ of a grating is a measure of its ability to separate adjacent spectral lines of average wavelength:

$$R = mN = \frac{Nd(\sin\alpha + \sin\beta)}{\lambda} \tag{3-4}$$

where $N$ is the number of the illuminated on the surface grooves.

From the above equations it could be inferred that the properties of a grating element strongly depend on its geometry. On the other hand, the desired geometry and functionality of a grating, is a function of the manufacturing process and the properties of the used materials.

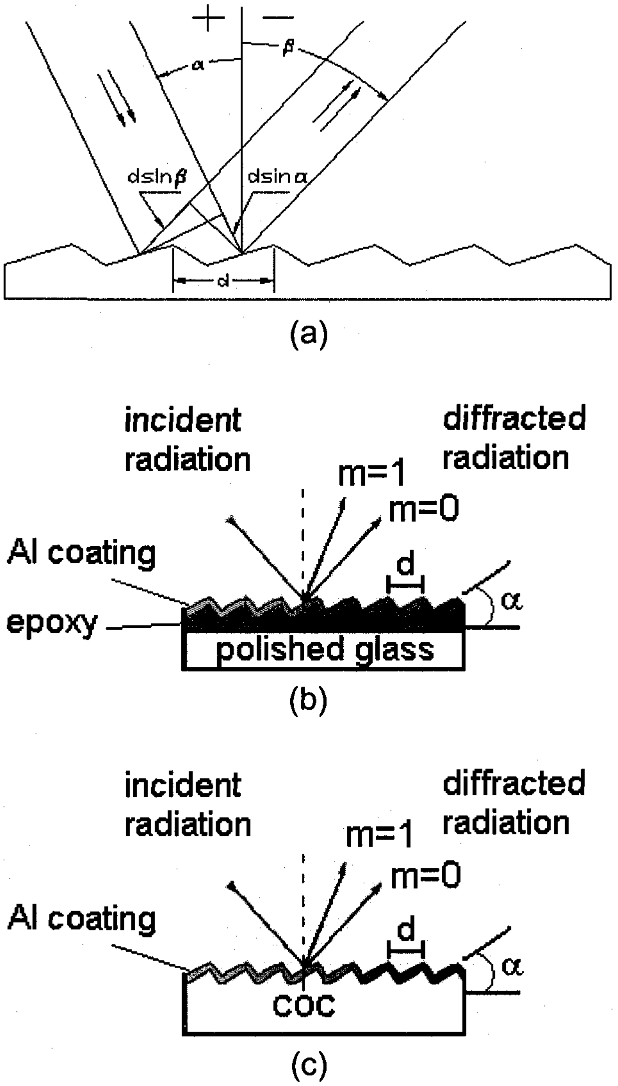

**Figure 3-1.** (a) Geometry of diffraction - formation of planar wavefronts, (b) current design of a ruled (e.g. with saw-tooth profile) diffraction grating employing multiple materials, (c) proposed conceptual design of an injection molded and metallized ruled diffraction grating.

### 3.3 Experimental Details

In this sets of experiments ruled diffraction gratings were fabricated and tested via injection micro-molding. A unique aspect of the present study was the utilization of commercially available optical grating as the injection molding tooling. The mold and replicated polymer gratings were characterized via atomic force and scanning-electron microscopy. After thermally evaporating a reflective aluminum (Al) coating with 150 and 250 nm thickness onto the untreated patterned area of the polymer replicas, diffracted power profiles of the polymer gratings were compared with that of the mold. It was found that $T_{mold}$ and $T_{noz}$ are important parameters influencing the reliable replications of the grooves. Statistical analysis, however, revealed that the cyclic olefin copolymer (COC) replicated well the micro-topography of the mold but did not replicate properly (within ~20 nm) the nano-topography formed by the Al grains. Also, the grooves underwent small shrinkage and the thermal deposition did not change the pitch of the bare gratings after metallization. Grain size quantification, performed with two-dimensional linear filtering of the topographic images, revealed that the Al coating with 150 nm thickness had smaller grains than that with the 250 nm coating. Furthermore, testing of delamination of the reflective coatings via boiling in deionized water revealed good adhesion between the COC and Al interface.

Lastly, photoelasticity measurements revealed detectable stress levels only around the gate of the molded components suggesting that COCs are excellent materials for optical applications requiring low level of stress. In what follows, a detailed description of the gratings fabrication and characterization procedures is presented.

### 3.3.1. Replication Process

The replication process or micro-molding was performed by building a customized electrically-heated mold base and mounting it on a 12 ton BOY (BOY

Machines Inc.) digitally controlled micro-molding machine as seen in Figure 3-2. The mold used was a commercially available 12.7x12.7 mm ruled diffraction grating with 1200 grooves/mm and a blaze angle $\alpha=17^{0}27'$, coated with Aluminum (Al), and having a service temperature range between - 20 to +100 °C. This approach was cost-effective for testing the polymer moldability over large patterned surfaces and allowed for addressing issues related to injection molding of diffractive optical components. It did not, however allow for a robust optimization of the molding process. Consequently, as it will be seen later in Chapters 4 and 5, a procedure for silicon (Si) based mold manufacturing suitable for the manufacture of components for other possible applications has been successfully developed and implemented. In this round of experiments, two different sets of processing conditions, e.g. A and B, were chosen based on the polymer manufacturer's recommendations and previous experience with molding of COC, as seen in Table 3-2.

| Parameter | Units | Set-up | | Measured Height, nm | |
|---|---|---|---|---|---|
| | | A | B | A | B |
| $T_{noz}$ | °C | 249 | 291 | | |
| $P_{hold}$ / time | MPa / sec | 7.5/3 | 7.5/10 | | |
| n | 1/min | 200 | 200 | min~40 | |
| $V_{inj}$ | mm/s | 100 | 100 | max~100 | ~180 |
| $T_{mold}$ | °C | 85 | 116 | | |
| $T_{sep}$ | °C | 70 | 70 | | |
| Sprue Temp | °C | 22 | 140 | | |

**Table 3-2.** Molding conditions and their influence at the DG (bare) grooves height.

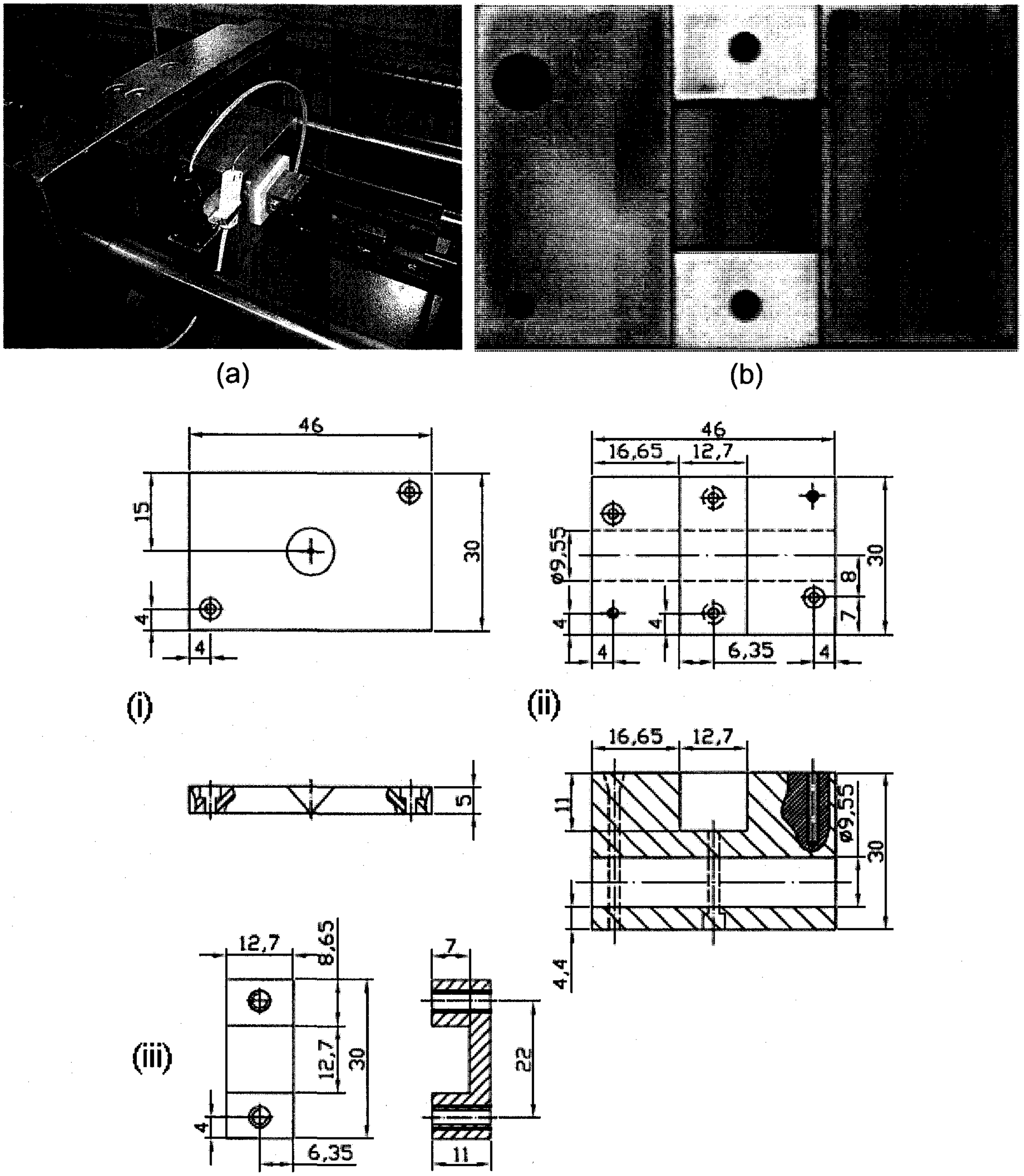

(c)

**Figure 3-2**. Digital pictures of (a) mold base with attached cartridge heater and thermocouple and (b) the mold tooling (a commercial ruled diffraction grating) mounted in the mold base – the space formed between the edges of the mold tooling and the mold base were sealed (not shown in the image) with special epoxy to prevent polymer flow during the filling stage; (c) CAD drawing of the mold fixture – (i) cover plate, (ii) mold base, (iii) removable mold base.

### 3.3.2 Scanning Electron Microscopy

Prior to molding the original commercial diffraction grating was imaged with Scanning Electron Microscope (SEM - LEO 1550 VP equipped with a Gemini column) while running in a variable pressure mode with a Nitrogen rich environment, Figure 3-3.

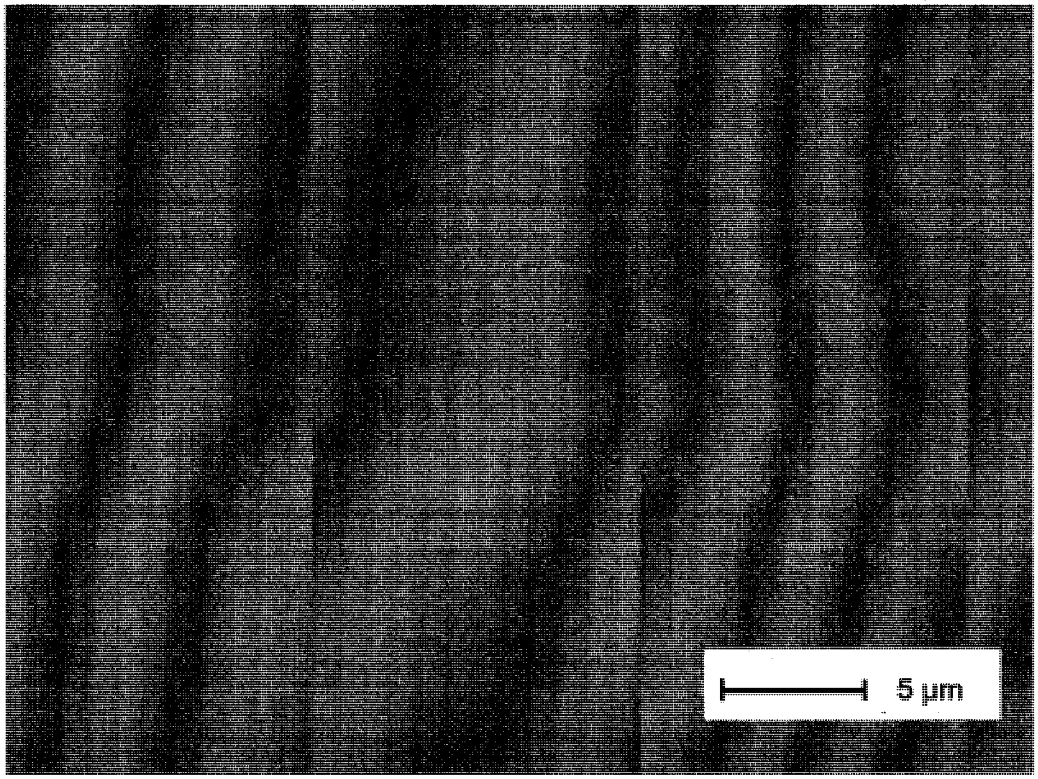

(a)

**Figure 3-3**. SEM-VP mode image of commercial ruled DG utilized in this study as a mold tooling. Grooves structure is clearly seen.

Following the replication process, several bare polymer replicas were also inspected in the same way. To image the metallized polymer replicas, however, a standard mode of operation of the SEM was chosen since a conductive adhesive copper tape was attached at the very, non-patterned but metallized, edge of the gratings. Images with good contrast were obtained allowing for an evaluation of the achieved grain structure of the Al coating, Figure 3-4. Such an approach was not possible during imaging of the molds since the copper tape could have peeled off the patterned surface during its removal after the inspection. Following imaging, all samples were scanned with Atomic Force Microscope (AFM).

### 3.3.3 Metallization Process

Metallization of the bare, untreated diffraction gratings, rinsed in 2-propanol ($C_3H_8O$, isopropyl alcohol) in advance, was performed by means of a physical vapor deposition (PVD) technique [85] on Telemark TT6 evaporator by Indel Systems, Figure 3-5. The e-beam induced thermal evaporation was achieved at an operating chamber pressure of ~ $1.3\text{x}10^{-5}$ Pa with a deposition rate of 1.0 – 1.4 nm/s. The magnetized deflection of the e-beam was set so that the e-beam followed a spiral trajectory while impinging on the 99.999% pure Aluminum (Kurt J. Lesker company) in the crucible, thus enabling uniform temperature of the melt. Other e-beam trajectories, as well as the dwell time and frequency could have been chosen to influence the rate of metal deposition and consequently the quality of the Al film but have not been implemented. Metallized gratings with two different coating thicknesses were produced, e.g. 150 nm and 250 nm.

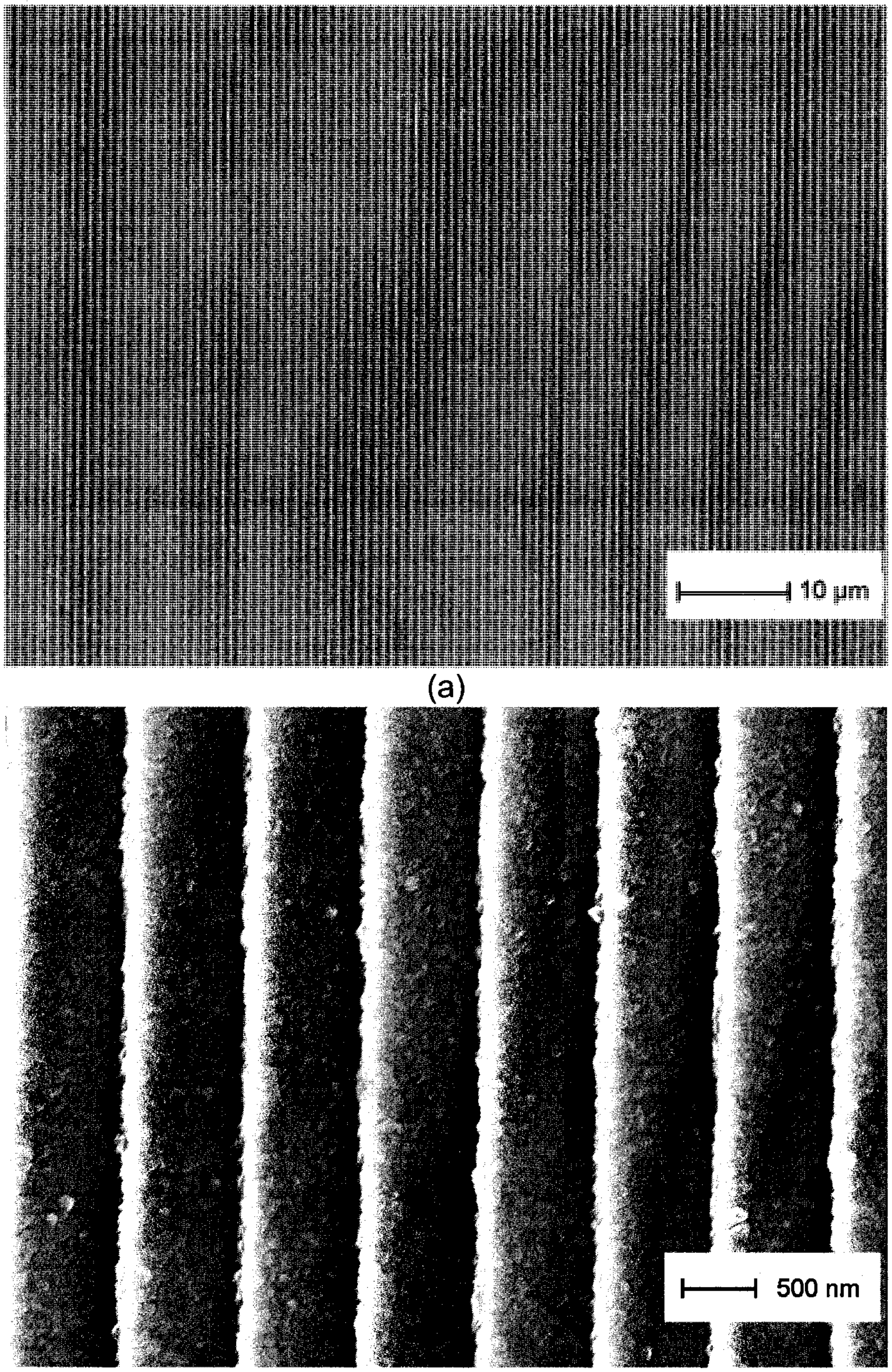

(a)

(c)

**Figure 3-4.** SEM images of injection molded and coated grating with 150 nm Al (a) top view of a large area with uniform grooves, (b) magnified area of a region from the top image. The Al grains are clearly visible.

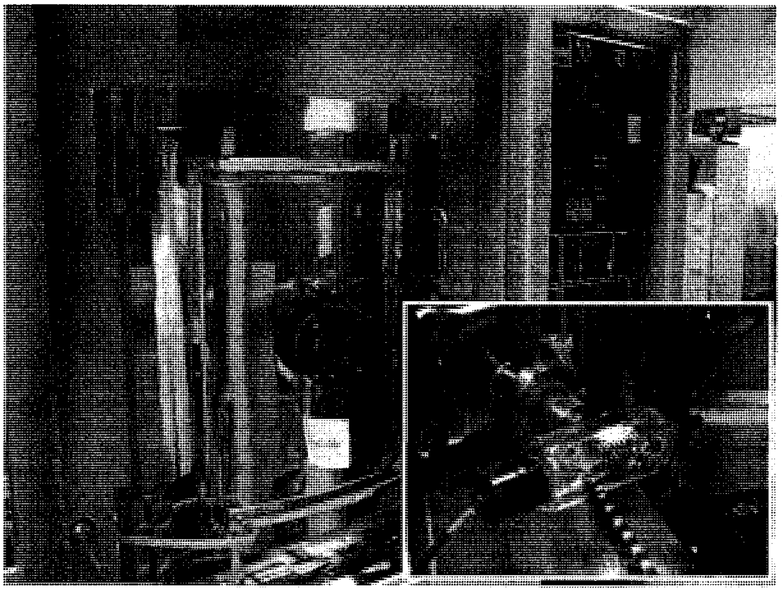

**Figure 3-5.** Digital photograph of the PVD tool utilized for Al deposition of the injection molded gratings. Inset shows the high vacuum pressure gauge of the e-beam evaporator.

### *3.3.3.1 Grain Size Quantification*

Two-dimensional linear filtering of the spatial domain was implemented to quantify the grain sizes of the metal reflective coatings on the original grating, e.g. the mold, and on the molded and metallized gratings with 150 and 250 nm Al films. The procedure was performed via WSxM® and Matlab. First, matrix convolution of the original AFM images (details about AFM imaging are given later in the chapter) was implemented. The procedure is a neighborhood operation in which each output pixel of the resulted convoluted image matrix is a weighted sum of the neighboring input pixels of the original AFM image. The weights were defined by a convolution kernel *K* chosen to be a 5x5 matrix with the following elements:

$$K = \begin{pmatrix} 1/6 & 1/6 & 1/12 & 1/6 & 1/6 \\ 1/6 & 0 & -1/3 & 0 & 1/6 \\ 1/12 & -1/3 & -1 & -1/3 & 1/12 \\ 1/6 & 0 & -1/3 & 0 & 1/6 \\ 1/6 & 1/6 & 1/12 & 1/6 & 1/6 \end{pmatrix} \qquad (3\text{-}6)$$

The matrix convolution operation yielded an improved edge enhancement and sharpened boundaries of the surface topography, e.g. the Al grains. Second, the convoluted images were converted to binary ones, with black and white pixels. The black regions constituted the background and the white regions (the grains) constituted the foreground of the binary images. Third, the area measured by the number of the white pixels was calculated via a build-in procedure in MATLAB. The latter calculates the area of an individual pixel by looking at its 2-by-2 neighborhood. For example, pattern with one white (*on*) pixel is defined to have an area $A = 1/4$, Figure 3-6. Five more patterns were utilized, e.g. patterns with zero *on* pixels, two adjacent *on* pixels , two diagonal *on* pixels, three *on* pixels, and all four *on* pixels, having area 0, 1/2, 3/4, 7/8, and 1 respectively. Two AFM 256x256 pixel images of 5x5 µm scanned areas of the mold and the metallized gratings were processed and the average pixel size areas per group were found, Figure 3-7. The results were used to measure the grain size distribution, as well.

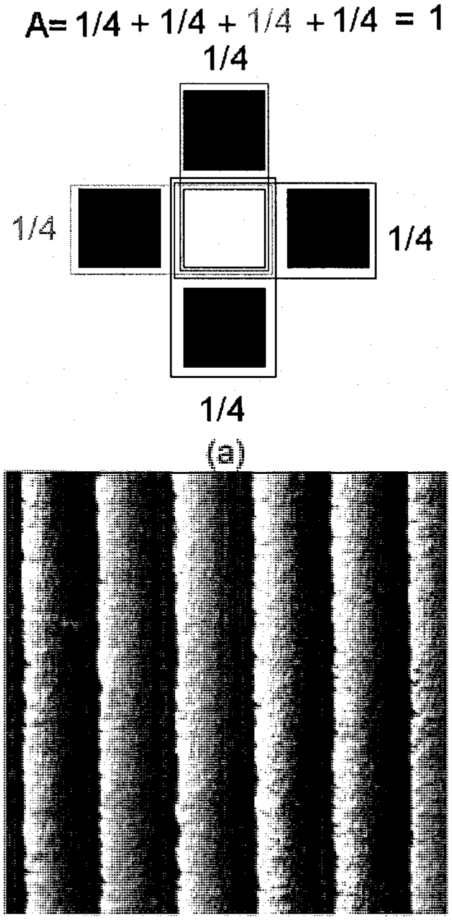

(a)

(b)

**Figure 3-6.** (a) An example for calculating the area of one *on* pixel surrounded by 2x2 off pixels (b) AFM topography image of the commercial grating before digital processing (image convolution).

### 3.3.4 Scanning Probe Microscopy

Scanning Probe Microscopy, performed in air with Digital Instruments Dimension 3000 AFM in a TappingMode™, was used to collect quantitative data of the surface topographies, of the commercial grating and the injection molded polymer replicas molded with "A" type, Figure 3-8, and "B" type, Figure 3-9, molding conditions. The probe used was an Antimony (n) doped Tapping Mode Etched Silicon Probe, Aluminum coated (TESPA), for enhanced laser detection

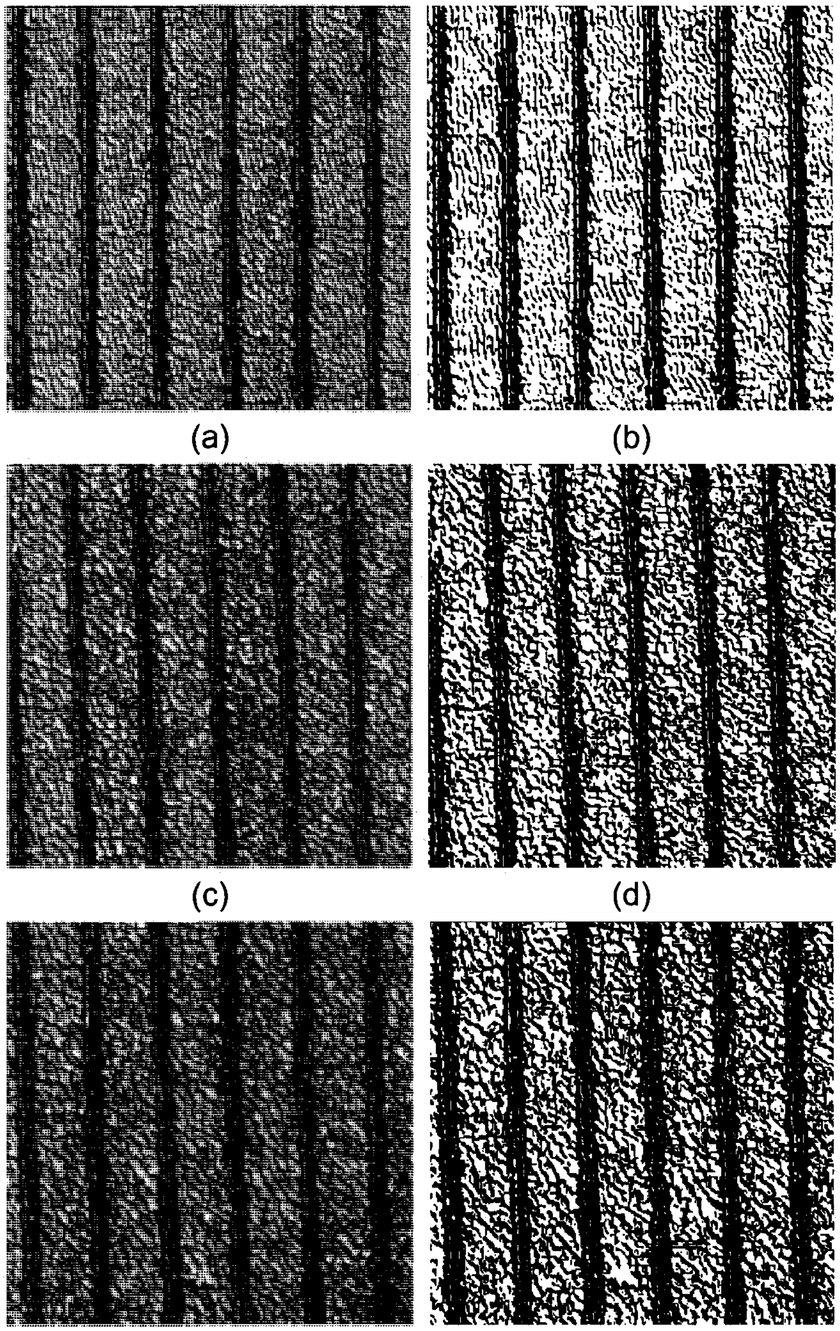

(a) (b)

(c) (d)

(e) (f)

**Figure 3-7.** Matrix convoluted AFM images, above left, and binary images, above right: (a, b) mold; (c, d) metallized grating with 150 nm Al; (e, f) metallized grating with 250 nm.

signal with nominal spring constant k=42 N/m, nominal resonant frequency f=320 kHz, tip radius of curvature ROC<10 nm (max ROC=15 nm) ant tip height h=10-15 µm. Prior to section analysis, the data was modified to eliminate unwanted features from the scan lines by using a polynomial filter. It removed the Z – offset between scan lines, and the tilt and the bow in each scan line, by calculating a third order, least-squares fit for the selected segment and subtracting it from the scan line. The samples were oriented in such a way that they were scanned across the grooves in the fast X-direction. To assure proper scanning of the sample topography, the feedback parameters Setpoint Amplitude (SA), Integral Gain (IG), Proportional Gain (PG), and Scan rate (SR) were set so that the trace and retrace scans looked identical. They were regularly monitored throughout the scanning process. The mold, a bare grating, and two metallized gratings were scanned at ten different 5x5 µm locations each. As criteria for judging the quality of replication of the surface topography of the samples, the following parameters obtained by the section analysis were considered - the root-mean-square deviation of the z-values (RMS); the mean roughness of the roughness curve relative to the center line ($R_a$); the maximum height ($R_{max}$) defined as the difference between the highest and lowest points on the cross-sectional profile; the ten-point mean roughness ($R_z$) defined as the difference between the five highest peaks and the five lowest valleys; the pitch (horizontal) distance and the peak-to-valley (vertical) distance. The quantitative data was statistically analyzed via one-way analysis of variance (ANOVA), a robust procedure that determines if groups (mold and replicas) are similar or not in the measured characteristics.

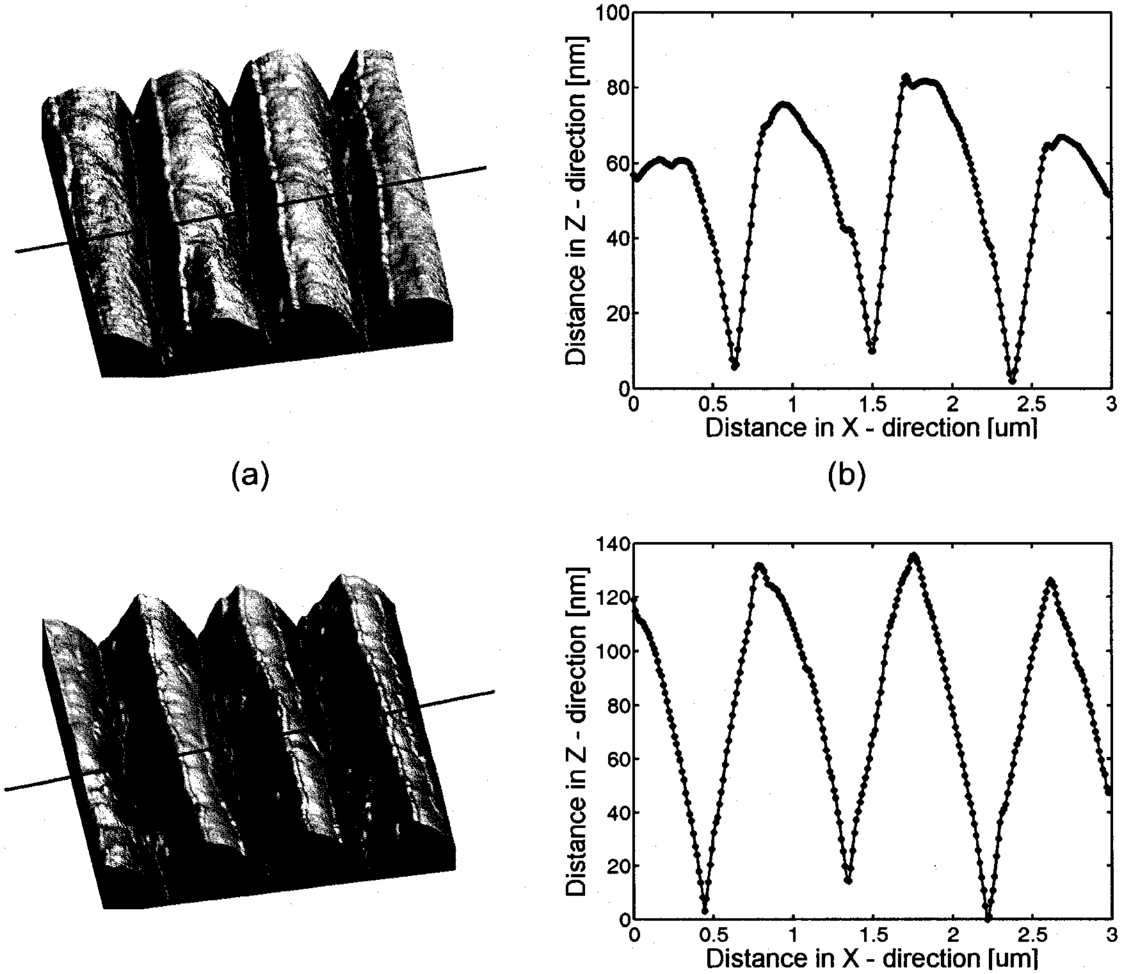

(a) (b)

(c) (d)

**Figure 3-8.** (a, c) AFM surface plots and (b, d) undesired profile cross sections along the solid line of typical scanned areas of the bare gratings achieved by molding with type "A" molding conditions. Scan size 3x3 µm. *Data post-processing performed with WSxM®.*

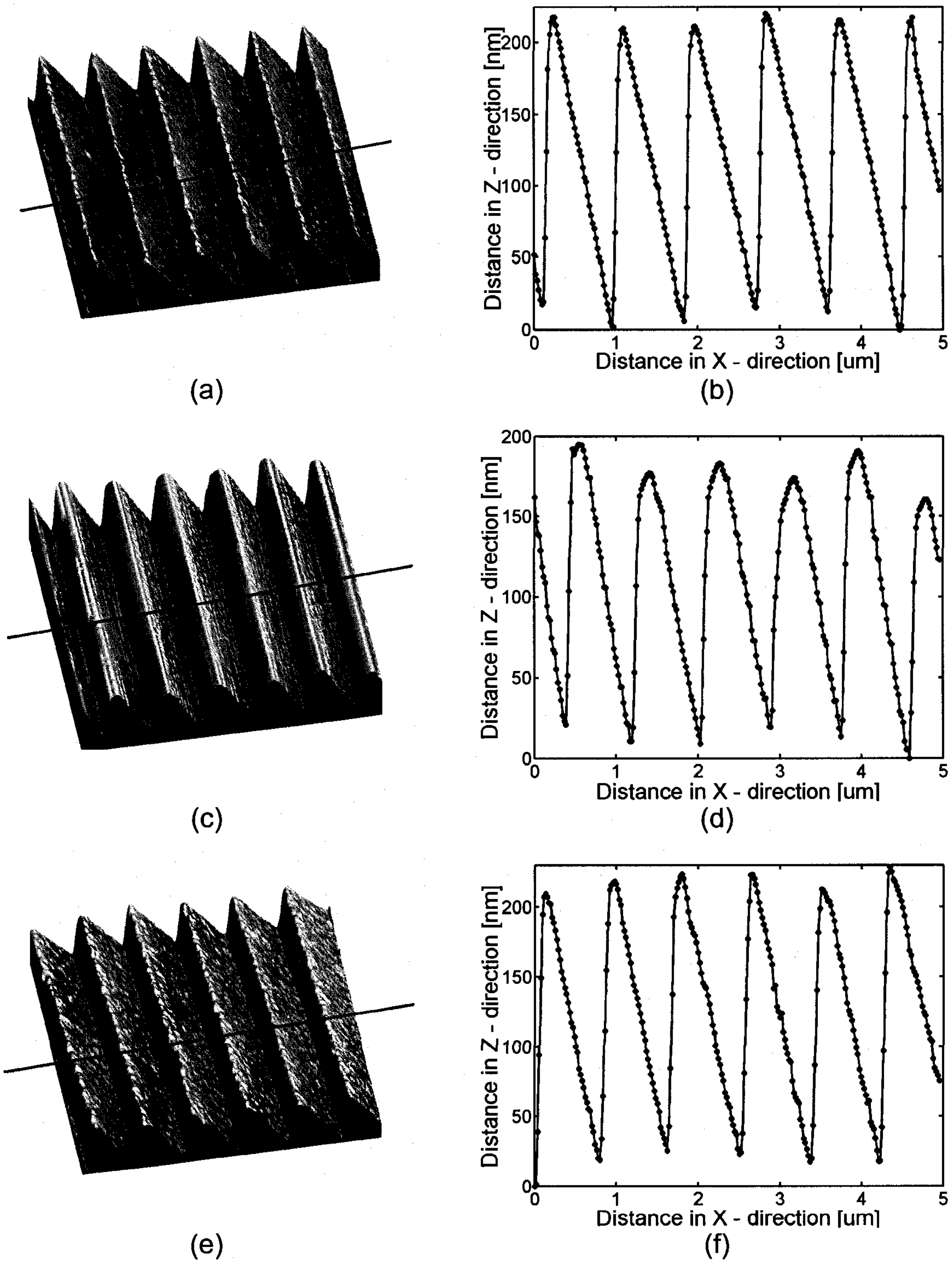

**Figure 3-9.** AFM surface plots, above left, and profile cross sections along the solid lines, above right, of typical scanned areas: (a, b) the mold, (c, d) the bare gratings, (e, f) the metallized gratings. The gratings were molded with "B" type molding conditions. Scan size is 5x5 μm. *Data post-processing performed with WSxM®.*

### 3.3.5 Diffracted Power Measurement

An industry standard approach for measuring the efficiency of a grating is by calculating the absolute efficiency in a Littrow configuration in which the incident and diffracted rays are in auto collimation, e.g.

$$m\lambda = 2d \sin\alpha \tag{3-7}$$

In any other off Littrow configuration the efficiency of a grating element decreases. The grating that was utilized as a mold in this study had two major maxima at around 500 nm and 1600 nm according to the manufacturer's specification. A different and less difficult to implement testing approach was used in our experimental setup, Figure 3-10. An infrared (IR) tunable laser (Agilent 8164A) was utilized to provide monochromatic IR light in the range between 1460 nm to 1580 nm. A single mode fiber was used as a waveguide to a monochromator unit in which the gratings were mounted. At the exit slit of the monochromator, an IR power phtodetector (InGaAs detector) detected the diffracted light from a grating under test. It was connected to a power meter (Newport, Model 2832C), calibrated for the used wavelength, which measured the diffracted power. Since it was difficult to attach every single grating at the same exact location on the mount fixture only normalized diffracted power values were reported, Figure 3-11. This approach allowed for the comparison between the output diffracted power curves of the commercial grating and molded polymer replicas since any deviation of the groove shape would change the shape of the curve. The whole surface of the grating was illuminated with a monochromatic light with six different wavelengths, thus forming diffracted surfaces of constant phase (wavefronts). Ten polymer molded gratings were optically characterized along with the commercial grating.

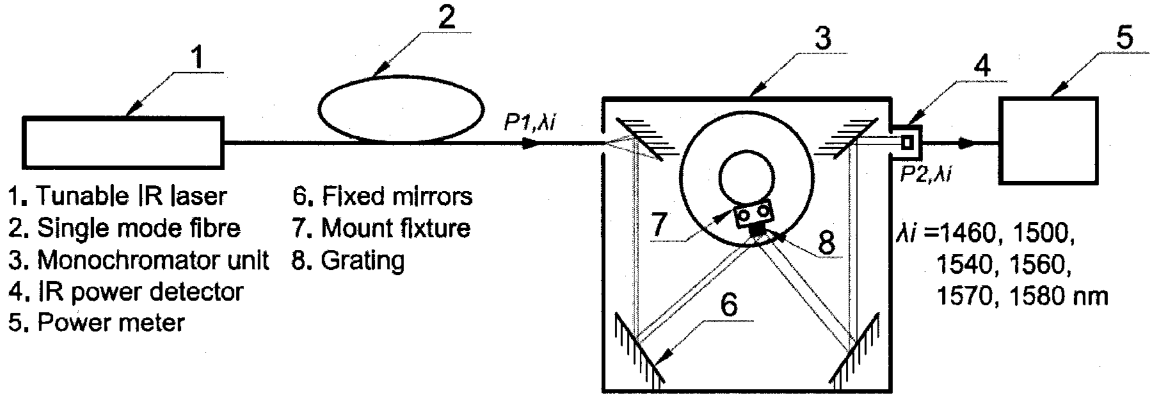

**Figure 3-10.** Optical bench set-up with a constant input power $P_1$=5 mW and the six wavelengths used.

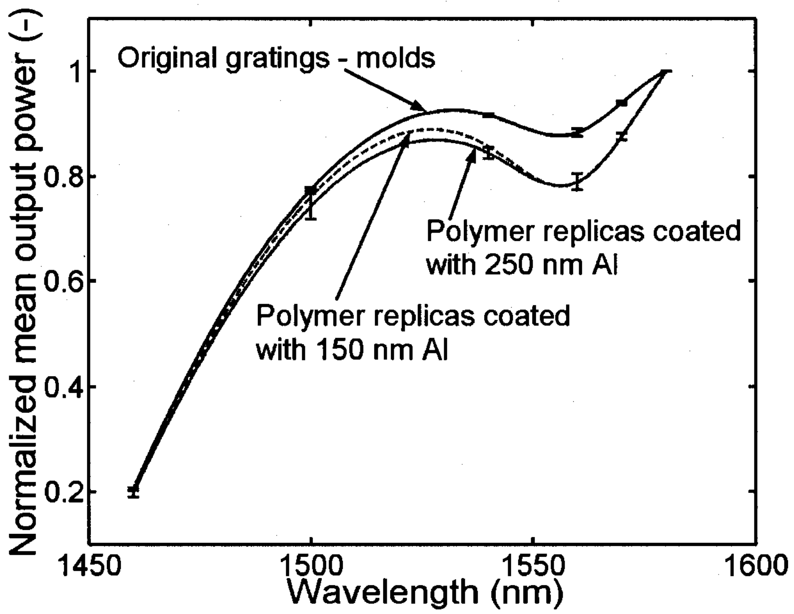

**Figure 3-11.** Normalized mean output power as a function of the wavelength. All values normalized at 1580 nm.

### 3.3.6 Photoelasticity Measurements

A standard polarimeter (Strainoptics PS-100) was used to observe the direction of stress and to measure the retardation and the stress magnitude of a chosen point of interest (POI) located at a close distance to the gate of the polymer gratings, Figure 3-12. The measurement technique of choice was chosen to be "Senarmont" analyzer rotation method, requiring plane polarizers with clockwise rotation of the analyzer filter. Only polymer replicas produced by B processing conditions were evaluated since their grooves were well replicated.

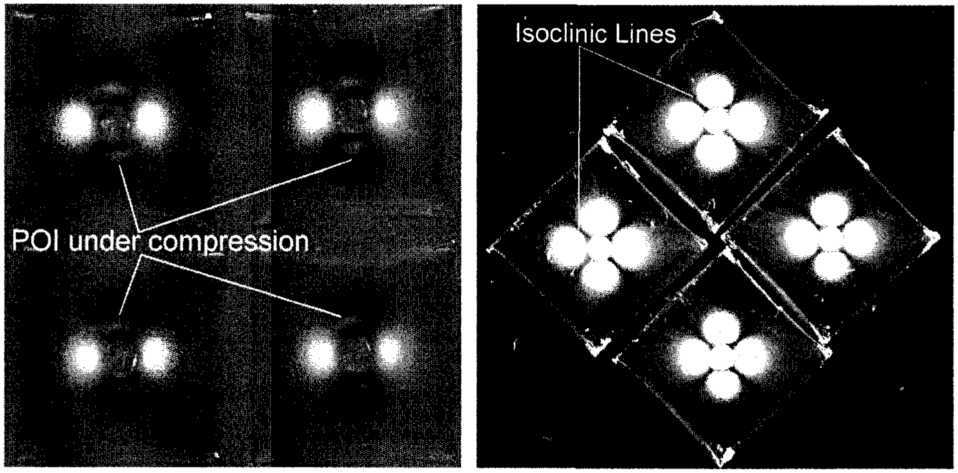

(a) (b)

**Figure 3-12.** Photoelasticity measurements of four bare gratings: (a) with highest order fringe (n = 1.05, blue color) around the gate with low stress levels everywhere else, (b) isoclinic lines - locus of points which have the same direction of stress.

### 3.4. Boiling Water Test for Delamination

To test the adhesion strength of the Al coatings a simple boiling water delamination testing was performed. Two metallized gratings, one with 150 nm and a second one with 250 nm Al were immersed into boiling deionized water with temperature ~100 $^0$C for a time 120 sec. Following that the components were left to cool down to room temperature, blow dried with nitrogen gas and imaged with SEM while running in a variable pressure mode with Nitrogen rich environment to detect defects formation, Figure 3-13.

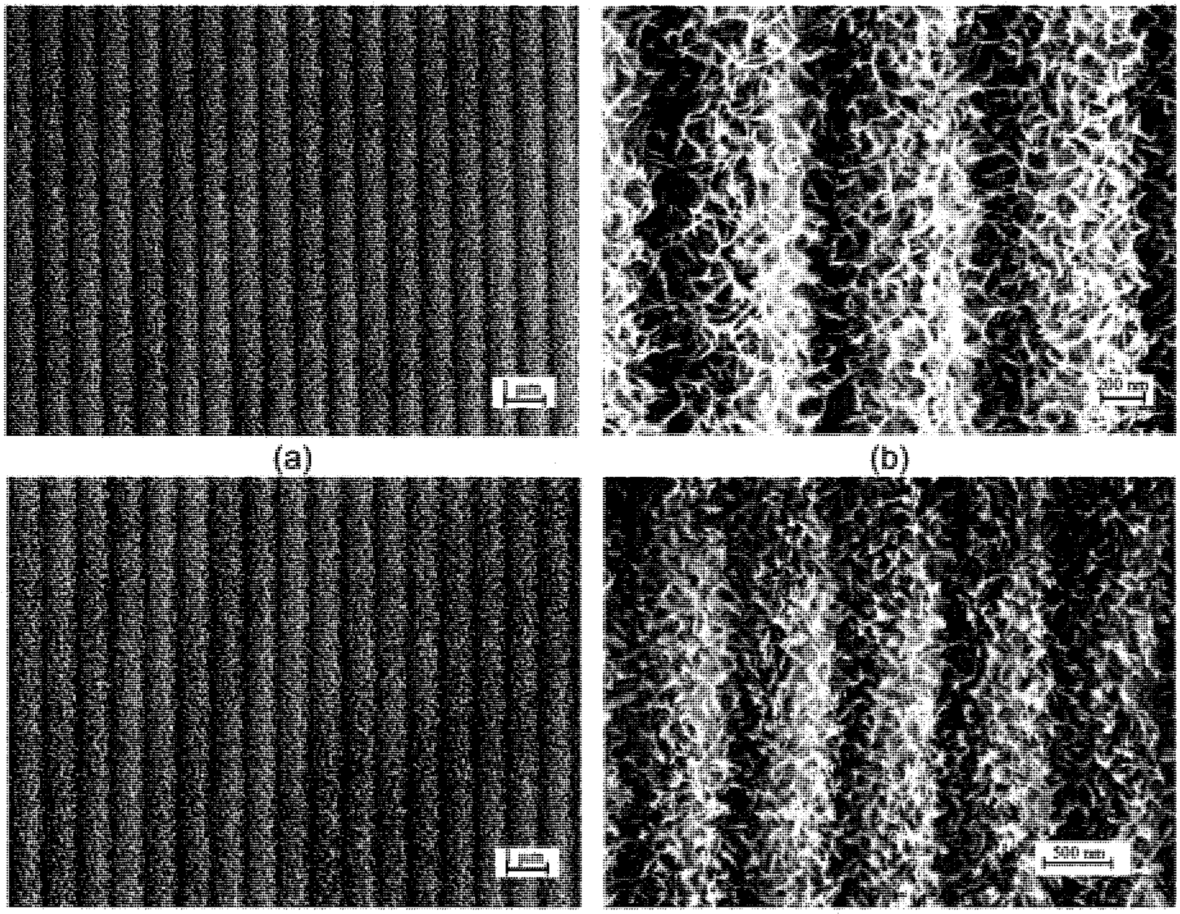

(a) (b)

(c) (d)

**Figure 3-13.** SEM images of diffraction gratings, with 150 nm (a, b) coating and 250 nm (c, d), that underwent boiling testing. It is clearly visible that no delamination occurred at the interface between the COC substrate and Al films. Al film coherence was destroyed by the boiling water, which formed Al/$Al_xO_y$ spikes having large surface area.

## 3.4. Results

The results after replication with the two sets of molding conditions were found quite different. Molding with type "A" conditions led to a very poor replication of the grating profile as seen from AFM measurements on Figure 3-8. The replicated groove height was not uniform, and values between 40 nm and 100 nm were measured. It was found that the $T_{mold}$ and $T_{noz}$ were lower than those required for a full profile replication. Therefore, their values were accordingly increased in type "B" setup and 30 gratings were injection molded, Table 3-2. Additionally, the channel from the end of the nozzle to the gate, e.g. the sprue bushing, was also heated to temperature above $T_g$ of the polymer, which is ~ 130 $^0$C, by inserting cartridge heaters. More detailed description related to this temperature management can be found in Chapter 5. The achieved effect was similar to using heated extension of the nozzle. AFM measurements of the profile confirmed the improved replication.

| Criterion | Mold and Bare Replica # 5 | Mold Coated Replicas # 5 and 16 |
|---|---|---|
| | p-value | p-value |
| RMS | $0 < \alpha\_val$ | 0.2649 |
| $R_a$ | $0 < \alpha\_val$ | 0.8458 |
| $R_{max}$ | $0 < \alpha\_val$ | 0.9250 |
| $R_z$ | $0 < \alpha\_val$ | $0.0343 < \alpha\_val$ |
| Peak-to-Valley | $0 < \alpha\_val$ | 0.1903 |
| Pitch | 0.3422 | 0.7131 |

**Table 3-3.** P-value statistics results obtained from the one-way ANOVA test. The accepted level of significance was chosen to be $\alpha\_val=0.05$.

The data collected from the AFM measurements was statistically analyzed and the probability *p-value* was calculated for each measured parameter, Table 3-3. Any *p-value* smaller than *α_val* suggests that the groups are not statistically similar in the measured parameter. The mold profile was compared with that of the bare replicas, Figure 3-14 and that of the metallized replicas Figure 3-15. The results were then represented with box-plots. As seen in Figure 3-14(e), a box-plot consists of a box and whisker lines for each group number. The box has horizontal lines at the lower quartile, median, and the upper quartile values. The whiskers are lines that extend from each box and represent the extent of the rest of the data. The dot in the middle of the lower whisker line is placed if there are no outliers. The notches graph a robust estimate of the uncertainty about the sample means and could be used for box-to-box comparison.

From Figure 3-14, it is clearly visible that the replica's groove height distribution is statistically different from that of the mold, which was confirmed by the very small p-value from the ANOVA analysis, Table 3-3. The outliers suggest that some scanned areas had acceptable groove heights. The difference between the two medians, though, is ~ 20 nm, a very small value, and was improved to about ~ 5 nm after metallization of the grating, resulting in statistically more equal mold and metallized micromolded gratings as seen in Figure 3-15(e). The Pitch values distribution for the two groups is similar, with group two, having larger sample distribution, median and upper quartile than group one, suggesting that the polymer-structured grooves underwent shrinkage.

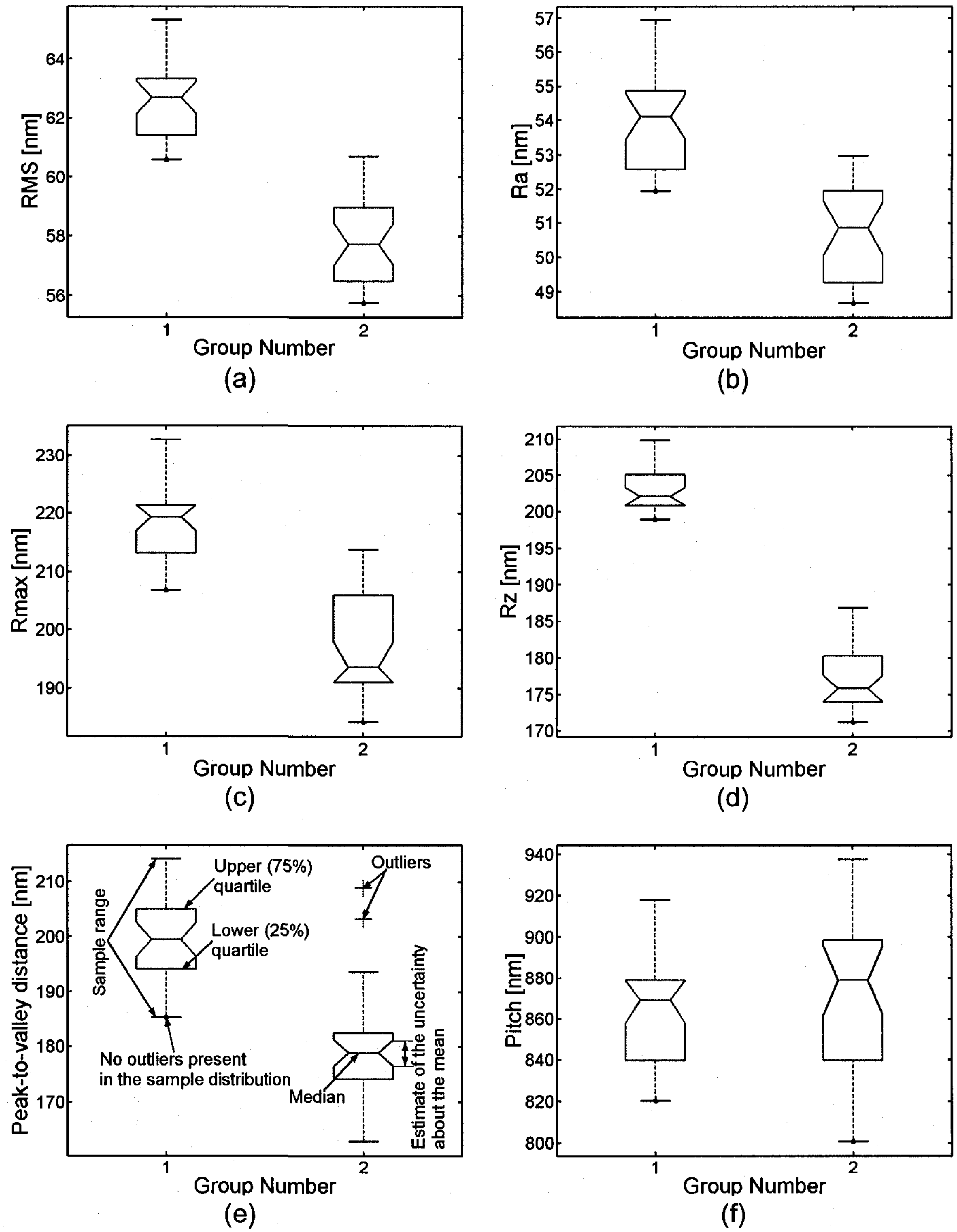

**Figure 3-14.** Box-plot statistics of all the observed parameters, obtained by the AFM, comparing the mold (group number 1) and the bare replica (group number 2, molded with type "A" conditions).

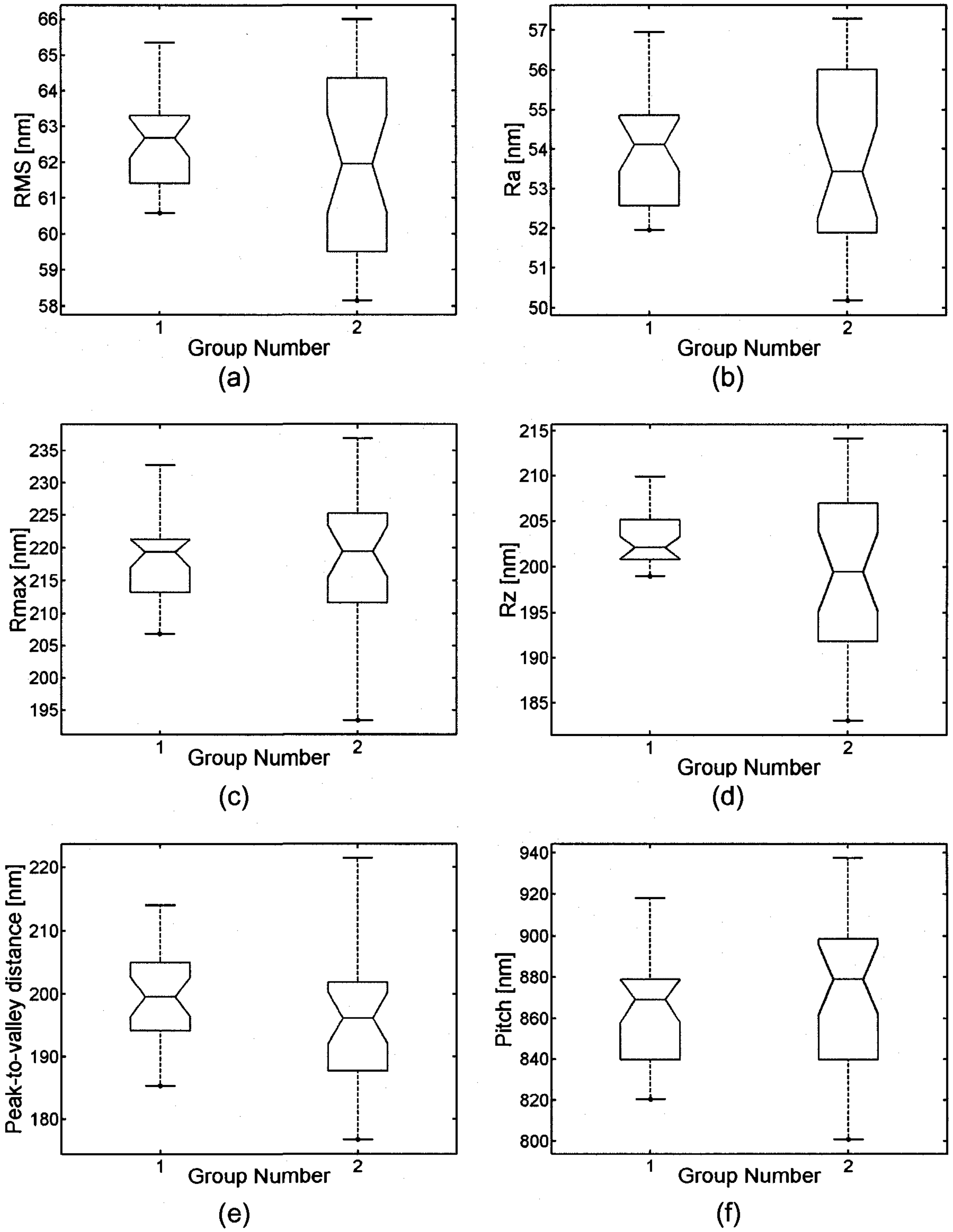

(a) (b) (c) (d) (e) (f)

**Figure 3-15.** Box-plot statistics of all the observed parameters, obtained by the AFM, comparing the mold (group number 1) and the metallized replicas (group number 2, molded with type "B" conditions, 150 nm Al coating).

The calculated RMS, $R_a$, $R_{max}$, and $R_z$ *p-values* were very small due to the fact that the polymer did not replicate the surface topography formed by the finite Al grains size. This finding was attributed to the low value of $T_{mold}$. Therefore, the original and replicated surfaces were not statistically equal. It was estimated by AFM measurement, e.g. matrix convolution of the AFM images of the mold that the grain size is ~ 40-50 nm. In addition, it is worth indicating that the mold is actually a diffraction grating, which exhibits its highest efficiency (from manufacturer's specification) at $\lambda \sim 500$ nm. As a general rule, an optical surface's roughness should be less than $\lambda/10$ in magnitude. The metallization of the grating, on the other hand, changed the distribution of the parameters towards improving the statistical similarity between the two groups, as seen from Figure 3-15. The RMS and $R_a$ box-plot statistics could be regarded as criteria for estimating the smoothness of the diffractive coatings, Fig. Figure 3-15(a) and Figure 3-15(b). Group one was with narrower distribution than group two, which suggests that the Al coatings were deposited with different conditions compared with those for the mold. Indeed, SEM imaging, Figure 3-4, coupled with the matrix convolution of the AFM image, Figure 3-7 unambiguously revealed that the metallized polymer gratings had larger grain sizes. It was estimated that the grain sizes of the 150 nm and 250 nm coatings were 50-80 nm and 50-95 nm respectively. The $R_z$ and $R_{max}$ statistics could be used to estimate the height distribution (saw-tooth profile height or the micro-topography) coupled with the grain size variation (nano-topography). The $R_{max}$ statistics revealed a *p-value* smaller than the accepted level of significance, which is attributed to the variations in the micro-topography. Finally, the AFM measurements illustrate that, at least for the 150 nm coated gratings, the PVD preserved the pitch distribution and changed (towards improving) the Peak-to-Valley distance of the polymer gratings, Figures 3-15(e) and 3-15(f).

The two-dimensional linear filtering revealed also that the average calculated pixel area of the micromolded polymer gratings vs. that of the commercial grating were 73% and 63% for the 150 nm and 250 nm Al coated components. These results suggest and support the previously discussed conclusions about the grain size distribution. In addition, it can be inferred that the smaller grains, e.g. in the case of the 150 nm Al coating, covered the area better than the larger ones, e.g. in the case of the 250 nm Al coating. Finally, SEM imaging of the coated gratings that underwent boiling testing, as seen from Figure 3-13, revealed that no delamination occurred on the interface formed by the patterned COC surface and the Al coating. Interestingly, the Al film coherence was destroyed by the boiling water, which formed surfaces with spikes having large surface area. The spikes are believed to be formed of $Al/Al_xO_y$ since some oxidation inevitably occurred during testing. Two-dimensional Fourier transform was used to assess the geometric characteristics of the spatial domain (SEM) images before and after boiling test, Figure 3-16. Because the image in the Fourier domain is decomposed into its sinusoidal components, it is easy to examine the geometric structure in the spatial domain. The dominating direction of the vertical regular pattern (grooves) seen from the insets, is shown as a horizontal line on the transformed images. It is constructed by dots or reflexes which form the images' characteristic frequencies. Within a single domain area, the integrity of the grooves was lost, as seen from the decreased number of reflexes of the Fourier images after the boiling test. At last, it is important to be noted that, though no treatment of the gratings was done in this work, formation of new carbonyl and carboxyl groups on COC surfaces via pretreatment with oxygen rf plasma leads to an increase of the adhesion strength between COC and metals and could be used if required [85].

The diffracted power measurement, Figure 3-11, shows that the replicated micromolded gratings had the same response to the IR radiation regardless of the thickness of the coating. This can be attributed to the fact that their geometry and surface imperfections are similar. The lower value of the local minima, compared with that of the original and observed around 1550 nm, might be due to the larger grains, the scattering loses from the surface, and due to the reduced patterned surface area of the replicas (the mold was inserted into the mold fixture and the gaps between the walls and its edges were sealed with an epoxy, thus also covering some of the patterned area of the mold which was not transferred onto the replicas). Despite this, the shape of the curves is similar, which strongly suggests that the original and replicated gratings are comparable with each other.

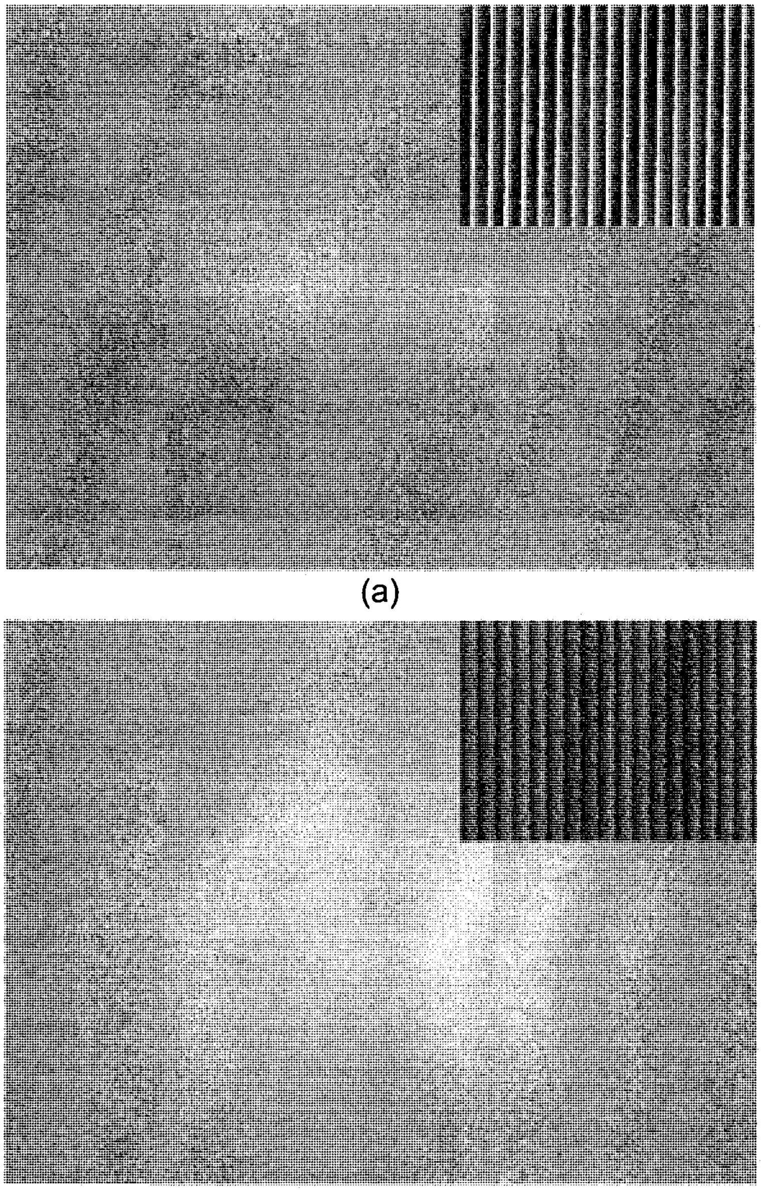

(a)

(b)

**Figure 3-16.** The two-dimensional Fourier transform of gray scale SEM images of a diffraction grating (a) before boiling test and (b) after boiling test. The sharp reflexes visible at the top image clearly suggest for a conformal, well-defined periodical grooves' structure that has been lost after the boiling test. The insets show the original SEM images.

The photoelasticity measurements of the bare gratings revealed that the stress was primarily concentrated only around the gate, which suggests the future implementation of a different gate design and location. The calculated retardation and stress value (maximum for the entire area) at the point of interest (POI) were R = 370.5 nm and σ = 92.625 MPa, respectively. The observed isoclinic lines, e.g. the lines that connect points with the same direction of stress were found to spread out of the gate towards the edges. The highest order fringe observed at the POI was n = 1.05 (blue color), Figure 3-12. These results also strongly suggest that the COCs could be used in optical components requiring low stress.

## 3.5 Summary

Injection micromolding with cyclic olefin copolymer was utilized to replicate polymeric ruled diffraction gratings with two different processing conditions. Characterization of the mold, an optical grating element itself, and a number of molded replicas revealed that higher melt and mold temperatures are vital for improving the fidelity of replication. Statistical analysis confirmed that for improved replication of the nano-topography, formed by the Al grains, even further increase of their values is necessary. It also unveiled that the polymer material had experienced small shrinkage. Two-dimensional linear filtering of the topographic images revealed that the Al coating with 150 nm thickness had smaller grains than that with a 250 nm coating and that the mold had finer grain sizes. The diffractive power measurements showed performance of the micromolded and metallized gratings to be similar to that of the commercial optical grating. A boiling test in deionized water showed good adhesion between the untreated COC and Al surfaces. These results strongly suggest that COC and injection micromolding could be used for manufacturing of low cost diffraction gratings.

Finally, potential applications which can benefit from this study are envisioned to be: (i) manufacture of transmission diffraction gratings in which there will be no need for index-matching epoxy, (ii) patterning diffraction grating profiles right on moldable polymeric microfluidics-based platforms [79] for integration of spectroscopy analysis capability [86] in the device, (iii) employing diffraction grating as light couplers of diverging LED emitted light [87], (iv) antireflective binary crossed diffraction gratings [88].

# CHAPTER 4

# INJECTION MOLDING BASED ON Si MOLDS

*"Research cultivates Creativity."*

## 4.1. Introduction

In this chapter it is reported on the successful development of an experimental multi-step manufacturing capability suitable for processing of silicon (Si) molds utilized in polymer injection micro-molding. In this work, molds were fabricated via E-beam lithography and Deep Reactive Ion Etching (DRIE). A brief description and analysis of the processing parameters of the utilized micro-fabrication techniques is presented. Process parameters and their influence on the Si mold quality manufacture are also explained. Successfully manufactured molds were characterized with scanning electron microscopy (SEM) and used as molds in injection micro-molding studies. Various structured objects at the micron and sub-micron scale were replicated and imaged with SEM as well. Careful investigation of the entire manufacturing process sequence, from mold fabrication to replication with injection molding, revealed a domain of unexpected and intricate problems. Those issues were addressed and their solution presented in details in Chapter 5.

In addition, static parametric structural finite element (FE) analysis was performed to investigate the structural integrity of, structured on a micrometer level, Si molds subjected to process conditions (pressure and temperature fields) normally used in polymer injection micro-molding. Maximum principle stresses and total displacements were found for three types of loading conditions resulting from: (i) coupled pressure and temperature fields, (ii) pressure field only, and(iii) temperature field only).

## 4.2. Experimental details

In what follows, a detailed description of the Si mold manufacturing sequence is presented. Process parameters and their influence on the Si mold quality manufacture are also given.

### 4.2.1 Mold Fabrication

#### *4.2.1.1 Pattern Generation via E-beam Lithography*

The fabrication process of the structured Si molds was initiated with CAD pattern generation using a combination of DesignCAD$^{TM}$ LT 2000 and Nanometer Pattern Generation System (NPGS, JC Nabity Lithography Systems). Following pattern generation, the NPGS system, installed on and controlling a SEM–LEO 1550VP equipped with a Gemini column, Figure 4-1, was employed to write the structures on substrates spin coated with a resist, Figure 4-2. The system made use of the microscope's Schottky-type field emission electron gun and the beam blanker mounted under the condenser lens. The NPGS uses a true vector-writing mode, which allows maximum control over the electron beam. For instance, the beam moves along sloped lines and it is tangent to arcs and circles. Three different object types can be defined in NPGS, e.g. polygons, lines, and points. Each object is defined by its geometry and its type of exposure. Polygons are written by specifying an area dose measured in $\mu C/cm^2$, lines – by specifying a line dose measured in nC/cm, and point objects – by specifying a point dose measured in fC. Only area and line objects were used in this

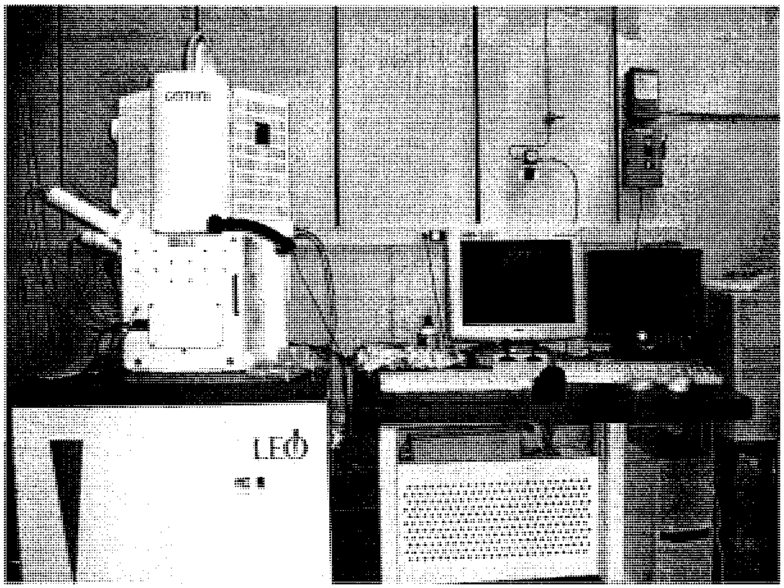

**Figure 4-1.** Scanning Electron Microscope (SEM LEO 1550 VP) with installed NPGS was utilized throughout the experimental work presented in this chapter and the entire comprehensive study for (i) imaging and (ii) e-beam lithography purposes.

experimental work to specify the NPGS format of several different types of geometries. The geometries of interest were considered to be: (i) the official logo of Lehigh University, PA, (ii) the official logo of BOY Machine Inc., (iii) the official logo of the Athletic Department of Clemson University, SC, Figure 4-3; (iv) two alphanumeric strings "BOY 12A" and "SPE-ANTEC-2006" (Society of Plastics Engineers – Annual Technical Conference – 2006), (v) six concentric ring channels with decreasing diameters and widths, and (vi) an array with trapezoid channels. All objects were exposed with line or area doses. Since no prior knowledge for exposing such geometries was available, several exposure levels during e-beam lithography were considered for each designed object. The most important settings which define the quality of the exposed patterns are

(a) Silicon wafer.

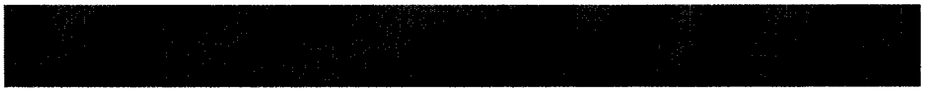

(b) Spin-coating with PMMA resist. Resist baking.

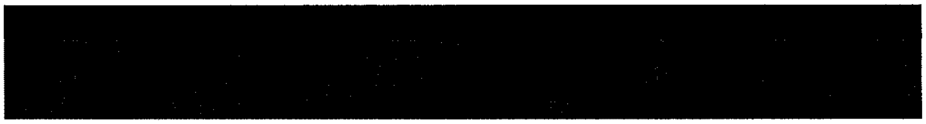

(c) E-beam lithography.

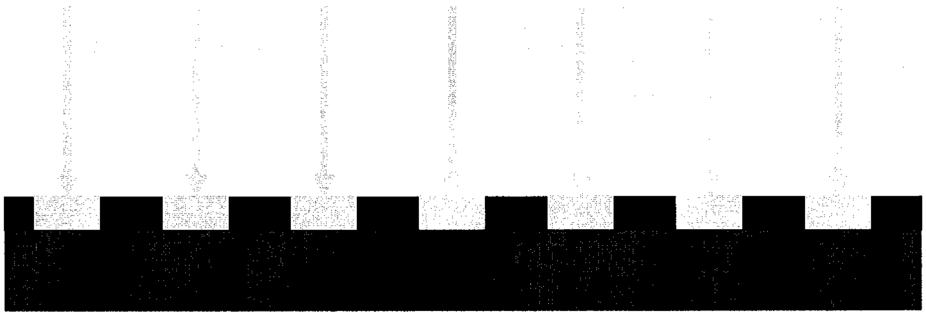

(d) Resist development and post-baking.

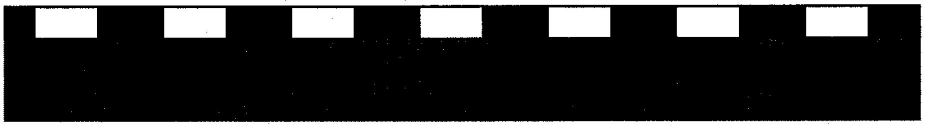

(e) Deep Reactive Ion Etching (DRIE). Resist Stripping.

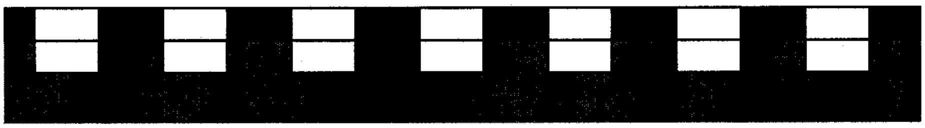

(f) Si mold. Encapsulation of the mold in a mold base.

**Figure 4-2.** Schematic of the micro-fabrication process flow for Si mold development.

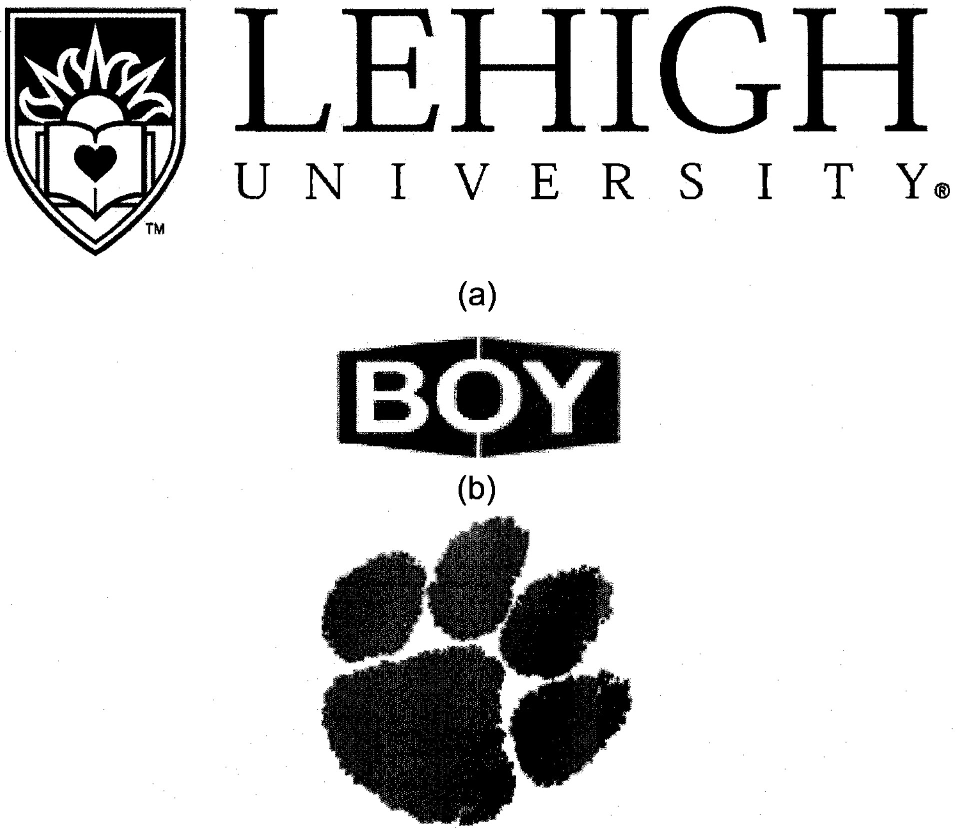

(a)

(b)

(c)

**Figure 4-3.** Pictures of the official logo designs of (a) Lehigh University, PA with a shield and letters written in a Palatino font type, (b) BOY Machines Inc., (c) the Athletic Department of Clemson University, SC depicting an actual tiger paw print. All geometries were specified as polygons (exposed with an area dose) with exception of the trade mark (™) and registration (®) symbols in the Lehigh University logo design which were written as line objects (exposed with a line dose).

considered to be the type and magnitude of the dose level, the magnification, the center-to-center distance and the line spacing, as seen in Figure 4-4. The center-to-center distance is defined as the distance between adjacent exposure points as the beam is moved to write a line. When the value of this parameter is changed the exposure time changes as well to keep the prescribed dose unchanged. This parameter affects only area and line doses as seen from eqns. 4-1. If the parameter accepts larger values along a line then discrete points may result instead of a solid line. The line spacing is defined as the distance between adjacent lines when the beam makes multiple passes to fill in an area or to write a wide line. This parameter affects only the area dose and does not affect the line and point doses. If the center-to-center distance is equal to the line spacing a square grid of exposure points would be formed. This approach was used during writing of polygon objects. The magnification is a parameter which ensures that the written pattern would always fit the microscope field of view. If the magnification is changed, the grid spacing of possible exposure points

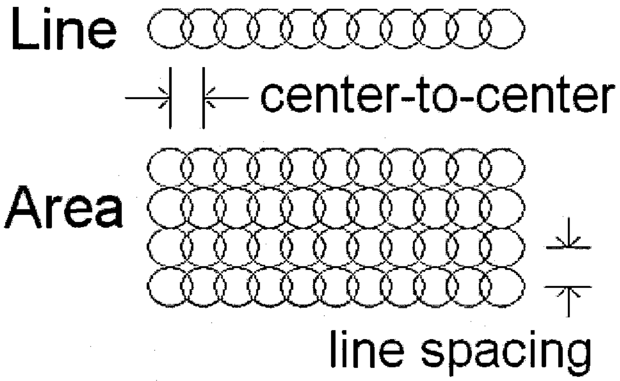

**Figure 4-4.** Schematic representation of e-beam parameters – center-to-center distance and line spacing.

$$Area\_Dose = \frac{beam\_current \bullet exposure\_time}{center-to-center \bullet line\_spacing}$$

$$Line\_Dose = \frac{beam\_current \bullet exposure\_time}{center-to-center} \qquad (4\text{-}1)$$

$$Point\_Dose = beam\_current \bullet exposure\_time$$

changes as well. This change reflects the center-to center distance and the line spacing which are changed to the nearest multiple of the grid spacing. In general, if filling line objects the beam passes only once in the specified location and if arbitrary polygons are written the beam sweeps parallel to one side of the polygon.

| | | SPE-ANTEC-2006 | BOY 12A | BOY logo | Lehigh U. logo | Rings & Trapezoids | Tiger Paw |
|---|---|---|---|---|---|---|---|
| c-c distance [1] | nm | 1.50 | 1.50 | 4.51 | 6.16 | 6.93 | 6.01 |
| line spacing | nm | 1.50 | 1.50 | 4.51 | 6.16 | 6.93 | 6.01 |
| beam current [2] | pA | 425 | 425 | 425 | 425 | 380 | 380 |
| magnification | - | 922 | 922 | 922 | 225 | 200 | 3000 |
| 1. exp. time | μsec | 0.836 | 0.435 | - | 1.369 | - | - |
| 1. line dose | nC/cm | 2.500 | **1.300** | - | **1.000** | - | - |
| 2. exp. time | μsec | 1.448 | 0.505 | - | 2.054 | - | - |
| 2. line dose | nC/cm | 4.333 | **1.509** | - | **1.500** | - | - |
| 3. exp. time | μsec | 2.061 | ' | - | 2.739 | - | - |
| 3 line dose | nC/cm | 6.167 | ' | - | 2.000 | - | - |
| 4. exp. time | μsec | 2.674 | 2.674 | - | - | - | - |
| 4. line dose | nC/cm | 8.000 | **8.000** | - | - | - | - |
| 1. exp. time | | - | - | - | - | - | 0.333 |
| 1. area dose | | - | - | - | - | - | 350 |
| 2. exp. time | μsec | - | - | 0.200 | 0.338 | 0.569 | 0.380 |
| 2. area dose | μC/cm$^2$ | - | - | 400 | 400 | 450 | 400 |
| 3. exp. time | μsec | - | - | 0.204 | 0.380 | - | 0.428 |
| 3. area dose | μC/cm$^2$ | - | - | 450 | 450 | - | 450 |
| 4. exp. time | μsec | - | - | 0.226 | 0.422 | - | 0.475 |
| 4. area dose | μC/cm$^2$ | - | - | 500 | 500 | - | 500 |

[1] c-c distance stands for center-to-center distance.

[2] actual measured beam current right before exposure, measured with a picoammeter and a Faraday cup.

**bold** font- doses that resulted in either underexposure (lower range) or overexposure (higher range).

**Table 4-1.** E-beam lithography processing conditions used for PMMA exposure of the objects.

In order to eliminate the deleterious effect of the secondary electrons emitted by the Si substrate during e-beam exposure, the maximum available beam voltage of the e-beam system, e.g. 30 kV was utilized. To focus the electron beam, e.g. wobble and stigmatism, a gold sputtered Si substrate was employed. Comprehensive description of the E-beam lithography procedures performed with NPGS, pattern design tutorials and system specific information can be found in the NPGS User's manual and online at www.jcnabity.com.

As a result of the above discussed considerations a range of e-beam lithography parameters was chosen. The detailed tabulated data is given in, Table 4-1 and Figure 4-5.

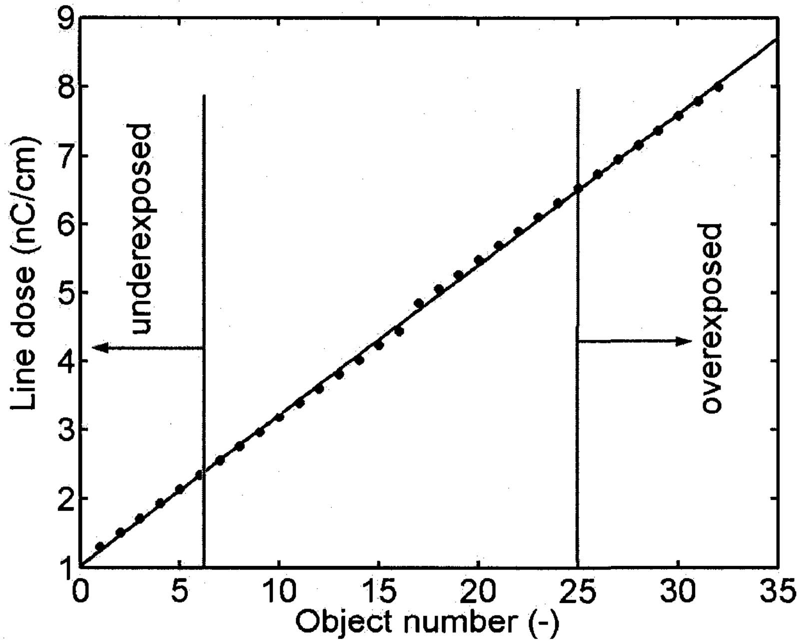

**Figure 4-5.** Line exposure doses as a function of the object number for 32 "BOY 12A" alphanumeric strings. Some of the chosen doses resulted in underexpose (lower range) or overexposure (higher range).

An important step during the micro-fabrication process of Si molds is the quality of the applied, most of the times via spin-coating, resist on the wasfers. Therefore a simple procedure was employed which description follows. A positive tone poly(methylmetacrylate) (950PMMA-A4, MicroChem Corp.), 950,000 Mw, e-beam sensitive resist was spin-coated for 40 sec at 3000 $min^{-1}$ onto single crystal silicon (100) wafers with resistivity 15 to 30 Ω-cm and baked in an oven at temperature 150 $^0$C for 60 min. The resist was diluted with anisole solvent in 1:1 ratio. No other treatment prior coating was done. The wafer was rinsed in DI water and dehydrated for 30 min at 130 $^0$C. Subsequent to the e-beam exposure, the resist was developed for 70 sec in 3:1 solution of 2-propanol: methyl isobutyl ketone (IPA:MIBK, $C_3H_8O$:$C_6H_{12}O$) and the wafer was rinsed in IPA only to prevent undesired further development of the resist, thus forming a mask [89]. The etching of the Si substrate was performed on a Deep Reactive Ion Etcher (DRIE, Adixen AMS 100 I-Speeder) in a BOSCH® process mode. Following that, the molds were stripped of the resist mask in acetone for 1 h dried with $N_2$ and encapsulated in a machined brass mold with an epoxy composition with fast cure kinetics.

### *4.2.1.2 Pattern Transfer via Deep Reactive Ion Etching*

Pattern transfer from the mask to the substrate was performed by DRIE in a BOSCH® process mode (repeated etching and passivation cycles). The etcher, as seen in Figures 4-6 and 4-7 consists of a plasma source, a diffusion chamber,

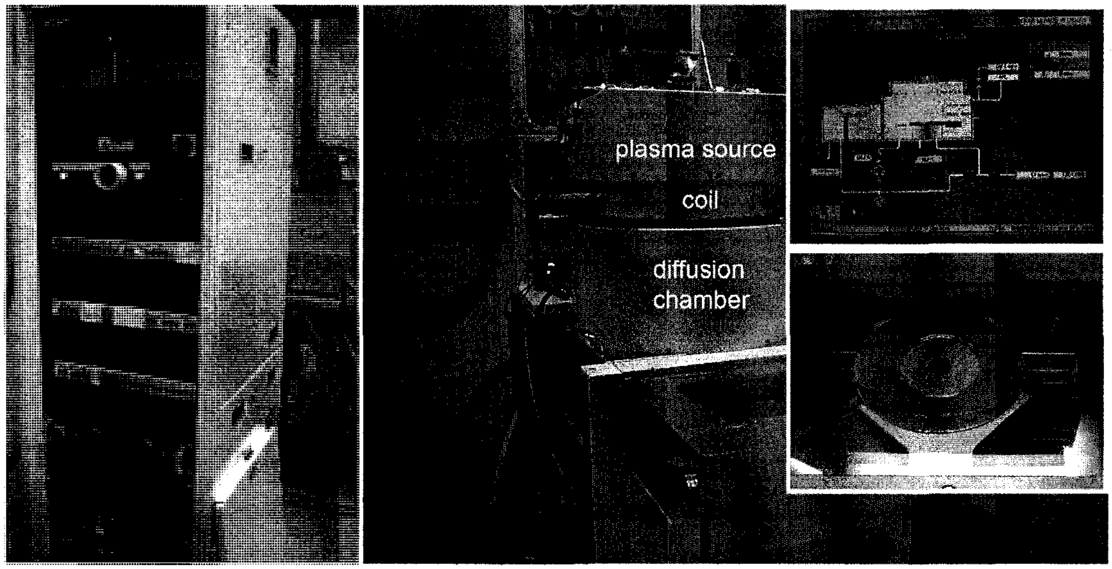

**Figure 4-6.** Deep Reactive Ion Etching (DRIE) tool with controller unit on the left and the DRIE unit in the middle, with insets on the right showing the computer controller interface and loading chamber.

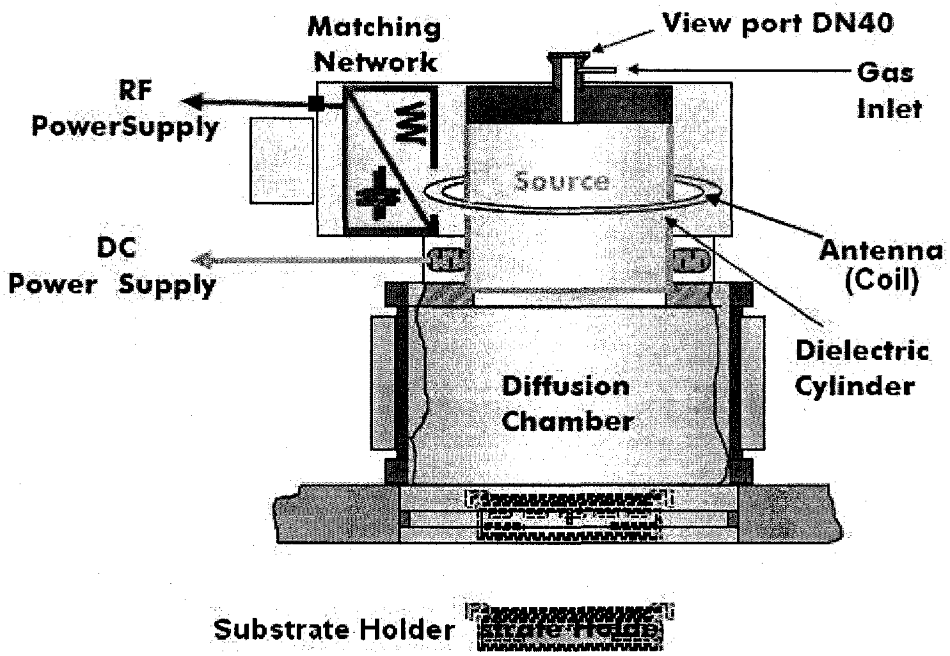

**Figure 4-7.** Schematic of the DRIE process chamber which consists of a plasma source, a diffusion chamber, and an antenna (coil).

and a coil (or antenna). The plasma source is inductively coupled plasma (ICP) source which generates plasma at rf power at 13.56MHz in a dielectric cylinder. The chamber walls are fitted with permanent magnets that direct ions towards the wafer placed on the substrate holder. Such a configuration reduces the loss of plasma to the chamber walls and makes the plasma more homogeneous [20].

The processing conditions which have been utilized for etching of the features were chosen to be the same as those described in details in Chapter 5. The Si molds (pieces) were most of the time manually scribed from the Si wafer and mounted on a large substrate holder by means of OSG-825 resist followed by 45 min baking at 75 $^0$C. This approach was found to lead to good etching results and was very convenient to use while working with small area Si substrates. In addition, it is worth mentioning that the BOSCH® process mode yields to a very fine but still measurable surface roughness on all inner walls of the etched cavities, termed scalloping [90], which can be seen in Figure 4-8. Nonetheless, it has been previously shown that by utilizing of BOSCH® mode, features with straight walls can be achieved [90-92]. Therefore this mode of DRIE operation was implemented in the molds development.

The utilization of two types of gases, namely sulfur hexafluoride ($SF_6$, main etching gas) and $C_4F_8$ (octafluorocyclobutane, OFCB) enabled achieving two different plasma etching rates in the Si substrate. It is well known fact that $SF_6$ plasmas can effectively etch inorganic Si substrates [93, 94] and this method has been extensively used for years. In addition, the surface reaction mechanism for fluorocarbon plasma initiated etching of silicon (Si) (with any type

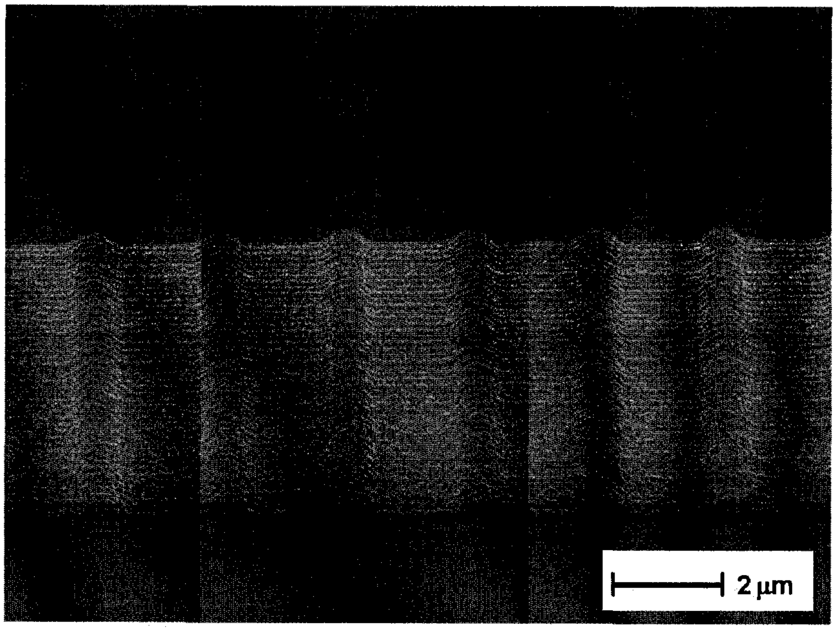

**Figure 4-8.** SEM picture of a test structure with etched array of holes with d~500 nm and depth ~4.5 μm. Scallops are seen as repeated lamellar structures on the vertical walls.

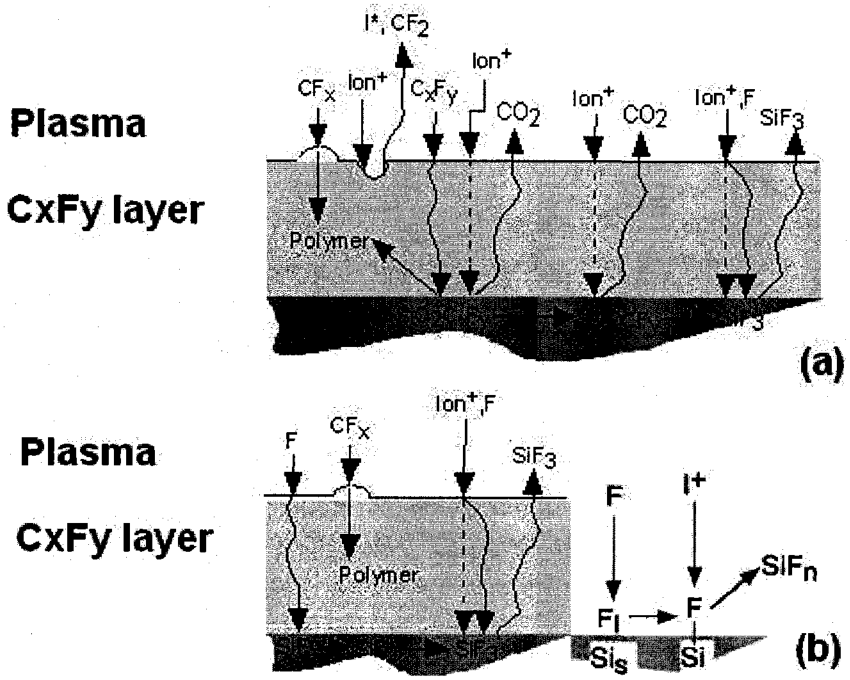

**Figure 4-9.** Schematic representation of the surface reaction mechanism for fluorocarbon etching of (a) $SiO_2$ and (b) Si through a layer of passivation fluorocarbon film and (b) bare Si (right hand-side of the image). Images adapted from [95, 96]. wavy arrow denotes a diffusion process, dashed arrow – energy dissipation from an ion.

of fluorocarbon gas precursor) proposed by *Standaert et.al* influences the etch rate of Si as well [95-97] and for illustrative purpose is given below. Moreover, it is believed that the successfully etched sub-100 nm features, which work has been described in Chapter 5, is partially a result exactly of this phenomenon.

As seen in Figure 4-9 (b), the etching of bare Si results from an adsorption of fluorine atoms F from the plasma onto random Si locations or sites denoted with $Si_S$. The adsorbed fluorine $F_l$ passivates the underlying Si by chemiosorption (=Si-F). Ion bombardment $I^+$ then provides the activation energy to desorb the etch product $SiF_n$. This etching mechanism is similar to that found in $SF_6$ plasma but is slower. In addition whenever a fluorocarbon plasma is generated during the passivation step, a fluorocarbon radical flux $CF_n$ forms that deposits fluorocarbon film as well. F atoms adsorb on top of the polymer and diffuse through the polymer where they adsorb on the bare Si sites at the interface. The adsorbed fluorine passivates the Si as in the bare Si case. Ions incident on the polymer dissipate energy through the layer to desorb etch products which diffuse back out of the organic layer $SiF_n$. It is believed that exactly this mechanism played an important role during etching of the sub-100 nm features. In the more complicated scenario, Figure 4-9(a), when $SiO_2$ is formed on the Si surface which happens naturally due to the normal oxidation of the Si and is believed to occur at the very beginning of the Si etching process, the etching of the $SiO_2$ through the fluorocarbon film is initiated via chemiosorption of $CF_x$ species. This process is followed by 2-step ion activation, through the polymer layer, etching of the $SiO_2$/Si [95-97].

Finally, upon successful etching of Si molds with the DRIE the resist masks were stripped of with acetone in accordance with the previously discussed procedure. No further treatment of the molds was undertaken. They were imaged with SEM and subsequently used in the injection molding studies. Representative images of the manufactured molds are given in Figures 4-10 to 4-15. As seen in Figure 4-10(b) the high magnification images show that the starting and ending points during e-beam writing shifted with about 100 nm due to beam hysteresis. This possibly happened due to the stage drift while exposing large surface areas and is considered current limitation of the utilized system. Figure 4-11 depicts the mold cavities of BOY Machines Inc. logo and two of the "BOY 12A" alaphanumeric strings. Unexpectedly, the location mark, in the form of a rectangle, and placed purposefully at the end of the string array, received large exposure by accidentally keyed-in large dose level in the NPGS run file, that led to re-polymerization of the PMMA resist after radiation induced polymer chain scission [98]. In other words, the resist acted as a negative instead of as a positive one. The ellipsoidal area around the rectangle received less radiation which process was possibly governed by proximity effects. As seen in Figure 4-12, the alphanumeric string SPE-ANTEC-2006 was etched very well having smooth lines in the order of 250 nm widths. Note that the white regions around the lines are artifacts from the imaging, e.g. the SEM images in general are gray scale intensity images of secondary electrons emitted by the substrate upon its impinging with the high energy e-beam (imaging beam). Since at the very edge that emission is increased those regions appear to be brighter.

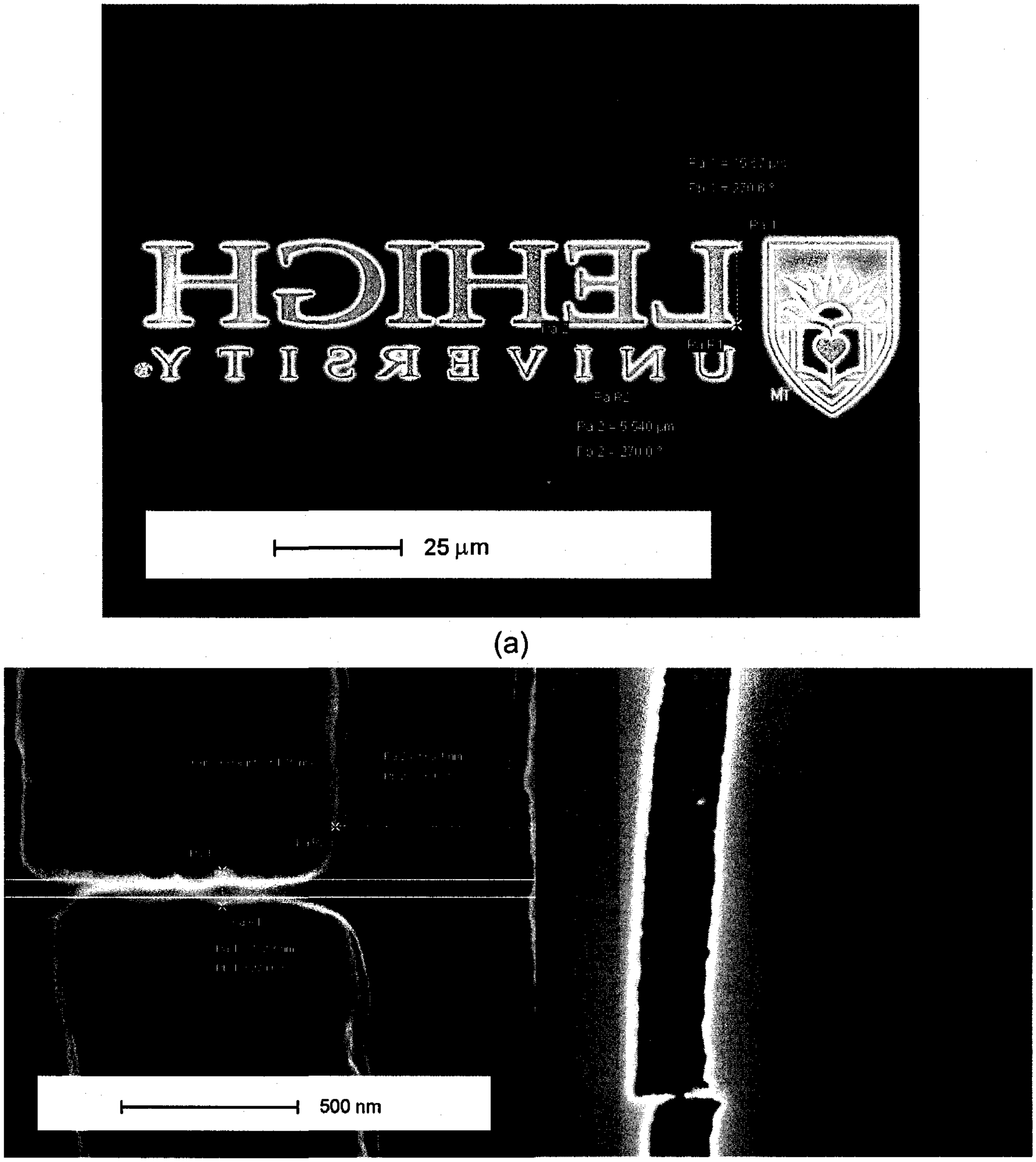

(a)

(b)

**Figure 4-10.** SEM pictures, obtained after DRIE etching and PMMA stripping by employing the secondary electrons (SE) detector of the microscope of the (a) Lehigh University logo mold, (b) detailed blow-up images of the logo's shield (left) and inner-most channel (right) from the array of concentric channels seen in Figure 4-13.

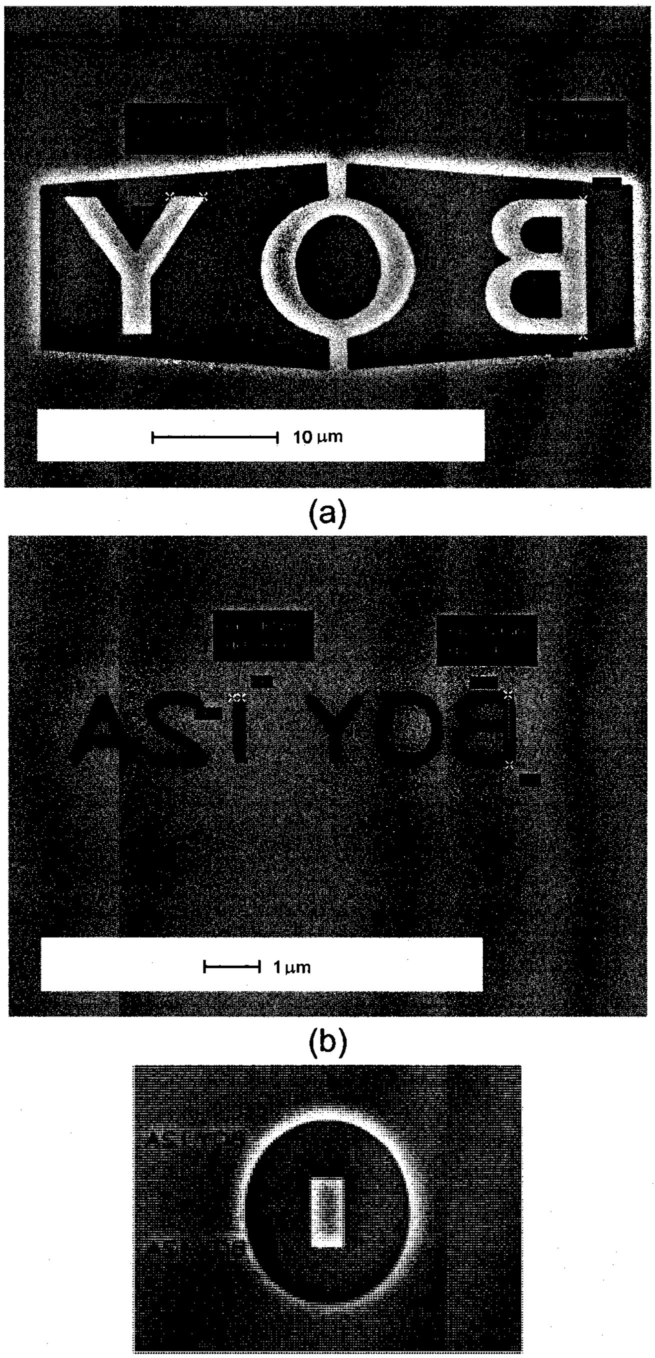

(a)

(b)

(c)

**Figure 4-11.** SEM images of structures that resulted after DRIE etching and PMMA stripping, and obtained with a mixed signal from the in-lens and secondary electrons (SE) detectors of the microscope to acquire images with "depth" perception of (a) BOY Machines Inc. logo, (b) BOY 12A alphanumeric string, and (c) a rectangular region next to the alphanumerics that was formed due to overexposure of the PMMA. This region was placed as a mark to identify the right lower corner of the array of "BOY 12A" strings that were written with different exposure doses.

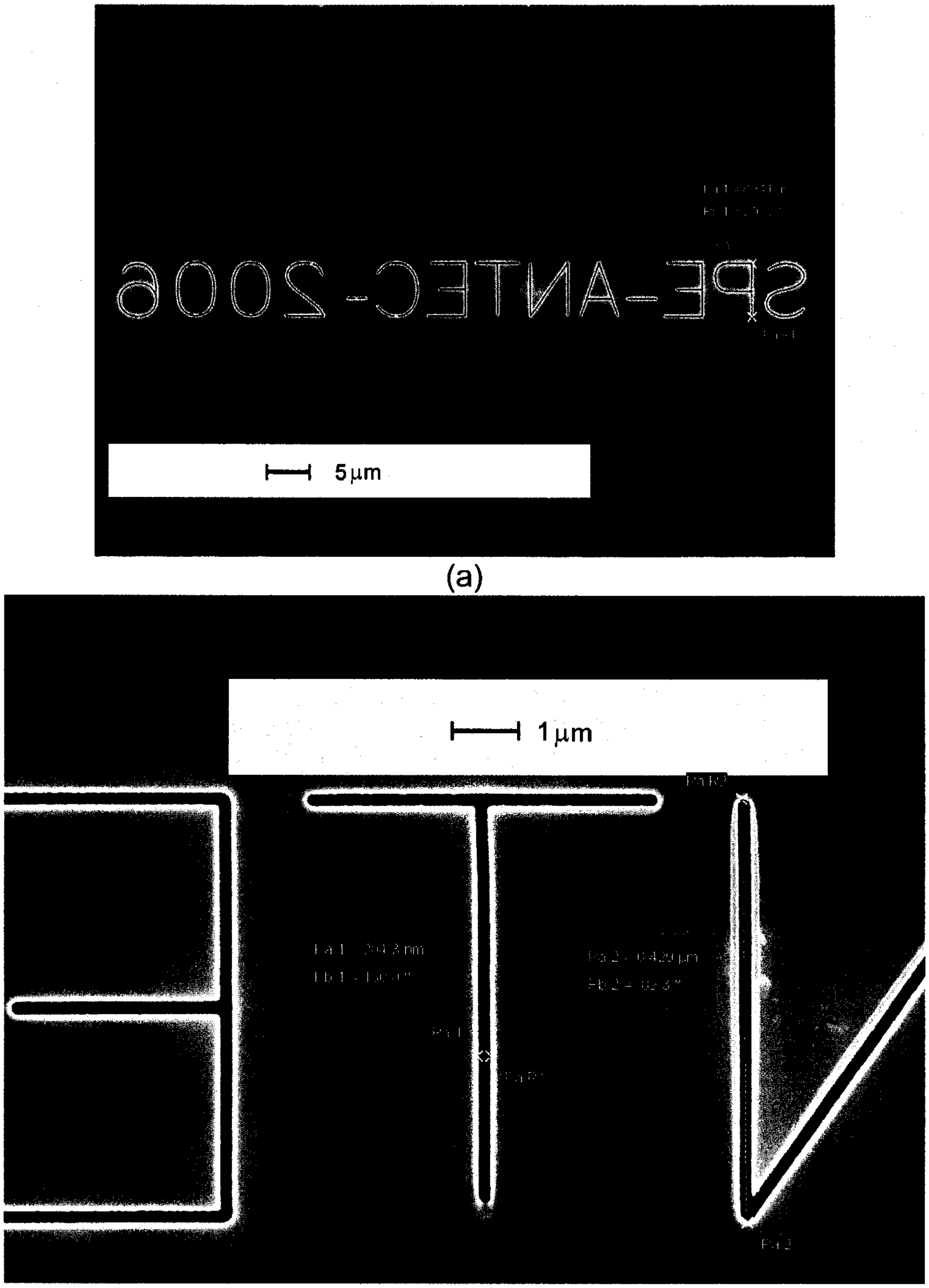

(a)

(b)

**Figure 4-12.** SEM images of structures that resulted after DRIE etching and PMMA stripping, and obtained with the secondary electrons (SE) detector of the microscope, to acquire images of (a) SPE-ANTEC-2006 alphanumeric string and (b) detailed blow-up view.

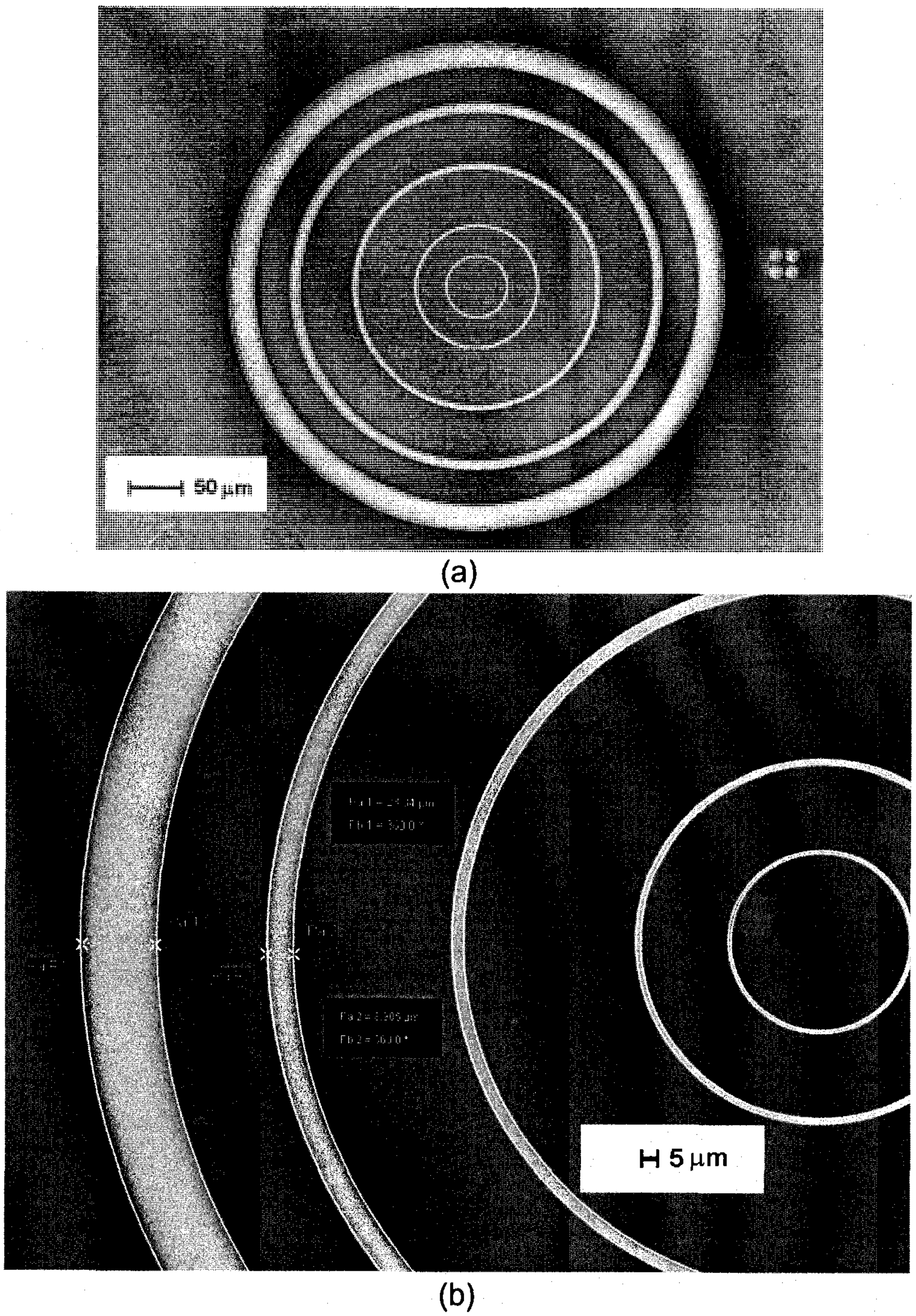

**Figure 4-13.** SEM images of structures that resulted after DRIE etching and PMMA stripping, and obtained with a mixed signal from the in-lens and secondary electrons (SE) detectors of the microscope to acquire images with "depth" perception of (a) the concentric ring channels with four cavities of the tiger paw objects at the right and (b) zoom-in of the array which consists of five circular channels with outer diameter $d_1$ and width w as follow: $d_1/w$ = 560/50, 400/20, 200/2, 100/1, 50/0.5 all in µm.

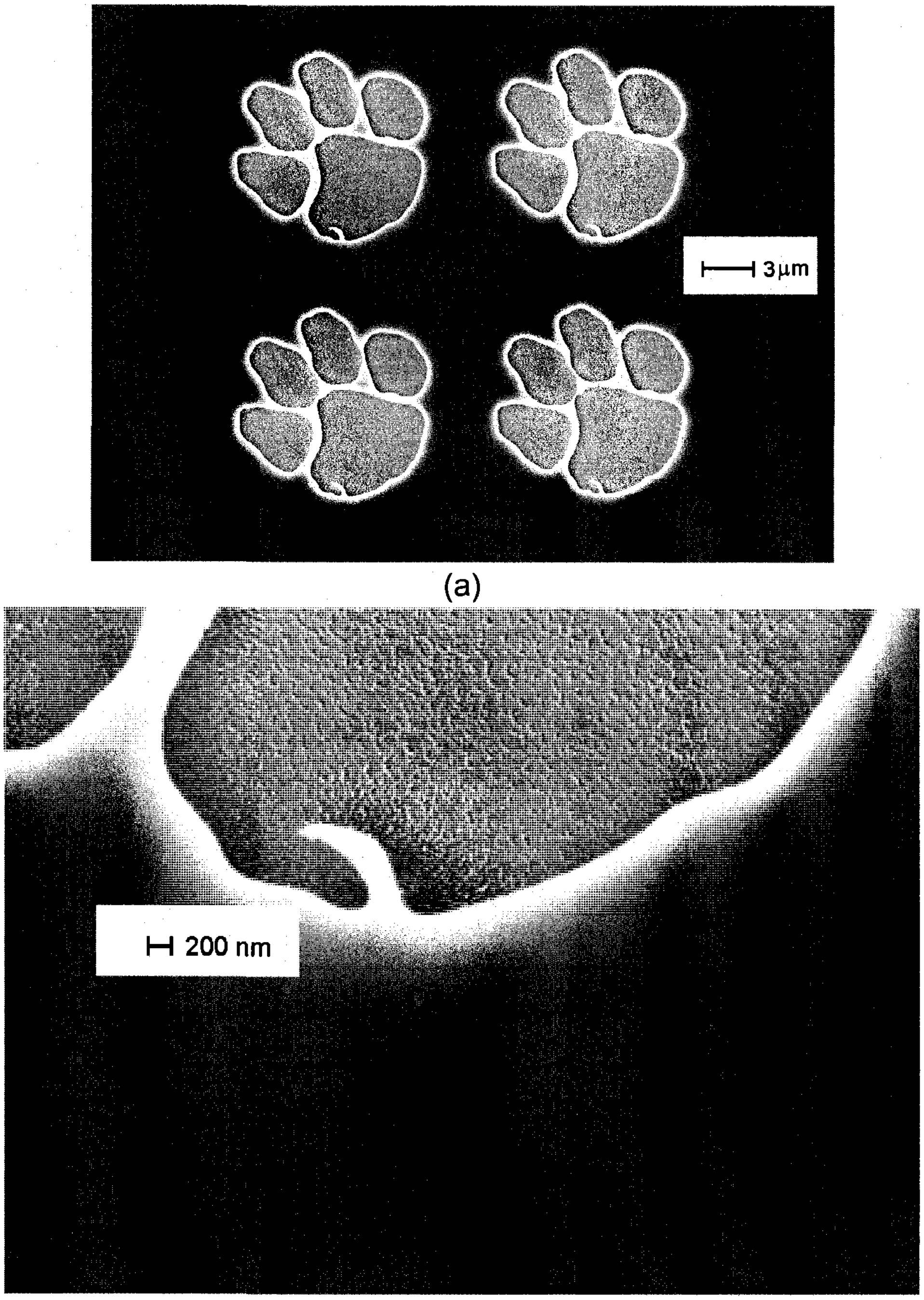

(a)

(b)

**Figure 4-14.** SEM images of structures that resulted after DRIE etching and PMMA stripping, and obtained with a mixed signal from the in-lens and secondary electrons (SE) detectors of the microscope to acquire images with “depth” perception of (a) the four cavities of the tiger paw objects and (b) blow-up of the left upper corner cavity.

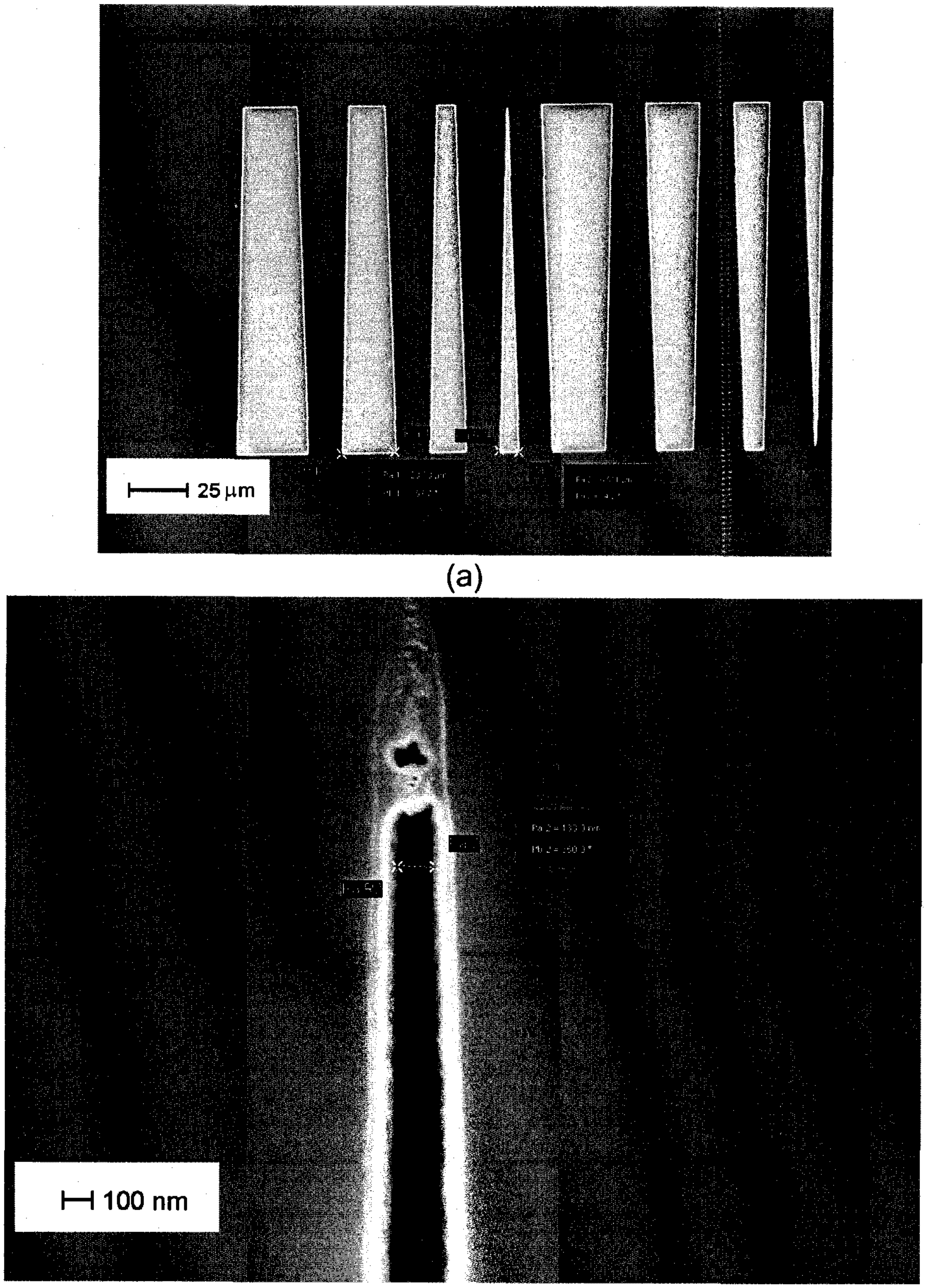

(a)

(b)

**Figure 4-15.** SEM images of structures that resulted after DRIE etching and PMMA stripping, and obtained with a mixed signal from the in-lens and secondary electrons (SE) detectors of the microscope to acquire images with "depth" perception of (a) the array of trapezoids and (b) blow-up of the apex of the trapezoid which appears to have sharp vertex in (a).

Figures 4-13 to 4-15 depict the etched circular channels, the logo of the Athletics Department of Clemson University, and the trapezoids structures. No polymer replication has been attempted with those molds. Surprisingly, as seen in Figure 4-14(b), it was found that the surface roughness on the bottom of the cavities had noticeable difference in the surface topography. The regions around the "claw" have smoother texture while those in the middle are rougher. It is believed that this observation can be explained with the shadowing effect of fluorinated plasmas during etching of small features [90, 91]. This phenomenon played an important role during etching of the sub-100 nm cavities, which related work is presented in details in Chapter 5. No further attempts for surface topography quantification have been undertaken.

### 4.3 Mold Structural FEM Based Analysis

One of the primary sources of replication inaccuracy, e.g. the critical dimension (CD) variation, during injection molding with Si molds has been considered to be the Si substrate itself. It has been previously identified that unregulated heating during micro-contact printing, a.k.a. stamping, can induce a thermal stress field in structured Si wafers (molds) and displace surface topography in the three dimensions with out-of-plane total displacements reaching as far as ~900 nm [99]. For example, in projection lithography systems the wafer distortions are controlled by employing continuous magnification corrections at the lenses by utilizing real-time feedback control of the alignment mark that senses wafer distortion. Interestingly, attempts were made to control Si wafer distortions (during micro-contact printing as well) with active thermal control systems [99]. It is obvious that similar control system in terms of practicality can also be installed on standard injection micro-molding machines. Such control systems though, can be successfully built if information about the structural integrity change of the mold during injection molding is known in advance.

Therefore in this study, an attempt has been made to numerically calculate feature distortions of structured Si mold subjected to coupled load fields from pressure and temperature. Moreover a range of processing conditions, e.g. the injection pressure and the mold temperature, relevant to injection molding processes and practices, and in particular, such that have been utilized throughout this comprehensive study were investigated. Furthermore the analysis was performed by investigating the influence of three types of conditions on the stress and strain distribution in a Si mold, e.g. (i) the injection pressure and mold temperature, (ii) the injection pressure only, and (iii) the mold temperature only. Finite element analysis was carried out with COMSOL Multiphysics software. The ring channels structured Si mold, Figure 4-13, which manufacture has been already discussed earlier, was chosen as a prototype model of the FEM analysis. Only two closely spaced rings have been considered for simplification of the analysis. The rings were modeled to be of an equal depth of 50 μm, Figure 4-16(a) deeper than that of the prototype structure (e.g. ~0.750 μm). Such deep etched features can readily be manufactured by utilizing

UV-lithography and optical resists with high selectivity during plasma etching.

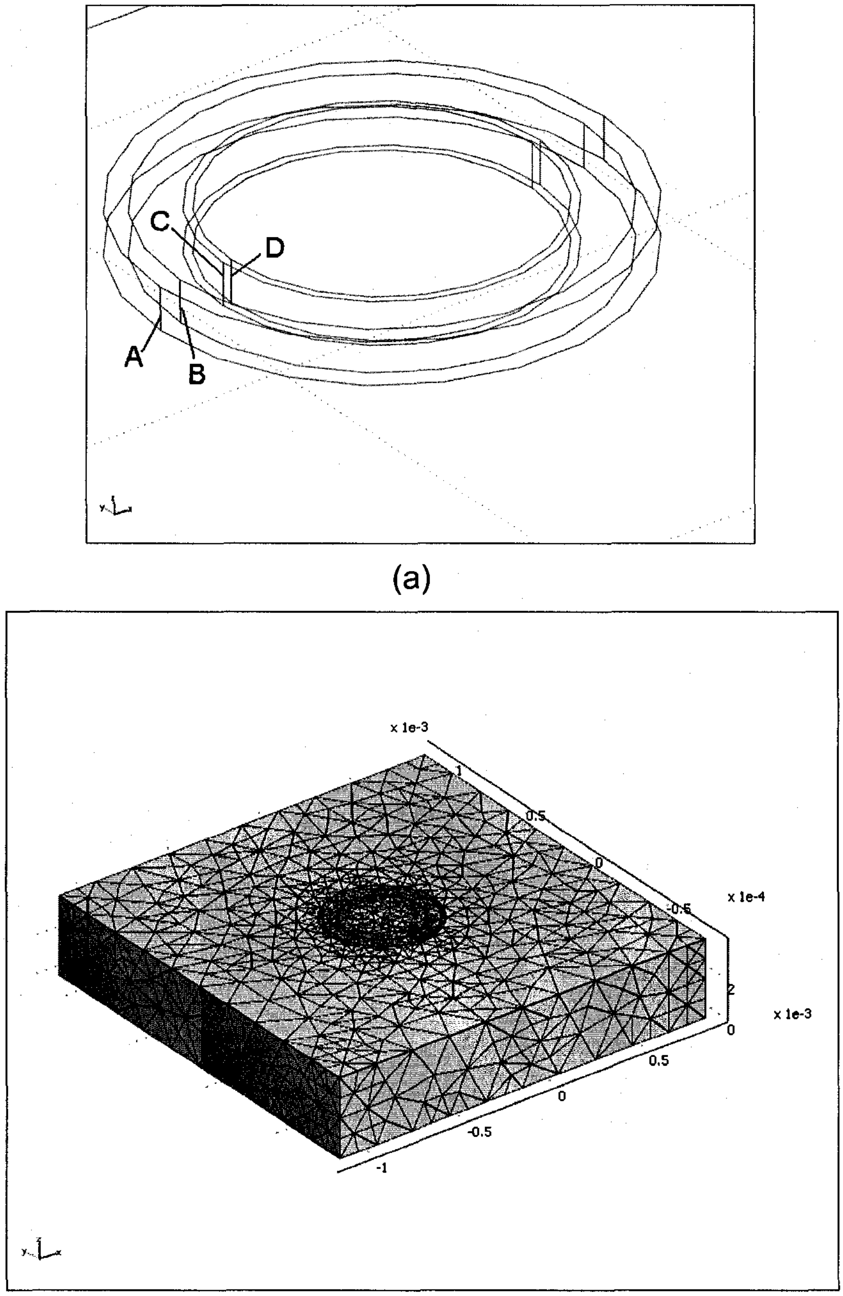

(a)

(b)

**Figure 4-16.** (a) Prototype of a structured Si mold with two ring channels having outer $d_1$ and inner $d_2$ diameters as follow: $d_1/d_2$ =560/510 µm and $d_1/d_2$ =400/380 µm and four vertical edges of interest A, B, C, and D (b) Solid meshed model of the structured Si mold 2000x2000x400 µm with the ring channels located in the center.

### 4.3.1 Failure Analysis and Model Description

Failure analysis was carried out by employing the theory of maximum principle stress which can describe the failure mechanism of brittle materials [100]. This approach has been chosen due to the brittle nature of the mold material especially at pressures and temperatures employed during polymer injection molding, e.g. those ranges can not induce plastic yield in Si [101]. It is well known that brittle materials exhibit a behavior which is totally elastic up to the point of fracture. The brittle fracture is a catastrophic failure which occurs without yielding and at very fast speeds usually initiated by substrate's cracks presence.

To compare the influence of the molding conditions on the structural integrity of the Si mold, the six highest principle stresses – two in each direction $x$, $y$, $z$ were recorded and the total displacement of four edges, e.g. *A*, *B*, *C*, and *D* was also monitored for all three load scenarios, Figure 4-16(a). Principle stresses are defined to be those normal stresses $\sigma_1$, $\sigma_2$, $\sigma_3$ at locations where the shear stresses vanish, Figure 4-17.

The principle stress of greatest magnitude for the three scenarios was also compared with an experimentally obtained value for the yield stress of Si at 150 $^0$C, $\sigma_{yield}$=2.9±0.5 GPa [101] to predict any possible brittle failure of the Si mold during injection molding.

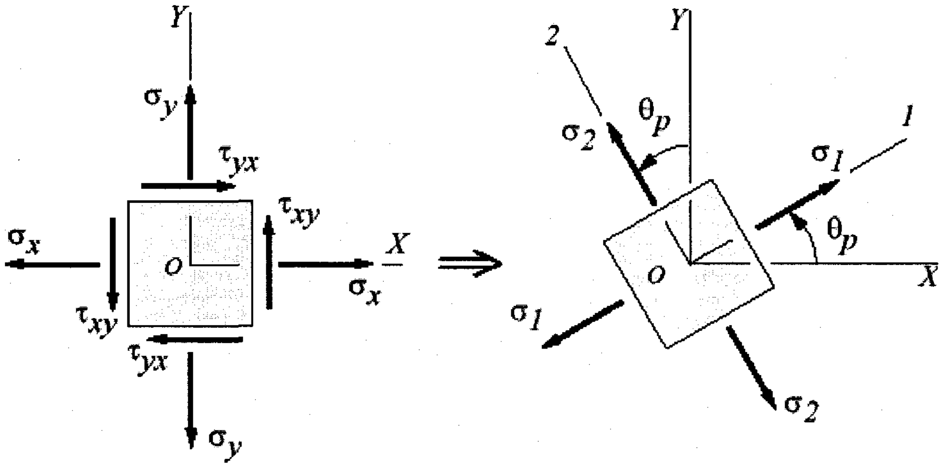

Stresses in given coordinate system

Principal stresses

**Figure 4-17.** A 2D representation of the equilibrium state of an element with normal, shear and principle stresses distribution.

The model was build by assuming the classical linear elastic behavior of isotropic Si where only small deformations occur and the stress $\sigma$ defined in fixed directions is not following the body (Cauchy stress). The strain $\varepsilon$ has been decomposed in thermal $\varepsilon_{th}$, elastic $\varepsilon_{el}$, and initial $\varepsilon_0$ strain so that

$$\varepsilon = \varepsilon_{el} + \varepsilon_{th} + \varepsilon_0 \tag{4-1}$$

The thermal strain $\varepsilon_{th}$ depends on the present temperature $T$, the stress-free reference temperature $T_{ref}$, and the thermal expansion vector $\alpha$, as follow:

$$\varepsilon_{th} = \begin{bmatrix} \varepsilon_x \\ \varepsilon_y \\ \varepsilon_z \\ \varepsilon_{xy} \\ \varepsilon_{yz} \\ \varepsilon_{xz} \end{bmatrix}_{th} = \alpha(T - T_{ref}) = \begin{bmatrix} \alpha \\ \alpha \\ \alpha \\ 0 \\ 0 \\ 0 \end{bmatrix} (T - T_{ref}) \tag{4-2}$$

The stress-strain relationship or the constitutive equation including initial stress and strain and thermal effects reads as follow

$$\sigma = D\varepsilon_{el} + \sigma_0 = D(\varepsilon - \varepsilon_{th} - \varepsilon_0) + \sigma_0 \tag{4-3}$$

where $D$ is the 6x6 elasticity matrix, $\sigma_0$ is defined as the initial stress and the stress and strain are both given in column form

$$\sigma = \begin{bmatrix} \sigma_x \\ \sigma_y \\ \sigma_z \\ \tau_{xy} \\ \tau_{yz} \\ \tau_{xz} \end{bmatrix} \qquad \varepsilon = \begin{bmatrix} \varepsilon_x \\ \varepsilon_y \\ \varepsilon_z \\ \varepsilon_{xy} \\ \varepsilon_{yz} \\ \varepsilon_{xz} \end{bmatrix} \tag{4-4}$$

where $\sigma_x$ , $\sigma_y$ , $\sigma_z$ and $\tau_{xy}$ , $\tau_{yz}$ , $\tau_{xz}$ are the three normal and shear stresses respectively and $\varepsilon_x$ , $\varepsilon_y$ , $\varepsilon_z$ and $\varepsilon_{xy}$ , $\varepsilon_{yz}$ , $\varepsilon_{xz}$ are the three normal and shear strain components respectively. The initial strain and initial stress refers to the strain and stress before the system applies any loads and/or displacements.

The elasticity matrix $D$ for isotropic material is given as:

$$D = \frac{E}{(1-\nu)(1-2\nu)} \begin{bmatrix} 1-\nu & \nu & \nu & 0 & 0 & 0 \\ \nu & 1-\nu & \nu & 0 & 0 & 0 \\ \nu & \nu & 1-\nu & 0 & 0 & 0 \\ 0 & 0 & 0 & \frac{1-2\nu}{2} & 0 & 0 \\ 0 & 0 & 0 & 0 & \frac{1-2\nu}{2} & 0 \\ 0 & 0 & 0 & 0 & 0 & \frac{1-2\nu}{2} \end{bmatrix} \tag{4-5}$$

where $E$ is the modulus of elasticity and $\nu$ is the *Poisson's ratio* defining the contraction in the perpendicular direction. Upon taking the assumption of small displacements, the normal strain components and the shear strain components are related to the deformations *u, v, w* in *x, y, z* directions respectively as follows:

$$\begin{aligned}
\varepsilon_x &= \frac{\partial u}{\partial x} & \varepsilon_{xy} &= \frac{\gamma_{xy}}{2} = \frac{1}{2}\left(\frac{\partial u}{\partial y} + \frac{\partial v}{\partial x}\right) \\
\varepsilon_y &= \frac{\partial v}{\partial y} & \varepsilon_{yz} &= \frac{\gamma_{yz}}{2} = \frac{1}{2}\left(\frac{\partial v}{\partial z} + \frac{\partial w}{\partial y}\right) \\
\varepsilon_z &= \frac{\partial w}{\partial z} & \varepsilon_{xz} &= \frac{\gamma_{xz}}{2} = \frac{1}{2}\left(\frac{\partial u}{\partial z} + \frac{\partial w}{\partial x}\right)
\end{aligned} \tag{4-6}$$

For symmetric conditions the strain and stress sensors are as follow:

$$\varepsilon = \begin{bmatrix} \varepsilon_x & \varepsilon_{xy} & \varepsilon_{xz} \\ \varepsilon_{xy} & \varepsilon_y & \varepsilon_{yz} \\ \varepsilon_{xz} & \varepsilon_{yz} & \varepsilon_z \end{bmatrix}, \ \sigma = \begin{bmatrix} \sigma_x & \tau_{xy} & \tau_{xz} \\ \tau_{xy} & \sigma_y & \tau_{yz} \\ \tau_{xz} & \tau_{yz} & \sigma_z \end{bmatrix} \tag{4-7}$$

Finally, the equilibrium equations utilized for the calculation of the strain and stress in the Si structured mold are as follow:

$$\begin{aligned}
-\frac{\partial \sigma_x}{\partial x} - \frac{\partial \tau_{xy}}{\partial y} - \frac{\partial \tau_{xz}}{\partial z} &= F_x \\
-\frac{\partial \tau_{xy}}{\partial x} - \frac{\partial \sigma_y}{\partial y} - \frac{\partial \tau_{yz}}{\partial z} &= F_y \\
-\frac{\partial \tau_{xz}}{\partial x} - \frac{\partial \tau_{yz}}{\partial y} - \frac{\partial \sigma_z}{\partial z} &= F_z
\end{aligned} \tag{4-8}$$

or in a compact version with **F** describing all body forces the above equations are written as follow:

$$\nabla \cdot \sigma = \mathbf{F} \tag{4-9}$$

The model was constructed with the following assumptions:

- Upon complete epoxy curing no initial stress and strain is imposed on the boundaries of the Si mold, e.g. $\sigma_0$=0 and $\varepsilon_0$=0.

- The boundaries are constrained, e.g. fixed $u$=0, $v$=0, and $w$=0.
- The body forces **F** acting in x, y, z directions are only from uniformly distributed, including the micron-sized channels, pressure which is equal to the specific injection pressure of the machine.
- Temperature is uniformly distributed in the whole domain.

### 4.3.2 Mold FEM Analysis Results

The FEM simulation was performed with generating a mesh with Lagrange-Quadratic elements. Si material's properties were chosen as follow: $E$= 179 MPa, $\nu$ =0.278, $\alpha$=2.6x10$^{-6}$ K$^{-1}$, $\rho$=2329 kg/m$^3$. An iterative solver GMRES (generalized minimum residual) was utilized due to the large system possessing ~38 000 tetrahedral elements with ~166 000 degrees of freedom. To improve the convergence of the solver geometric multigrid preconditioner was chosen which resulted in fast convergence as seen in Figure 4-18. In general a preconditioner is a matrix $M$ that approximates $A$ in the linear systems of equations $Ax = B$ which results in $M^{-1}Ax = M^{-1}b$. Since the system matrix $M^{-1}A$ is simplified, the iterative linear system solver converges faster when applied on the preconditioned linear system. The classical multigrid algorithm uses one or several auxiliary meshes that are coarser than the original (fine) mesh. The main goal is to perform only a fraction of the computations on the fine mesh and mainly on the coarser meshes. This approach leads to an iterative algorithm that is both fast and memory efficient.

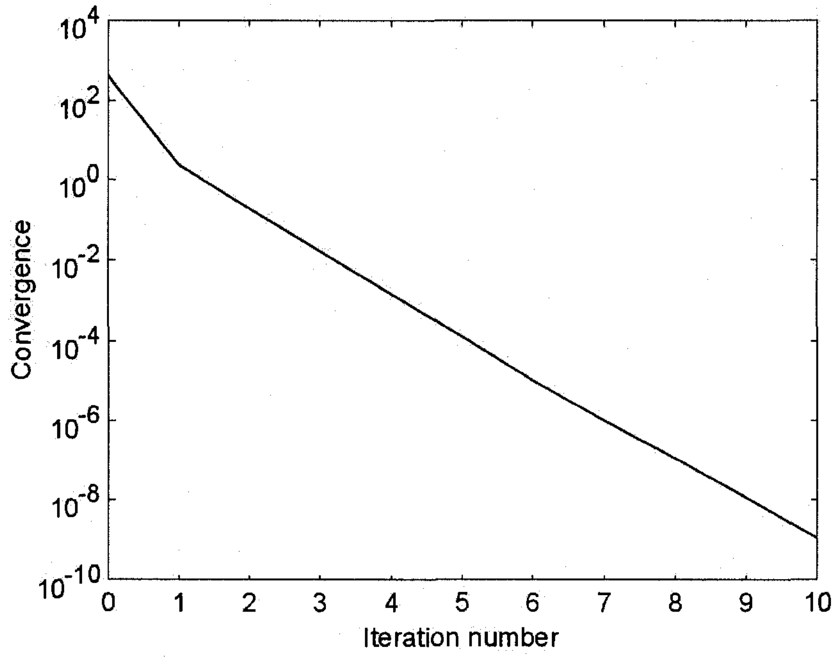

**Figure 4-18.** GMRES solver convergence as a function of the iteration number.

The simulations were run for several injection pressures, e.g. 5.0, 7.5, 20, 38, 100, and 180 MPa and temperatures 80, 100, and 130 $^{0}$C. In order to investigate the combination of applied pressure and temperature on the mold's topography change during molding, the whole pressure range was coupled with the highest temperature of interest, e.g. 130 $^{0}$C.

Upon analyzing of the simulation output results several important conclusions were formulated. As evident in Figure 4-19, the magnitude of max. principle stress values at low pressure depends mostly from the applied mold temperature while at high pressures it is not true. In other words, at low pressures the temperature is the processing condition that influences most the magnitude of the stress distribution in the Si mold. At very high pressures, which are unlikely to be used during micro-injection molding the principle stresses reach values larger than $\sigma_{yield}$ and irreversible brittle failure of the mold is expected.

In addition it can be concluded as well, that the temperature field changes the linear behavior of the increase of the max. principle stress with pressure. Figure 4-20 presents the distribution of all six principle stresses with maximum values as a function of the applied load and temperature (130 $^0$C).

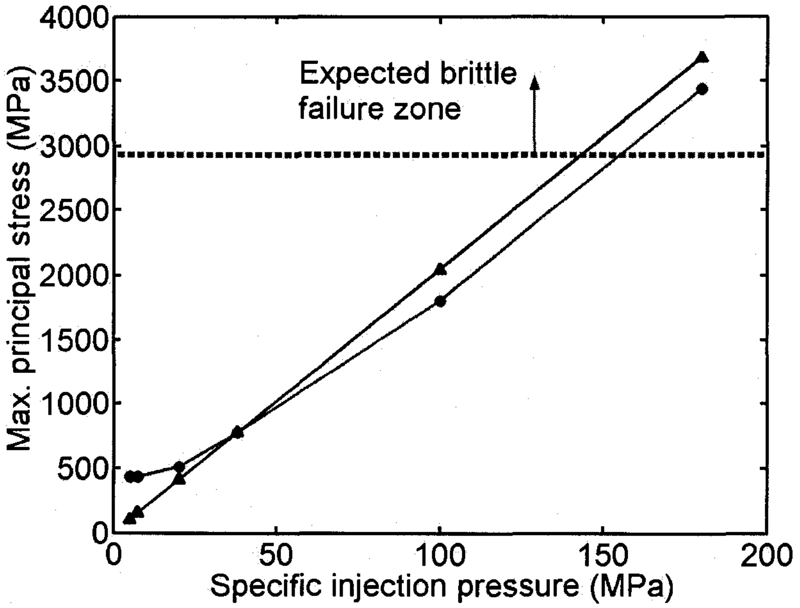

**Figure 4-19.** Max. principle stress distribution in the Si mold as a function of applied ▲- pressure only, and applied • – pressure and temperature -130 $^0$C. Pressure values were chosen to be 5.0, 7.5, 20, 38, 100, and 180 MPa.

In order to investigate the behavior of the Si mold integrity during mold base heating but before applying pressure, simulation were run with load that results only from the thermal expansion of the Si. The reference temperature, e.g. stress-free temperature $T_{ref}$ was chosen to be equal of the room temperature ~22 $^0$C. It is important to be noted, that in general upon curing, epoxy compositions have coefficient of thermal expansion (CTE) from at least 10 to 100 times more than the CTE of Si [102, 103].

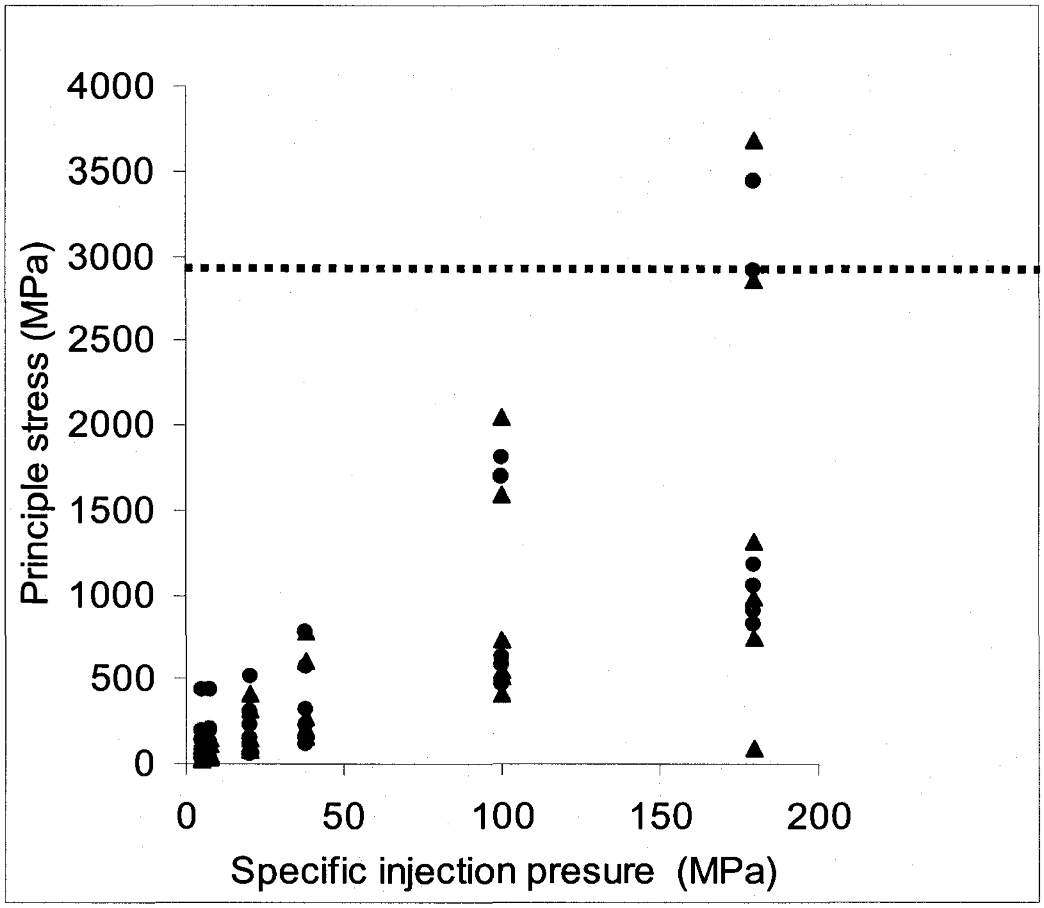

**Figure 4-20.** The six highest principle stress values, all of them located at points in the vicinity of the channels, as a function of the applied specific injection pressure. The load that resulted from ▲- the pressure filed only, and both • – the pressure and temperature fields. Pressure range: 5.0, 7.5, 20, 38, 100, and 180 MPa.

The latter fact means that possibly some initial stress could have been built around the boundaries of the Si mold but that scenario was not investigated. Determination of the thermal expansion for cured epoxy and shrinkage during curing can help building the physical model for this type of simulation. It is expected that the initial stress on the boundaries can have adverse effect on the resulted internal stress and strain magnitudes in the Si mold. As seen in Figure

4-21 the maximum principle stress values increase linearly with increase of the mold temperature reaching as high as 431.78 MPa for 130 $^0$C.

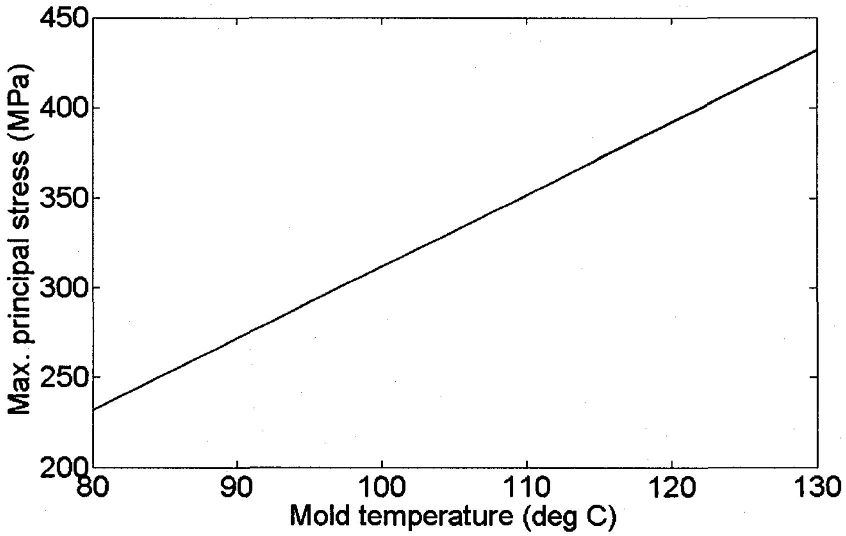

**Figure 4-21.** Max. principle stress as a function of the mold temperature. This result simulates the stress (or strain) state reached by the Si mold during heating before molding. Temperature values were chosen to be 80, 100, and 130 $^0$C.

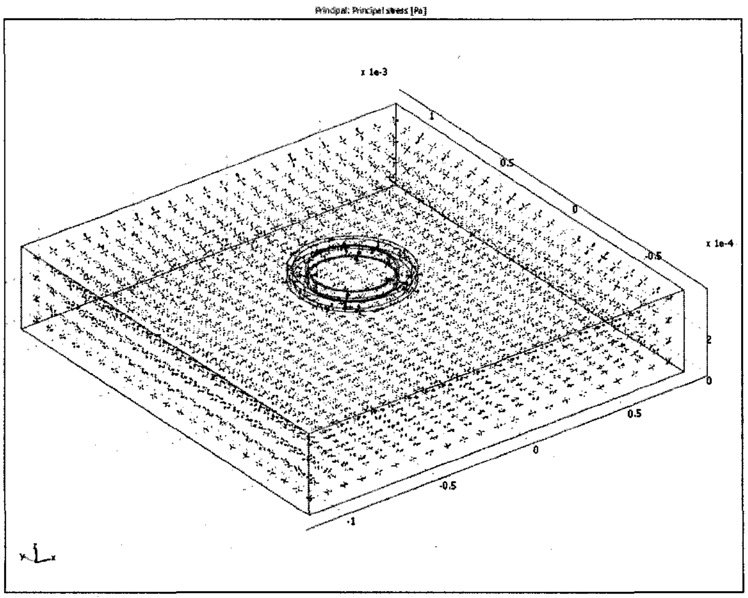

**Figure 4-22.** Principle stress distribution in the Si mold during thermal load which results after temperature increase to 100 $^0$C. Note that the highest principle stresses are in the vicinity of the channels. Similar distribution of the principle stresses was observed after simulations with coupled pressure and temperature fields but those results are not given for brevity.

Figure 4-22 shows the principle stress distribution in cross sectional profiles during initial heating of the mold upon reaching steady-state at a moment of time right before polymer injection. Note that the principle stresses with high magnitude are located only in the vicinity of the channels but their magnitude is lower than $\sigma_{yield}$=2.9±0.5 GPa and no brittle failure is expected.

Finally, the maximum value of *von Misses* stress through the entire domain was also found. It is important to be noted that *von Misses* stress is not considered reliable predictor of brittle failure of materials but since it can be expressed as a function of the principle stresses in 3D, eqn. 4-10, it is given only for visualization purpose in the case with load resulting from P=38 MPa and T=130 $^0$C, Figure 4-23. Note that the highest stress concentration is in the base of the channels.

$$\sigma_{Misses} = \sqrt{\frac{(\sigma_1-\sigma_2)^2+(\sigma_2-\sigma_3)^2+(\sigma_3-\sigma_1)^2}{2}} \tag{4-10}$$

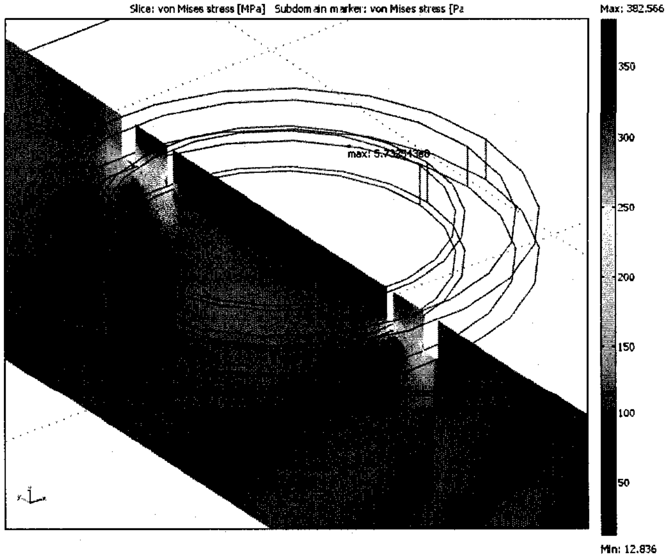

**Figure 4-23.** A cross sectional plot of *von Misses* stress through the middle of the channels with a max value of ~573.25 MPa in the vicinity of the channels.

Under important parameter which is expected to be an important factor influencing the replication accuracy during molding is the total displacement. Therefore, it was monitored for all load case scenarios. For simplification and consistency the total displacement of four edges, as seen in Figure 4-16(a) was monitored. Total displacement is a cumulative property that depends on the displacements along *x, y, z* axes in Cartesian coordinates and is given by

$$Displacement = \sqrt{u^2 + v^2 + w^2} \tag{4-11}$$

Figures 4-24 and 4-25, show the edges' total displacement as a function of the vertical distance z. As seen from the plots even only the thermal field induced measurable displacements for all considered objects. Note that the shape of the displacement curves is similar - only the magnitude of the total displacement increases with increase of the temperature.

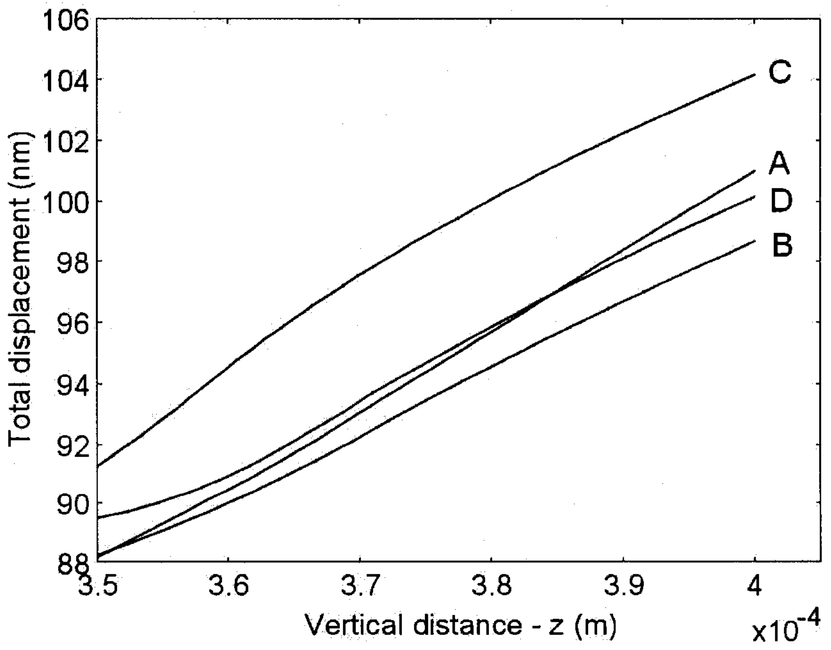

**Figure 4-24.** Total displacement of edges A, B, C and D vs. the vertical distance – z for temperature induced strain at 80 $^0$C.

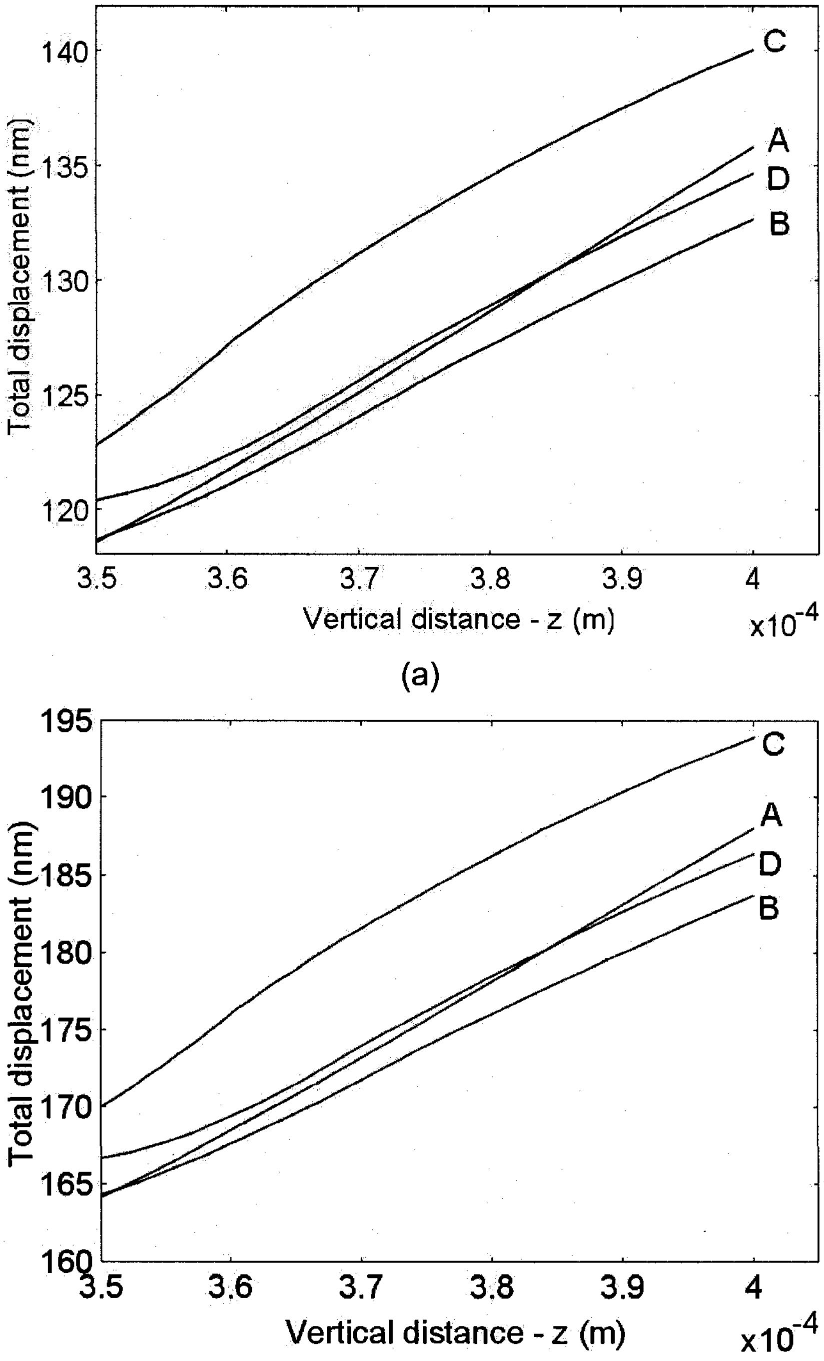

(a)

(b)

**Figure 4-25.** Total displacement of edges A, B, C and D vs. the vertical distance – z for temperature induced strain at (a) 100 $^0$C mold temperature, and (b) 130 $^0$C mold temperature. Note that the shape of the curves is similar - only the magnitude of the total displacement increases with increase of the temperature. The largest displacement was recorded for edge C for all simulated temperature fields. This temperature was the highest mold temperature utilized during molding of the nano-structured polymeric surfaces described in Chapter 5.

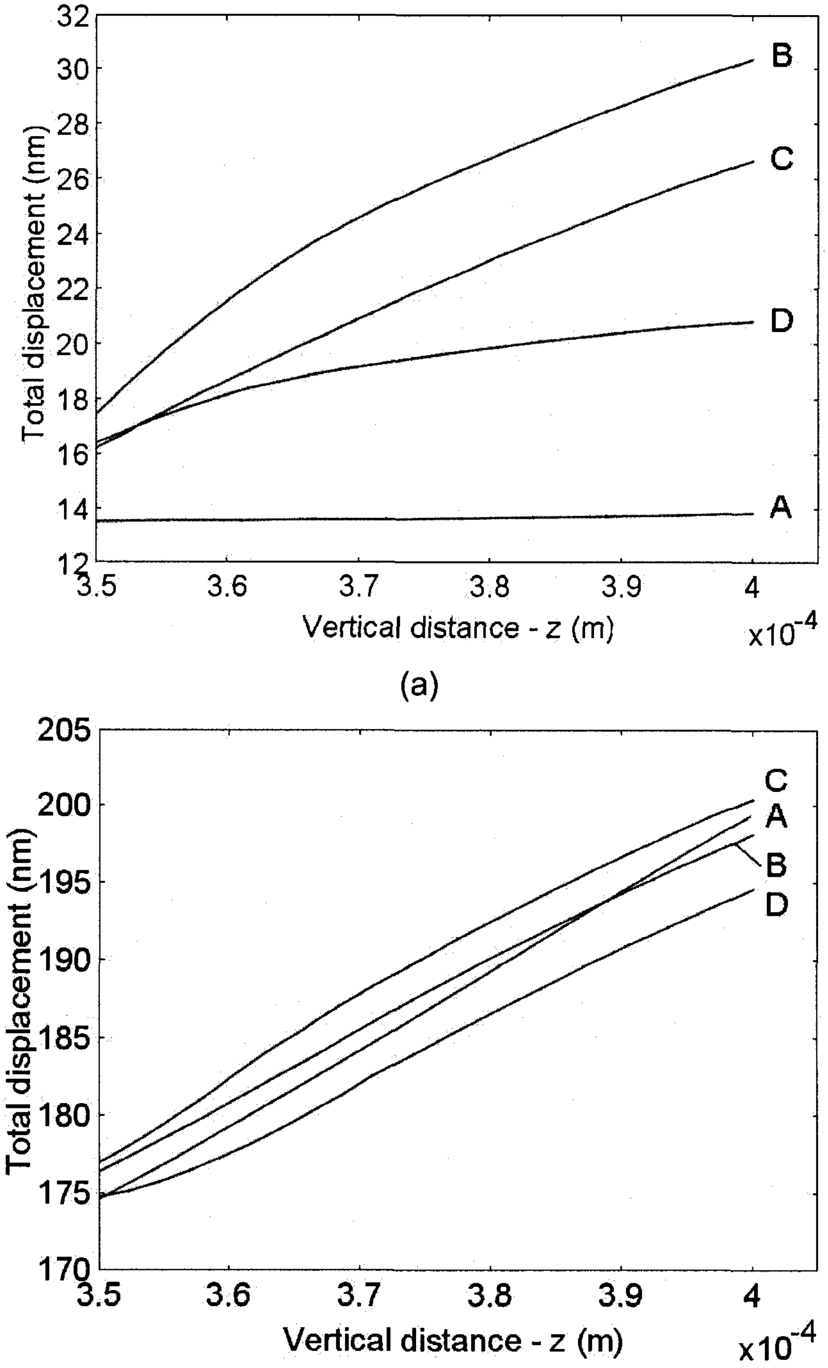

(a)

(b)

**Figure 4-26.** Total displacement of the edges A, B, C and D vs. the vertical distance – z which results from application of (a) pressure field only and (b) pressure and temperature fields. Specific injection pressure was kept at 5 MPa and the mold temperature at 130 $^0$C. Parameters uniformly distributed throughout the entire domain.

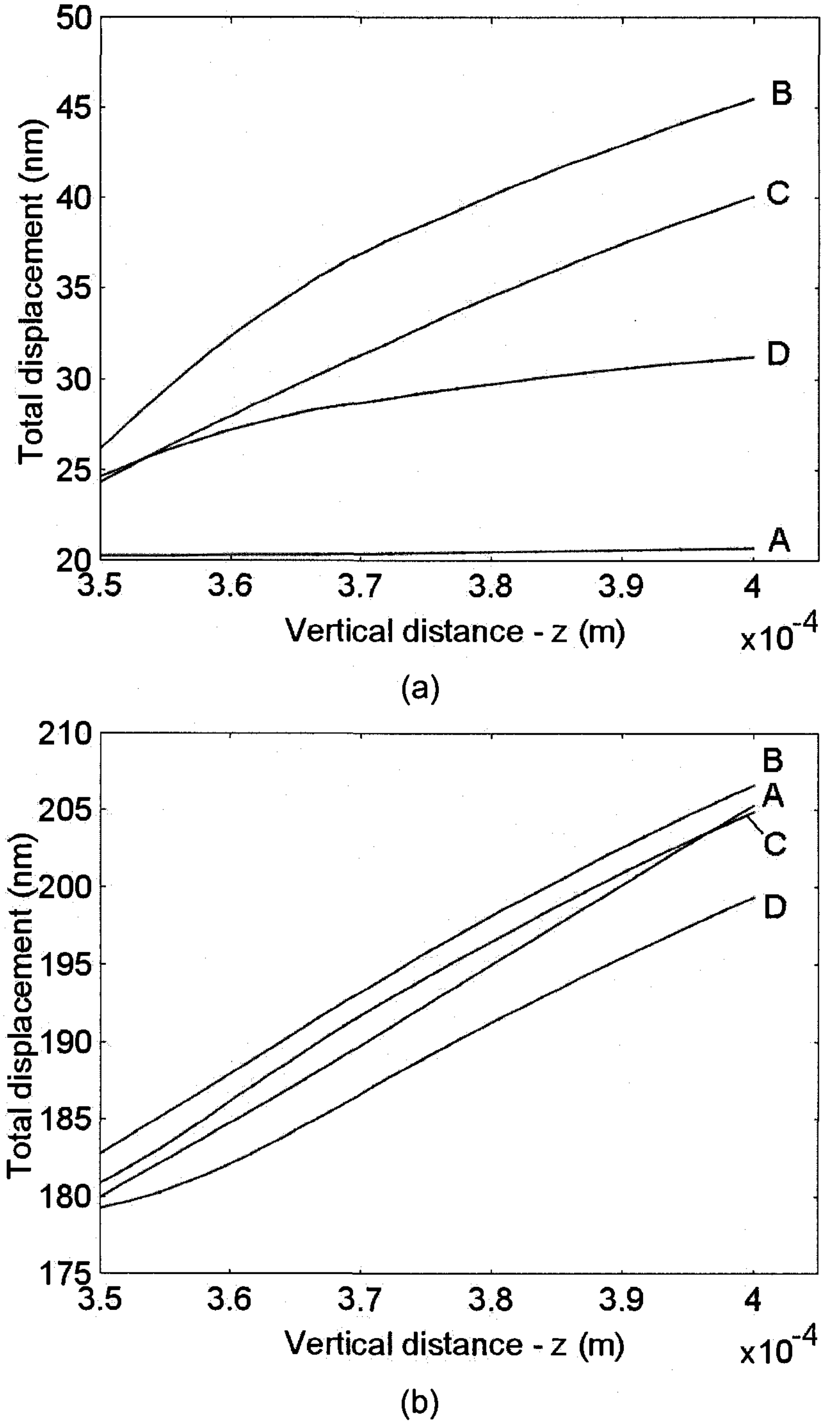

**Figure 4-27.** Total displacement of the edges A, B, C and D vs. the vertical distance – z which results from application of (a) pressure field only and (b) pressure and temperature fields. Specific injection pressure was kept at 7.5 MPa and the mold temperature at 130 $^0$C. Parameters uniformly distributed throughout the entire domain.

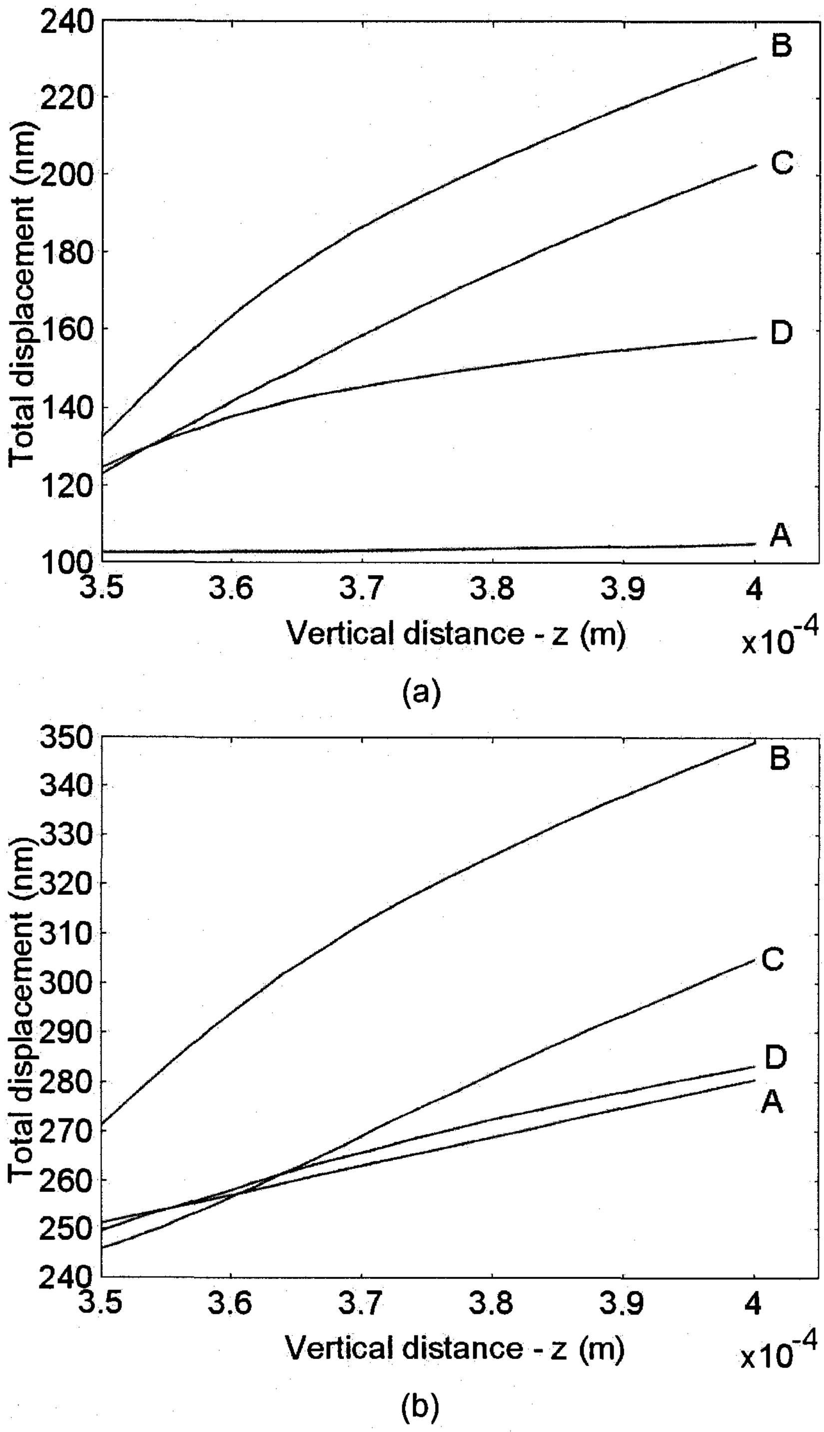

(a)

(b)

**Figure 4-28.** Total displacement of the edges A, B, C and D vs. the vertical distance – z which results from application of (a) pressure field only and (b) pressure and temperature fields. Specific injection pressure was kept at 38 MPa and the mold temperature at 130 $^0$C. Parameters uniformly distributed throughout the entire domain.

Upon running simulations with loads initiated from applied pressure with or without temperature, the edges displacement was quite different in comparison with that recorded from the simulations with applied temperature field only. As seen from Figures 4-26, 4-27, and 4-28 the applied temperature filed has a profound influence on the edges displacement. In all cases the applied temperature resulted to an increase of the edges displacements which influence was more noticeable at small pressures. When high pressures were used (plots are not given for brevity) that was not the case. Nonetheless, in the latter cases the displacements were substantial up to 1.1 μm for pressure 180 MPa where brittle failure is expected as well. The average relative increase in simulated displacement with applied pressure and temperature compared with the displacement that results only from pressure field was about 10-15% at high pressures, while the average displacement with applied pressure and temperature at low pressures was substantial to about 550%.

In conclusion, the results strongly suggest that the mold temperature is the most important factor which influences the generation of internal stresses and displacements in the Si mold. High principle stresses with values above $\sigma_{yield}$ were found to arise only at very high pressures which are unlikely to be used in injection micro-molding. Therefore, brittle failure of the Si mold with the considered geometry is not expected to occur during injection micro-molding. Other factors, though, such as mold handling and scribing technique can have detrimental effect on the mold structural integrity during molding. For example, manual scribing of the Si induces cracks at the edges of the Si mold piece which can propagate/brake the mold during application of loads. Consequently, care must be taken during the whole process of mold manufacture.

## 4.4 Replication Process and Results

The replication process was initiated in the same manner as the already discussed one in Chapter 3. In this round of experiments, the processing conditions were chosen to be as follow: $T_{noz} \sim 288\ ^0C$, $P_{hold} = P_{inj} \sim 7.5$ MPa, $P_{back} \sim 0.7$ MPa, $n \sim 125$ 1/min, $V_{inj} \sim 100$ mm/s, $T_{mold} \sim 130\ ^0C$. Due to the brittle nature of the mold a unique approach has been implemented to successfully fix the mold in the mold base. As seen in Figure 4-29, the Si mold was inserted in the metal base and encapsulated via fast curing epoxy adhesive (thixotropic paste, two component epoxy T-515 A/B obtained from Zymet Inc.). The epoxy was chosen due to its high glass transition temperature, thermal shock resistance and thermal stability. Upon mixing the epoxy resin (Part A) with

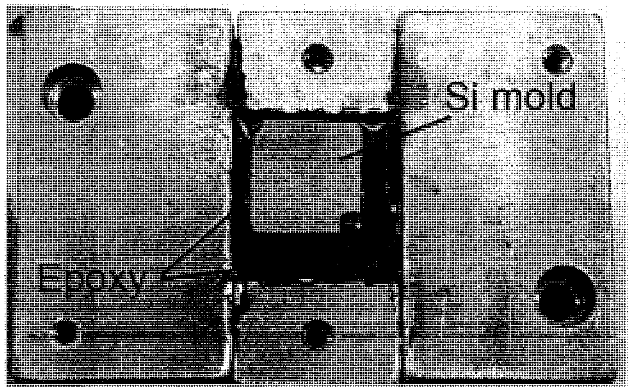

**Figure 4-29.** Digital picture depicting the metal mold base with inserted Si mold encapsulated with the epoxy. The lower right corner of the Si mold chipped during molding – a result from manual scribing - and was successfully "repaired" by curing a small blob of the epoxy in that region.

the epoxy hardener (Part B), the temperature of the whole assembly was risen to 155 $^0$C, just above the adhesive bondline temperature to initiate the cure process. Since the epoxy had very fast cure kinetics ("snap" cure) the Si mold was manually dropped in the mold base pocket and let to float for 5 min onto a film of epoxy before temperature increasing. The whole assembly was also leveled before epoxy curing.

Upon injection molding of approximately a dozen polymer samples with COC polymer, the replicas (#2, 4, and 7) were imaged with a SEM - LEO 1550 VP in viable pressure mode (VP ~40Pa). Each polymer sample had on its surface replicas of 6 Lehigh University logos, 3 BOY Machines Inc. logos, 3 "SPE-ANTEC-2006" and 32 "BOY 12A" alphanumerics. Due to the bad lithography step of some of the "BOY 12 A" strings not all of the objects were replicated. Excellent replication fidelity was observed after imaging sample #2, as seen in Figures 4-30 to 4-34. Unexpectedly, during imaging of the samples unordered striations in the order of 50-100 nm in width were found on the ground surface, as seen in Figures 4-31- 4-32. It was presumed that those striations or lines resulted from "frozen-stress" on the surface due to uneven heat distribution. The latter, could have been initiated from the fact that the polymer melt passed from a hot zone (the nozzle) through a cold zone (formed by the sprue bushing and stationary "A" platen of the injection molding machine) to another hot zone (the mold base). It was assumed that heating of the cold zone can eliminate the surface "frozen-stress" and this was successfully implemented in other experiments described in Chapters 3 and 5 of this comprehensive study.

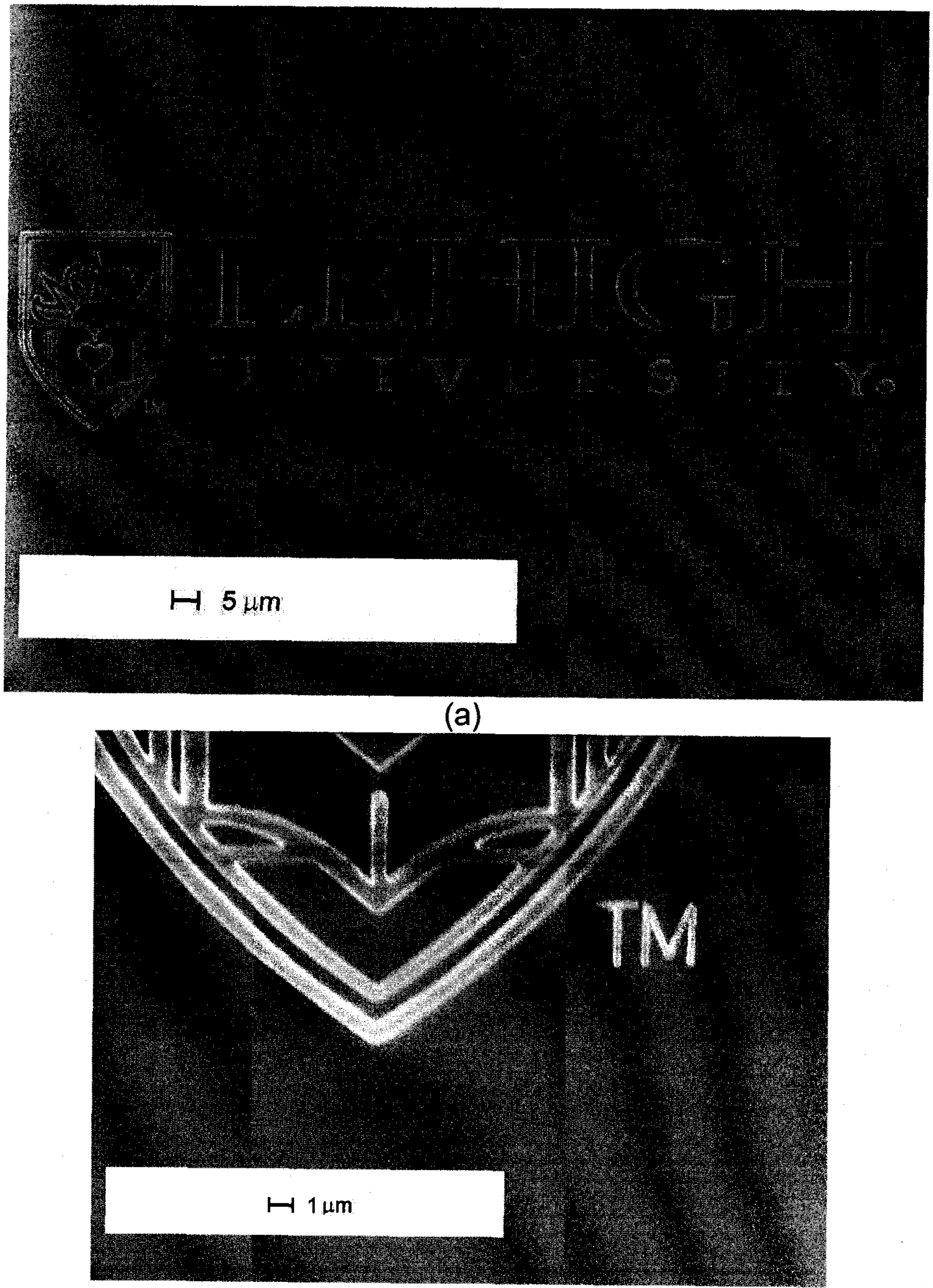

(a)

(b)

**Figure 4-30.** SEM-VP mode top-view images of (a) the official logo of Lehigh University injection micro-molded from the structured mold seen in Figure 4-10 and (b) the detailed top-view of the bottom part of the logo's shield depicting an open book with a heart in the middle and rising Sun behind them. (Images taken from polymer replica #2).

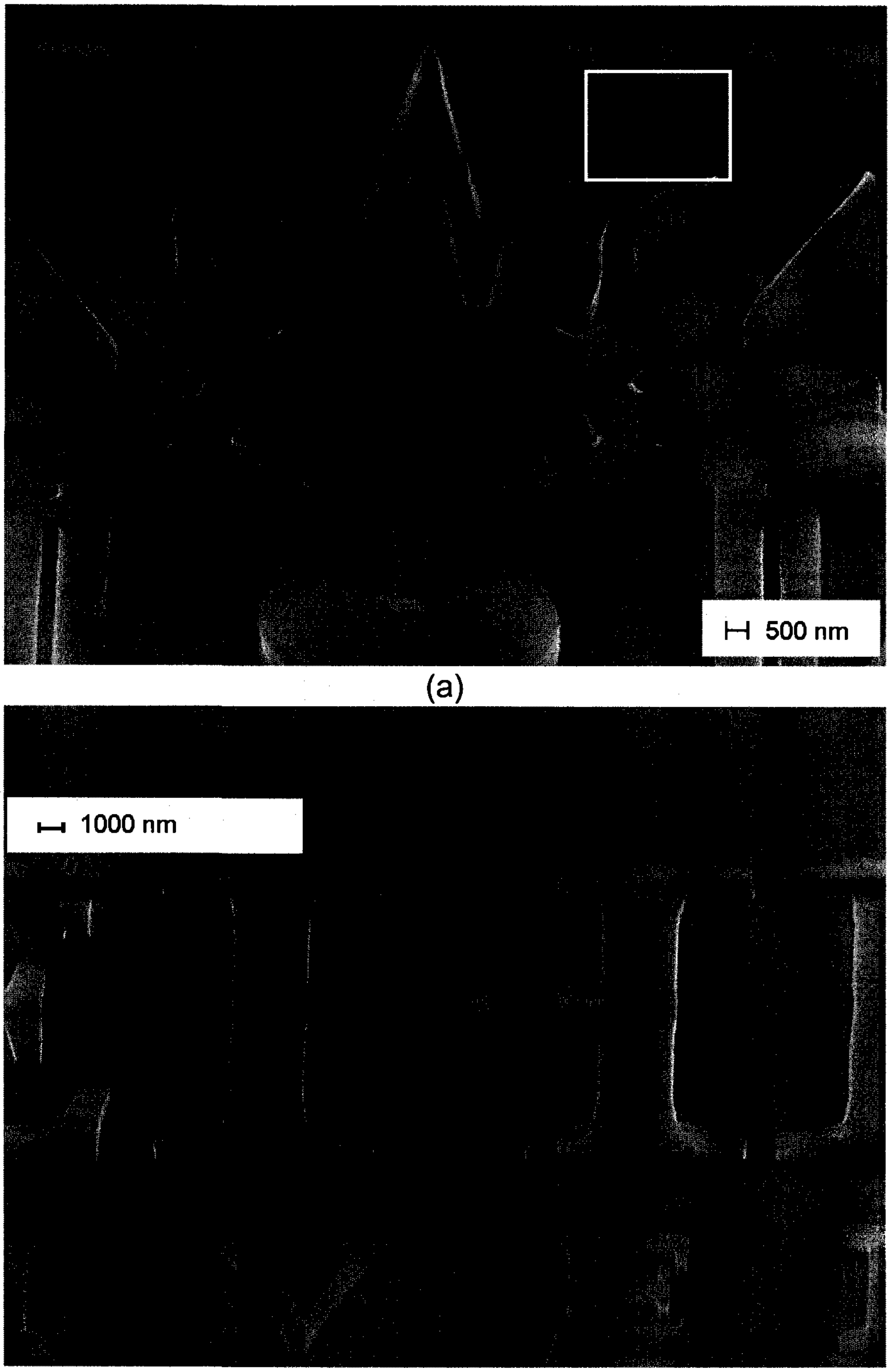

(a)

(b)

**Figure 4-31.** SEM-VP mode tilted-view images of details of the official logo of Lehigh University (a) shield with replicated mold scallops on the vertical walls. The region in the white square was further investigated and the findings were described in Chapter 5 and (b) Palatino font type letters. Note the formation of surface "frozen-stress" lines on the replica. (Images taken from polymer replica #2).

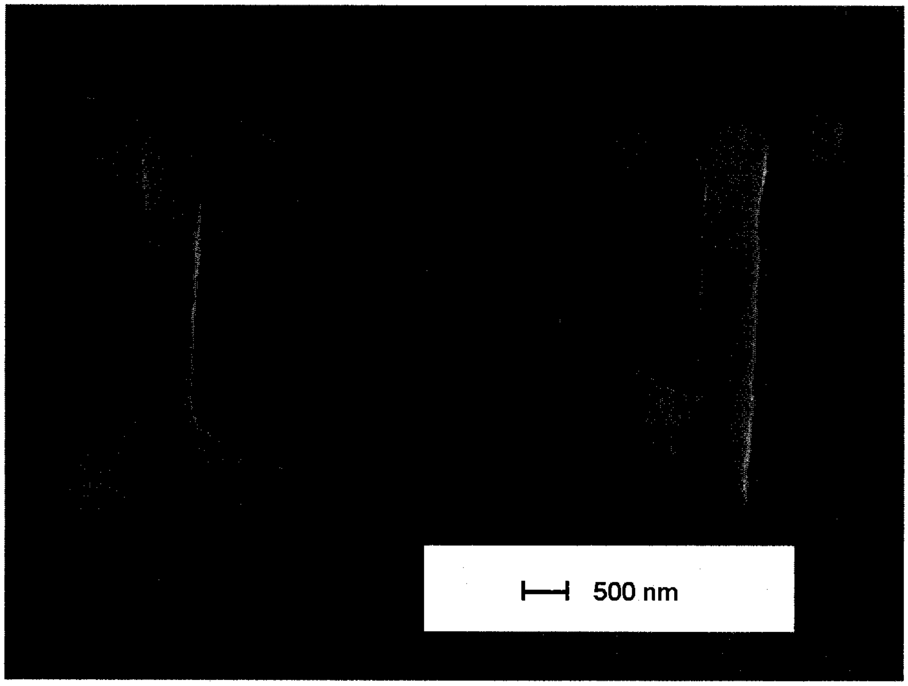

(a)

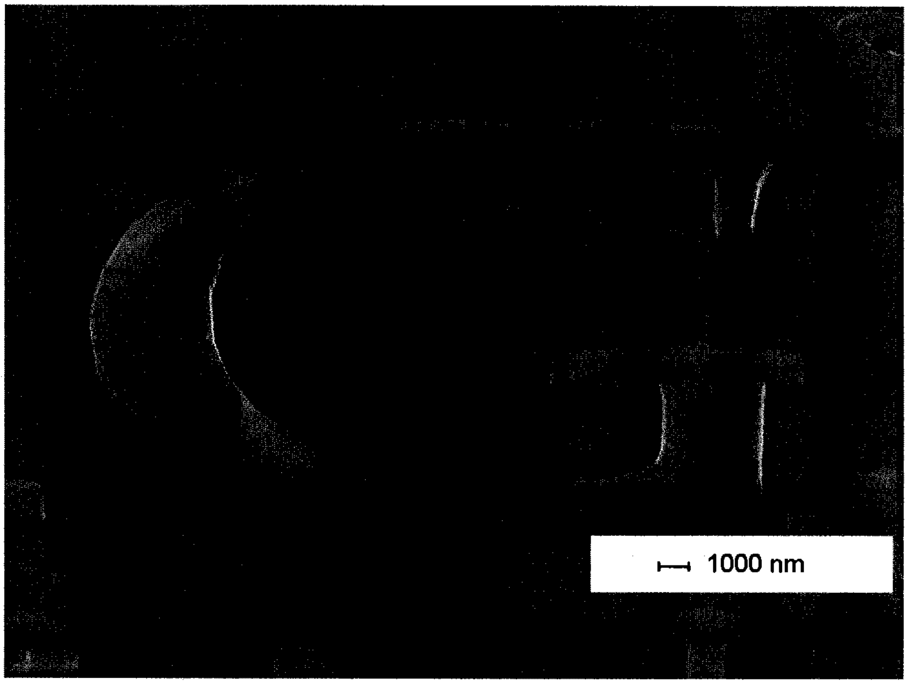

(b)

**Figure 4-32.** SEM-VP mode tilted-view images of details of the injection micro-molded official logo of Lehigh University. Note that the replicated scallops are seen but some of them are also smeared. (Images taken from polymer replica #2).

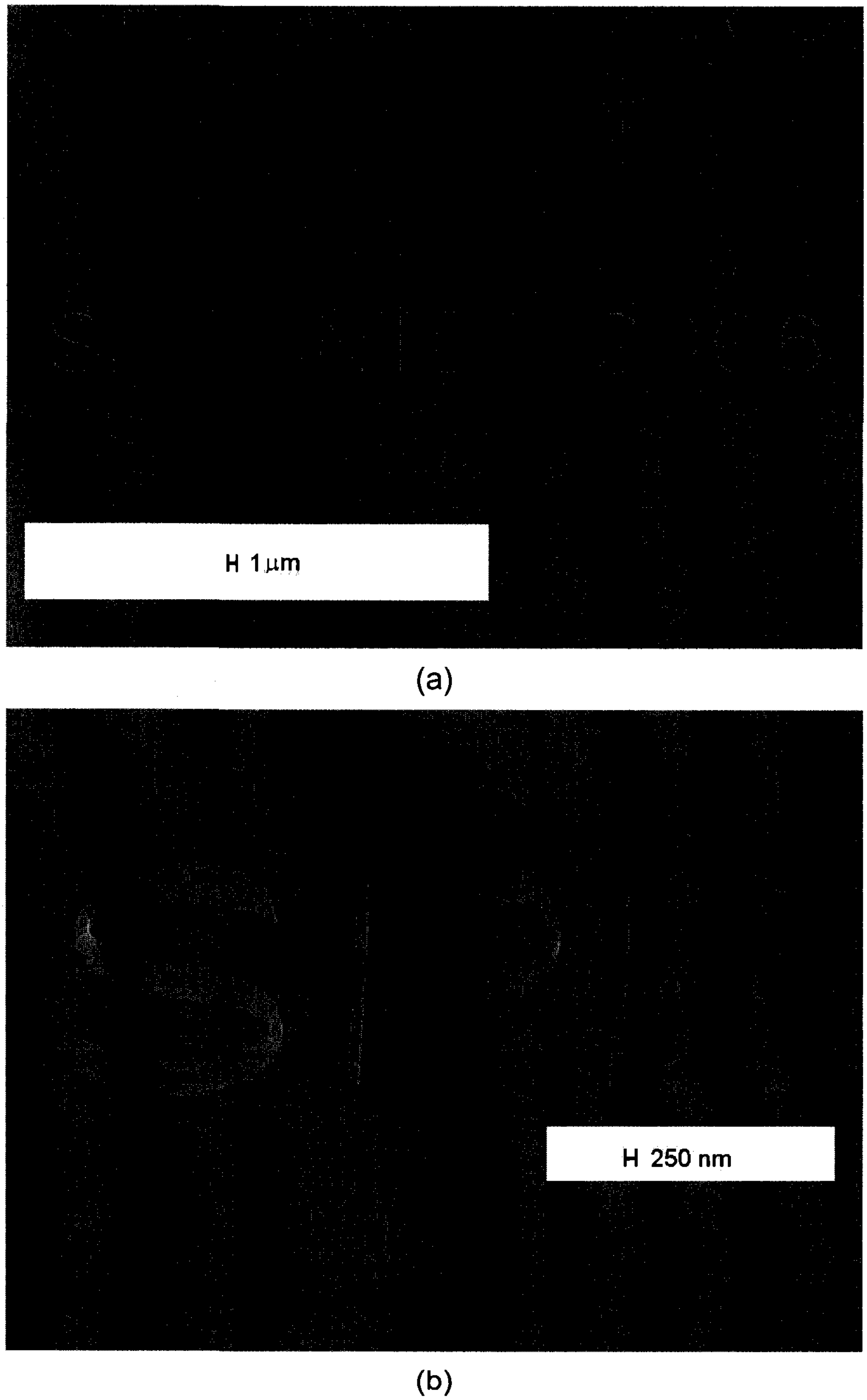

**Figure 4-33.** SEM-VP mode images of injection micro-molded replicas of (a) the "SPE-ANTEC-2006" alphanumeric and (b) tilted image of the SPE acronym. Note that since the images were not taken with focus on the surface, the "frozen-stress" lines are not seen. (Images taken from polymer replica #2).

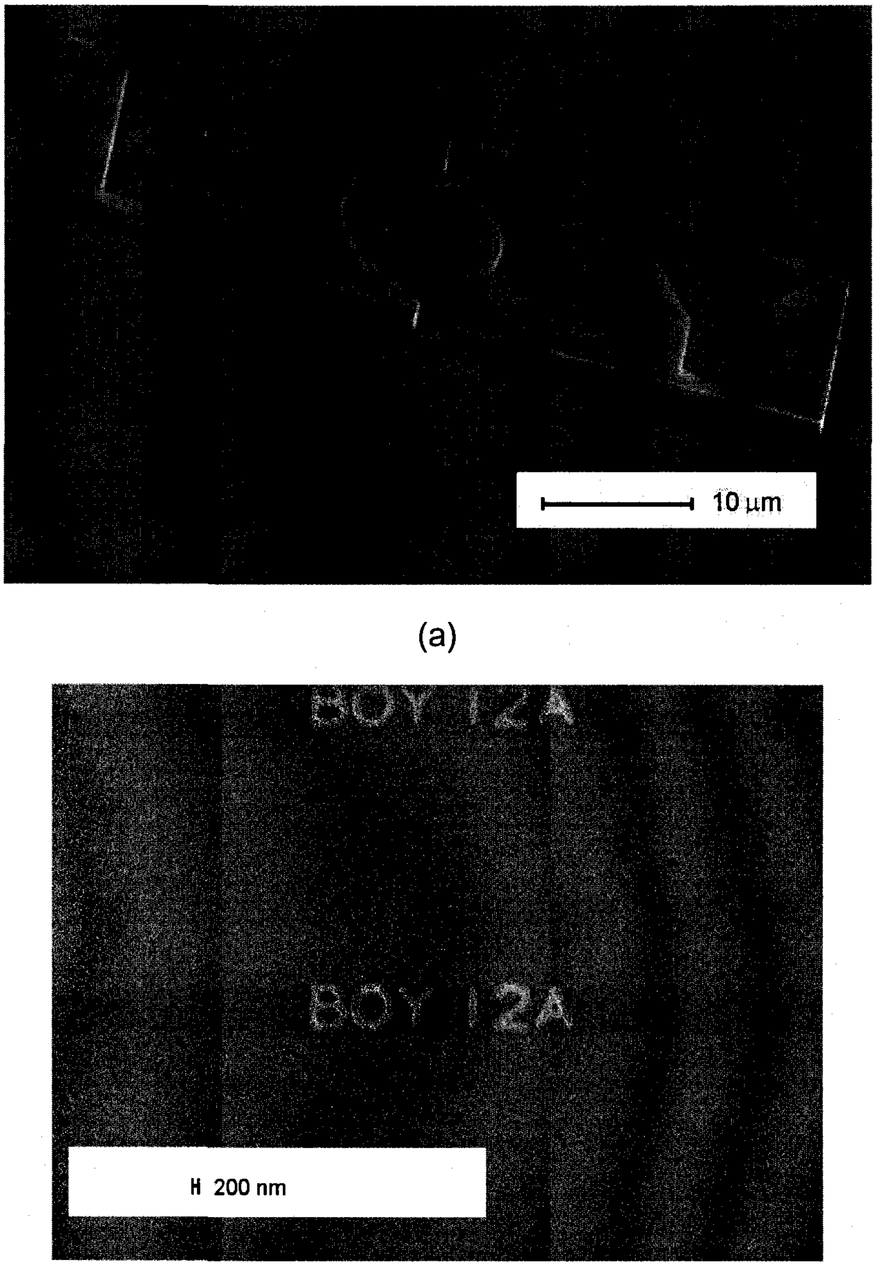

(a)

(b)

**Figure 4-34.** SEM-VP mode images of injection micro-molded replicas of (a) the official log of BOY Machine Inc. and (b) "Boy 12A" alphanumeric. Note that since the images were not taken with focus on the surface the "frozen-stress" lines are not seen. (Images taken from polymer replica #2).

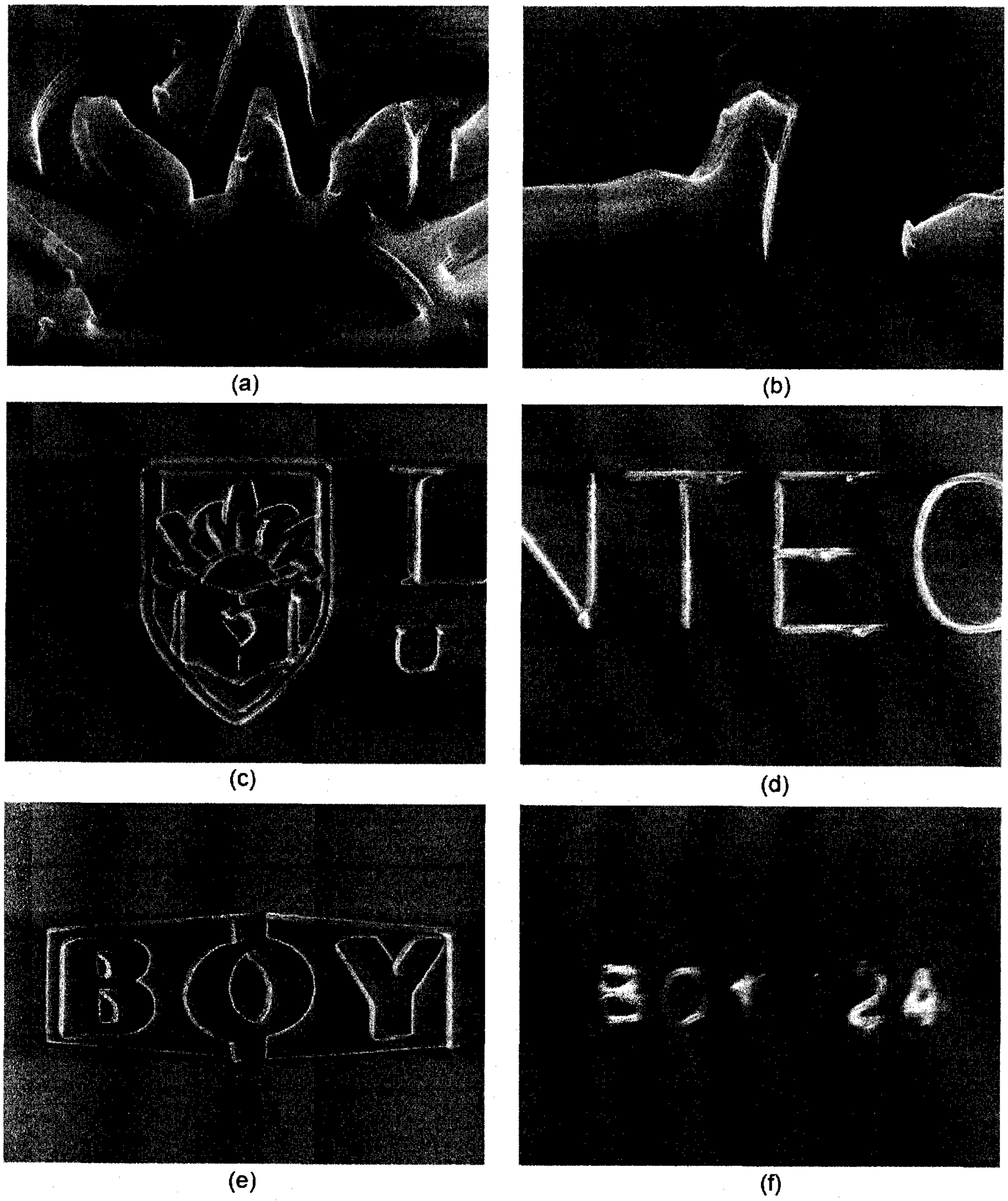

**Figure 4-35.** SEM-VP mode images of examples of polymer replicas with deteriorated quality of replication. It has been assumed that the cavities virtually got "plugged" with polymer remnants after subsequent moldings – a result from polymer sticking due to the high surface energy of bare Si. Images in (a, b) taken from sample #4, Note the small "chipping" of the COC structures at the corners; images in (c, d, e, f) taken from samples #7 and #10.

Upon imaging of polymer samples (#4, 7, and 10) it was discovered that the quality of replication was lowered as evident from Figure 4-35. It is believed that the COC polymer was sticking in the cavities and every subsequent molding cycle was adding more and more material (polymer) into them to the point when no further replication with high fidelity was possible. The excellent replication of the cavities at the begging could be explained with the relevantly low surface energy of COC [85] which did not allow for repeated high quality replication of the micro-topography of the Si molds. Consequently, a new approach has been sought which resulted in the development of special anti-sticking coating deposited on the Si molds.

### 4.5 Summary

In this study injection micro-molding based on Si molds was presented. Standard micro-fabrication techniques, namely E-beam lithography and Deep Reactive Ion Etching were utilized and their use validated as tools suitable for Si mold fabrication at Lehigh University. Several types of different micro-structured cavities were successfully etched in Si and replicated with thermoplastic cyclo olefin copolymer. Relevant process parameters and process limitations were also formulated and discussed.

In addition, static parametric stress-strain structural FE analysis was performed on a model consisting of micro-structured ring channels. Simulation results revealed that the Si mold holds its structural integrity at the range of commonly used pressures and mold temperatures during polymer injection micro-molding. It was also shown that the mold temperature is the most important factor which influences the total displacement of the micro-structured features in the mold.

Finally, potential application which could benefit from this study are envisioned, among others, to be: (i) micro-tagging of molded components to eliminate counterfeiting; (ii) fabrication of inexpensive high-Q optical micro-ring filters and modulators utilized in micro-photonic integrated circuits [62, 104, 105] and such that can be used in bio/chemical sensors [106], as seen in Figure 4-36.

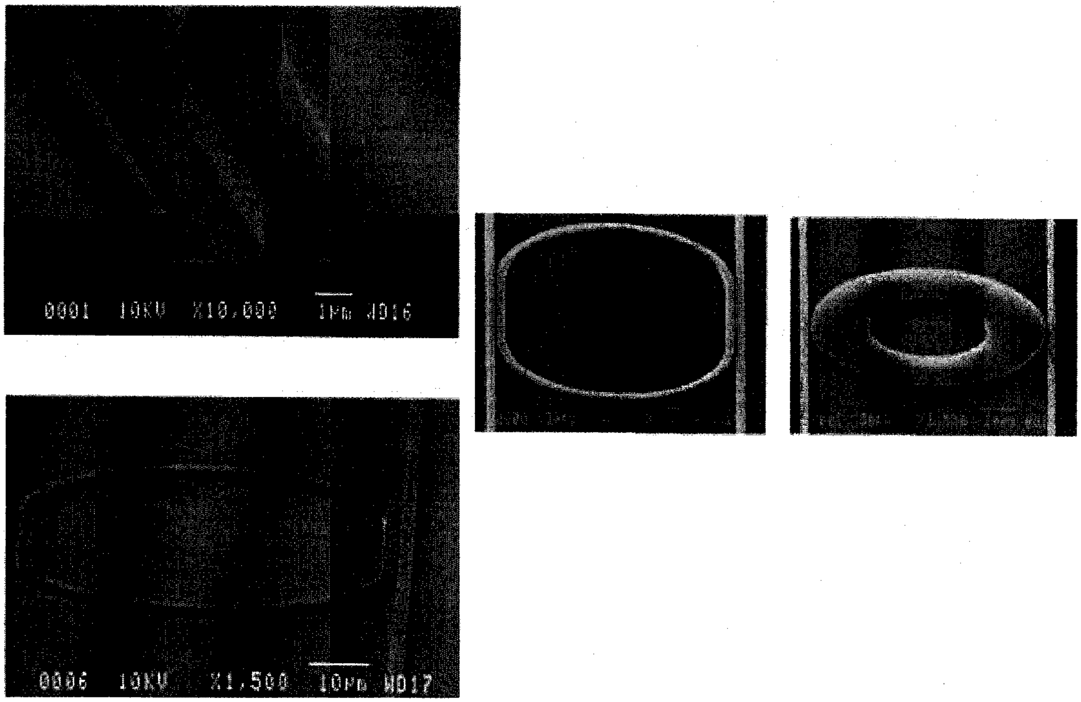

(a) (b)

**Figure 4-36.** SEM pictures of a (a) top -$SiO_2$ reactive ion etched mold utilized as a mold to replicate Poly(methyl methacrylate) micro-ring resonator – bottom image and (b) from left to right – imprinted in Polycarbonate micro-racetrack and micro-disk (different shapes of ring resonators). *Reprinted with permission from [62], © 2002, American Institute of Physics.*

# CHAPTER 5

# SUB-100 nm INJECTION MOLDING BASED ON Si MOLDS

*"Creativity generates Technology."*

## 5.1 Introduction

In this chapter a unique set of experiments was developed and successfully implemented to initiate and advance the experimental capabilities at Lehigh University suitable for the manufacture of sub-100 nm feature-size patterned surfaces. The experimental work described here is a continuation of the work presented in Chapter 4 of the this comprehensive study.

In this set of experiments, it is reported on the feasibility to use injection molding to replicate polymeric nano-sized patterned surfaces from Si molds treated with plasma polymerized (PP) anti-adhesive ultra-thin fluorocarbon coating. In this very challenging work, Si molds were manufactured by E-beam lithography and DRIE in Bosch® process mode. Deposition of the low surface energy fluorocarbon film, from $C_4F_8$ (octafluorocyclobutane, OFCB) precursor gas was done by utilizing the high-density inductively coupled plasma (ICP) reactor of the DRIE tool [92]. The PP-OFCB was characterized by X-ray photoelectron spectroscopy (XPS), Fourier transform infrared spectroscopy (FT-IR), ellipsometry, and goniometry. The patterned, injection molded surfaces with COC, were imaged with scanning electron and atomic force microscopes. By employing the anti-sticking fluorocarbon film treated molds, high aspect ratio (AR~8) submicron-sized pillars were produced as well. Fluorine transfer during molding from the film to the polymeric replicas with nano-futures was analyzed via XPS. Thermal degradation analysis of a molded polymer replica and unprocessed polymer was carried out by comparison of the valence band spectra ($C_{2s}$, $C_{2p}$). Finally, based on the currently accepted theoretical models, prediction of the mechanical stability of the replicated high AR pillars was performed and the results were compared with the observed stability of successfully replicated features.

One of the most interesting results, obtained upon completion of the work in Chapter 4, was the observation that the COC did replicate the fine nano-topography formed at the bottom of the Si mold during ion etching, Figure 5-1. It was estimated [13] that the peak-to-valley distance of the nano-topography is less than 5 nm. Consequently, a special routine was developed to produce structured molds with ordered nano-features suitable for injection molding.

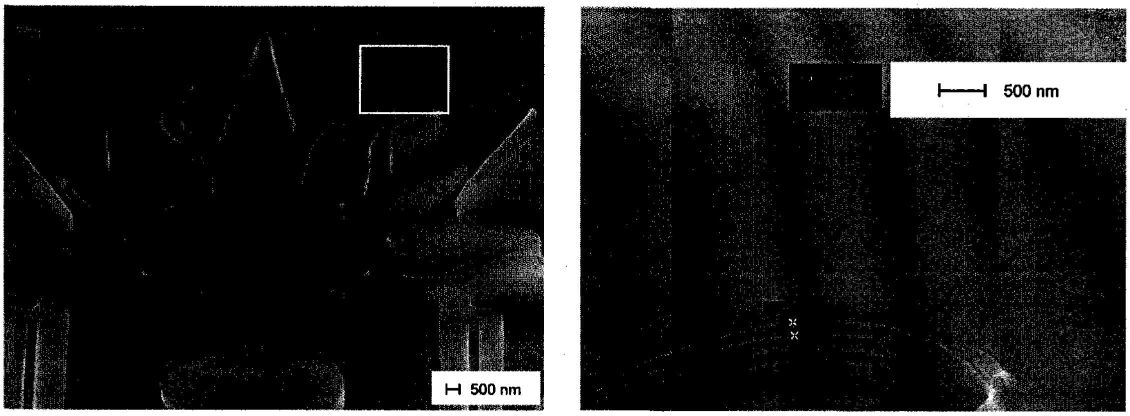

(a) (b)

**Figure 5-1.** SEM-VP mode images of the polymer replica of (a) Lehigh University logo shield with a rectangular region in the upper right corner shown with higher magnification in (b). Note the high fidelity of replication of 1) scallops inherent for DRIE processed Si, that represent lines on the vertical wall that a separated by ~150 nm, and 2) the surface roughness from the bottom of the etched Si mold, e.g. the top flat surface of shield. The nano-topography on the top surface (peak-to-valley distance) was estimated to be less that 5 nm from [13].

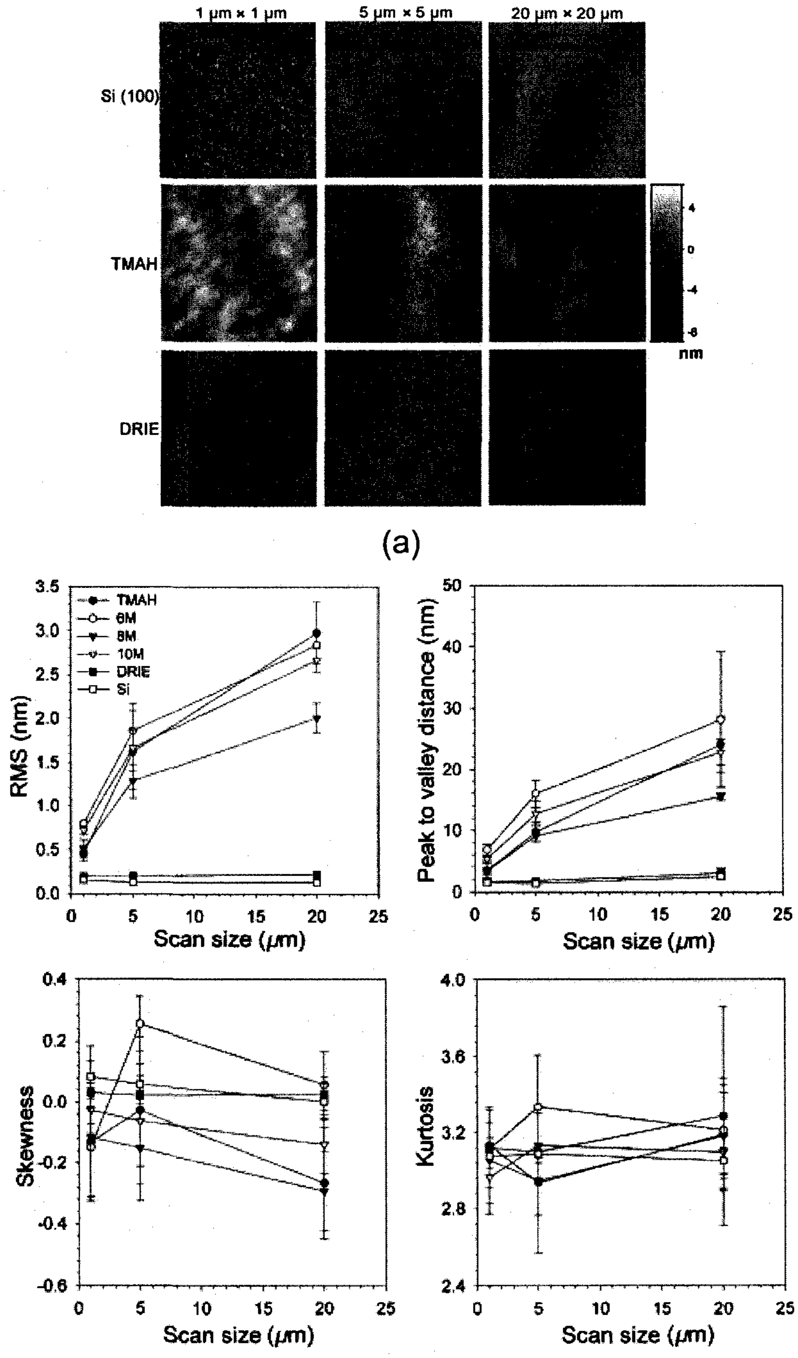

(a)

(b)

**Figure 5-2.** (a) AFM topography images of unetched Si (100), tetramethylammonium hydroxide (TMAH) and DRIE etched Si surfaces of scanned sizes of 1, 5, and 20 µm, respectively. (b) Variation of surface roughness amplitude parameters as a function of scan size for various etched samples. *Reprinted from [13], © 2004 with permission from Elsevier.*

One of the major problems related to replica molding has been identified to be the quality of the molds. Utilizing masters with low surface energy that prevent adhesion of the solidified polymer during demolding, a prevalent failure mechanism [77, 107, 108], has been suggested to improve the fidelity of replication and thus the quality of the molds. These application-based problem solving approaches during fabrication have lead to implementation of organosilanes for deposition of self-assembled monolayers (SAMS) mainly because they have widespread usage in microsystems fabrication. Tridecafluoro-1,1,2,2-tetrahydrooctyl trichlorosilane ($CF_3(CF_2)_5(CH_2)_2SiCl_3$) monolayer [77, 109, 110] and *n*-dodecanethiol ($CH_3(CH_2)_{11}SH$) monolayer [111] have been considered among others. Thermal stability of various SAMS have been also investigated [112].

On the other hand, very thin amorphous fluorocarbon films with low surface energy can be deposited by plasma polymerization. Such films can achieve good conformality and can preserve the master's feature sizes intact as well. Plasma polymerized (PP) fluorocarbon films are also being investigated due to their excellent photonic properties, high chemical inertness, low dielectric constants, excellent solvent resistance, low moisture absorption [113-115] and due to their high temperature stability especially if polymerized at low pressures [116] .

However, reports on utilizing PP fluorocarbon films as anti-adhesive layers [117-120] on structured masters used for replica molding are limited. Thus, in these sets of experiments it is reported on the feasibility to use injection micro-molding to fabricate, for the first time to the author's best knowledge, polymeric patterned surfaces from nano-structured molds treated with PP-OFCB anti-sticking film.

## 5.2 Experimental Details

In what follows, a detailed description of the mold fabrication and characterization procedures is presented. Processing conditions and factors influencing mold quality, related to the current study are also discussed.

### 5.2.1 Mold Fabrication

#### *5.2.1.1 Pattern Generation via E-beam Lithography*

The fabrication process of the nano-structured Si molds was again initiated with pattern generation using a combination of DesignCAD$^{TM}$ LT 2000 and Nanometer Pattern Generation System (NPGS, JC Nabity Lithography Systems). Several exposure levels during e-beam lithography were considered based on the previous experience with writing structures larger than 100 nm as described in Chapter 4. Several object types were considered, namely 2D hole-arrays, 2D long and short trenches, and 2D array of square posts with different geometry and spacing between the features. As shown in Table 5-1 some of the prescribed doses led to unacceptable exposures that resulted in overexposure or underexposure of the resist as seen in Figure 5-3.

| object type | dose type | dose level | exposure result |
|---|---|---|---|
| holes | point dose, fC | 31.15 | accepted |
| holes | point dose, fC | 62.29 | accepted |
| holes | point dose, fC | 124.58 | accepted |
| holes | point dose, fC | 249.15 | rejected |
| holes | point dose, fC | 373.15 | rejected |
| long trenches | area dose, $\mu C/cm^2$ | 300.00 | accepted |
| short trenches | area dose, $\mu C/cm^2$ | 300.00 | accepted |
| square posts | area dose, $\mu C/cm^2$ | 300.00 | accepted |

**Table 5-1.** Summary of the used dose levels to expose different objects during e-beam lithography.

As already discussed in Chapter 4, elimination of the deleterious effect of the secondary electrons emitted by the Si substrate during e-beam exposure was achieved by using the maximum available beam voltage of the e-beam system. To focus the electron beam, e.g. wobble and stigmatism, a gold sputtered Si substrate was again employed. It was demonstrated that by varying only the dose levels holes with different sizes can be achieved, e.g. the diameter decreases with the point dose, Figure 5-4. On the other hand, by varying the geometry of the features and keeping the appropriate dose constant short and long lines were also successfully exposed and etched. Only filled polygons were used to expose these objects with specified area doses since as it was discovered in Chapter 4 line doses did not produce acceptable results.

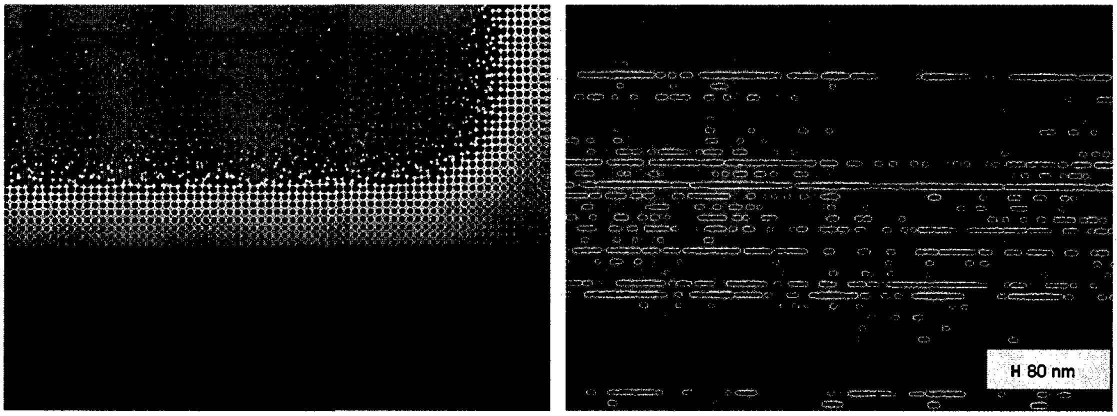

(a) (b)

**Figure 5-3.** SEM images of Si molds after ion etching. The patterns are a result of PMMA resist mask that was (a) overexposed with point dose 373.15 fC and (b) underexposed. The patterns should have been 2D hole-array and horizontal parallel long trenches (lines). The well developed pattern at the corner of the 2D hole-array resulted due to proximity effects, e.g. features at the edge of the patterned zone are less exposed. In this case it was beneficial since the dose level in general was set too high. Proximity effect controlling was not possible with NPGS system but is readily available in commercial and very expensive e-beam systems.

To write the 2D holes and short trenches arrays, while keeping the distance or the pitch between the objects to a constant value, a special procedure was successfully developed and implemented for the first time at Lehigh University since no related prior art was available addressing such issue. Specifically, in the NPGS system's run files 1) the center-to-center and 2) the line spacing variables where changed to accept values equal to the distance or the pitch between two holes or trenches. More information about the influence of those parameters on the e-beam lithography can be found in Chapter 4. As a result that approach allowed for controlling the exact locations in which the beam fires, Figure 5-5.

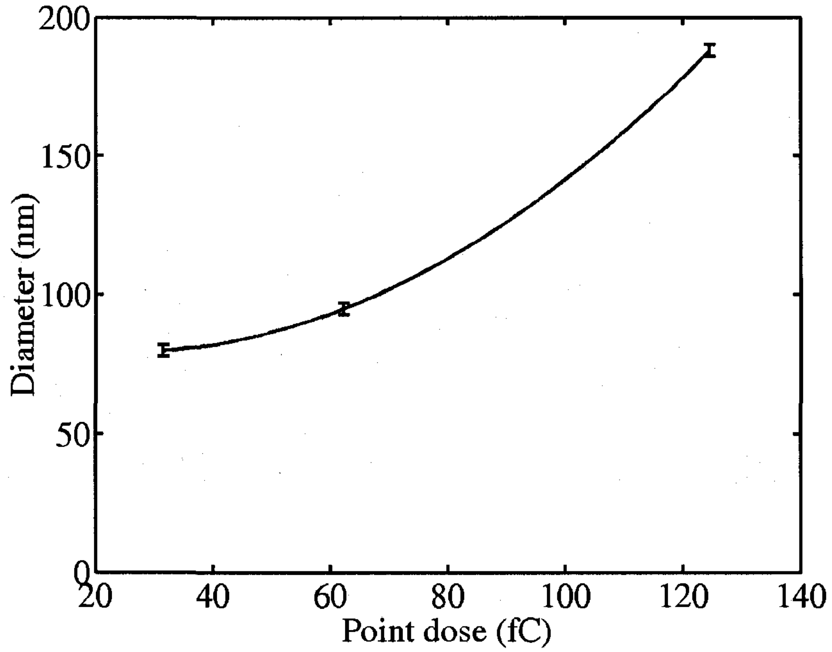

**Figure 5-4.** Holes diameter (measured after etching) dependence of the point dose level during an e-beam exposure of PMMA resist with V=30 kV, I~30 pA and 10μm aperture.

In that round of experiments, it was also observed that PMMA resist failed during e-beam lithography. It was concluded that the resist failure is a result of bad adhesion at the interface between the Si wafer and the resist. Resist failure areas were comparable with the size of the exposed features and prevented achieving high quality mask. It was assumed that similar process occurred during e-beam lithography of larger features, as described in Chapter 4. In those experiments though, resist failure did not prevent obtaining masks with good quality. Consequently, a new improved procedure, for resist deposition on the Si wafers as compared with that described in Chapter 4, was developed which detailed description follows, Figure 5-5.

A positive tone poly(methylmetacrylate) (950PMMA-A4, MicroChem Corp.), 950,000 Mw, e-beam sensitive resist was spin-coated for 40 sec at 3000 $min^{-1}$ onto single crystal silicon (100) wafers with resistivity 15 to 30 Ω-cm and baked in an oven at temperature 150 $^{0}C$ for 60 min. The resist was diluted with anisole solvent in 1:1 ratio. Prior coating, an RCA Type I cleaning procedure, 5:1:1 solution of deionized water: hydrogen peroxide: ammonium hydroxide (DI $H_20:H_2O_2:NH_4OH$) was employed for 10 min at 20 $^{0}C$ to remove any organics which could have been present on the surface of the Si wafer. The wafer was rinsed in DI water and dehydrated for 30 min at 130 $^{0}C$. Following that, it was primed in a closed container with a vapor bath of 1:1 solution of hexamethyldisilazane:xylene (HMDS:xylene, $C_6H_{19}NSi_2:C_8H_{10}$). Subsequent to the e-beam exposure, the resist was developed for 70 sec in 3:1 solution of 2-propanol: methyl isobutyl ketone (IPA:MIBK, $C_3H_8O:C_6H_{12}O$) and the wafer was rinsed in IPA only to prevent undesired further development of the resist, thus forming a mask [89]. The etching of the Si substrate was performed on a Deep Reactive Ion Etcher (DRIE, Adixen AMS 100 I-Speeder) in a BOSCH® process mode. Following that, the molds were stripped of the resist mask in acetone for 1 h and the resist remnants were cleaned with $O_2$ plasma for 5 min on a parallel plate plasma etcher (Technics PE-II A). The plasma was formed at pressure 40 Pa, power 310 W, and $O_2$ flow of 50 $cm^3$.

(a) Silicon wafer. **RCA Type I cleaning. Wafer priming with HMDS:Xylene.**

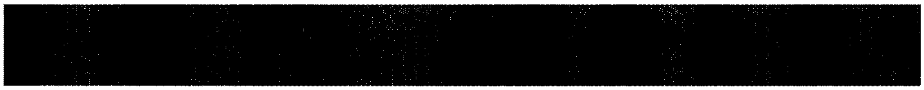

(b) Spin-coating with PMMA resist. Resist baking.

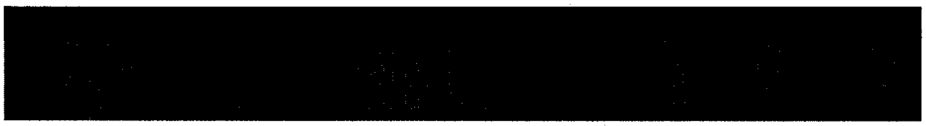

(c) E-beam lithography – point and line doses.

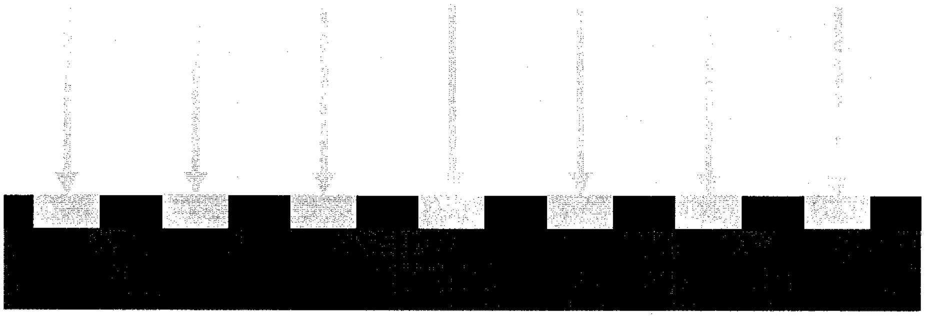

(d) Resist development and post-baking.

(e) Deep Reactive Ion Etching (DRIE). Resist Stripping. **$O_2$ plasma cleaning**.

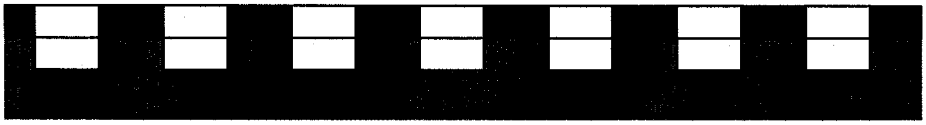

(f) **Plasma Polymerization of $C_4F_8$ coating.**

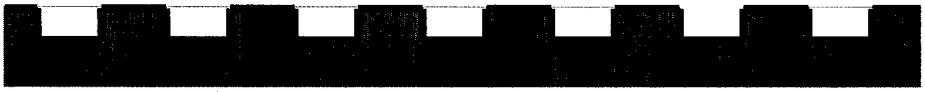

**Figure 5-5**. Schematic of the improved micro-fabrication process flow for Si mold development. The bold font denotes the new steps which have been add to the process sequence.

#### *5.2.1.2 Pattern Transfer via Deep Reactive Ion Etching*

In order to overcome the deleterious shadowing effect of the ion flux observed during etching of very small features, the degree of ionization of the etching sulfur hexafluoride ($SF_6$) plasma and therefore the ion flux reaching the silicon surface was increased. This was achieved by setting the DRIE coil power to its maximum value of 1500 W and by using high flow rates of the etching gas of 200 $cm^3$ [90, 91]. High values of the latter parameter have been also shown to decrease the redeposition of silicon tetrafluoride ($SiF_4$) products onto the surface [91]. In addition, it was previously shown [90] that the resist etching rate increases with applied electrode power which increases ion bombardment energy therefore, increasing ion bombardment improves the etching anisotropy but lowers the selectivity. Since the PMMA resist exhibits high etching rate (low selectivity) in fluorinated plasmas, BOSCH® process mode was utilized. Furthermore, ellipsometry measurements have shown that spin-coating of the resist yielded film with thickness ~100 nm. Consequently, this finding imposed restrictions on how deep features can be achieved during plasma etching. Additionally, decreasing of the resist mask removal, required for a robust operation in ion etching, was achieved by introducing a passivation cycle with duration 1 sec. In order to achieve high deposition rates during the passivation cycle high flow rate of $C_4F_8$ gas and high coil power were also chosen [92]. Lastly, due to the finite time response of the mass flow controllers the natural overlap between the etching and passivation steps decreased the resist removal rate further. The Si mold was mounted on a substrate holder wafer in the same way described already in Chapter 4. Several regions were successfully etched onto the Si substrates: (i) long parallel trenches (lines) having widths in the order of 150, 125, 115, 85 and 35 nm covering an area of 110x60 µm, (ii) short parallel trenches (lines) 40x60 nm and 60x200 nm covering areas of 35x35 µm and 60x35 µm respectively, (iii) square posts 100x100 nm covering an area of 25x25 µm, and (iv) three hole arrays with diameters ~190, 95, and 80 nm and pitch ~300 nm covering 30x30 µm areas and a hole array with diameter ~80 nm and

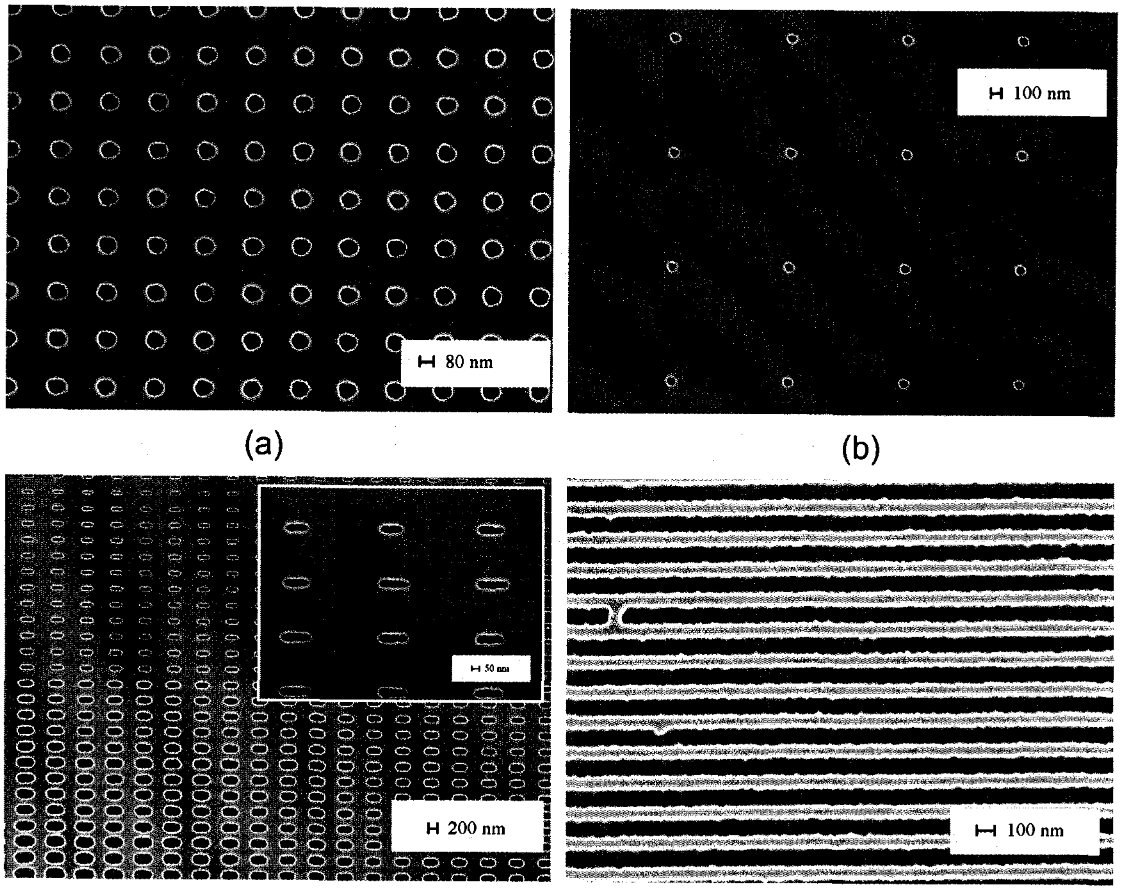

(a) (b)

(c) (d)

**Figure 5-6.** SEM images of Si mold regions, acquired before plasma polymerization of OFCB and after oxygen plasma treatment: (a, b) 2D arrays of holes with different diameter and pitch, scale bars 80 and 100 nm, (c) short trenches with an inset (scale bar 50 nm) showing a magnified region. Note that due to e-beam defocusing widening of the trenches occurred, (d) long trenches or lines, scale bar 100 nm.

pitch ~1 μm covering 100x100 μm area. Representative SEM images of the successfully etched regions from a Si mold with total process time 6 sec, are given in Figures 5-6 and 5-7. Si molds processed for total time of 9 sec were

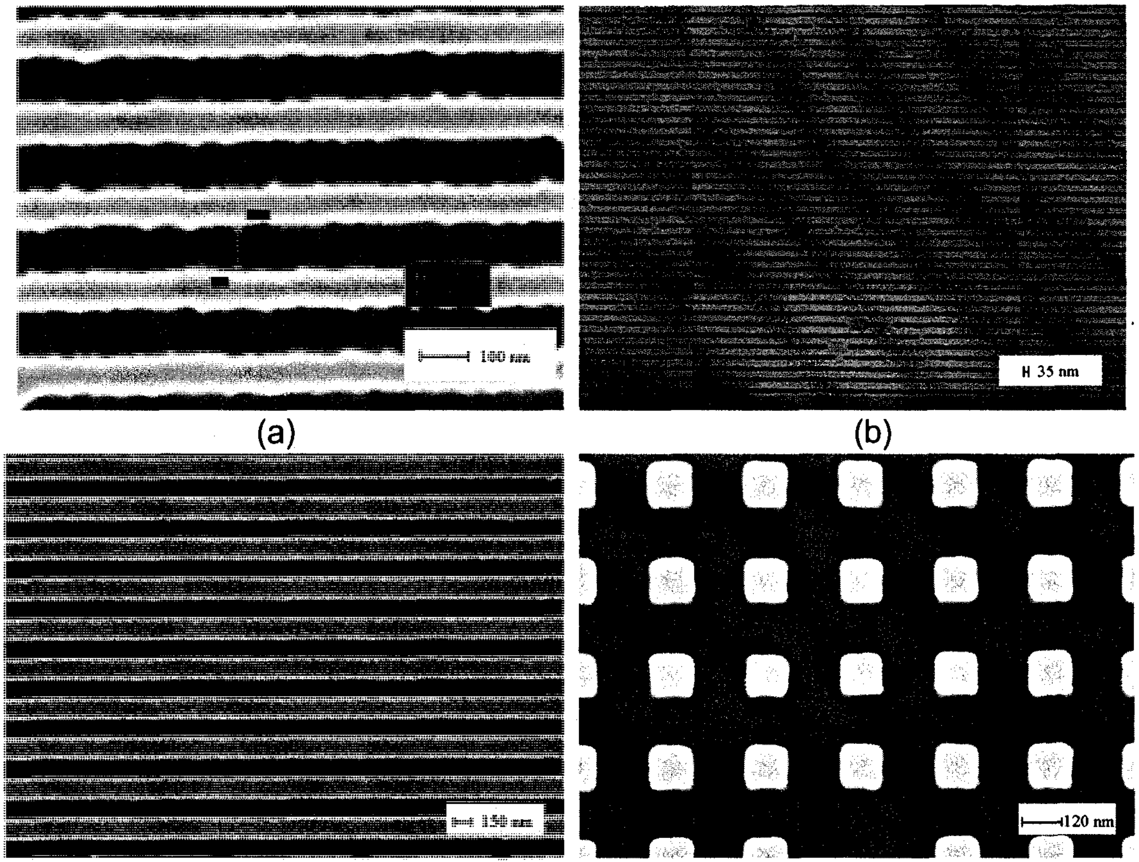

(a) (b)

(c) (d)

**Figure 5-7.** SEM images of Si mold regions, acquired before plasma polymerization of OFCB and after oxygen plasma treatment (a, b) showing (a) 85 nm wide long trenches (lines). The roughened vertical walls of the trenches resulted after increased resist etching rates, suggesting the necessity of utilizing more stable in aggressive plasma discharges "hard" oxide masks, and (b) smallest lines etched with the DRIE at Lehigh University, width ~35 nm. Note, that due to the very small features removing of the resist during the resist stripping step was precluded. 1-2 sec mild oxygen plasma cleaning after the stripping step could have potentially solved the problem; (c, d) SEM images of Si molds having the developed PMMA resist still on. It is obvious that the e-beam lithography step was excellent and that the roughening of the features happened during the DRIE etch. The high contrast images were obtained after sputtering 3-4 nm gold, which step prevented their subsequent processing with the DRIE tool.

used for replication as well.

### *5.2.1.3 Plasma Polymerization of Low Surface Energy Coating from $C_4F_8$ precursor gas*

The deposition parameters of the fluorocarbon film, presented in Table 5-2, were chosen to be the same as those of the passivation cycle during etching. In this regime, though, in order to decrease the detrimental influence of ion sputtering of the film during its formation, the electrode power was controlled by setting the generator in pulsed mode, since high continuously applied electrode power is known to prevent fluorocarbon film formation [92]. Substrate temperature was kept by cooling with He at 10 $^0$C since low value of this parameter has been previously shown to increase film deposition rate [117].

| gas | gas flow sccm | duration sec | priority - | source generator W | substrate source generator W | duration $10^{-3}$ sec |
|---|---|---|---|---|---|---|
| $C_4F_8$ | 150 | 1 | 1 | 1500 | - | - |
| $SF_6$ | 200 | 2 | 2 | 1500 | - | - |
| $C_4F_8$[a] | 150 | 8 | 1 | 1500 | 80 | 10 |
| | | | | | 0 | 90 |

[a] Fluorocarbon anti-adhesive coating deposition with substrate temperature 10 $^0$C.

**Table 5-2.** Summary of the used processing condition during etching and plasma polymerization of $C_4F_8$ gas.

### 5.2.2 X-Ray Photoelectron Spectroscopy of Plasma Polymerized $C_4F_8$ Coating

X-ray photoelectron spectroscopy (XPS) was used to quantify the elemental composition and chemical bonding structures of the deposited fluorocarbon film onto the molds. All spectra were recorded with Scienta

ESCA300 system equipped with a rotating anode giving Al Kα (1486.7 eV) radiation after monochromation. All scanned areas were ~0.9 mm$^2$. To probe the PP-OFCB film, surveys, at a pass energy (PE) of 300 eV, and high resolution spectra, at PE of 150 eV, were collected for the $C_{1s}$, $O_{1s}$, and $F_{1s}$ regions at take-off angles of $90^0$, $39^0$, and $15^0$. The chamber pressure was always kept below $5x10^{-7}$ Pa. All spectra were referenced to the C-C peak, which was assigned a binding energy (BE) of 284.2 eV.

Unexpectedly, two major problems were identified during XPS examination of the PP-OFCB coating. First, in the spectrum of the fluorocarbon film traces from two chemical elements were identified, namely Tantalum (Ta, N=73) and Aluminum (Al, N=13), as seen in Figure 5-8 (a, b, c). Second increased moisture in the plasma reactor was detected as well. Both factors were believed to have adverse influence on the tribological properties of the fluorocarbon film. Thus attempts were made to deposit films with improved chemical composition. While the second issue was considered a normal occurrence, the first one was not a trivial problem.

The moisture presence in the reactor was detected by the increased C-C/C-H peak intensity [115] in the high resolution $C_{1s}$ spectrum, as seen in Figure 5-8(d), which was acquired at $90^0$ take-off angle to eliminate any influence of potential moisture absorption on the film surface. Since, sample was promptly stored in a container after the deposition step, any possible contamination from the environment was eliminated. It was assumed that a possible route for the increase of the moisture content in the plasma reactor was the moisture accumulation in the loading chamber of the DRIE. This problem was solved by loading the sample in the plasma reactor and waiting for 120 min before initiating the plasma discharge. It was assumed that for that period of time the turbo-pump of the machine would lower the humidity in the reactor.

The presence of Ta and Al, elements with a superb chemical corrosion resistance, was found to be due to a manufacturer installed component inside of the chamber. After careful examination of the XPS spectra, it was noticed that elements content decreased with decreasing of the take-off angle which determined the probing depth during XPS, Figure 5-8 (b, c). It was concluded that during the first few moments of the highly aggressive $C_4F_8$ plasma discharge, F atoms attack the surface of the part, knocking away Ta and Al that redeposit inside of the reactor including the sample. Upon reaching plasma equilibrium state, the atomic percentages of the contaminants in the PP-OFCB film decreased as all inner surfaces of the reactor were gradually covered with the fluorocarbon film. Consequently, this problem was solved by running the DRIE tool in a passivation mode for 240 sec before loading the Si sample. It was assumed that for that period of time all inner surfaces of the plasma reactor would passivate with the fluorocarbon film. Upon implementation of the above steps (240 sec reactor passivation, sample loading, 120 min reactor venting) excellent film chemical composition was achieved. Details are provided later in this chapter.

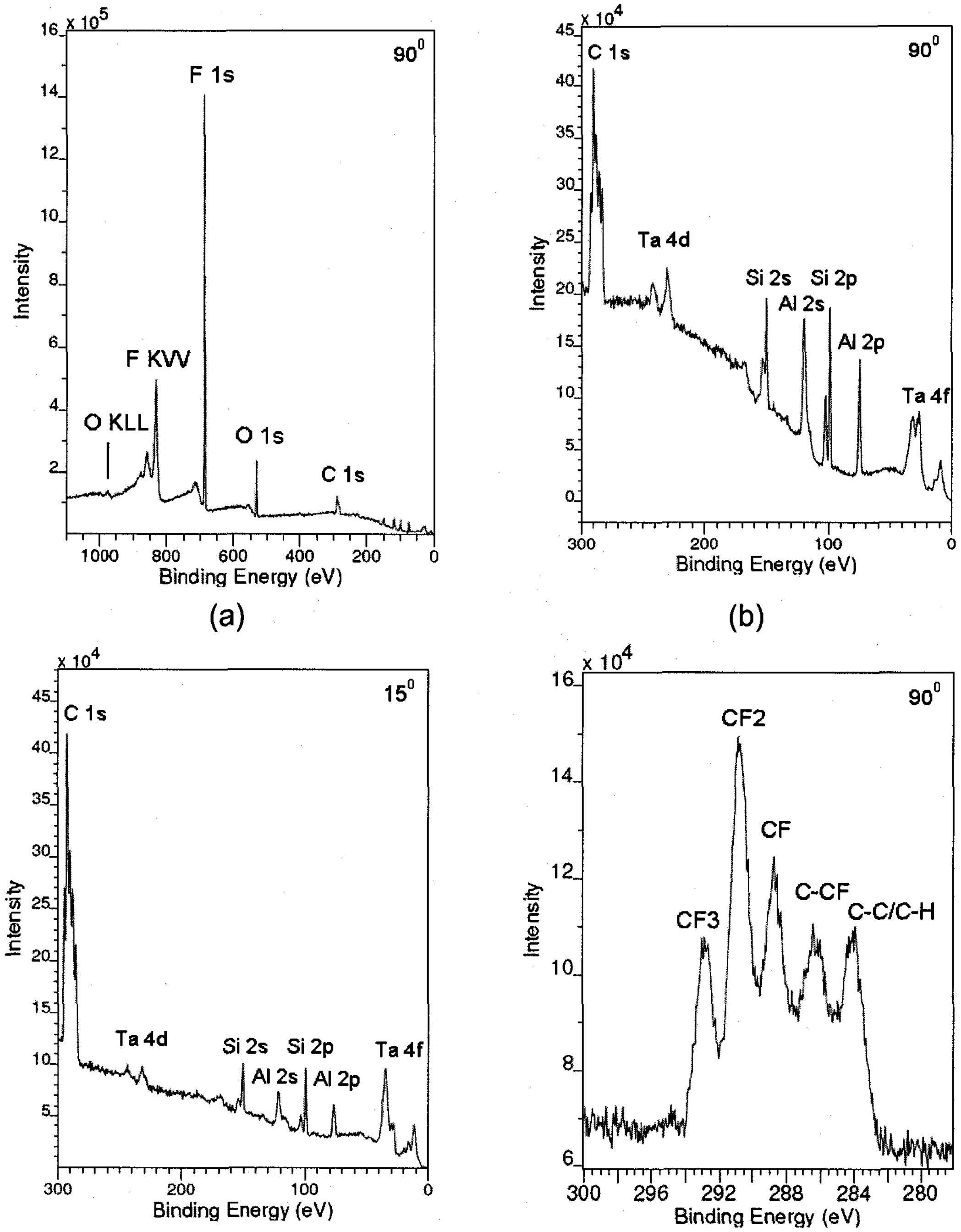

(a) (b)

(c) (d)

**Figure 5-8.** Al Kα XPS spectra of PP-OFCB film deposited on unstructured Si (a) low resolution survey spectrum of the film, (b, c) high resolution survey tail (0-300 eV) spectra of the film at $90^0$ and $15^0$ take-off angles. Abnormal $Ta_{4d}$ and $Al_{4f}$ peaks clearly seen, (d) high resolution $C_{1s}$ spectrum collected from PP-OFCB film deposited in high moisture content environment as seen from the high C-C/C-H peak intensity.

### 5.2.3 Fourier Transform Infrared Spectroscopy of Plasma Polymerized $C_4F_8$ Coating

Fourier transform infrared spectroscopy (FT-IR) measurements of the PP-OFCB film were performed with a Sense IR system. The FT-IR spectrometer was equipped with a $LN_2$ cooled mercury-cadmium-telluride (MCT) detector that has a spectral resolution of 4 $cm^{-1}$. The FT-IR spectra were collected in the diffuse reflectance mode using a total-reflecting objective (Cassegrain/Schwarzschild type). The spectral collection time was typically 36 seconds (0.3 second/scan and 120 scans).

### 5.2.4 Raman Spectroscopy of Plasma Polymerized $C_4F_8$ Coating

The Raman spectra were collected with a single stage monochromator (LabRam-HR), focal length of 800 mm, 900 grooves/mm grating (Horiba Jobin Yvon, 53011140HR) and a $LN_2$ cooled CCD detector (Horiba Jobin Yvon-CCD 3000 with 2048x13.5 $\mu m^2$ pixels). The Raman excitation was achieved with a 532 nm Nd-YAG laser. A 50X objective (Olympus BX-30) was employed for both focusing the laser beam on the sample and collection of the scattered photons. The Rayleigh scattering component was blocked by a notch filter (Kaiser Super Notch) having ~100 $cm^{-1}$ cut-off. The chosen operating conditions (800 mm focal length, the 200 μm confocal hole size and the 900 grooves/mm grating) provided a Raman spectral resolution of ~2 $cm^{-1}$. Typical Raman spectral collection times were 100 seconds (20 seconds/scan and 5 scans per spectrum). The Raman spectra were calibrated by using the Hg 546.07 line and the Si 520.07 $cm^{-1}$ shift.

### 5.2.5 Contact Angle Measurements of Plasma Polymerized $C_4F_8$ Coating

Contact angle measurements were performed on custom built goniometer with DI water as a probing liquid. Unstructured Si wafer stored in a container without any treatment, oxygen plasma treated one, and unstructured wafer with PP-OFCB film were tested. Oxygen plasma etching was performed on a parallel plate plasma etcher (Technics PE-II A) for 5 min. The plasma was formed at pressure 40 Pa, power 310 W, and $O_2$ flow of 50 $cm^3$. The contact angle measurement distribution was represented with a box-plot. The size and volume of the drops were kept constant since it is known that variations in the volume of the drops can lead to inconsistent measurements [121]. In order to minimize transient droplet shape variations due to droplet relaxation and spreading, the final measurements were taken within 10-12 sec [122].

### 5.2.6 Ellipsometry Measurements of Plasma Polymerized $C_4F_8$ Coating

Ellipsometry was used to measure the thickness of the PP-OFCB film, assuming refractive index of 1.39 [123]. Measurements were carried out on Rudolph AutoEL-2 ellipsometer, equipped with HeNe laser working at operating wavelength of 632.8 nm.

### 5.2.7 Replication Process

The replication process was performed by building a custom electrically-heated metal mold base that was mounted on a digitally controlled micro-molding machine (BOY 12A). To mount and fix the fragile Si mold into the brass mold base, the same encapsulation scheme described in details in Chapter 4 was implemented. The molding processing conditions chosen in concord with the supplier's specification and prior experience with injection molding of the COC were as follows: $T_{noz} \sim 288\ ^0C$, $P_{hold} = P_{inj} \sim 38$ MPa, $P_{back} \sim 0.7$ MPa, $n \sim 125$ 1/min, $V_{inj} \sim 70$ mm/s, $T_{mold} \sim 130\ ^0C$. In this set of experiments the earlier reported finding, described in Chapter 4, of surface "frozen stress" was solved by heating the space between the nozzle and the mold, e.g. the sprue bushing (Sprue T ~140 $^0C$). This approach was very practical, cost-effective and was used instead of a nozzle extension. Heating of the zone was achieved by inserting two identical cartridge heaters in drilled holes in the vicinity of the sprue bushing. Drilling of the holes to a prescribed inner diameter approximately 0.064 mm over the nominal diameter of the heaters (d~ 9.53 mm, power ~250 W) was done to allow expansion of the heaters and good thermal contact, Figure 5-9. This solution fully solved the problem associated with the surface "frozen stress" and its beneficial influence upon surface stress-free solidification was later confirmed by SEM imaging of the injection molded samples. The same temperature management was utilized in the experimental procedure described in Chapter 3 as well, where surface-stress free injection molded ruled diffraction gratings were also successfully manufactured.

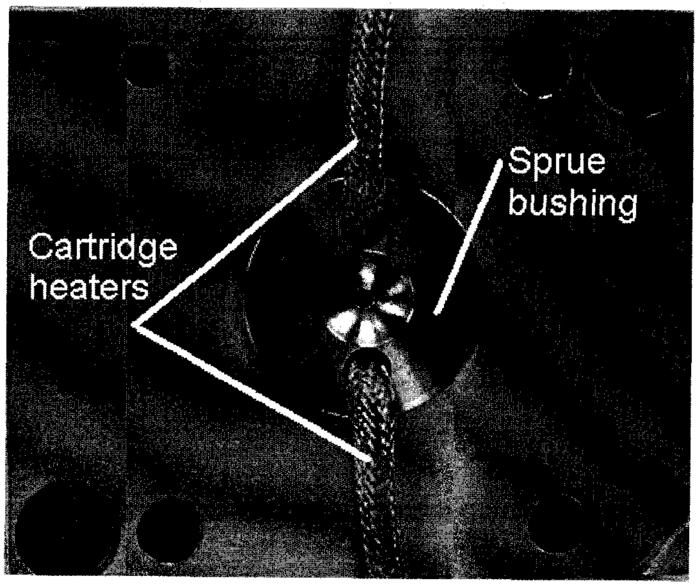

**Figure 5-9.** Digital photograph of the mounted sprue bushing on the fixed plate "A" of the base mold with two cartridge heaters inserted in the machined holes.

### *5.2.7.1 X-Ray Photoelectron Spectroscopy of Patterned Polymer Samples*

X-ray photoelectron spectroscopy (XPS) was used as well to quantify the elemental composition of the melt processed COC and record any possible fluorine transfer from the film to the molded replicas [118]. Probing the surfaces of COC replicas was performed by collecting surveys, at PE of 300 eV, and high resolution spectra, at PE of 150 eV, for the $C_{1s}$ and $F_{1s}$ regions at take-off angles of $90^0$ and $15^0$. All scanned areas were ~0.9 $mm^2$ in size. The chamber pressure was always kept below $5x10^{-6}$ Pa. Valence band spectra of the melt processed COC and in the form of pellets polymer, e.g. unprocessed one, were also collected to detect any polymer thermal degradation during melt processing. Flood gun was used to overcome the positive charge accumulation in the insulating polymer samples which resulted from the ejection of photoelectrons [124, 125].

### *5.2.7.2 Imaging of Patterned Polymer Samples with SEM*

Imaging of the polymer samples was carried out on a SEM - LEO 1550 VP equipped with a Gemini column. Following the replication process, polymer replicas were imaged either as molded or sputtered with 3-4 nm gold. In both cases, the microscope was run in a variable pressure (VP, P~30 Pa) mode with Nitrogen as an imaging gas. In the latter case attaching of conductive adhesive copper tape at the very, non-patterned, but metallized edge of the replicas was also implemented. Such approach allowed obtaining sharp images with good contrast. Following imaging, all samples were scanned with Atomic Force Microscope (AFM).

### *5.2.7.3 Imaging of Patterned Polymer Samples with AFM*

AFM was used to evaluate the surface topographies of the molds and polymer replicas and was performed in air with Digital Instruments Dimension 3000 AFM in TappingMode™. The probe used was a STING probe (DP15/STING/Al BS), obtained from MikroMasch USA, Aluminum backside coated for enhanced laser detection signal with nominal force constant k=40 N/m, nominal resonant frequency f=325 kHz, extended tip radius of curvature ROC=5..10 nm and extended tip height at least 600 nm. Such approach allowed estimating the sizes and depths of the patterned features without losing resolution due to tip-surface features wedging.

## 5.3 Results

Representative XPS survey spectra collected from the PP-OFCB film are shown in Figure 5-10(a, b). As expected, silicon and oxygen peaks in the spectra were observed due to Si/SiO$_2$ – PP-OFCB interface. In the 15$^0$ take-off angle spectrum the oxygen is mainly a surface contaminant and its small atomic percent (~ 0.02 at %) can be explained with the presence of the more electronegative fluorine [113]. In those spectra Auger electrons from O anf F are also seen from. C$_{1s}$ core level XPS spectra of the film are shown in Figure 5-11 and their peak intensities are given in Table 5-3. The results are in good agreement with C$_{1s}$ spectra of PP-OFCB films observed by *Bunning et al* [113], *Agraharam et al* [114], *Jaszewski et al* [118], and *Ayon et al* [92].

| take-off angle | Binding energy, eV | | | | |
|---|---|---|---|---|---|
| (deg) | CF3 | CF2 | CF | C-CF | C-C/C-H |
| 15 | 293.2 | 291.1 | 289.1 | 286.7 | 284.2$^a$ |
| 39 | | | | | |
| 90 | | | | | |

$^a$ All spectra referenced to the C-C/C-H peak.

**Table 5-3.** Assignment of C$_{1s}$ XPS component peaks of the fluorine containing PP film.

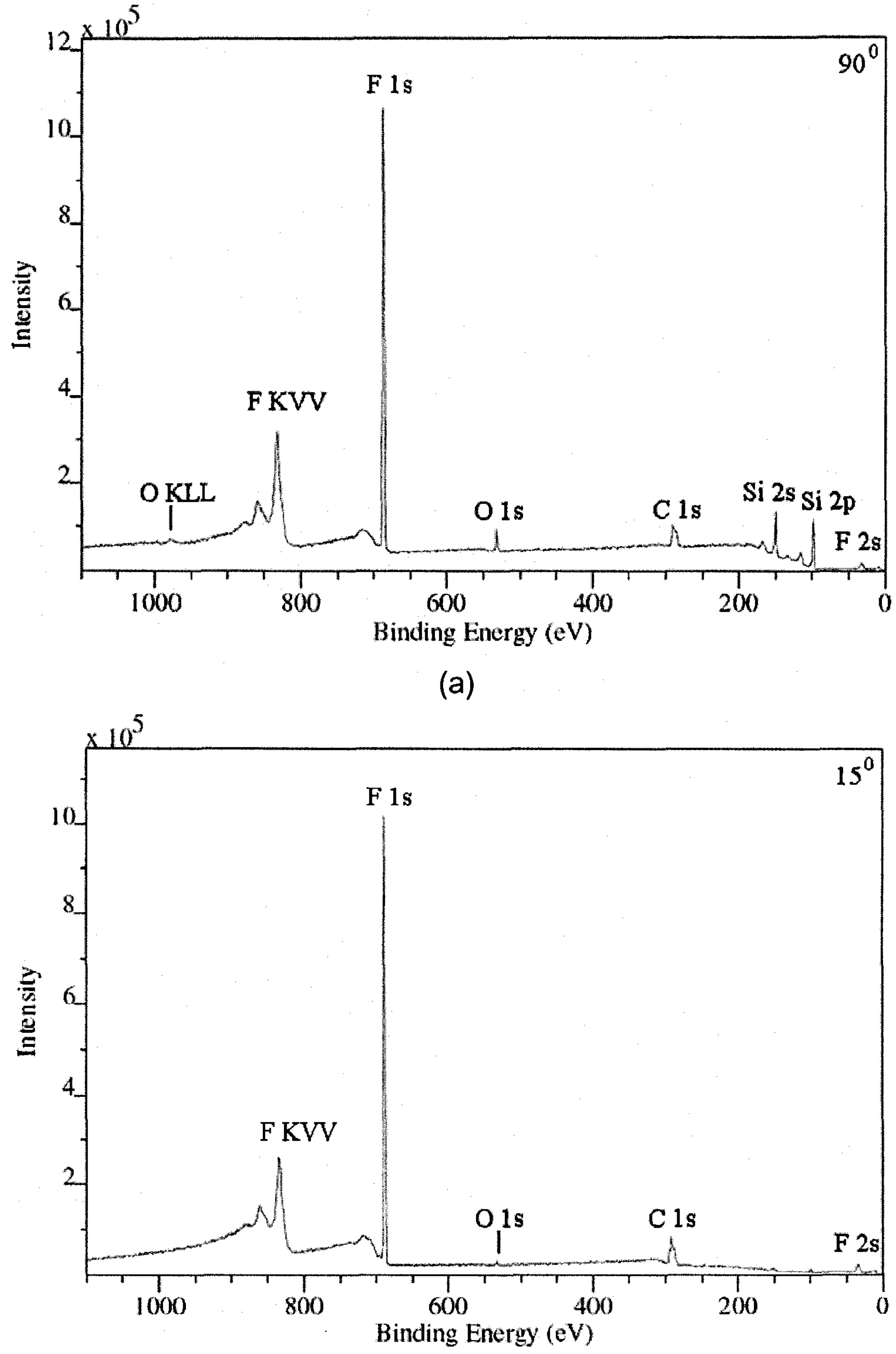

(b)

**Figure 5-10.** Low resolution Al Kα XPS survey spectra of the $C_4F_8$ fluorocarbon film deposited on unstructured Si, (a) spectrum from the interface between Si and fluorocarbon film, $90^0$ take-off angle, (b) spectrum from the top most monolayer of the fluorocarbon film, $15^0$ take-off angle. Auger electrons are clearly seen.

In the $C_{1s}$ region, the highest peak intensity corresponding to $CF_2$ (291.1 eV) is a result of the transformation of the $CF_x$ to $CF_2$ functionalities and implies that the film possesses low surface energy [118], and consequently excellent anti-adhesive properties, as confirmed by the high values of contact angles (~ $105^0$), Figure 5-12. In these films the presence of CF and C-CF groups indicates crosslinking and branching which are known to reduce the flexibility of the films and to increase the friction coefficients [92]. The results though, reveal that the top most layer ($15^0$ take-off angle) possesses lower intensity of the CF and C-CF groups, Figure 5-11, compared with the bulk of the film, which could be explained with the initial non-equilibrium state between etching and polymerization in the fluorocarbon plasma discharge [118]. The atomic % concentration of C, F, and O as well as the F/C and F/O ratios of the PP-OFCB are given in Table 5-4. The decrease in the F/C ratio at $15^0$ take-off angle as compared with the one at $90^0$ was expected and is attributed to the higher flux and energy of the ions bombarding the growing film, a result of the chosen high value of coil power.

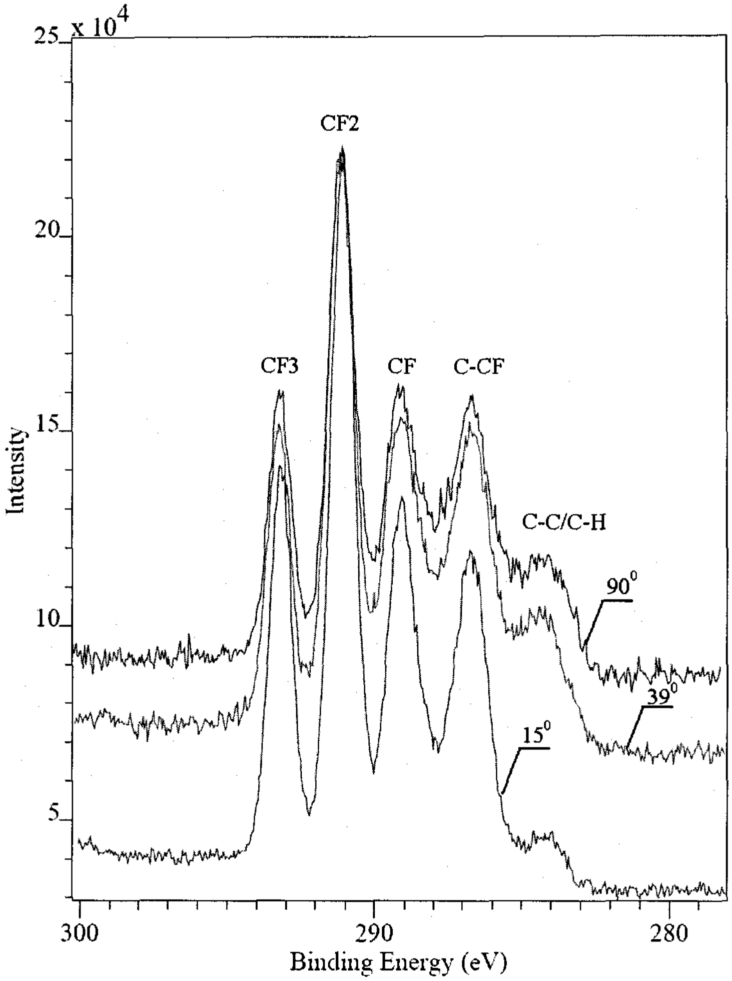

**Figure 5-11.** High resolution Al Kα $C_{1s}$ XPS spectra of the $C_4F_8$ fluorocarbon film deposited on unstructured Si. Pass energy 150 V. Spectra collected at $90^0$, $39^0$, and $15^0$ take-off angles. All spectra charge corrected to C-C/C-H peak with BE 284.2 eV.

Contact angle distribution of DI water droplets on the three substrates was represented with box-plots. As seen from Figure 5-12, it consists of a box and whisker lines for each group number, e.g. (1) Si wafer with PP-OFCB coating and (2) Si wafer as received from manufacturer and stored in a container box, defined as not treated. The meaning of the box plots representation is described in details in Chapter 3. Each reported distribution represents eighteen measurements per group.

As evident from Figure 5-12, contact angle distribution of DI water droplets on PP-OFCB is narrower than that of the as obtained Si wafer, which implies that good chemical composition uniformity has been achieved. In addition, the SEM pictures on the same figure demonstrate that the oxygen plasma treatment is a required step of the mold fabrication process that removes fine resist redeposits after resist stripping but renders the surface superhydrophilic as seen in Figure 5-13. Consequently, utilizing of low-surface energy coating must be employed to improve fidelity of polymer replication.

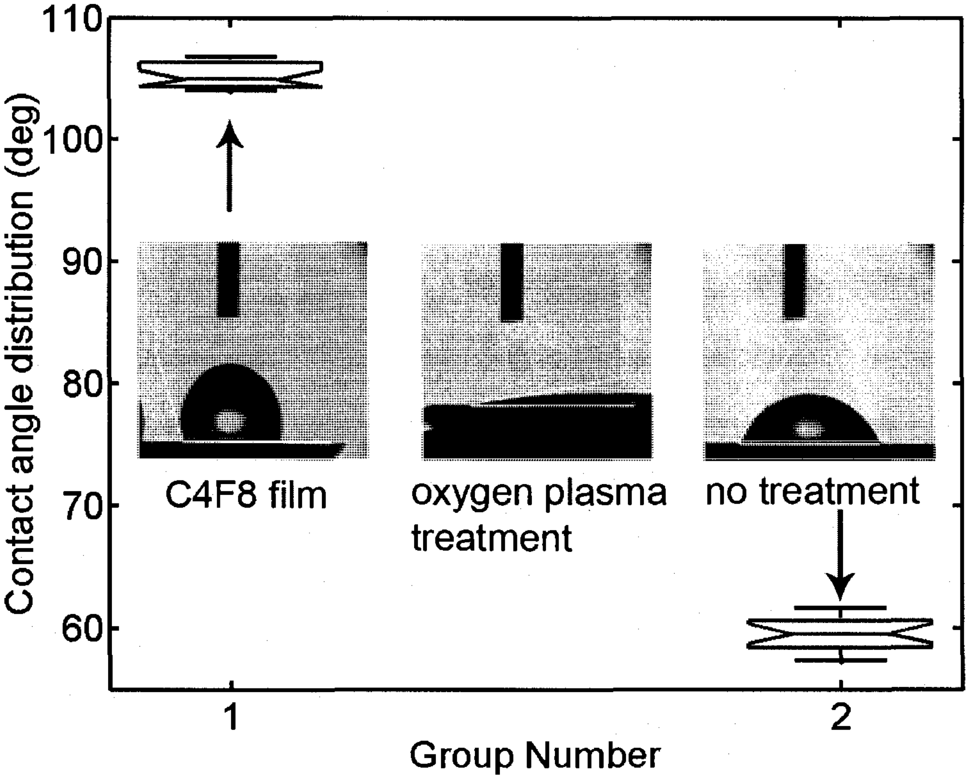

**Figure 5-12.** DI water contact angle distribution on unstructured Si piece from a wafer coated with plasma polymerized $C_4F_8$, group number 1, and as received from the manufacturer (no treatment), group number 2, represented by box-plots. Contact angle measurements of unstructured Si piece treated with oxygen plasma, 310 W, 40 Pa, 50 $cm^3$ (image in the middle of the graph) revealed (not shown) very small contact angles $< 10^0 \pm 2^0$.

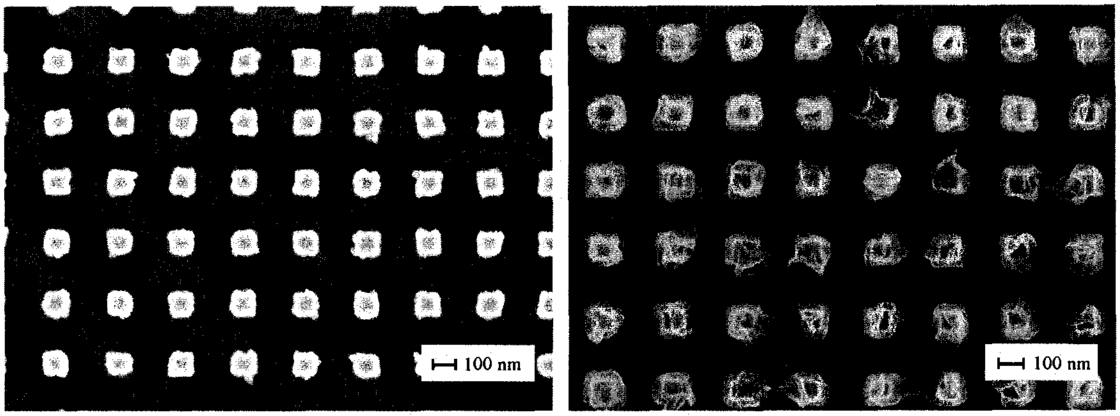

(a) (b)

**Figure 5-13.** SEM pictures of a structured Si mold with ~100x100 nm posts suggesting that the oxygen plasma treatment is a required step that removes fine organic resist redeposits after resist stripping but renders the surface superhydrophilic as seen from the middle image on the graph in Figure 5-12. (a) mold after oxygen plasma treatment and (b) before oxygen plasma treatment. Resist remnants are clearly seen.

| take-off angle (deg) | Concentration, at % | | | Component ratio, - | |
|---|---|---|---|---|---|
| | C | F | O | F/C | O/C |
| 15 | 42.72 | 56.39 | 0.82 | 1.32 | 0.02 |
| 39 | 41.51 | 55.06 | 3.43 | 1.33 | 0.08 |
| 90 | 38.27 | 55.91 | 5.82 | 1.46 | 0.20 |

**Table 5-4.** Depth resolved atomic percentages concentration of detected elements, F/C and O/C ratios from XPS analysis. Component ratios are based on the peak area.

FT-IR spectra, shown in Figure 5-14, revealed stretching mode vibrations of $CF_x$ (x=1-3) species, which peak is centered at 1109 $cm^{-1}$ and is typical for such films [92, 114]. $H_2O$ was also detected as a background signal due to the moisture content in the ambient air. Other absorption peaks were not identified, though reported elsewhere in the literature [126], which was attributed to the very thin film (~ 10 nm) confirmed by ellipsometry measurements and the absence of Raman signal as seen in Figure 5-15.

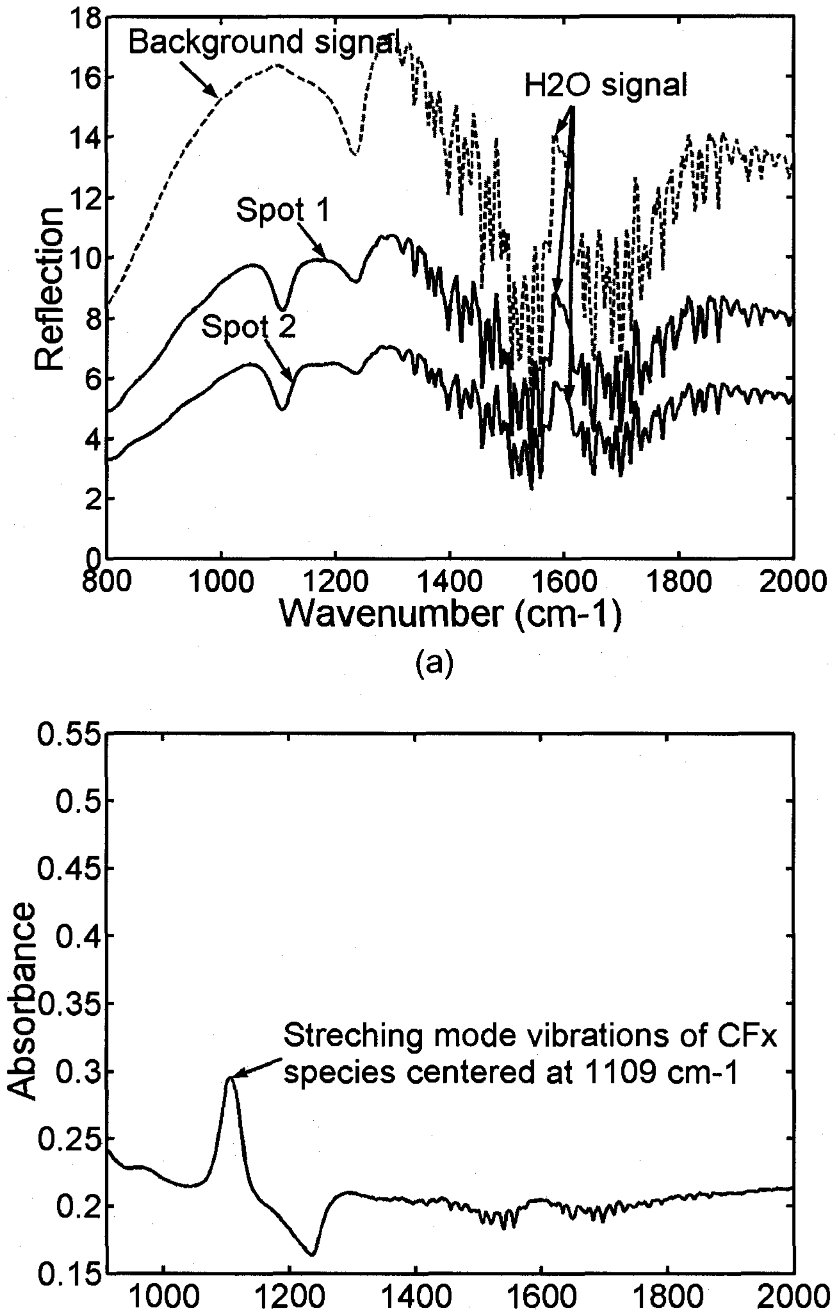

(a)

(b)

**Figure 5-14.** FT-IR spectra of the $C_4F_8$ fluorocarbon film deposited on unstructured Si. Deposition conditions: 1500 W (source generator), 10 $^0$C, 150 cm$^3$, 10$^{-3}$ Pa. (a) Reflection spectra for two measured spots and the background signal, which was removed from the absorbance spectrum (spot 2) (b). The detected signal around ~1580 cm$^{-1}$ comes from the finite moisture content in the ambient air. The formula used to calculate the absorbance is: Absorbance = (-1)*log$_{10}$(sample signal/background signal).

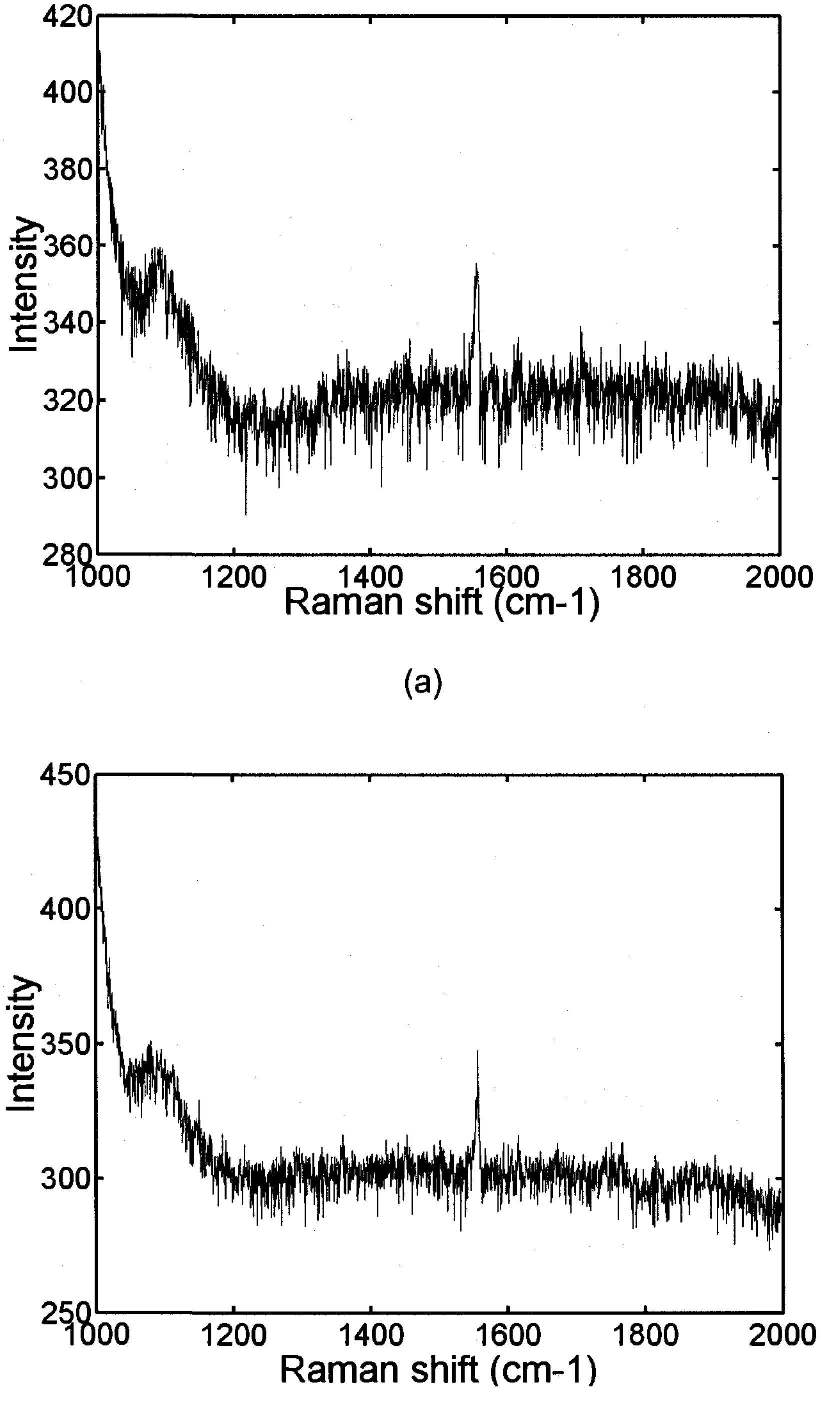

(a)

(b)

**Figure 5-15.** Raman spectrum of ~10 nm thin PP-OFCB/$SiO_2$/Si. No signal from the fluorocarbon composition is detected possibly due to the very thin coating. The peak at ~1100 $cm^{-1}$ is from the $SiO_2$ and the peak at ~1550 $cm^{-1}$ is from the oxygen in the air. (a) background signal and (b) signal from the sample. No other peas were resolved.

Replication with Si molds, etched for 6 sec, produced excellent results as evident from Figures 5-16 and 5-17. Results show good fidelity of replication for all patterned regions. The smallest objects which were replicated were lines with width ~25-30 nm. The PP-OFCB film performed well as protective anti-adhesive coating. No sticking of the COC polymer was noticed after 40 consecutive moldings. One of the most important factors which influenced the exactness of the replication was found to be the temperature of the mold which was kept close to the glass transition temperature of the used thermoplastic amorphous polymer.

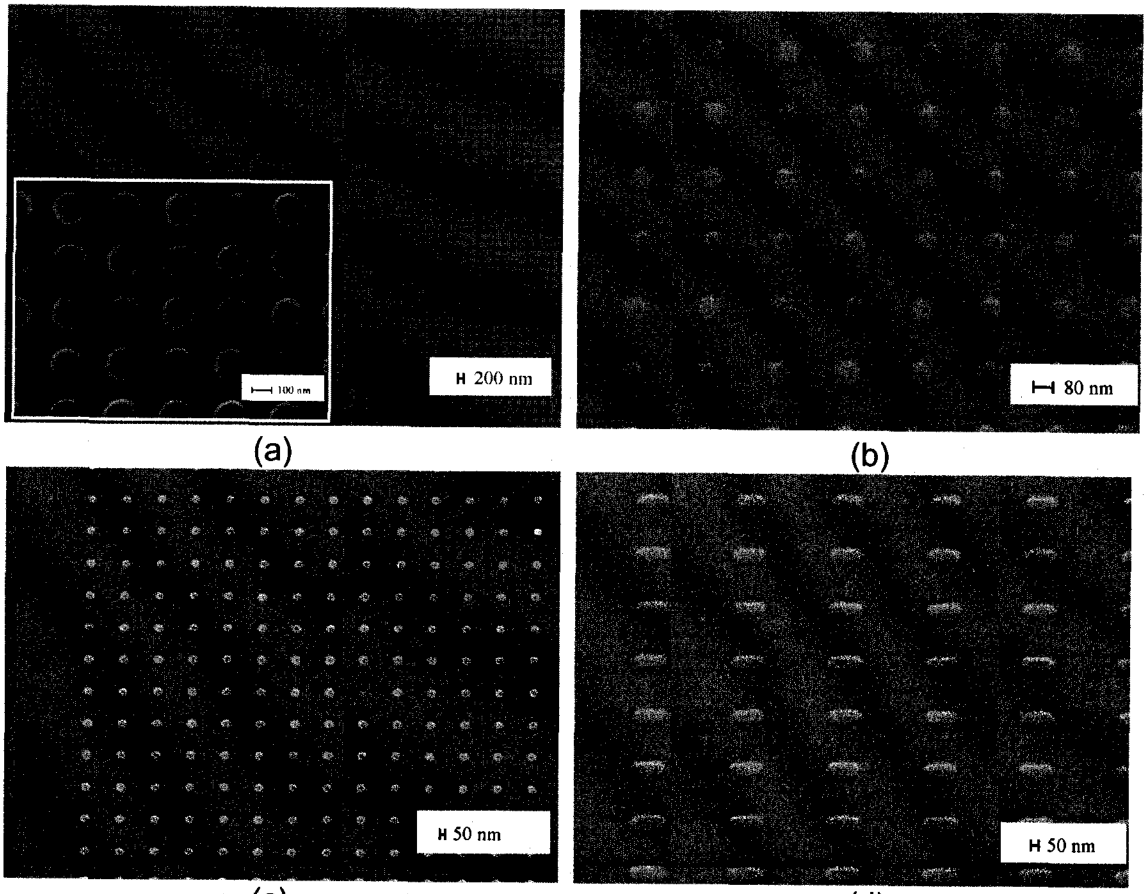

(a) (b) (c) (d)

**Figure 5-16.** Representative SEM-VP mode images of different injection molded polymer features sputtered with gold for imaging (a, b) 2D arrays of nano-posts, scale bars 50 and 80 nm respectively with an inset in (a) showing a magnified region, scale bar 100 nm, (c) 2D array of short lines which look like dots due to the small size, scale bar ~50 nm, (d) 2D array of short lines, scale bar ~50 nm.

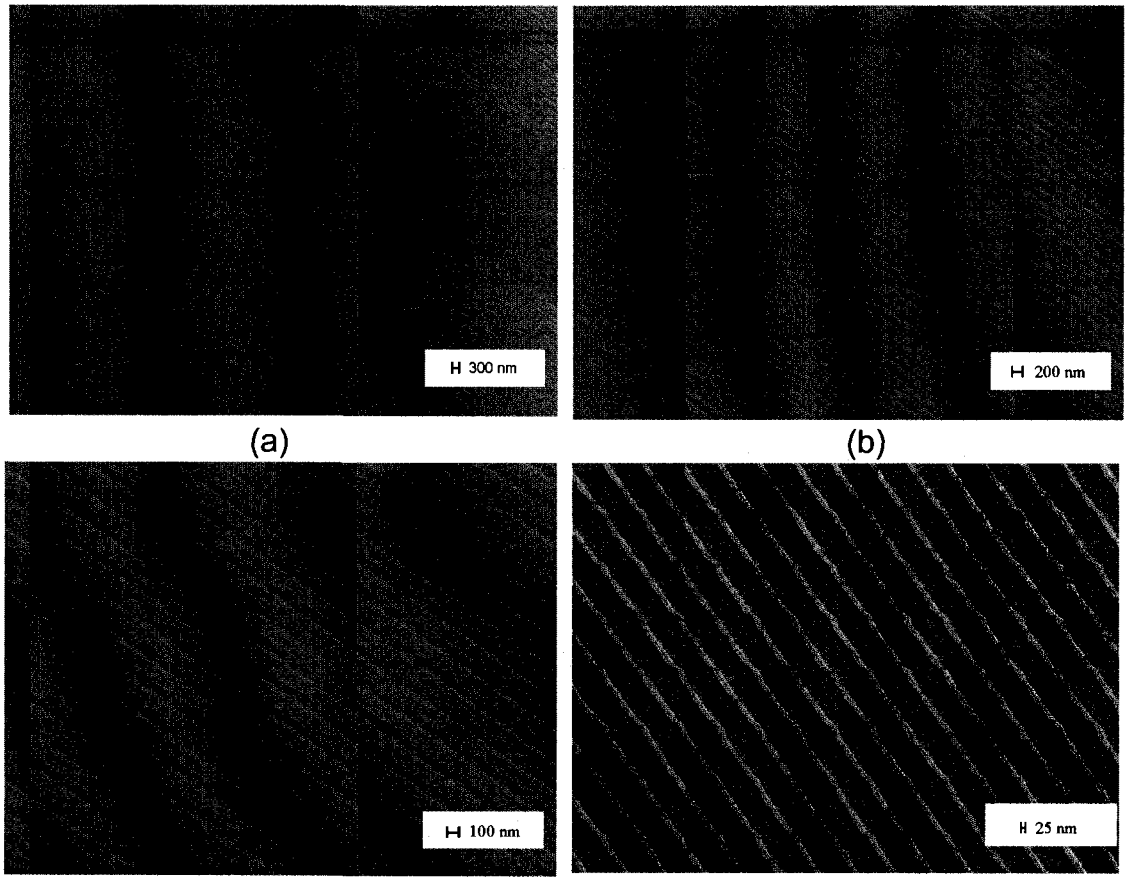

(a) (b)

(c) (d)

**Figure 5-17.** Representative SEM-VP mode images of regions with injection molded nano-lines with different pitch sputtered with gold for imaging (a) larger magnification of three regions with lines with different widths and pitch, scale bar 300 nm, (b, c) larger magnification of those regions, scale bars 200 and 100 nm respectively. The fidelity of replication is excellent, (d) line with width ~25-30 nm - the smallest features replicated via injection molding at Lehigh University. Note that the polymer replicated very well the mold features but since the PMMA resist was not properly developed the resulted lines have small dimples.

It has been previously stipulated that high aspect ratio structures might induce fluorocarbon film degradation through abrasion during replication, and thus prevent polymer demolding from the cavities. However, it has been also shown that there is no difference in the film degradation between mold with low aspect ratio features and flat surfaces [74]. During XPS examination, the spots where the X-rays were positioned at the surfaces were in close proximity of the patterned regions. Thus, it is believed that the results in the present study are reasonable. As seen in Figure 5-18(a) and Table 5-5, XPS data taken from the COC replicas revealed fluorine transfer from the coating to the polymer. Such behavior of the PP-OFCB films was previously reported during hot embossing with different polymers [118] and was expected. In contrast with that report, in the present study no fluorine transfer was detected during subsequent replications. The initial fluorine transfer can be explained with the fact that freshly deposited polymerized film contains loose fluorinated molecules weakly bound to the carbon-rich network [118]. Those species are easily transferable through diffusion from the film to the injection molded polymer. After the initial "cleaning" process of the film no diffusion was detected. Despite the observed fluorine migration, the coating preserved its anti-adhesive and lubrication properties. As seen in Figure 5-18(a), oxygen was detected in the first processed COC replica. It is believed that the oxygen presence is a result of oxidation of the polymer melt in the molding machine's barrel during the initial and normal setting period of the machine. After achieving normal processing conditions no oxygen in the melt processed polymer replicas was detected, Figure 5-18(b).

|  | take-off angle | COC replica No. |  |  |  |  |
|---|---|---|---|---|---|---|
|  | (deg) | 1 | 5 | 13 | 20 | 40 |
| F, at % | 90 | 4.96 | 0.00 | 0.00 | 0.00 | 0.00 |
|  | 15 | 15.17 | 0.88 | 0.00 | 0.00 | 0.00 |

**Table 5-5.** Atomic percentages of fluorine contents in COC polymer replicas after an increasing number of injection moldings with the same mold.

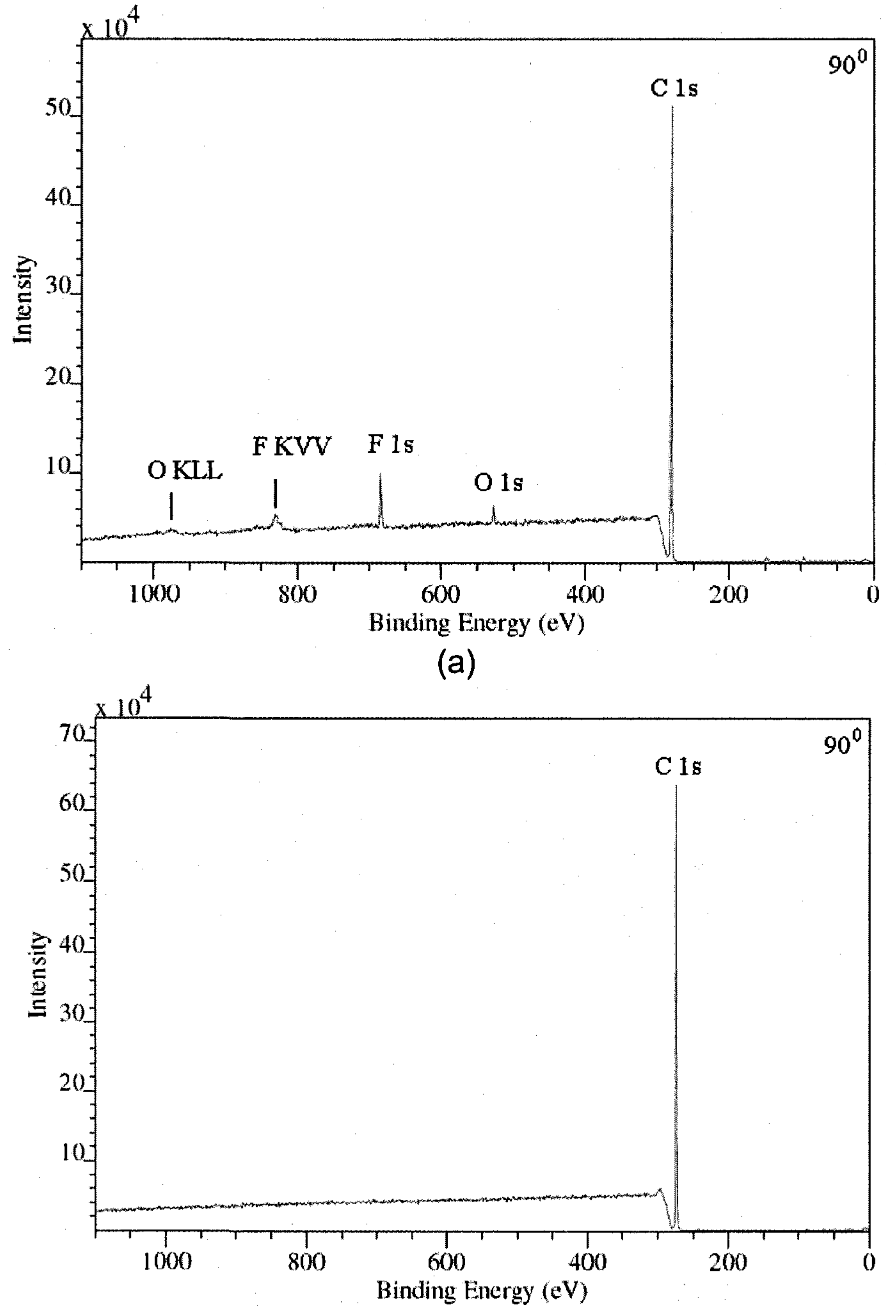

(a)

(b)

**Figure 5-18.** Low resolution Al Kα XPS survey spectra of molded COC replicas (a) spectrum from the bulk of COC replica No. 1, $90^0$ take-off angle. The fluorine, which diffused from the fluorocarbon film to the COC during molding, is detected by the F Auger and $F_{1s}$ peaks. The O Auger and $O_{1s}$ peaks are possibly due to small thermal degradation of the polymer in the barrel of the injection molding machine (b) spectrum from the bulk of COC replica No. 13, $90^0$ take-off angle. No oxygen and fluorine are detected due to reaching normal temperature levels in the barrel and due to film "cleaning" of loose fluorinated molecules from the surface, respectively.

Furthermore, to assess potential COC thermal degradation [127, 128] during melt processing with the injection micro-molding machine, valence band spectra of the melt processed (replica No. 13) and pristine (in pellet form) polymer were acquired. To perform the XPS analysis, a pellet was sliced with a razor blade and the fresh surface was analyzed. This was done in order to eliminate any possible influence of surface contaminants on the valence band spectra collection [129]. As seen in Figure 5-19(a), no detectable difference in the $C_{2s}$ and $C_{2p}$ peaks between the melt processed and unprocessed polymers was detected. In addition, a comparison between $C_{2s}$ bonding and anti-bonding peaks with those of the high density polyethylene (HDPE), seen in Figure 5-19(b) indicates the presence of bicyclo{2.2.1}-2-heptene (norbornene, $C_7H_{10}$) compound in the COC [84]. Finally, it can also be inferred that due to the almost identical valence spectra of the melt processed and unprocessed COC, the injecting molding conditions were chosen correctly. The small gaps in the $C_{2s}$ peaks were attributed to the difference in the number of scans during the collection of the spectra, e.g. pristine COC spectrum was collected with more scans which reduced noise-to-signal ratio as evident from the small amplitude of the spikes in the spectrum.

To prove the advantage of utilizing PP-OFCB as an anti-adhesive coating during polymer molding high aspect ratio (AR) features were also replicated, Figure 5-20. Interestingly, when attempts were made to image the high AR pillars with a reduced raster, Figure 5-20(a) or at higher magnification,

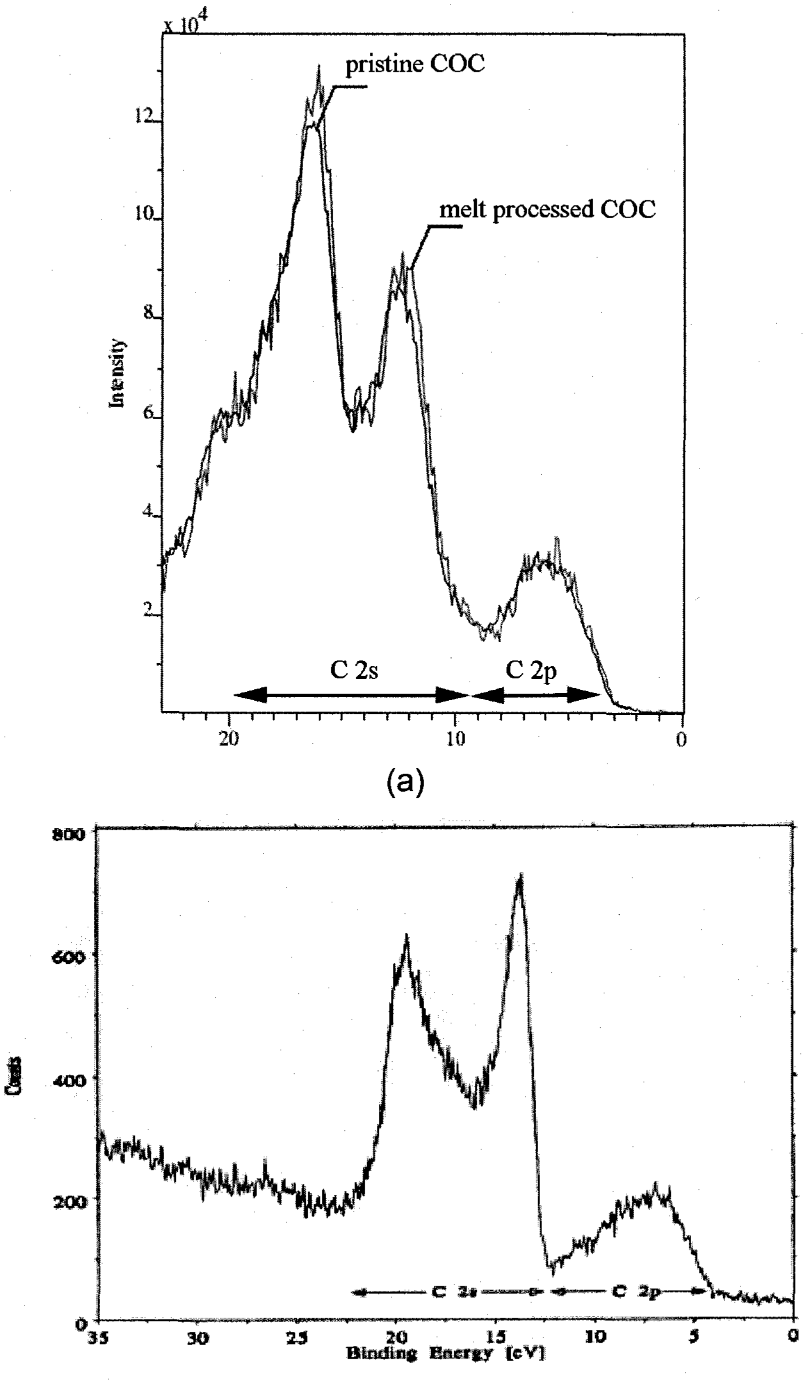

**Figure 5-19.** (a) High resolution Al Kα C valence band spectra of melt processed (replica No. 13) and pristine (in pellet form) polymer. Spectra charge corrected to C-C/C-H peak BE 284.2 eV, (b) Valence band spectrum of HDPE. *Reprinted from [125] (pp. 55).*

Figure 5-20(b), the straight standing pillars collapsed onto the base surface in an organized fashion repeatedly. To the author's best knowledge such failure mechanism has not been previously reported. A close observation of the resulted pattern led to the conclusion that, under the imaging beam, the pillars were positively charged with respect to the base surface, which was negatively charged. In such distribution and since the temperature was inevitably also increased during imaging, the pillars softened and responded as positively charged test particles that followed an electrostatic field directed towards the negative potential in the center. Smaller AR pillars, having the same diameter did not respond in the same way and stayed stable, Figure 5-20(c, d). The charge separation in the vertical direction could have been initiated by the increased conductivity of the pillars due to molecular chains orientation during melt flow in the deep cavities. The longer the posts are, the higher the molecular orientation is, the higher the electron conductivity is. Additionally, since the imaging was done at a tilt angle of $45^0$, it was concluded that the attractive force, which resulted by the electrostatic field, was larger than the gravitational force acting on each pillar. Lastly, the center of the negative potential was shifted left, Figure 5-21(a) due to the fact that the microscope's imaging beam has a finite residence time at the left side of the image after each scan, as seen in Figure 5-22, that moved the potential center left from the geometric center of the image.

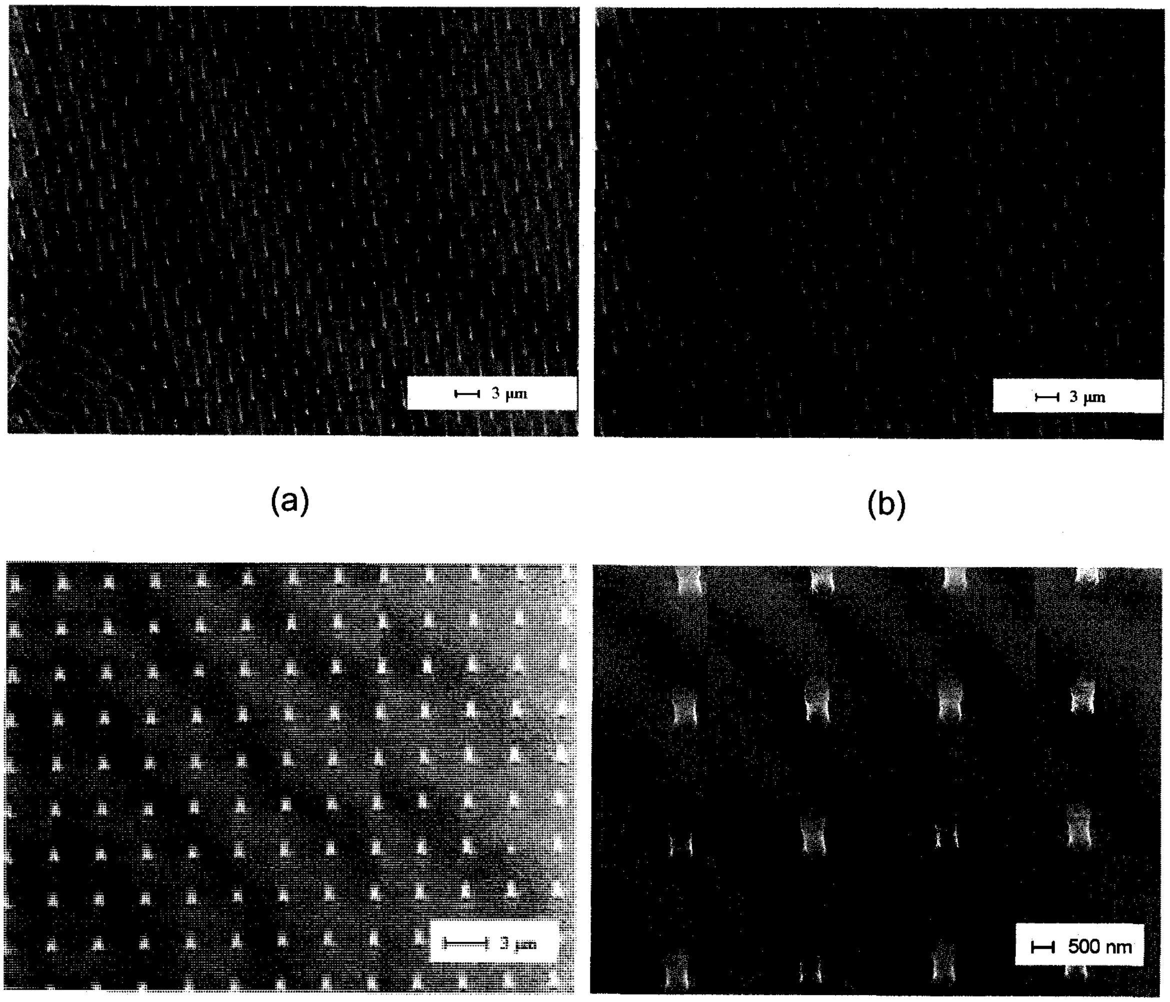

(a) (b)

(c) (d)

**Figure 5-20.** SEM-VP mode images of polymer patterned surfaces with different aspect ratios (a) replica molded from Si mold fabricated by similar approach as that presented earlier (not discussed for brevity) but having PP-OFCB film deposited for longer time 15 sec. AR ~8, diameter ~500 nm, and pitch ~3µm. Posts ground collapsed (lower left corner of the picture) during zooming in. It is suggested, that the observation is a result of induced charge separation between pillars (positively charged) and the ground surface (negatively charged), imaging beam current density ~ 0.695 A/m$^2$ (b) different region with no induced ground collapse of pillars, imaging beam current density ~ 0.695 A/m$^2$, (c) low aspect ratio (AR ~1.5) pillars with diameter ~500 nm, imaging beam current density ~ 0.294 A/m$^2$ (d) the same array with pillars at higher magnification. Note that the imaging beam current density is ~ 2.79 A/m$^2$, almost 11 times larger than that used obtaining image (b) and still no ground collapse was observed.

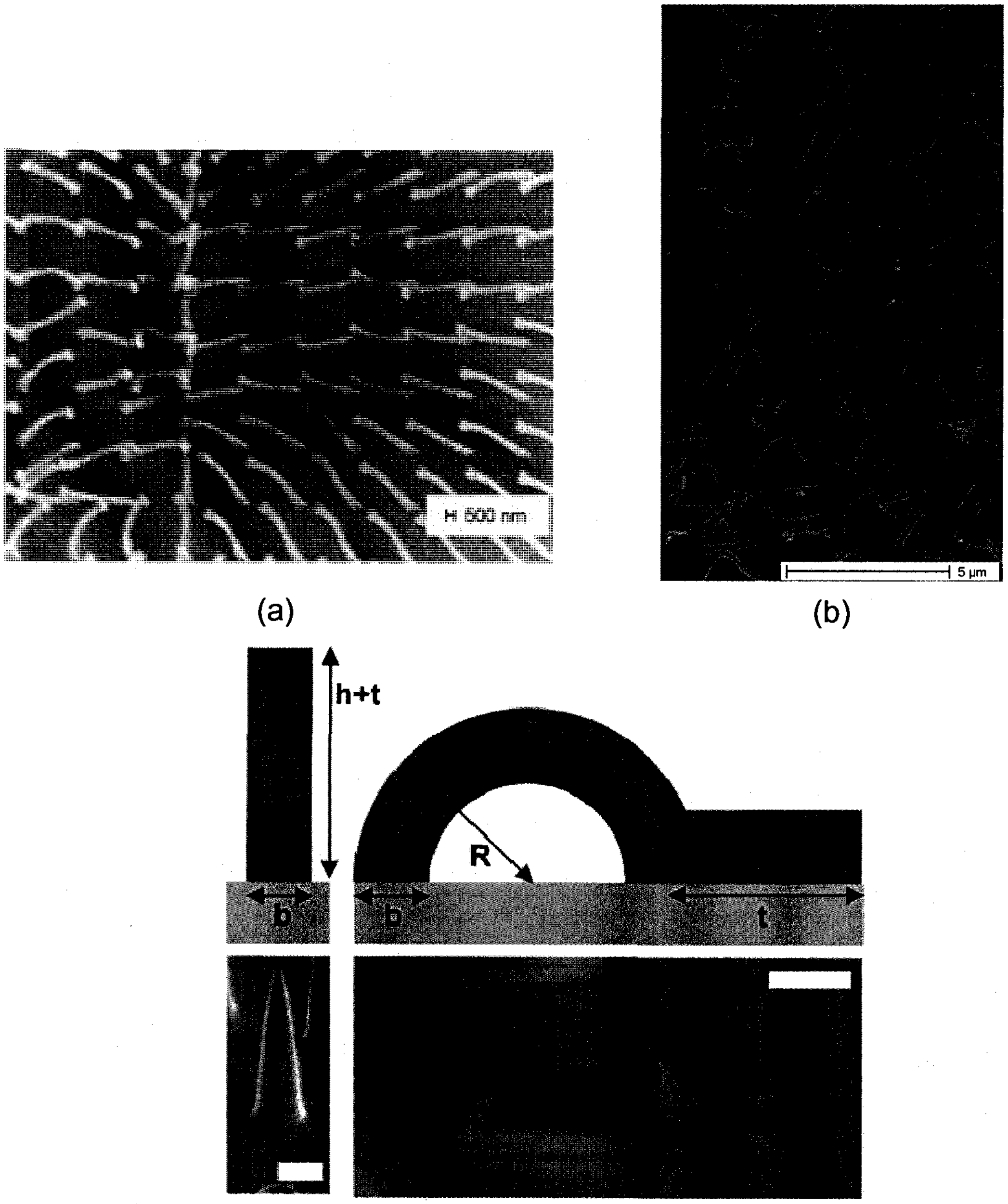

(a)

(b)

(c)

**Figure 5-21.** SEM-VP images of ground collapsed polymer pillars due to (a) charge separation between the pillars and the ground surface and (b) AR initiated loss of mechanical stability; (c) Image *reprinted from [130], figure 1, © 2005 with permission from American Chemical Society.* Comparison between the shape of the posts used in *Roca-Cusachs et. al.* model and that observed in their experiments. Top: geometrical model for stable (left) and collapsed (right) posts used in the theoretical calculations with its different parameters. Bottom: SEM images of examples of stable (left) and collapsed (right) PDMS posts (view angle is $52^0$). Scale bars indicate 2 μm. Note the similarities in PDMS and COC pillars ground collapse.

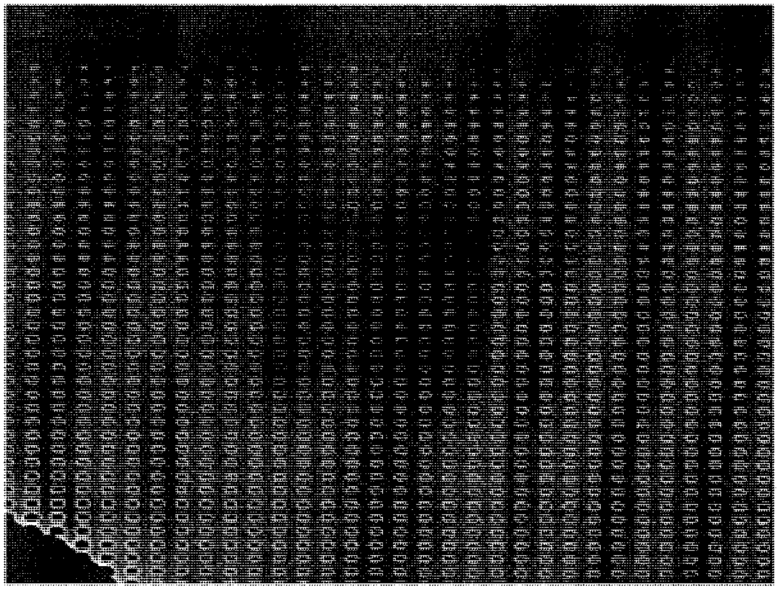

(a)

**Figure 5-22.** SEM image of an etched Si mold with 2D array of short trenches. The non-uniformity of the array is due to beam astigmatism introduced as a result of a large beam deflection of the e-beam during lithography. In the center of the image a black rectangular is seen with two black regions on its left edge, a result of zooming with the microscope in that region first. The regions on the left side are a result of the finite residence time of the microscope's beam at this side of the image after each scan.

In that round of experiments, it was also shown that bad replication occurs if the coating is not properly deposited, Figure 5-23. Since the mold utilized to replicate these features possessed deeper cavities (as a result of 9 sec etch time) the subsequent deposition step with PP-OFCB for 8 sec did not produced conformal coating inside the cavities, as happened with the shallower etched mold. This observation can be explained with the limited deposition time in this case and the previously discussed shadowing effect in fluorinated plasmas. In conclusion, it can be concluded that the deposition time is important parameter that influences the deposition of conformal coatings and it does vary with the size and AR of the cavities. Similar findings though, related to replication of high AR micron-sized features, and in agreement with those in the present report, have been recently reported by *Gao et al.* [119]. As seen from the images, the nano-posts had cracks at their base – a result of sticking of the solidified polymer in the Si cavities during demolding. This finding is also in concord with the failure modes observed during polymer replication with no anti-adhesive coating discussed in Chapter 4. In addition, the polymer melt flow in the cavities was along their inner surfaces which could be explained with the high surface energy of the Si surface that was not covered properly with the fluorocarbon film. As a result, hollow tubes or hollow cylinders (instead of solid pillars) were formed and bent due to loss of mechanical stability.

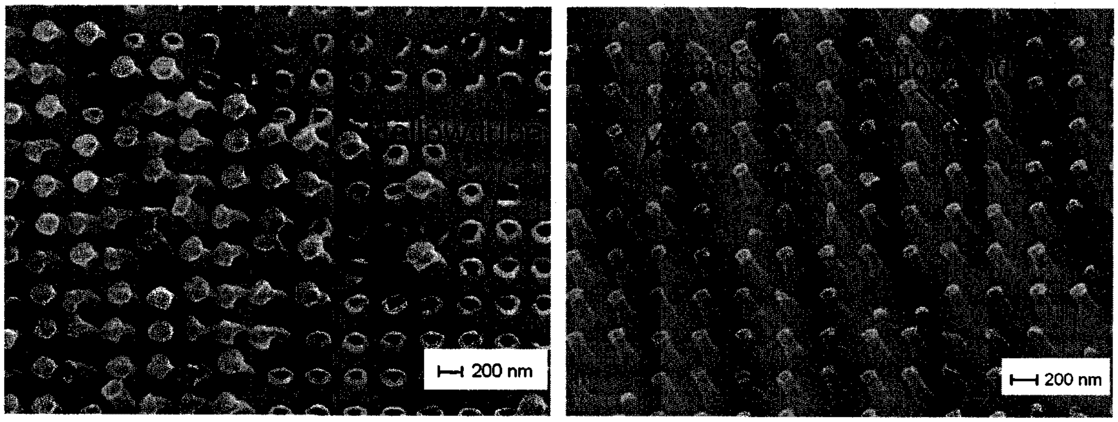

(a) (b)

**Figure 5-23.** SEM-VP mode images of 2D arrays of polymer nano-posts, gold sputtered for imaging, with defects that resulted from the not conformal PP-OFCB coated cavities: (a) diameter of the posts ~200 nm, (b) diameter of the posts ~130 nm.

AFM examination of the polymeric features, performed after XPS analysis to prevent surface contamination prior to the analysis, and the Si molds before PP-OFCB and after oxygen plasma treatment, revealed excellent profile replication, as seen in Figures 5-24 and 5-25. It was observed that the reactive ion etching lag in the fluorinated plasma during etching of structures with different widths, e.g. etching rate decreasing with feature size [91] as seen in Figure 5-26, influenced the achieved depths of the etched nano-features and subsequently the heights of their replicas.

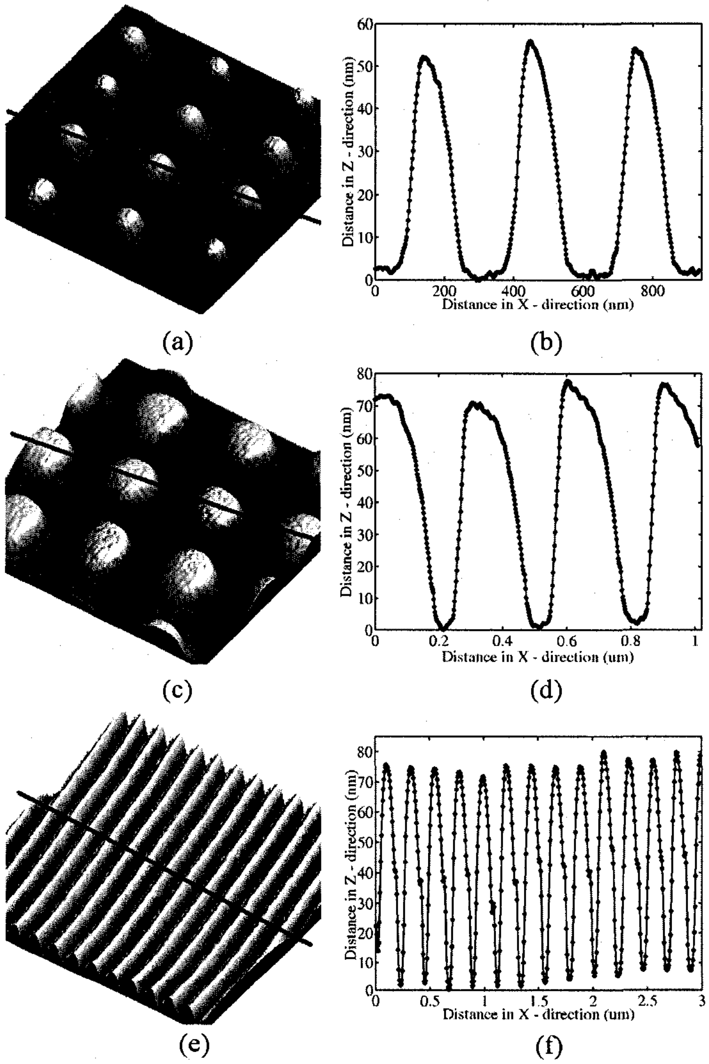

**Figure 5-24.** AFM images of 2D arrays with injection molded (a, c) nano-posts with different diameters (a, c) and their respective cross section profiles (b, d) along the lines, nano-lines (e) with its respective cross section profile (f) along the line. *Data post-processing performed with WSxM®.*

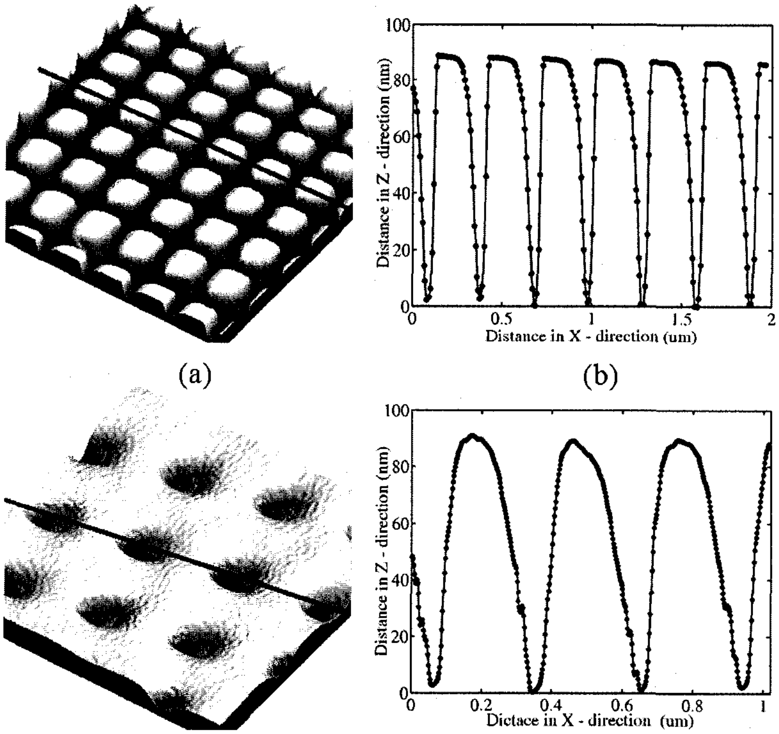

(a) (b)

(c) (d)

**Figure 5-25.** AFM images of 2D arrays with nano-patterned surfaces (a) Si mold with square posts and its representative cross section profile (b) along the line, (c) COC replica of the Si mold with its representative cross section profile (d) along the line. *Data post-processing performed with WSxM®.*

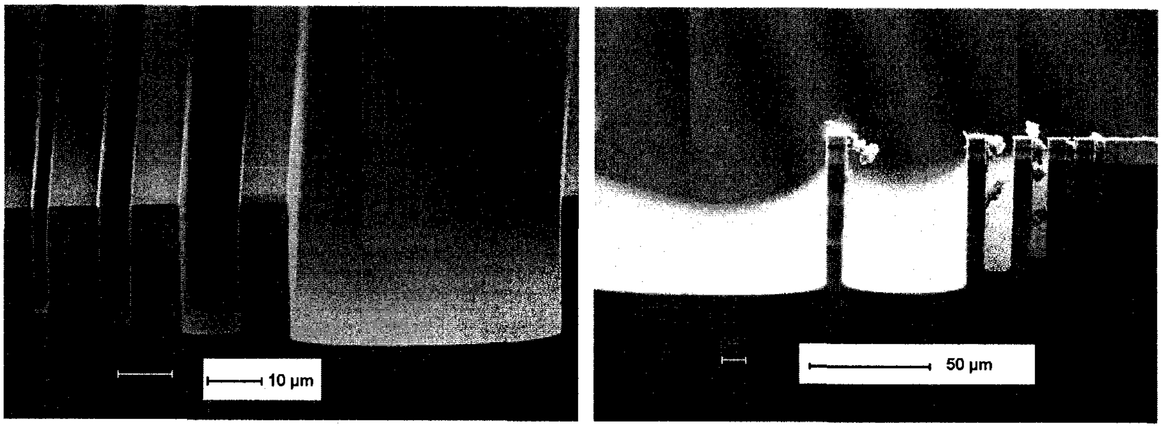

(a) (b)

**Figure 5-26.** SEM pictures of test structures which clearly indicate the aspect-ratio dependent etching (e.g. reactive ion etching lag), (a) test structure with resist stripped off, scale bar 10 µm, (b) test structures with resist on and some debris, scale bar 50 µm. *Images courtesy Dr. Floyd Miller of Lehigh University.*

### 5.3.1 Theoretical Prediction of the Mechanical Stability of High Aspect Ratio Submicron-Pillars

In this subsection, experimental results are compared with the theoretical predictions that address the mechanical stability of high aspect ratio polymer submicron-pillars. At present mainly two proposed and widely used by the research community models are accepted. The models explain the ground of replicated tall objects collapse, a prevalent failure form, due to various factors. Ground collapse refers to the collapse of pillars onto the ground or base surfaces due to pillar's own weight [131, 132] or the base surface's adhesive force [130, 132]. Lateral collapse is described when very closely spaced pillars fail due to adhesion [131]. *Hui et al.,* [131] have assumed that nanostructures fall under their own weight. In contrast *Roca-Cusachs et al.* [130], have assumed that the adhesion force is dominant in structures with nano- and micro-scale dimensions. At present few polymers have been successfully utilized to replicate high AR features, mainly poly(dimethylsyloxane) (PDMS), polyurethane, and epoxy resins [130, 132]. As a processing method liquid molding followed by UV-curing has been accepted. However, no studies are reported that describe the mechanical stability of successfully injection micro-molded high AR pillars with amorphous thermoplastic polymers. Thus, as a result of the successful molding of such features, those currently available theoretical models were implemented. Table 5-6 presents the physical properties of the COC used to calculate the critical elastic modulus, based on the above described concepts, and critical aspect ratio of lateral collapse for the molded circular pillars.

| parameter | value | dimension |
|---|---|---|
| surface tension, $\gamma_s$ | $32.83 \times 10^{-3}$ | N/m |
| work of adhesion, W | $65.66 \times 10^{-3}$ | N/m |
| Poisson ratio, $\nu$ | 0.41 | - |
| Young's modulus, E | 3100 | MPa |
| density, ρ | 1020 | $kg/m^3$ |
| acceleration due to gravity, g | 9.81 | $m/s^2$ |

**Table 5-6.** Physical properties of COC used in predicting the stability and critical aspect ratio of COC circular nano-pillars.

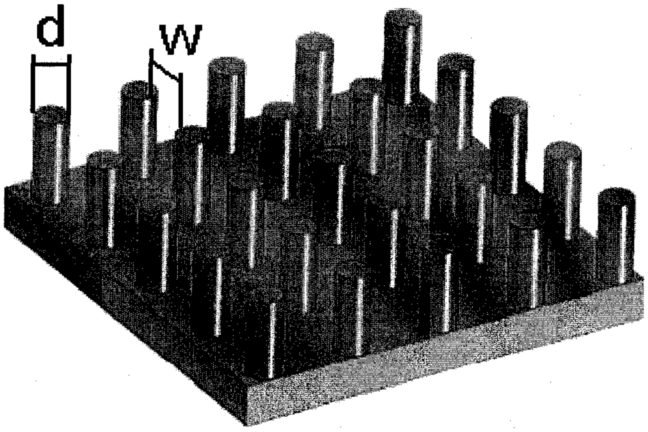

**Figure 5-27.** 3D drawing showing the pillars, where *d* is the pillar diameter and *w* is the pitch in x- and y-directions of the pillar's array.

Based on the Hui's model that a nano-pillar ground collapses under its own weight, the critical elastic modulus of ground collapse, $E_g^{*,1}$ can be estimated as:

$$E_g^{*,1} = \frac{qh^3}{7.837 * I} \qquad (5\text{-}1)$$

where $I = \pi d^4 / 64$ for a circular cylinder, and $q = \rho g \pi d^2 / 4$ is the weight per unit length of the cylinder.

Based on the model proposed by *Roca-Cusachs et al.,* if ground collapse is mainly caused by adhesion force to the ground, the critical elastic modulus of ground collapse, $E_g^{*2}$ can be estimated as:

$$E_g^{*2} = \frac{2^{11/2} 3^{3/4} (1-\nu^2)^{1/4} h^{3/2} W}{(\pi d)^{5/2}} \tag{5-2}$$

where $W$ is the work of adhesion which was estimated as $W \sim 2\gamma_s$, and $\nu$ is the Poisson ratio.

Using the lateral collapse theory established by *Hui et al.,* the critical elastic modulus of lateral collapse of nano-pillars with circular cross-section, $E_L^*$ can be estimated as follows:

$$E_L^* = \frac{5.32 * h^3 \gamma_s (1-\nu^2)^{1/4}}{d^{5/2} w^{3/2}} \tag{5-3}$$

To predict the critical aspect ratio of lateral collapse, the model of *Glassmaker et al.* [132, 133], for circular pillars was adopted:

$$(h/d)_c^* = \frac{0.57 * E^{1/3} w^{1/2}}{\gamma_s^{1/3} d^{1/6} (1-\nu^2)^{1/12}} \tag{5-4}$$

Upon implementation of equations 5-1 to 5-3 the macro-scale Young's modulus, E was compared with the calculated critical elastic moduli. If E>E* then no collapse should occur and the pillars are referred as stable. If E<E* then collapse should be expected and the pillars are regarded as unstable. All three theoretical approaches predicted stable COC pillars for the considered geometry, Table 5-7. This behavior was also confirmed by imaging with SEM. Upon implementation of eqn. 5-4, the critical AR of lateral collapse was found to

be$(h/d)_c^* \sim 47$. In other words for the considered geometry and based on the theory circular pillars as high as 23 µm should be mechanically stable.

| critical elastic modulus | | aspect ratio h/d | | stability | |
|---|---|---|---|---|---|
| | | h=4 µm d=500 nm | h=0.75 µm d=500 nm | predicted | observed |
| $E_L^*$ | MPa | 15.28 | 0.10 | stable | stable |
| $E_g^{*,2}$ | MPa | 93.19 | 7.57 | stable | stable |
| $E_g^{*,1}$ | Pa | 5.23 | 0.035 | stable | stable |

**Table 5-7.** Values of calculated critical elastic modulus in accordance with the discussed theoretical models predicting stability of circular nano-pillars.

Upon implementation of eqns. 5-1 and 5-3 and considering the geometry of the pillars seen in Figure 5-21(b) it was found, Table 5-8, that gravitational collapsing theory did not predict the experimental results. Similar results where also previously reported by *Zhang et al.* [132]. It was assumed that the pillars stretched during demolding – a result of premature demolding before full solidification in the cavities. Upon their release from the cavities, an instantaneous solidification occurred due to the high surface area/volume ratio of the pillars. It is believed that this assumption is valid since the mold temperature was kept at ~130 $^0$C which was below the Tg of the polymer. Upon solidifying the pillars lost mechanical stability and collapsed on the surface due to increased AR. The failure location, where bending occurred, was right in the spot where the diameter of the pillar was reduced (to ~160 nm) as a consequence of the earlier demolding, as seen in the Figure 5-21(b).

| critical elastic modulus | | aspect ratio h/d | stability | |
|---|---|---|---|---|
| | | h ~6.6 μm<br>d ~160 nm, [a] | predicted | observed |
| $E_L^*$ | MPa | 3370.83 | unstable | unstable |
| $E_g^{*,1}$ | Pa | 224.25 | stable | unstable |

[a] Estimated diameter of the kink where bending occurred.

**Table 5-8.** Values of calculated critical elastic modulus in accordance with the discussed theoretical models predicting the stability of circular nano-pillars seen in Figure 5-21(b).

## 5.4 Conclusions

In this study injection molding of polymer nano- and submicron-patterned surfaces utilizing silicon molds with plasma polymerized anti-adhesive $C_4F_8$ coating was proposed and investigated. Si molds were manufactured with e-beam lithography and deep reactive ion etching. The inductively coupled reactor of the plasma etcher was successfully utilized to deposit a fluorocarbon film whose elemental composition and chemical bonding structure were investigated with x-ray and Fourier transform spectroscopies. The film exhibited low surface energy and good anti-adhesive properties which was confirmed by the contact angle measurements and the subsequent polymer moldings with melt processable amorphous cyclo olefin copolymer. As a result, polymer nano-features with different shapes and sizes, as small as 25 nm, were successfully replicated as well as high aspect ratio (AR~8) submicron-sized pillars. Theoretical predictions of the mechanical stability of the high aspect ratio polymer pillars were in excellent agreement with the observations. A new concept describing ground collapse of high aspect ratio pillars due to molecular orientation induced charge separation between pillars and ground surface was proposed as well. The excellent fidelity of replication of the polymer structures was confirmed by examination of the patterned surfaces with scanning electron and atomic force microscopes. Fluorine transfer from the film to the olefin polymer was also investigated and explained. It is believed that after optimization of the fluorocarbon deposition conditions excellent quality molds could be manufactured and subsequently used for mass production of low-cost patterned polymer substrates.

Finally, potential applications which could benefit from this study are envisioned to be: (i) discrete track recording (DTR) media for high capacity storage magnetic hard disks [134], Figure 5-28(a, b); (ii) near-field optical data storage media, Figure 5-28(d); (iii) substrates suitable for cell-substratum interaction studies which possess uniform nano-topography eliminating the drawbacks (e.g. uncontrolled nano-topography) associated with the current use of polymer demixing technique, Figure 5-29; (iv) platforms for generation of surface plasmon-polariton excitations (details can be found in Chapter 6); (v) electrically controllable nano-structured surfaces [135]; (vi) surfaces with controllable transparency and/or spectral reflection; (vii) sub-wavelength optics (wide band antireflective polarizers) [136]; (viii) drag reduction surfaces [137].

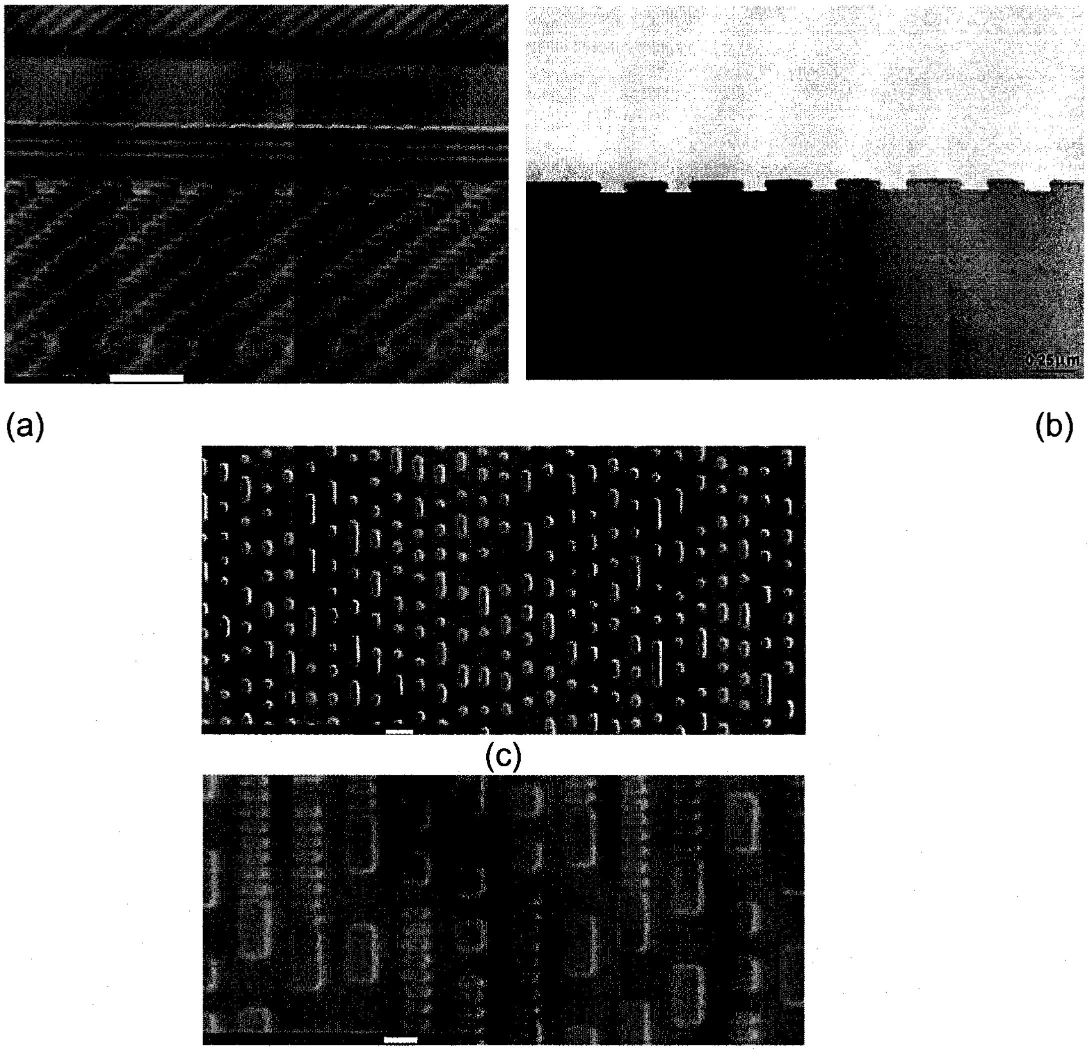

(a) (b)

(c)

(d)

**Figure 5-28.** (a) SEM image of nano-imprinted features for DTR media, www.obducat.com , scale bar ~200 nm, (b) a cross-section of a finished DTR disk with deposited magnetic layers, measured with a tunneling electron microscope. This structure is made with an electron-beam mastered mold on a 95 mm diameter disk substrate with grooves 140 nm wide and 50 nm deep, www.komag.com, (c) SEM image of current blu-ray type of pattern for optical storage, www.obducat.com, scale bar ~500 nm. (d) SEM image of a pattern of the future near field optical storage technology, scale bar ~200 nm, www.obducat.com.

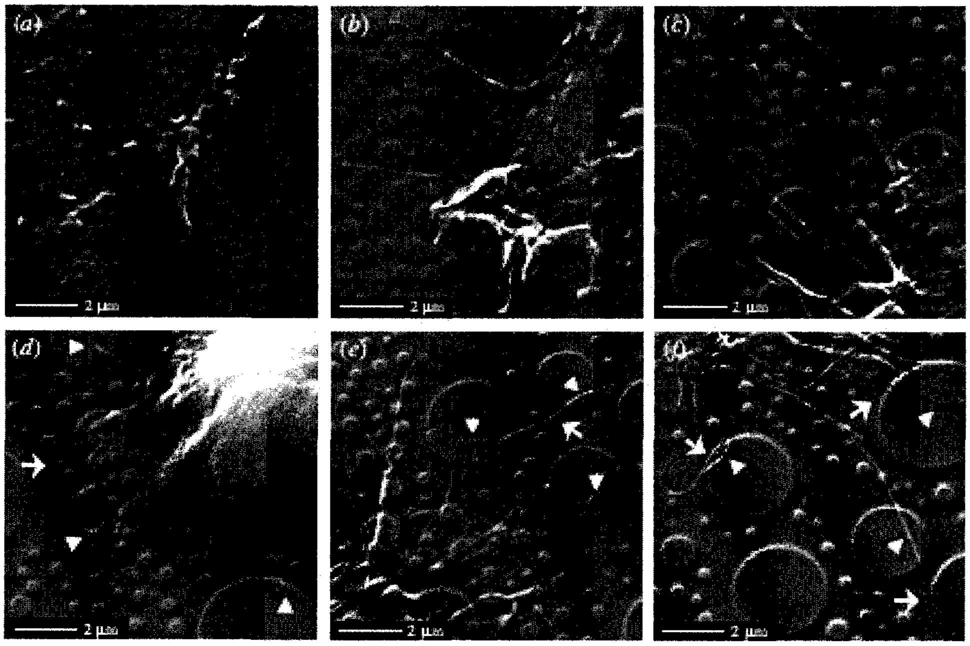

**Figure 5-29.** High-magnification SEM images of hFOB (human foetal osteoblast) cells cultured for 24h on surfaces obtained after polymer demixing of polystyrene/polybromostyrene with (*a*) 11nm, (*b*) 38nm and (*c*) 85nm surfaces. Additional examples of hFOB cells cultured on 85nm substratum are shown after 3h ((*d*), (*e*)) and 24h (*f*) of culture. Arrowhead and arrow indicate the interaction with top and other portions of island topography, respectively. *Reprinted from [138], © 2005 with permission from the Royal Society.*

# CHAPTER 6

# SCANNING NEAR-FIELD OPTICAL MICROSCOPY ANALYSIS OF GOLD DEPOSITED NANO-PATTERNED POLYMER SUBSTRATES

*"Technology stimulates Curiosity."*

## 6.1 Introduction – Surface Plasmon-Polaritons

The phenomenon of anomalous diffraction on diffraction gratings due to the excitation of surface plasma waves or surface plasmons from the metal antireflective coatings was first observed by *Wood* at the beginning of the twentieth century [139]. Surface plasmons, also known as surface plasmon-polaritons (SPP), represent quasi-two-dimensional waves that propagate along an interface between two media with real parts of permittivity of opposite signs - a condition fulfilled for metal/dielectric interfaces [140]. Many fundamental properties of SPPs have been studied and a number of applications have been investigated. Sensors utilizing SPP excitations were successfully introduced for chemical, biological, humidity, and displacement sensing [139]. SPP based sensing is a surface sensitive measurement technique that utilizes the fact that a surface plasmon wave propagating along the surface of a metal film or particle is extremely sensitive to changes in the refractive index close to the surface. Recently, SPP based super-resolution imaging or plasmon printing has been reported as a way to perform nano-lithography with a superb resolution [141-143].

There are several current technological limitations that prevent plasmonic based technologies to rich out from the specialized research and analytical laboratories and gain momentum elsewhere. Improvement of the detection limits; high channel performance, for high throughput systems; development of sensor elements with high signal-to-noise ratio; and utilization of low cost sensor elements need to be addressed among others [139]. One way to address those limitations is by utilizing materials with suitable properties and manufacturing techniques which are cost-effective. There is also a need for cost-effective fabrication of highly ordered nano-particle systems which properties can be readily adjusted during their manufacturing [144].

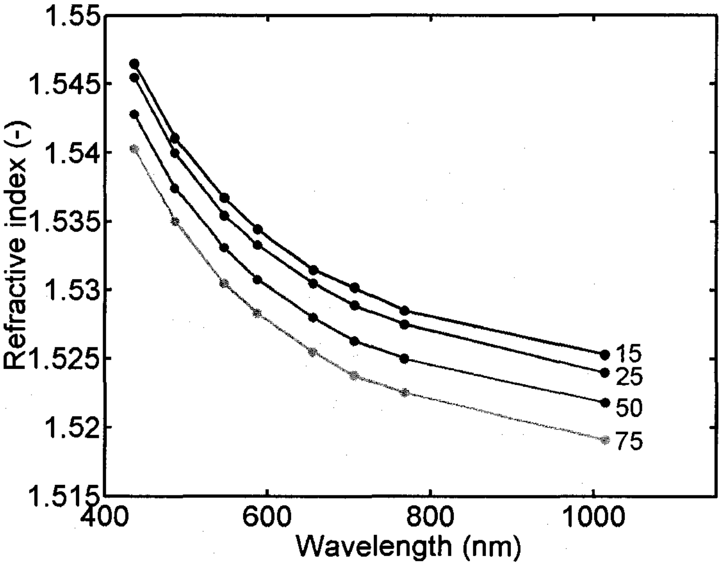

**Figure 6-1.** TOPAS™ COC 5013 refractive index change with light wavelength at four different temperatures 15$^0$C, 25$^0$C, 50$^0$C, and 75$^0$C, *Adapted from [84].*

Interestingly enough, polymer based waveguides at telecommunication wavelength utilizing SPP phenomena have been already reported [145, 146]. Moreover, injection molded patterned [147, 148] and non-patterned [149] cyclo olefin copolymer (COC) based sensors were also investigated. The choice of utilizing COC grades as substrates for SPP based sensors is mainly driven due to their optical properties, e.g. refractive index and light transmission, Figures 6-1 and 6-2.

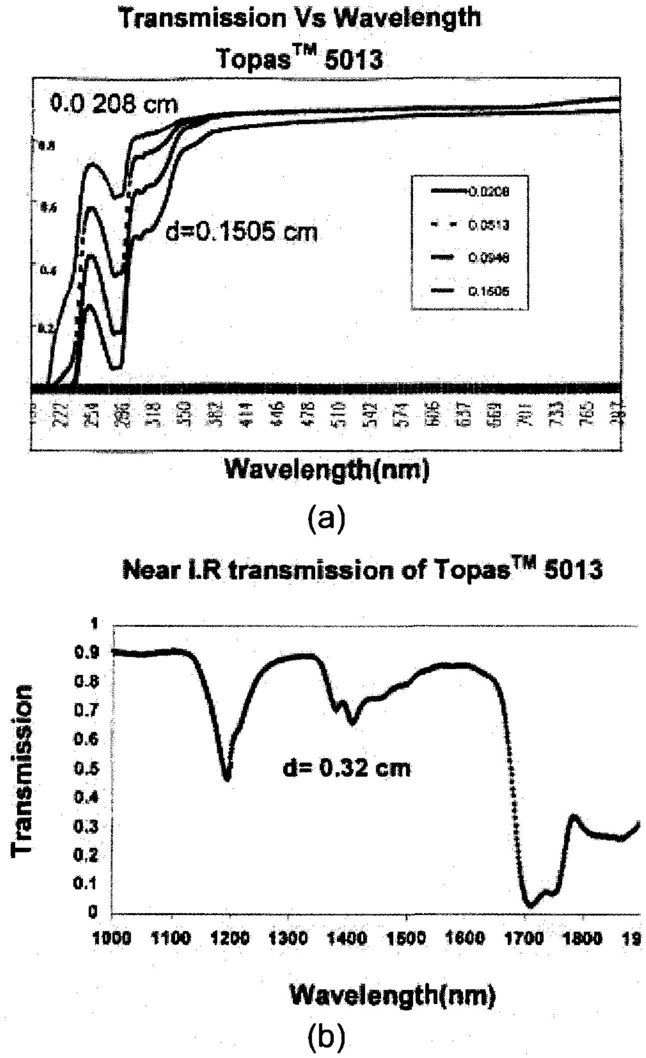

**Figure 6-2.** (a) Optical transmission of TOPAS™ COC 5013 with heat stabilization additives, for different film thicknesses, given in centimeters (b) Near IR transmission of TOPAS™ COC 5013 for sample thickness 0.32 cm. *Images reprinted from [84] ,© 2001 with permission from SPIE and Dr. Garo Khanarian.*

Furthermore, to the author's best knowledge, injection molded nano-patterned COC surfaces have not been investigated as potential templates for SPP generation. Therefore in this chapter, preliminary investigative work on utilizing successfully manufactured COC nano-patterned surfaces as cost-effective platforms for generation of surface plasmon-polariton (SPP) excitations is reported. For this purpose, near-field optical microscopy has been utilized since this technique is known to provide direct evidence for SPP excitations and allows for spatial imaging of the corresponding SPP modes [140, 150]. Gold sputtered injection molded nano-patterned COC samples were subjected to near field optical illumination with two laser wavelengths. A profound difference in the light transmission through the patterned and flat regions for the considered two wavelengths was observed and attributed to a wavelength dependent SPP excitation or damping influenced by the nano-topography. Light intensity (2D and 3D) and topographic images for chosen regions are presented. Intensity profiles of high resolution scanned regions are also given.

### 6.2 Experimental Details

Successfully molded nano-patterned COC samples from Chapter 5 were deposited with very thin 15 nm film of gold (Au) by utilizing magnetron sputtering tool (Hummer 6.6, Anatech, Ltd), Figure 6-3. The thickness of the film was monitored with a crystal thickness monitor (Maxtrex, Inc. model TM-330). The plasma was created at pressure ~10.7 Pa, plasma discharge current ~20 mA and air as a flow gas. The latter factor was expected to influence the quality of the deposited Au films but work addressing this potential problem was not carried out. The deposition process produced isolated Au nano-dots positioned on the top of the 50 nm high polymer nano-posts. It was estimated that the size of the resulted Au nano-dots is ~15x70 nm as seen in Figure 6-4.

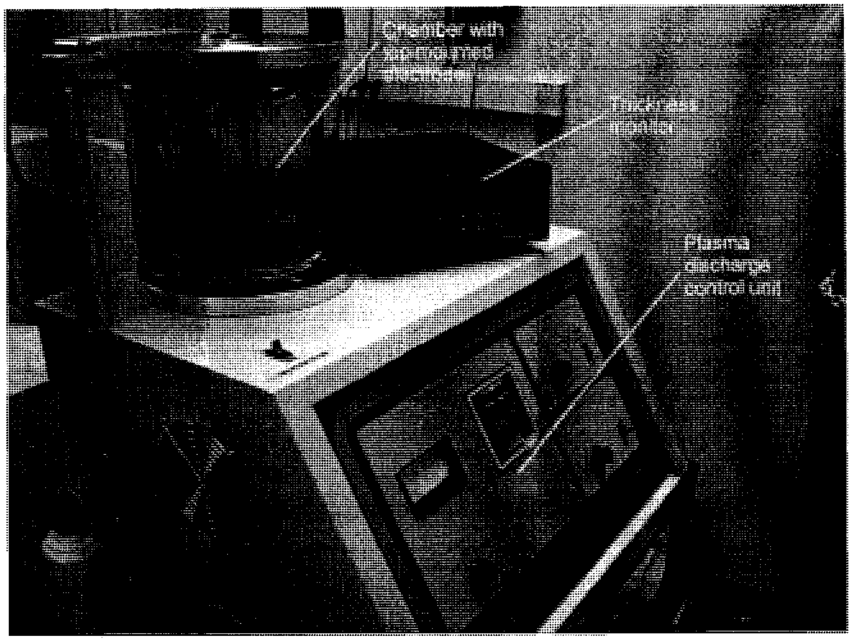

**Figure 6-3.** Digital picture of the magnetron sputtering machine depicting the chamber where the sample is loaded, the thickness monitor and the plasma discharge control unit.

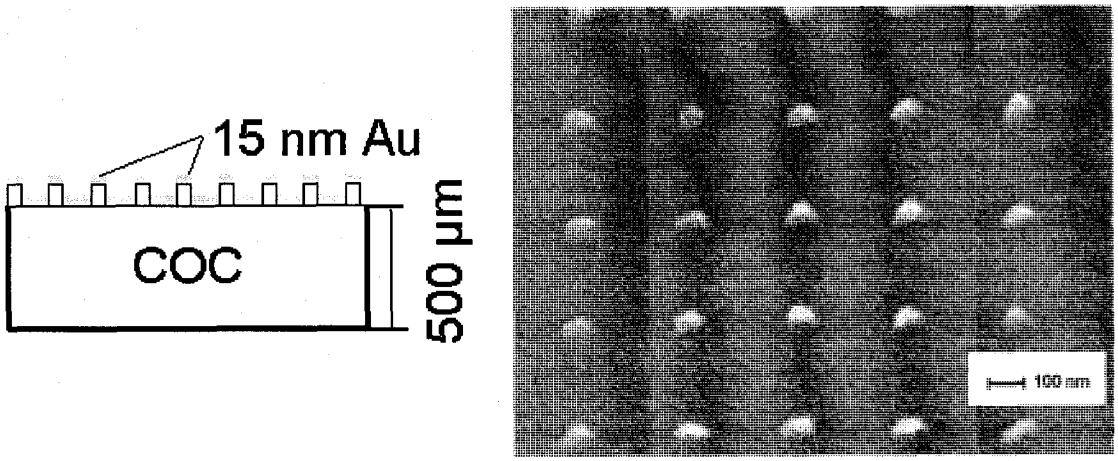

(a) (b)

**Figure 6-4.** (a) Schematic of the test structure used in SNOM imaging, (b) SEM-VP mode picture of patterned COC sample sputtered with 15 nm Au. Gold grains are clearly visible.

To probe the samples, Scanning Near-Filed Optical Microscopy (SNOM) analysis was carried out with near-field microscope equipped with a cantilever-type probe (α-SNOM, Witec Instrument Corp.) [151]. Imaging was carried out in a transmission mode using two different wavelength lasers. In this experimental set-up, the light transmitted through the transparent sample (polymer) is collected by the single photon counting detector of the tool via objective lens positioned below the sample. It is important to be noted that the transmission mode of operation was preferred since topography artifacts do not interfere with the light signal as they do in a reflection mode of operation. The cantilever-type probe used in the experiments had a pin-hole of approximately ~100 nm, thus the resolution of the system was enough to resolve two Au nano-dots from each other. Light intensity images were collected along with topographic ones since the probe acts as an AFM probe as well. A potential flaw in the experimental setting was considered the lack of modulation distance control during topography scanning. Thus, the lateral force exerted on the soft Au nano-dots was not minimized [151] and potential damage of the soft structures was expected. Raman spectroscopy was also implemented to potentially detect enhanced Raman scattering from the gold nano-dots but those experiments did not yield any conclusive results due to substrate failure, e.g. the laser melted the polymer virtually drilling holes into it. Raman spectroscopy set-up was the same as that used for the testing of plasma polymerized $C_4F_8$ film and detailed description of it is given in Chapter 5.

## 6.3 Results

The enhanced light transmission is an indication of surface plasmon-polariton modes which couple with the local electric filed of the light [145, 151]. Therefore, the SPP modes were recognized by the increase in the transmitted light intensity [145]. Other techniques suitable for SPP detection, such as angular and wavelength interrogation are also possible and used in commercially available sensors but for simplicity of the experiments intensity measurements were considered [139]. The evanescent field, emanating from the tip of the Si probe couples with SPP on the Au nano-dots and is re-emitted as a propagating wave in the far-field, traveling through the ~500 μm thick polymer replica [145]. On the other non-patterned side of the polymer sample the light signal is detected by the single photon counting detector. Following photon detection, intensity profiles are constructed by utilization of the tool's software. Based on literature research [149, 152, 153] two major wavelengths were considered for SNOM illumination of the structures, namely $\lambda_1$=488 nm and $\lambda_2$=635 nm, to reveal structures behavior in non-resonant and resonant modes, respectively. Pseudo-color SNOM images along with topography ones were collected in the vicinity of the patterned and non-patterned (termed as flat) regions to detected potential difference in the light intensity. When illuminating those structures with a laser light with wavelength $\lambda_1$=488 nm, as seen in Figure 6-5, light intensity was detected to be higher in the flat region. Interestingly enough, the patterned region had an area with increased light transmission, which is also seen in the 3D representation of the SNOM image, Figure 6-6(a). It is believed that this area is not patterned and is actually flat. During SEM imaging of the Si molds (details are given in Chapter 5 in this document) it was observed that certain areas were not properly etched, Figure 6-6(b). Contamination of the surface (particle which landed on the mask before etching blocked the plasma in that region) was assumed to be the reason for such outcome which in this type of experiments was beneficial, since it clearly depicts the different interaction of light with the patterned and non-patterned areas. When illuminating the same structures with a laser light with wavelength $\lambda_2$=635 nm, as seen in Figure 6-7(a), detected light intensity was higher in the patterned region which is also seen in the 3D representation of the SNOM image, Figure 6-7(c). This result was completely the opposite of what was previously observed.

Such wavelength dependent change in the transmitted light intensity can potentially be explained with damping ($\lambda_1$=488 nm) and excitation ($\lambda_2$=635 nm) of SPP influenced by the nano-topography. Other factors which influence this behavior and which potentially can change it are considered, among others, to be the geometry and size of the metallic nano-features [144, 154], the dielectric material [148], the deposition conditions and deposition process, and the wavelength used for illumination.

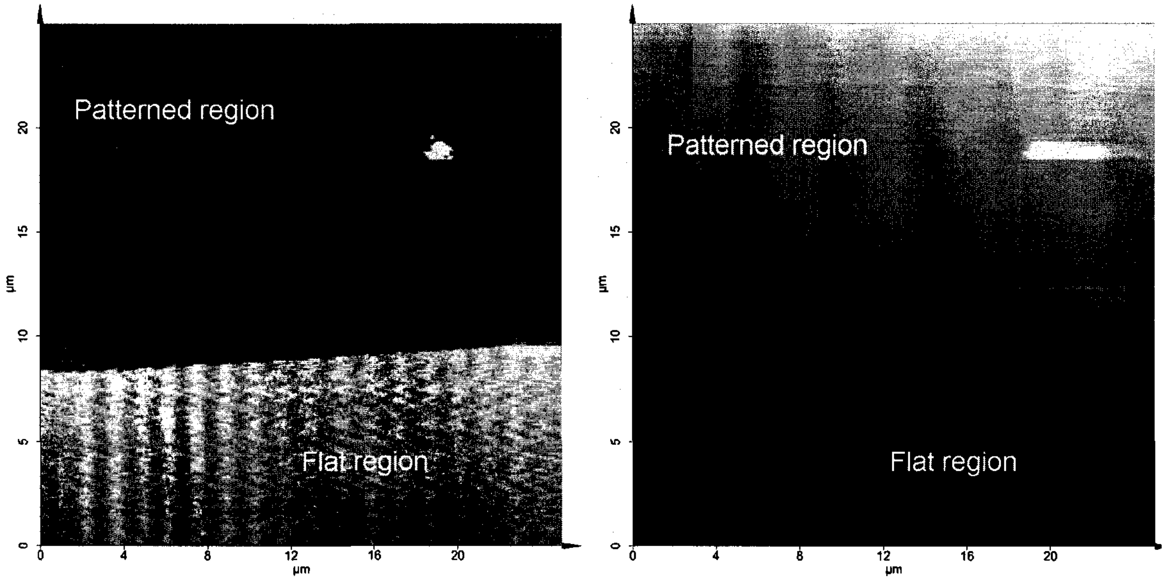

(a) (b)

**Figure 6-5.** Pseudo-color images of Au sputtered COC sample with 25x25 µm scanned area (a) near-field optical image obtained at $\lambda_1$=488 nm with high light intensity in the flat region, (b) topography image of the region. The boundary between the patterned and flat regions is clearly visible on both images.

It is believed that the observed SPP damping at $\lambda_1$=488 nm can be explained with the increased confining of light in the nano-patterned region. Such localization is a consequence of multiple scattering and interference events [155] that prevent the light propagation in the dielectric media (COC). The scatter events mainly depend on the scattering mean free path *L* which decreases with the wavelength due to the increase in the scattering cross-section, eqn. 6-1 [140, 155]:

$$L = \frac{1}{\sqrt{2}n\sigma(\lambda)} \qquad 6\text{-}1$$

where *n* is the number density defined in this case as the ratio of the number of Au nano-dots to unit area.

The mean free path, *L* is also defined as the average distance a photon travels in a medium between scattering events and the scattering cross section *σ(λ)* is the probability of interaction between photons with the spatially distributed Au nano-dots.

On the other hand, the observed increase in light transmission at $\lambda_2$=635 nm through the patterned region could be explained with the reduced scatter influenced by the increased wavelength and it is specific for that nano-topography distribution. Moreover, it is assumed that this regime is a result of a resonance mode of interaction, e.g. efficient photon coupling with the electron plasma of the Au nano-dots. Similar, observations of wavelength dependent interaction of randomly arranged Au nano-dots on a glass substrate were reported by Bozhevolnyi et al [156]. It is envisioned that such topography influenced wavelength dependant SPP mode can potentially be used for the cost-effective manufacture of sensor elements with improved signal-to-noise ratio. Upon taking high resolution scans of random patterned regions, cross-sectional distributions of the light intensity in two directions were obtained and representative scans are given in Figure 6-8. 3D representation of a SNOM image from such region was also constructed, Figure 6-9.

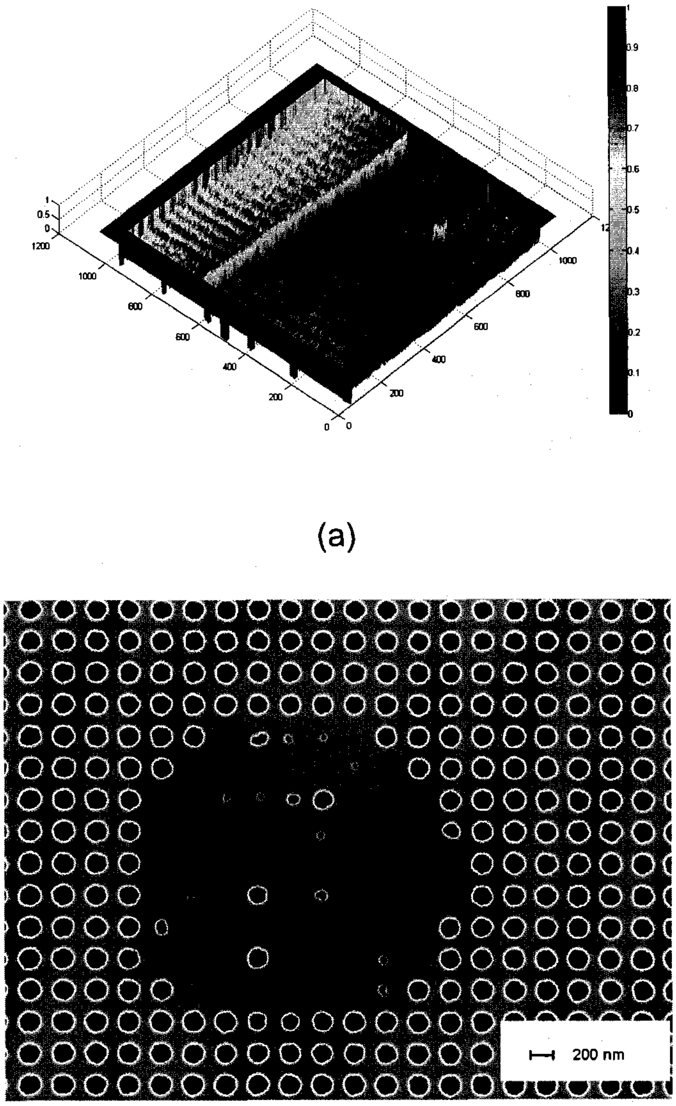

(a)

(b)

**Figure 6-6.** (a) 3D representation of near-field optical image (as seen in Figure 6-5(a)) obtained at $\lambda_1$=488 nm with high light intensity in the flat region, scanned area 25x25 μm. Note the high intensity peak in the patterned region. It is believed that this is a result from bad DRIE etching during mold fabrication which resulted in a not-patterned region; (b) SEM picture of a region with 2D hole-array from Si mold with improperly etched area whish was subsequently transferred during polymer replication. Few such areas were noticed during inspection of the Si molds *(detailed description of the Si mold development and polymer replication is provided in Chapter 5).*

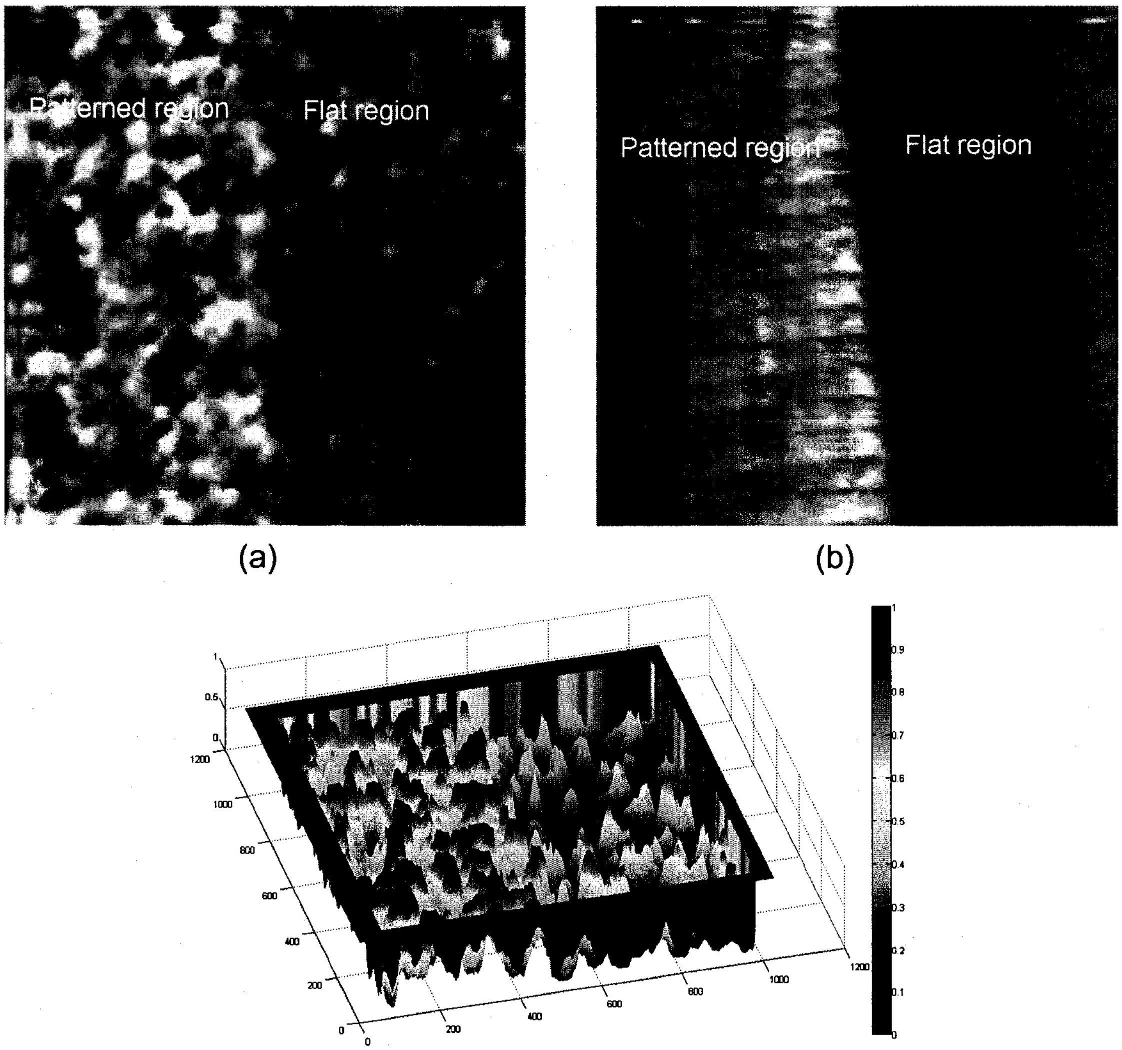

(a) (b)

(c)

**Figure 6-7.** Pseudo-color images of Au sputtered COC sample with 5x5 μm scanned area (a) near-field optical image obtained at $\lambda_2$=635 nm with increased light intensity in the patterned region induced by locally enhanced electric field on the nano-dots which resulted from SPPs excitations, (b) topography image of the region; (c) 3D image of the near-field optical image. The boundary between the patterned and flat regions is clearly visible in all images.

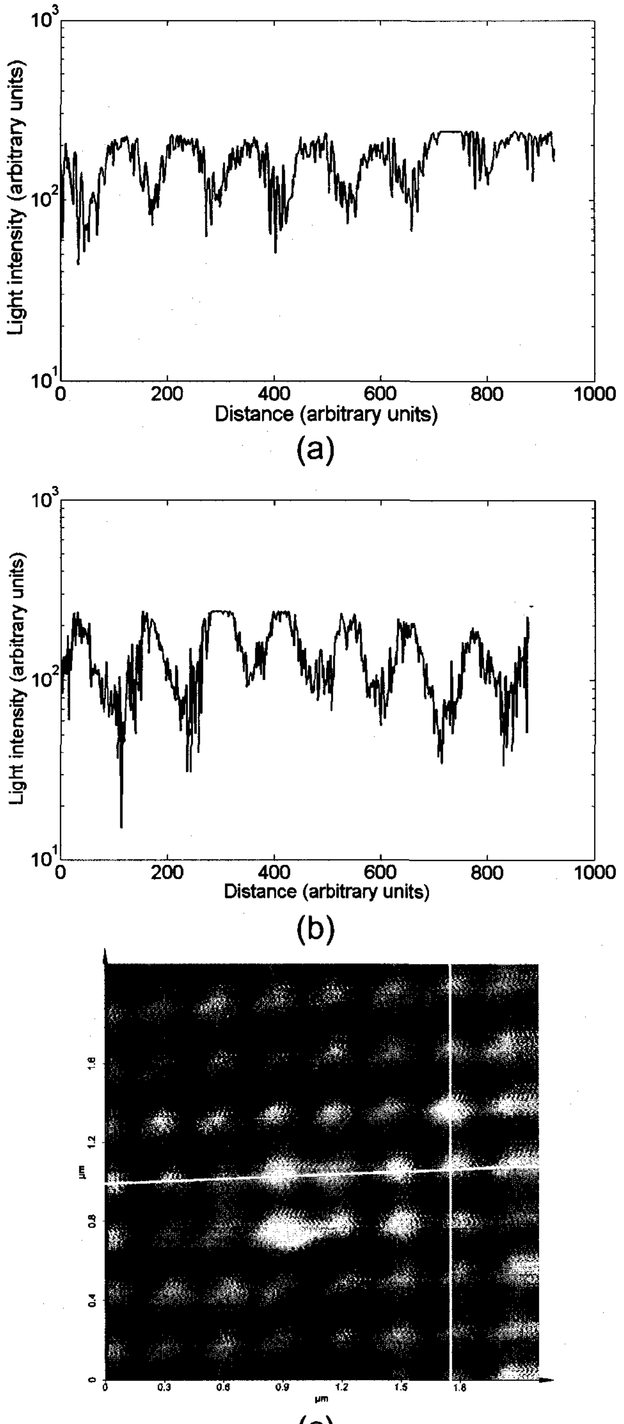

(a)

(b)

(c)

**Figure 6-8.** Cross-sectional view of light intensity along selected directions from patterned region (a) horizontal direction and (b) vertical direction; (c) high resolution SNOM optical image from patterned area, taken at $\lambda_2$=635 nm, with lines denoting the locations where the cross-sectional intensity profiles were taken, scanned area 2.2x2.2 µm.

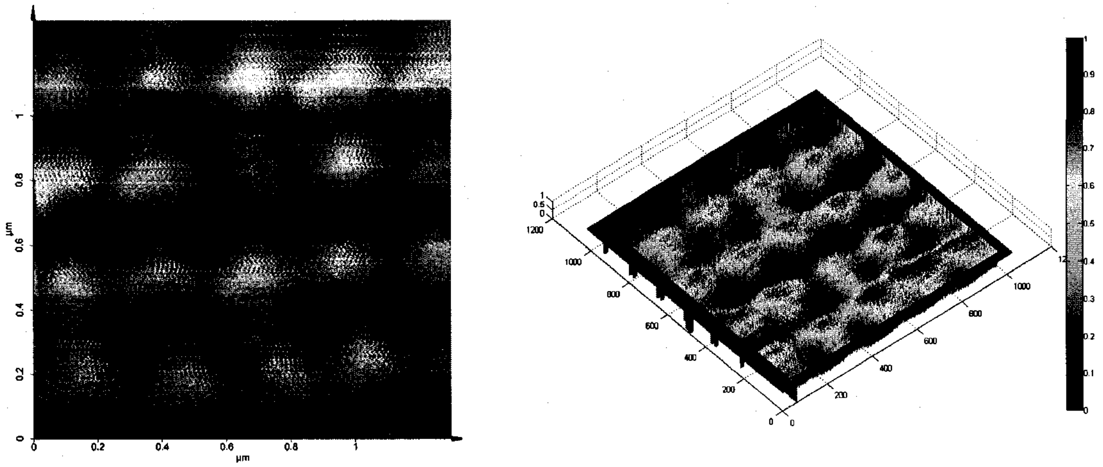

(a) (b)

**Figure 6-9.** (a) High resolution SNOM optical image from patterned area, taken at $\lambda_2$=635 nm, scanned area 1.3x1.3 µm, (b) 3D representation of the near-field optical image.

Finally, more thorough explanation of the observed in this study wavelength dependent change in the light transmission through the nano-patterned region can be given upon obtaining of the ground state spectrum of the structures, e.g. absorbance vs. wavelength which would potentially elucidate where the plasmon resonance occur. Furthermore, angular and wavelength resolved measurements of the reflectivity of those structures, along with SNOM imaging with other wavelengths could also help in identifying the reasons for the above discussed phenomenon.

## 6.4 Summary

In this study injection molded nano-patterned polymer COC substrates were tested as templates for generation of surface plasmon-polariton excitations. The as molded samples were deposited with 15 nm thin layer of gold by means of magnetron sputtering. This process formed isolated Au nano-dots on top of the polymeric nano-features. The complex of Au/nano-structured polymer was tested with scanning near-filed optical microscope with two different wavelengths. Two very distinct modes of light transmission were observed and their behavior was found to depend on the wavelength influenced scattering from the sub-wavelength-sized scatters.

Finally, potential applications which can benefit from this study are envisioned to be: (i) waveguiding on planar surfaces [152, 155] for highly integrated optical devices, similar to the waveguiding used in photonic crystals, Figure 6-10; (ii) integrated polymer based chips for SPP sensing with improved signal-to-noise ratio [147, 157] and such (iii) that are suitable for biological sensing [158], (iv) improving LEDs efficiency.

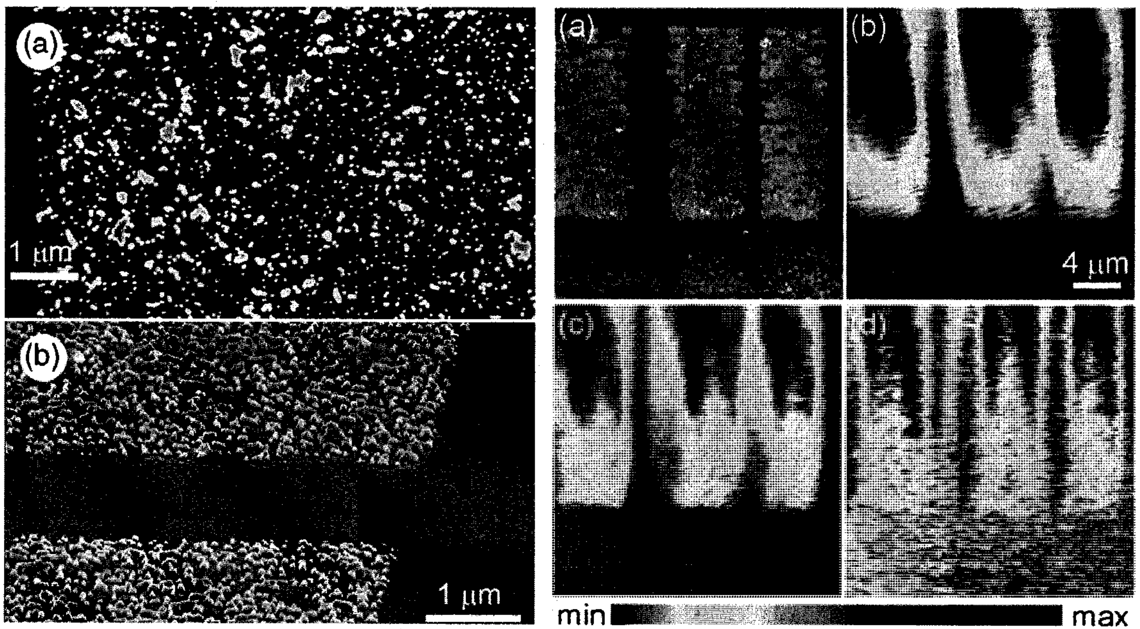

(a) (b)

**Figure 6-10.** (a) SEM images of two random (top-N1 and bottom-N2) Au structures with different number density onto glass substrates used for SPP generation (b) Pseudo-color topography image (upper left corner) and three SNOM images (25x25 µm) obtained from regions N1 and taken at 738, 785, and 850 nm (counterclockwise direction). *Images reprinted from [140], © 2003 with permission from Blackwell Publishing Ltd.* The SPP damping and its attenuation in the patterned regions at higher wavelengths is clearly visible. In this work planar SPP induced waveguiding with random Au structures was also reported.

# CHAPTER 7

# NUMERICAL SIMULATION OF POLYMER MELT FLOW IN MICRO-CHANNELS

*"In theory, there is no difference between theory and practice. But in practice, there is." - Yogi Berra*

## 7.1 Introduction

The lack of adequate modeling tools predicting the polymer flow in micro-channels is considered as one of the major problems related to the scientific advancement of injection micro-molding applications. Therefore, in this Chapter an attempt was made to address some of the limitations and to initiate both the implementation of a physical model and numerical procedure which better describe the polymer flow at micro-scale. Recent studies [29-33] indicate that the existing commercial simulation packages, successfully used in macro-scale simulations of polymer flow, do not incorporate important physical phenomena occurring during flow in micro-channels. This inadequacy can be attributed to the following limitations found in the standard modeling applications:

- The rheological data used in the current simulation packages are obtained from measurements of macroscopic scale and are not suitable for modeling melt through micro-channels.
- Wall slip condition is not incorporated.
- Anisotropic conduction of heat caused by molecular orientation is not addressed.
- Micro-scale surface effects which may also play significant effect on the flow behavior are neglected.

Therefore in the present study an attempt was made to address some of the above issues. Standard finite element (FE) based package MOLDFLOW

Plastics Insight 6.1 was used to simulate the filling stage in test cavities. The results were analyzed and compared with the results obtained from a 3D continuum based FE simulation which incorporates (i) viscosity model describing the melt flow in micro-channels, (ii) wall slip at the boundaries, and which also (iii) takes into account the effect of anisotropic conduction in polymer micro-flows. The improved physical model describing the flow in micro-channels was solved by utilizing COMSOL FEM libraries. In order to compare the output results from both MOLDFLOW and COMSOL simulations, a test structure modeled in 3D with Solid Edge was used in both analyses, Figure 7-1.

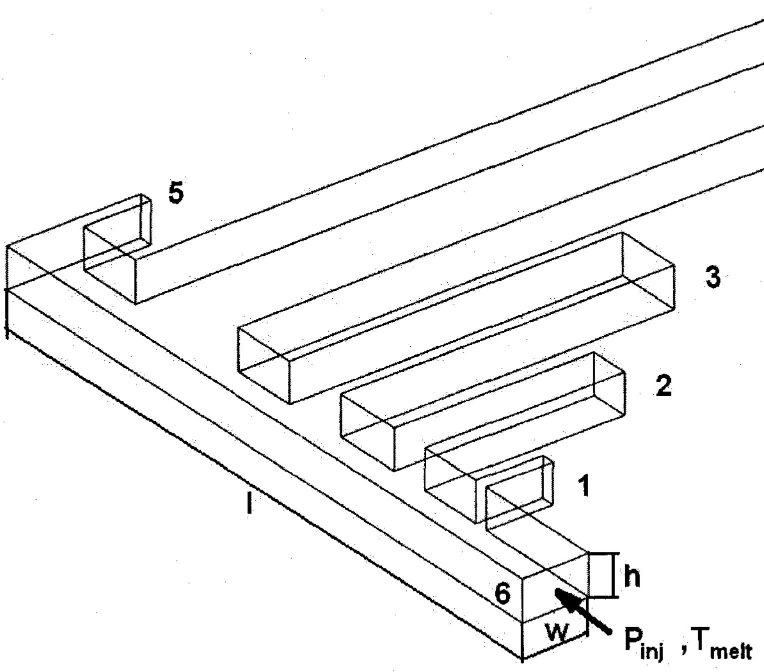

**Figure 7-1.** Schematic representation of the 3D geometry of the test structure used in the flow simulations. It consists of six channels with various width (w), and length (l) but the same height (h=30 μm, depth). wxl for each channel is as follow (**1**) - (10,50), (**2**)-(30,150), (**3**) - (50,250), (**4**) - (100,500), (**5**) - (10,50), and (**6**) - (50,500) all in micrometers.

The material utilized in the flow simulations studies was chosen to be poly(propylene) PP-1013 H1, Exxon Mobile. The material's properties obtained from Moldflow's comprehensive materials database where used in both types of simulations for consistency. Other material's properties, relevant to the flow in micro-channels were found from relevant scientific literature.

## 7.2 Moldflow simulation of the flow in micro-channels

Simulation of the polymer flow in the test cavity with Moldflow was performed by implementing 3D meshes using the Navier-Stokes equations with a non-Newtonian viscosity model coupled with the Energy equation for the filling stage [159]. The viscosity model was chosen to be Cross-WLF, Figure 7-2, since this model provides good physical representation of the viscosity data at macro-scale. Moldflow is also using the so called second order viscosity model which can be chosen by the user as well, Figure 7-3. This model describes the viscosity $\eta = \eta(\dot{\gamma}, T)$ as a function of the shear rate $\dot{\gamma}$ and the temperature of polymer melt $T$, eqn. 7-1, where A', B', C', D', E', and F' are data-fitted coefficients:

$$\ln(\eta) = A' + B'\ln(\dot{\gamma}) + C'T + D'\left[\ln(\dot{\gamma})\right]^2 + E'\ln(\dot{\gamma})T + F'T^2 \qquad (7\text{-}1)$$

The inertia and gravity effects were ignored by utilizing the user-friendly interface of the package. Since the inertia is the mass-velocity term in the momentum equations and the viscous forces which come from shear deformation are several orders of magnitude larger than the inertia forces, they were ignored, leading to solving the simplified Stokes equations. The above described steps were taken in order to make the physical model description implemented in Moldflow analysis similar to the one, developed specifically for polymer flow inside micro-channels and described in details later in this chapter. Thus the models used in both types of analysis were considered to be as close as possible. Importing of the 3D test structure, meshing with tetrahedral elements, and flow simulation were initiated as standard procedures described in details in Moldflow Help files. Therefore, these steps are considered trivial and are not further explained. It is worth noting that Moldflow analysis was performed by utilizing a coupled 3D solver which combines the pressure and the three velocity components into a single matrix, which is then solved. In addition, Moldlfow incorporates only one type of solver, claimed to be specifically designed for polymer flow in cavities [160]. The used solver, the algebraic multigrid preconditioned conjugate gradient solver, is considered as one of the most promising methods for solving large systems of linear equations arising from unstructured meshes. It is important to be noted that the Moldflow user has only a limited possibility for solver's parameters tuning, no possibility of changing the physical model description with exception of the already discussed options, which therefore leads to a "black-box" type of simulation analysis.

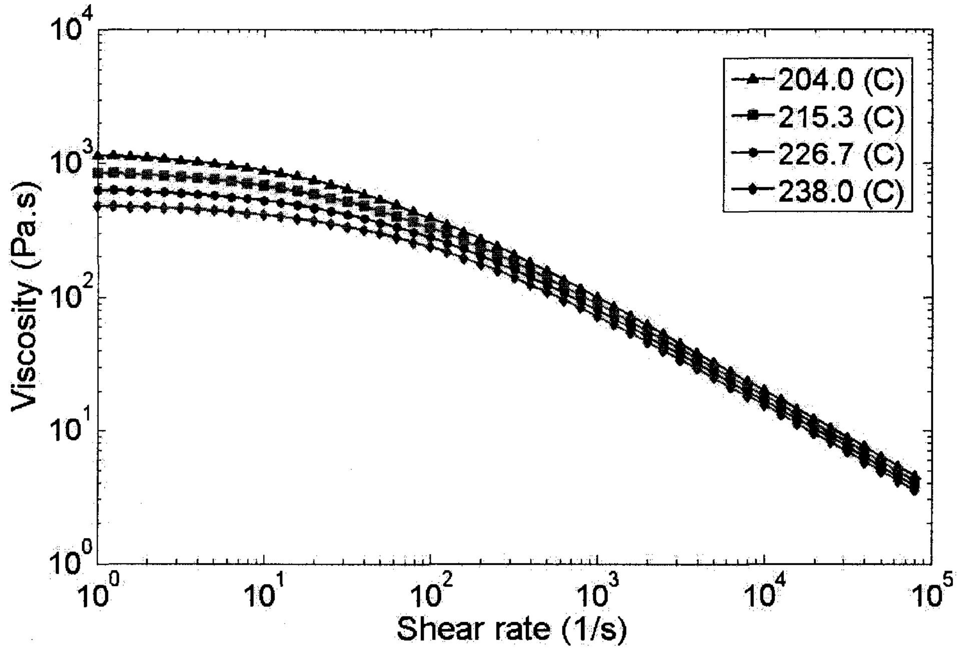

**Figure 7-2.** Moldflow Plastics Labs acquired viscosity vs. shear rate test data for PP-1013 H1. Cross- WLF viscosity model.

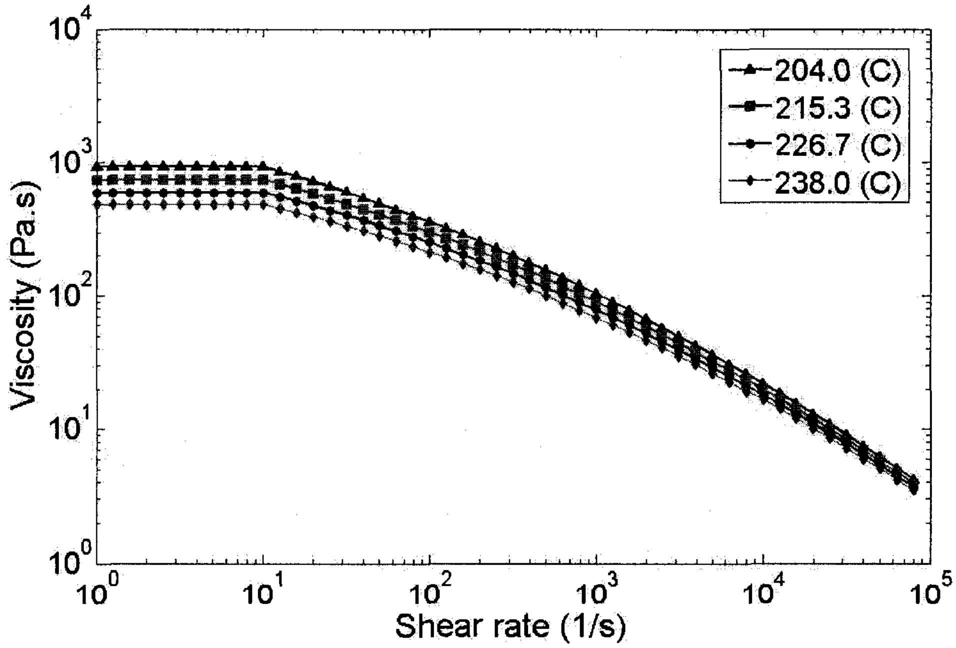

**Figure 7-3.** Moldflow Plastics Labs acquired viscosity vs. shear rate test data for PP-1013 H1. Moldflow second order viscosity model.

## 7.3 3D FEM Simulation of the Flow in Micro-channels Based on an Improved Physical Model

It has been shown that in a flow of highly viscous fluid with a low value of thermal conductivity and a highly temperature dependent viscosity, that a strong coupling between the momentum balance and the energy balance exists. Such coupling is caused be the fact that the dissipated energy (from viscous heating) leads to a local temperature rise, which in turn lowers the local value of the viscosity [161]. This model is at present adopted by Moldflow. On the other hand experimental investigations have shown that the molecular orientation leads to anisotropic conduction of heat that significantly influences the melt flow especially at micro-scale level [161]. As seen in Figure 7-4 the perpendicular to the flow direction thermal diffusivity, which is proportional to the thermal conductivity of the melt, is larger than that in the parallel direction and depends strongly on the mean velocity. The local energy generation rate due to shear is considered to be independent of the scale, while the thermal diffusion rate is proportional to the square root of the thickness. Therefore, in micro-scale the increased thermal diffusion effect results in uniformly distributed melt temperature inside the micro-channels which is equal to that of the mold temperature [29]. Consequently, the viscous heating effect in micro molding can be safely ignored during flow simulation analysis, and the flow can be assumed to be under isothermal conditions [29, 32, 33]. Therefore, in the following description of the physical model the momentum equations' coupling with the energy equation was not considered. It is important to be noted that the latter consideration simplified the physical model significantly and allowed for computationally less demanding flow simulations.

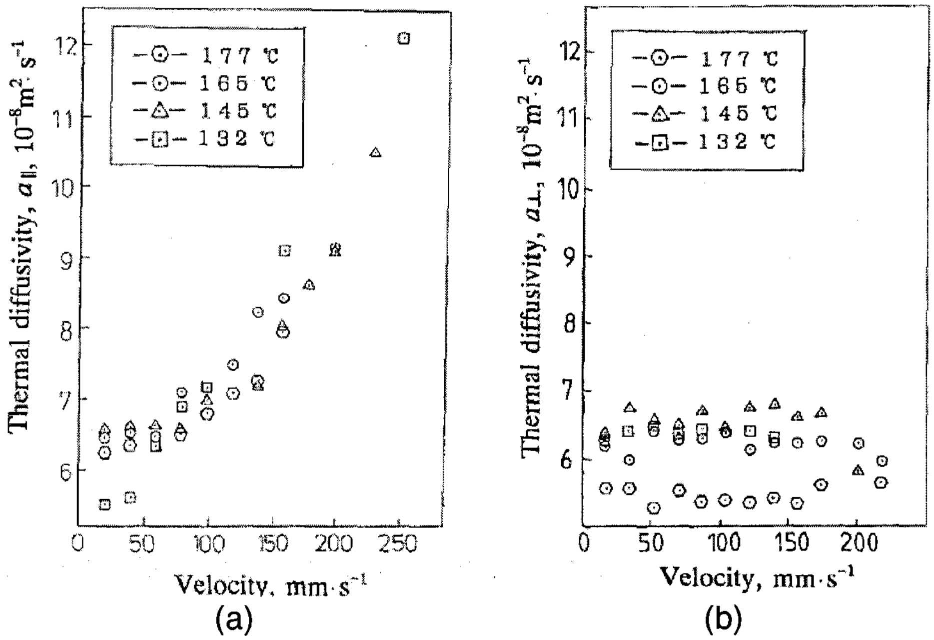

**Figure 7-4.** Measured dependence of the thermal diffusivity of PS (Polystyrene) on the mean velocity at direction (a) parallel to the flow and (b) perpendicular to the flow. *Reprinted from [162], © 1993 with kind permission from Springer Science and Business Media.*

### 7.3.3.1 Physical Model Description

The non-elastic generalized Non-Newtonian governing equations describing the behavior of a fluid motion hold for all common fluids and are used in Moldflow as well. The same continuum based approach was taken in the present study and those equations were used as a starting point for describing the physical model. In these expressions fluid viscosity is given as a function of the shear rate and material parameters. Therefore in the application of finite element schemes to Non-Newtonian flow, shear rate at the elemental level is calculated and used to update the fluid viscosity. As mentioned earlier the flow was considered to be under isothermal conditions. Furthermore, the melt flow was considered to be fully developed in the cavity and incompressible. With such made assumptions, a non-dimensional analysis was implemented which also allowed for further simplification of the non-linear problem. The improved physical description of the model resulted from the consideration of Cross-WLF viscosity model with added Erigen-Okada's term and slip velocity at the walls of the cavities. Detailed description of these procedures follows.

In order to estimate correctly the influence of each term in the momentum and continuity equations an estimate of the order of magnitudes was performed through dimensional analysis. Characteristic values of the relevant variables in the equations are given in Table 7-1.

### *Viscosity definition in 3D Cartesian coordinate system*

In general the motion of a fluid results from translation, deformation, and rotation. In order to characterize such motions it is important to identify the rate at which fluid deforms. The latter is described by the deformation tensor **D** which describes the rate of material change, eqn. 7-2

$$\mathbf{D} = \nabla \mathbf{u} + (\nabla \mathbf{u})^T \tag{7-2}$$

where the velocity vector **u** has components in 3D Cartesian system **u**=**u**(u,v,w) and the gradient of the vector field **u** gives the tensor $\nabla\mathbf{u}$. In 3D Cartesian coordinate system the deformation tensor can be written as:

$$\mathbf{D}=\begin{bmatrix} 2\frac{\partial u}{\partial x} & \left(\frac{\partial v}{\partial x}+\frac{\partial v}{\partial y}\right) & \left(\frac{\partial v}{\partial z}+\frac{\partial v}{\partial x}\right) \\ \left(\frac{\partial v}{\partial y}+\frac{\partial v}{\partial x}\right) & 2\frac{\partial v}{\partial y} & \left(\frac{\partial v}{\partial z}+\frac{\partial w}{\partial y}\right) \\ \left(\frac{\partial w}{\partial x}+\frac{\partial v}{\partial z}\right) & \left(\frac{\partial w}{\partial y}+\frac{\partial v}{\partial z}\right) & 2\frac{\partial w}{\partial z} \end{bmatrix} \qquad (7\text{-}3)$$

For incompressible fluids the shear rate $\dot{\gamma}$ can be defined as the scalar product (:) of the deformation tensor by itself

$$\dot{\gamma}=\sqrt{\frac{1}{2}(\mathbf{D}:\mathbf{D})} \qquad (7\text{-}4)$$

Therefore, adopting Cartesian coordinate system the shear rate in 3D can be defined in the following way:

$$\dot{\gamma}=\left(\frac{1}{2}\left(4\frac{\partial u^2}{\partial x}+4\frac{\partial v^2}{\partial y}+4\frac{\partial w^2}{\partial z}+2\left(\frac{\partial u}{\partial y}+\frac{\partial v}{\partial x}\right)^2+2\left(\frac{\partial v}{\partial z}+\frac{\partial w}{\partial y}\right)^2+2\left(\frac{\partial u}{\partial z}+\frac{\partial w}{\partial x}\right)^2\right)\right)^{1/2} \qquad (7\text{-}5)$$

*Continuum equation definition in 3D Cartesian coordinate system*

The continuum equation for incompressible fluid is described by eqn. 7-6

$$\nabla \bullet \mathbf{u}=0 \qquad (7\text{-}6)$$

or in full form it can also be written as:

$$\underbrace{\frac{\partial u}{\partial x}}_{1}+\underbrace{\frac{\partial v}{\partial y}}_{2}+\underbrace{\frac{\partial w}{\partial z}}_{3}=0 \tag{7-7}$$

*Momentum equation definition in 3D Cartesian coordinate system*

The momentum equation of the full Navier-Stokes equations can written as

$$\rho\frac{\partial \mathbf{u}}{\partial t}-\nabla\bullet[-p\mathbf{I}+\eta(\nabla\mathbf{u}+(\nabla\mathbf{u})^{T})]+\rho\mathbf{u}\bullet\nabla\mathbf{u}=\mathbf{F} \tag{7-8}$$

where $\tau$ is the viscous stress tensor and is given by

$$\tau=\eta(\nabla\mathbf{u}+(\nabla\mathbf{u})^{T}) \tag{7-9}$$

and $\sigma$ is the total stress tensor and $\mathbf{I}$ is the identity matrix

$$\sigma=-p\mathbf{I}+\eta(\nabla\mathbf{u}+(\nabla\mathbf{u})^{T}) \tag{7-10}$$

Note that the total stress tensor formulation of the momentum equation is used in the above formulation. In this case the pressure term is in the divergence operator. The viscosity is always included inside the operator to treat variation of the viscosity during flow. Upon rewriting the vector format of eqn. 7-8 in x, y, z directions it leads to the following three equations:

*x-component of momentum:*

$$\begin{aligned}&\underbrace{\rho\frac{\partial u}{\partial t}}_{i}+\underbrace{\frac{\partial p}{\partial x}}_{ii}-\underbrace{\frac{\partial}{\partial x}\left(2\eta\frac{\partial u}{\partial x}\right)}_{iii}-\underbrace{\frac{\partial}{\partial x}\left(-\eta\left(\frac{\partial u}{\partial y}+\frac{\partial v}{\partial x}\right)\right)}_{iv}-\underbrace{\frac{\partial}{\partial x}\left(-\eta\left(\frac{\partial u}{\partial z}+\frac{\partial w}{\partial x}\right)\right)}_{v}\\&+\underbrace{\rho\left(u\frac{\partial u}{\partial x}+v\frac{\partial u}{\partial y}+w\frac{\partial u}{\partial z}\right)}_{vi}=\underbrace{F_x}_{vii}\end{aligned} \tag{7-11}$$

*y-component of momentum:*

$$\begin{aligned}&\underbrace{\rho\frac{\partial v}{\partial t}}_{i}+\underbrace{\frac{\partial p}{\partial y}}_{ii}\underbrace{-\frac{\partial}{\partial y}\left(2\eta\frac{\partial v}{\partial y}\right)}_{iii}\underbrace{-\frac{\partial}{\partial y}\left(-\eta\left(\frac{\partial v}{\partial x}+\frac{\partial u}{\partial y}\right)\right)}_{iv}\underbrace{-\frac{\partial}{\partial y}\left(-\eta\left(\frac{\partial v}{\partial z}+\frac{\partial w}{\partial y}\right)\right)}_{v}\\&\underbrace{+\rho\left(u\frac{\partial v}{\partial x}+v\frac{\partial v}{\partial y}+w\frac{\partial v}{\partial z}\right)}_{vi}=\underbrace{F_y}_{vii}\end{aligned}\tag{7-12}$$

*z-component of momentum:*

$$\begin{aligned}&\underbrace{\rho\frac{\partial w}{\partial t}}_{i}+\underbrace{\frac{\partial p}{\partial z}}_{ii}\underbrace{-\frac{\partial}{\partial z}\left(2\eta\frac{\partial w}{\partial z}\right)}_{iii}\underbrace{-\frac{\partial}{\partial z}\left(-\eta\left(\frac{\partial w}{\partial x}+\frac{\partial u}{\partial z}\right)\right)}_{iv}\underbrace{-\frac{\partial}{\partial z}\left(-\eta\left(\frac{\partial w}{\partial y}+\frac{\partial v}{\partial z}\right)\right)}_{v}\\&\underbrace{+\rho\left(u\frac{\partial w}{\partial x}+v\frac{\partial w}{\partial y}+w\frac{\partial w}{\partial z}\right)}_{vi}=\underbrace{F_z}_{vii}\end{aligned}\tag{7-13}$$

where the terms (i) to (vii) denote (i) – the rate of change of momentum in x, y, z directions, (ii) – the pressure gradient term in x, y, z directions, (iii, iv, v) represent the viscous terms in x, y, z directions, (vi) represent the inertia forces in x, y, z directions, and (vii) represents forces due to gravity in x, y, z directions.

*Dimensional analysis*

By employing dimensional analysis, estimate of the order of magnitude of each term in the governing equations was performed. Since terms of lower order of magnitude have little influence and they are ignored from the equations. Important step to this analysis is the correct adoption of characteristic values which are considered to be relevant for polymer flow in micro-channels. Upon,

| Variables | Notation | Characteristic value |
|---|---|---|
| cavity thickness | $H$ | $10^{-3}$ m |
| cavity length/width | $L$ | $10^{-3}$ m |
| velocity of melt | $V$ | $10^{0}$ m/s |
| cavity pressure | $p_0$ | $10^{7}$ kg/m$^3$ |
| viscosity of melt | $\eta_0$ | $10^{4}$ Ns/m$^2$ |
| density of melt | $\rho_0$ | $10^{3}$ kg/m$^3$ |
| temp. difference between mold and melt | $T_0$ | 10 K |
| acceleration due to gravity | $g_0$ | 10 m/s$^2$ |

**Table7-1.** Characteristic values used in the dimensional analysis performed to estimate the significance (order of magnitude) of the terms in the relevant equations.

using the typical characteristic values, as seen in Table 7-1 the relevant variables in the equations can be defined in terms of dimensionless variables as follow:

x-coordinate: $x = Lx^* = Hx^*$, y-coordinate: $y = Ly^* = Hy^*$, z-coordinate: $z = Hz^*$

time $t = \left[\frac{L}{V}\right]t^* = \left[\frac{H}{V}\right]t^* \Leftrightarrow O\left[\frac{10^{-5}}{10^{0}}\right] = O\left[10^{-5}\right]$.

x-component of velocity: $u = \left[\frac{L}{t}\right]u^* = \left[\frac{H}{t}\right]u^*$.

y-component of velocity: $v = \left[\frac{L}{t}\right]v^* = \left[\frac{H}{t}\right]v^*$

z-component of velocity: $w = \left[\frac{H}{t}\right]w^*$

pressure: $p = p_0 p^*$, viscosity: $\eta = \eta_0 \eta^*$, and density: $\rho = \rho_0 \rho^*$, where the starred quantities are dimensionless and of order 1. Therefore it is sufficient to estimate the order of magnitude of the quantities in the square brackets [·]. Upon implementation of the procedure it can be written:

- *for the continuity equation*

$$(1)\,O\left[\frac{\partial u}{\partial x}\right]=O\left[\frac{10^{0}}{10^{-5}}\right]=\underline{O\left[10^{5}\right]}. \tag{7-14}$$

$$(2)\,O\left[\frac{\partial v}{\partial y}\right]=O\left[\frac{10^{0}}{10^{-5}}\right]=\underline{O\left[10^{5}\right]}. \tag{7-15}$$

$$(3)\,O\left[\frac{\partial w}{\partial z}\right]=O\left[\frac{10^{0}}{10^{-5}}\right]=\underline{O\left[10^{5}\right]}. \tag{7-16}$$

- *for the momentum equation in x-direction*

$$\text{(i)}\ O\left[\rho\frac{\partial u}{\partial t}\right]=O\left[10^{3}\frac{10^{0}}{10^{-5}}\right]=\underline{\xcancel{O\left[10^{8}\right]}}. \tag{7-17}$$

$$\text{(ii)}\ O\left[\frac{\partial p}{\partial x}\right]=O\left[\frac{p_0}{H}\right]=O\left[\frac{10^{7}}{10^{-5}}\right]=\underline{O\left[10^{12}\right]}. \tag{7-18}$$

$$\text{(ii)}\ O\left[\frac{\partial}{\partial x}\left(2\eta\frac{\partial u}{\partial x}\right)\right]=O\left[\frac{1}{H}\left(\eta_0\frac{H}{tH}\right)\right]=O\left[\frac{1}{10^{-5}}\left(10^{4}\frac{1}{10^{-5}}\right)\right]=\underline{O\left[10^{14}\right]}. \tag{7-19}$$

$$\text{(iv)}\ O\left[\frac{\partial}{\partial x}\left(-\eta\left(\frac{\partial u}{\partial y}+\frac{\partial v}{\partial x}\right)\right)\right]=O\left[\frac{1}{H}\left(\eta_0\left(\frac{H}{tH}+\frac{H}{tH}\right)\right)\right]=O\left[\frac{1}{10^{-5}}\left(10^{4}\left(\frac{1}{10^{-5}}+\frac{1}{10^{-5}}\right)\right)\right]$$
$$=\underline{O\left[10^{14}\right]}. \tag{7-20}$$

$$\text{(v)}\ O\left[\frac{\partial}{\partial x}\left(-\eta\left(\frac{\partial u}{\partial z}+\frac{\partial w}{\partial x}\right)\right)\right]=O\left[\frac{1}{H}\left(\eta_0\left(\frac{H}{tH}+\frac{H}{tH}\right)\right)\right]=O\left[\frac{1}{10^{-5}}\left(10^{4}\left(\frac{1}{10^{-5}}+\frac{1}{10^{-5}}\right)\right)\right]$$
$$=\underline{O\left[10^{14}\right]}. \tag{7-21}$$

$$\text{(vi)}\ O\left[\rho\left(u\frac{\partial u}{\partial x}+v\frac{\partial u}{\partial y}+w\frac{\partial u}{\partial z}\right)\right]=O\left[10^{3}\left(10^{0}\frac{10^{0}}{10^{-5}}+10^{0}\frac{10^{0}}{10^{-5}}+10^{0}\frac{10^{0}}{10^{-5}}\right)\right]$$

$$= \xcancel{O\left[10^{8}\right]}. \tag{7-22}$$

$$\text{(vii)}\; O[F_z] = O[\rho_0 g_0] = O\left[10^{3}10^{1}\right] = \xcancel{O\left[10^{4}\right]}. \tag{7-23}$$

Consequently, as evident from the order of magnitude all terms are kept in the continuum equation but the rate of change of momentum, the inertia forces and forces due to gravity terms in the momentum equation in x-direction are neglected. Note that the same results are valid for the equations in y- and z-directions and therefore they are not given for brevity.

*Viscosity model at micro-scale*

The macroscopic viscosity $\eta = \eta_{bulk}$ was modeled with the widely accepted seven-constant Cross-WLF model:

$$\eta_{bulk} = \frac{\eta_1}{\left(1 + \dfrac{\eta_1 \dot{\gamma}}{\tau^{*}}\right)^{1-n}} \tag{7-24}$$

$$\eta_1 = D_1 \exp\left( - \frac{A_1(T - (D_2 + D_3 p))}{\tilde{A}_2 + D_3 p + (T - (D_2 + D_3 p))} \right) \tag{7-25}$$

where the seven constants obtained from Moldflow database are given in Table 7-2. To model the viscosity in micro-scale, Figure 7-5, the above expression was corrected using the micro-scale size factor $\phi(z)$, based on the Erigen-Okada equation [29, 42]

$$\eta_{micro} = \phi(z)\eta_{bulk} = \left(1 + \xi \frac{R_g^{\ 2}}{z^2}\right)\eta_{bulk} \tag{7-26}$$

where $\xi$ is a non-dimensional constant, $R_g$ is the radius of gyration defined as the root-mean-square radius of an unperturbed random recoil of polymeric molecule, and $z$ is an external characteristic length chosen to be the depth (h) of the channels.

| Coefficients | Value | Dimension |
|---|---|---|
| n | 0.2763 | - |
| $\tau^*$ | 42894.9 | Pa |
| $D_1$ | $1.98688*10^{17}$ | Pa.s |
| $D_2$ | 263.15 | K |
| $D_3$ | 0 | K/Pa |
| $A_1$ | 40.614 | - |
| $A_2$ | 51.6 | K |

**Table 7-2.** Values of the seven constants from the Cross-WFL viscosity model which fit the viscosity data of the polypropylene polymer used as a prototype material in the simulations.

Note that there is a strong dependence between the radius of gyration $R_g$ and the magnitude of micro-scale viscosity as a function of the distance from the wall. It is expected that polymers with high molecular weight would have larger $R_g$ thus such polymers would exhibit increased viscosity close to the wall. Furthermore, this effect would be even more pronounced at larger distance from the wall. Such an increase of the viscosity near the wall can be explained with diffusional "jumps" of adsorbed molecules from the wall towards the center of the cavity which exchange momentum with moving molecules, thus slowing them down leading to an increase of the viscosity in the region [47].

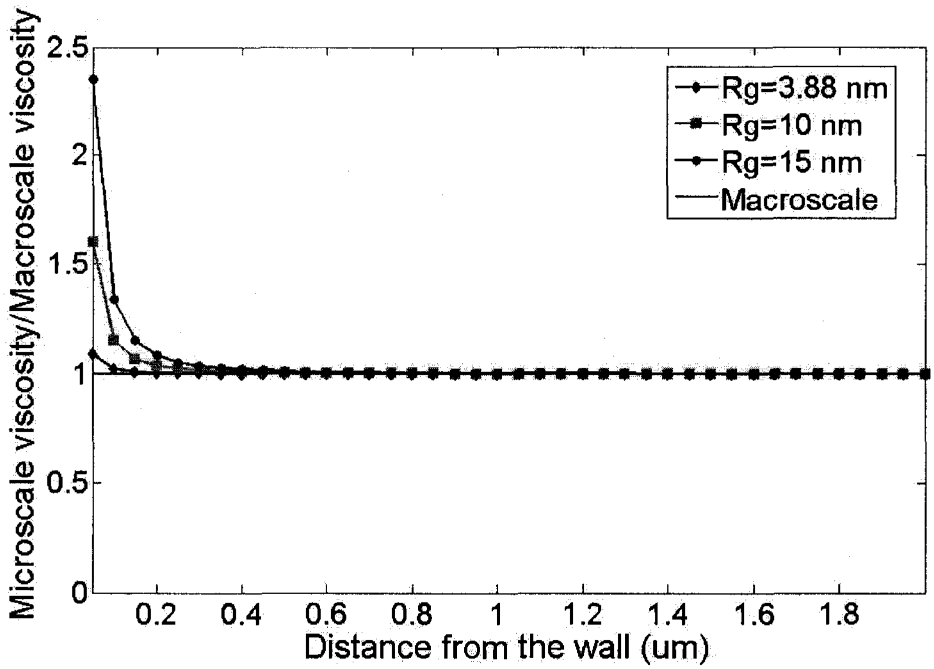

**Figure 7-5.** Micro-scale viscosity predicted by the Erigen-Okada equation for depth of a channel, z=30 μm.

*Slip velocity*

The local slip velocity $U_{slip}$ was modeled by using the modified power-law expression proposed by Hatzikiriakos and Dealy [43, 44], which can be written as follow:

$$U_{slip} = \frac{\zeta_0 f_1(T)}{1+\left(\frac{\sigma_{cr}}{\sigma_w}\right)^{10}} \left(1 - c_1 \tanh\left(\frac{E + c_2 \frac{\sigma_n}{\sigma_w}}{RT}\right)\right)\left(\frac{\sigma_w}{\sigma_{cr} l^{1/4}}\right)^m \qquad (7\text{-}27)$$

where $\zeta_0$, $c_1$, $c_2$, and $m$ are coefficients. $f_1(T)$ is a function of temperature and $C_1$ and $C_2$ are constants used. All coefficient and constants are given in Table 7-3.

$$f_1(T) = \frac{C_1 (T - T_0)}{C_2 + (T - T_0)} \qquad (7\text{-}28)$$

*E* is the activation energy for adsorption/desorption of the polymer chains to/from the mold walls, $\sigma_w$ is the local shear stress, $\sigma_n$ is the local normal stress at the wall which can be approximated by the following:

$$\sigma_n = p + \frac{50}{12}\sigma_w \tag{7-29}$$

$\sigma_c$ is the critical shear stress for the onset of slip at the wall; and *I* is the polymer polydispersity given as the ratio between the weight average molecular weight and number average molecular weight ($I=M_w/M_n$).

It is important to be noted the $U_{slip}$ depends both on the melt temperature and cavity pressure.

| Coefficients | Value | Dimension |
|---|---|---|
| $\zeta_0$ | $0.8219*10^{-2}$ | m/s |
| $C_1$ | 1.159 | - |
| $C_2$ | 109.43 | K |
| $c_1$ | 0.968 | - |
| $c_2$ | 7.19 | cal/mol |
| E | 1422.6 | cal/mol |
| $\sigma_c$ | $0.911*10^5$ | Pa |
| m | 4.897 | - |
| I | 1.2 | - |
| R | 1.987 | cal/(K.mol) |

**Table 7-3.** Values of the coefficients used in the slip velocity formula for the prototype material in the simulations [44].

### 7.3.3.2 FEM Simulation Utilizing COMSOL

In this study the influence of the modified shear rate dependent viscosity and wall slip on the flow of polypropylene melt was studied by implementing

COMSOL FEM libraries. COMSOL is regarded as a modern FEM based package which can interpret user equation-based input and treat an arbitrary system of equations for virtually any possible multiphysics application. It also has the capability of accepting user-defined variables, constants, and coupling variables. It also allows for user input in description of the model accounting for the real system, e.g. equations and boundary conditions. Furthermore, COMSOL has very comprehensive library of FEM direct and iterative state-of-the-arts robust solvers and advanced pre- and post-processing capabilities. Therefore, an attempt was made to utilize COMSOL in finding a numerical solution of the prior discussed physical model.

The COMSOL's Non-Newtonian flow application mode was used that handles viscosity variation due to the polymer's shear rate. A built-in expression variable for the shear rate *sr_chnn* was made use of to define the arbitrary expression of the viscosity in accordance with eqn 7-26. In addition, another variable name, describing the velocity at the wall (slip boundary conditions) was introduced in accordance with eqn. 7-27. A number of domain constants and coefficients, e.g. valid throughout the whole geometry, listed in Table 7-2 and Table 7- 3 were also introduced. Care was taken while naming the expression variables, constants and coefficients so that their names were not identical with such already used ("hard-wired") in COMSOL's FEM libraries.

The total stress tensor formulation of eqn. 7-8 in the PDE general form in COMSOL notation is given by eqn. 7-30 and is written in the form given below:

$$d_a \frac{\partial \mathbf{u}}{\partial t} + \nabla \cdot \mathbf{\Gamma} = \mathbf{F} \qquad (7\text{-}30)$$

where $\mathbf{u}=\mathbf{u}(u,v,w)$ is again the velocity vector and the term $d_a$ is the damping coefficient given in 3D as follow

$$d_a=\begin{bmatrix}\rho & 0 & 0 & 0\\ 0 & \rho & 0 & 0\\ 0 & 0 & \rho & 0\\ 0 & 0 & 0 & 0\end{bmatrix} \tag{7-31}$$

the term $\mathbf{\Gamma}$ is the conservative flux source term given in 3D Cartesian coordinate system as follow:

$$\mathbf{\Gamma}=\begin{bmatrix} p-2\eta\frac{\partial u}{\partial x} & -\eta\left(\frac{\partial u}{\partial y}+\frac{\partial v}{\partial x}\right) & -\eta\left(\frac{\partial u}{\partial z}+\frac{\partial w}{\partial x}\right)\\ -\eta\left(\frac{\partial v}{\partial x}+\frac{\partial u}{\partial y}\right) & p-2\eta\frac{\partial v}{\partial y} & -\eta\left(\frac{\partial v}{\partial z}+\frac{\partial w}{\partial y}\right)\\ -\eta\left(\frac{\partial w}{\partial x}+\frac{\partial u}{\partial z}\right) & -\eta\left(\frac{\partial w}{\partial y}+\frac{\partial v}{\partial z}\right) & p-2\eta\frac{\partial w}{\partial z}\\ 0 & 0 & 0\end{bmatrix} \tag{7-32}$$

the term $\mathbf{F}$ is the source term

$$\mathbf{F}=\begin{bmatrix} F_x-\rho\left(u\frac{\partial u}{\partial x}+v\frac{\partial u}{\partial y}+w\frac{\partial u}{\partial z}\right)\\ F_y-\rho\left(u\frac{\partial v}{\partial x}+v\frac{\partial v}{\partial y}+w\frac{\partial v}{\partial z}\right)\\ F_z-\rho\left(u\frac{\partial w}{\partial x}+v\frac{\partial w}{\partial y}+w\frac{\partial w}{\partial z}\right)\\ -\left(\frac{\partial u}{\partial x}+\frac{\partial v}{\partial y}+\frac{\partial w}{\partial z}\right)\end{bmatrix} \tag{7-33}$$

Upon taking into consideration the results from the dimensional analysis presented earlier in details, the source term $\mathbf{F}$ was written as:

$$\mathbf{F} = \begin{bmatrix} 0 \\ 0 \\ 0 \\ -\left(\dfrac{\partial u}{\partial x} + \dfrac{\partial v}{\partial y} + \dfrac{\partial w}{\partial z}\right) \end{bmatrix} \tag{7-34}$$

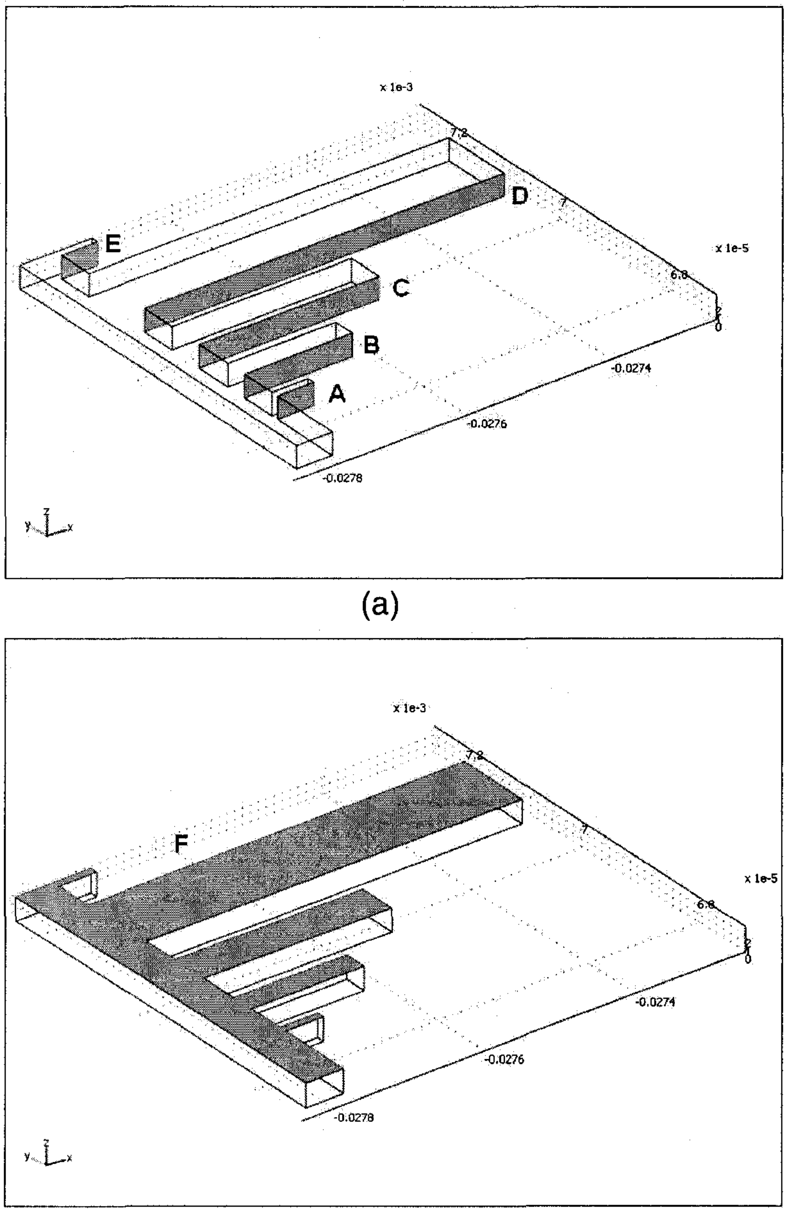

(a)

(b)

**Figure 7-6.** COMSOL 3D geometry. A to F denotes 2D domain boundaries (shaded regions) for which the velocity slip fields were later calculated.

Two cases were simulated with COMSOL to investigate the polymer melt flow behavior in micro-channels:

(A) Flow with micro-scale viscosity and no slip at the wall (boundaries).

(B) Flow with micro-scale viscosity and slip at the wall (boundaries).

As previously discussed isothermal flow was considered. This assumption was implemented by setting the temperature at the walls and melt temperature to have equal values. For case (A) - three melt temperatures were considered, e.g. $T_{melt}$= 180, 200, and 221 $^{0}$C. Variations of the injection pressure at the injection location were also considered. For each $T_{melt}$ value three pressures were considered, $P_{inj}$ =10, 20, and 30 MPa giving a total of nine simulation. For case (B) – only on temperature was considered, e.g. $T_{melt}$ =200 $^{0}$C since the variation of the local shear stress, $\sigma_w$ as a function of the shear rate $\dot{\gamma}$ was only available for this value of the melt temperature [44]. For both types of simulations the 3D geometry was meshed with ~16000 tetrahedrals which resulted in ~78000 degrees of freedom. To find a solution of the problem a direct UMFPACK solver was utilized. This solver uses the unsymmetric-pattern multifrontal method and direct LU factorization of the sparse matrix. It employs COLAMD and AMD approximate minimum degree preordering algorithms to permute the columns so that the fill-in is minimized [163, 164]. For larger systems, though the use of iterative multigrid solver with Vanka algorithm used as preconditioner/smoother combined with Galerkin Least-Squares type of streamline diffusion is recommended. COMSOL allows for very fine tuning of any solver parameters but such discussion is beyond the scope of this work. More information on this can be found in COMSOL's comprehensive help files.

### 7.4 Results

Upon constructing the physical model in COMSOL's notation, simulations were run with first with (A), and then with (B) type of conditions and the result were compared. In order to better evaluate the results obtained from each simulation, subdomain integration of several quantities were found and their values plotted. The shear rate, the dynamic viscosity (viscosity) for the 3D domain and the velocity field's distributions in the entire 3D domain and chosen 2D domains (boundaries), as seen in Figure 7-6 were found. This approach was taken since it describes better the distribution of physical quantities in the entire domain of interest and was the preferred one rather than that of reporting only the minimal and maximal value of the quantity of interest.

Upon running simulations with both types of conditions results were analyzed and the following conclusions were made. As seen in Figure 7-7 and Figure 7-8 during no slip conditions the shear rate and the velocity field in the entire 3D domain increase with the injection pressure. Similar dependence was found during imposed slip at the boundaries. The slip condition though influences the velocity field distribution in the 3D domain, Figure 7-9. This influence leads to an increase of the velocity field by a factor of 2 in the case of $T_{melt} = 200^0C$ and $P_{inj} = 30$ MPa which subsequently would increase the flow rate.

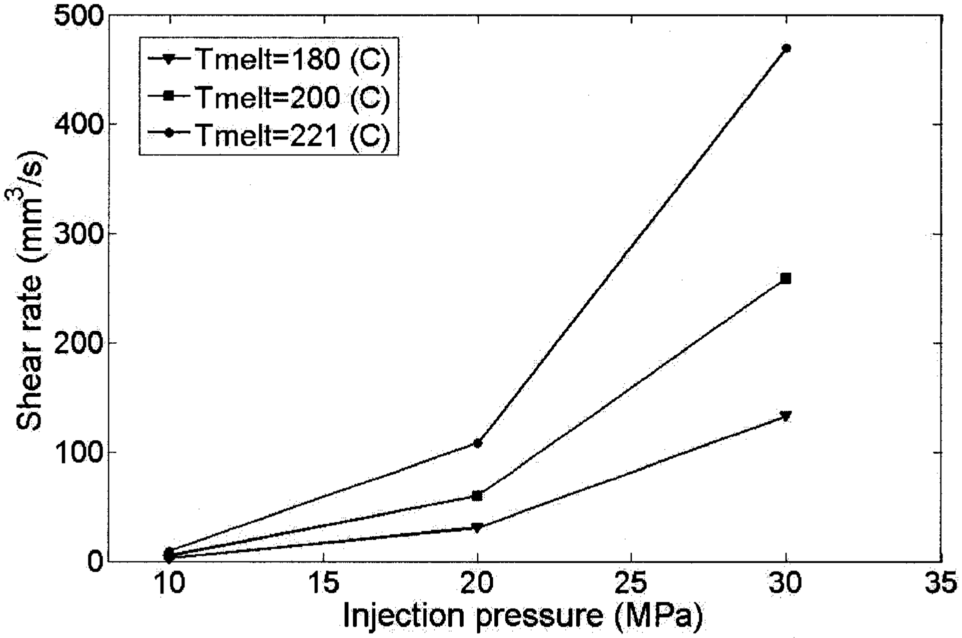

**Figure 7-7.** Calculated shear rate as a function of the injection pressure for $T_{melt}$ =180, 200, and 221 $^0$C. No slip at the boundaries. Note that the values of the shear rate were found upon integration over the entire 3D domain.

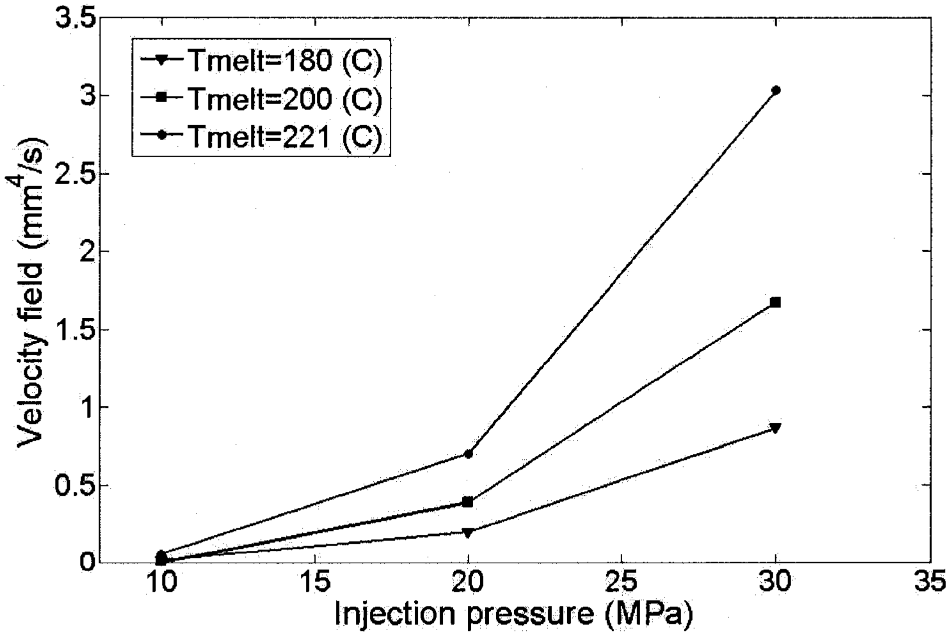

**Figure 7-8.** Calculated velocity filed as a function of the injection pressure for $T_{melt}$ =180, 200, and 221 $^0$C. No slip at the boundaries. Note that the values of the velocity filed were found upon integration over the entire 3D domain.

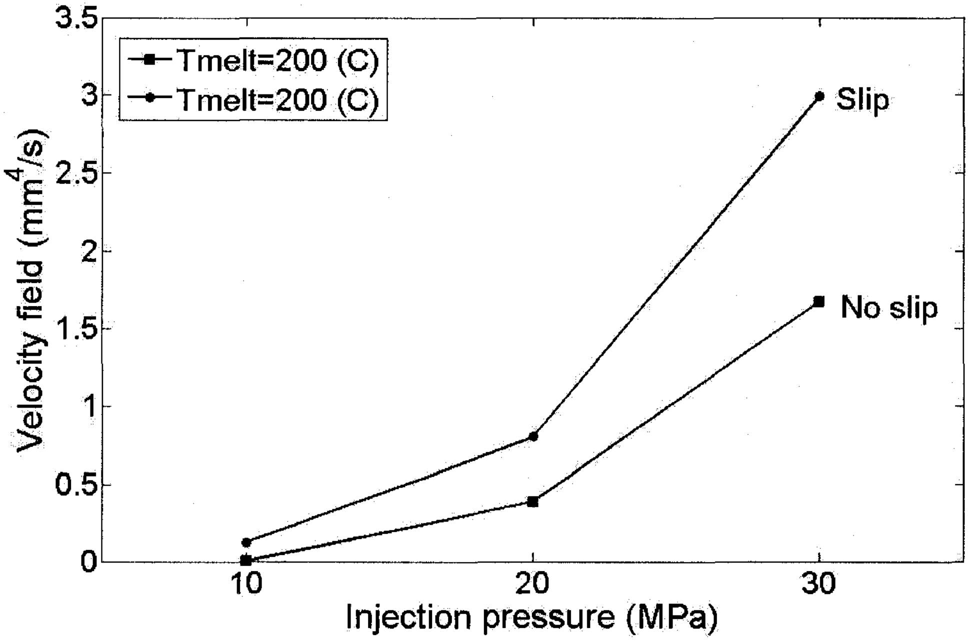

**Figure 7-9.** Calculated velocity field as a function of the injection pressure for $T_{melt}$ =200 $^0$C and no slip and slip at the boundaries. Note that the values of the velocity filed were found upon integration over the entire 3D domain.

Moreover an increase of the melt temperature during no slip conditions has the same effect. Since the slip condition describes better the polymer flow in micro-channels the conclusion which can be made in this case is that due to the slip $T_{melt}$ can be kept at lower values which would ensure the required flow for cavity filling but it should be higher than the temperature required for active desorption of polymer molecules.

As seen in Figure 7-10, the dynamic viscosity decreases with an increase of the melt temperature which is also influenced by higher injection pressure values. During slip at the boundaries the velocity in the channels increases with an increase of the wall shear stress, as seen in Figure 7-11. The wall shear stress depends on the material, the shear rate and the melt temperature.

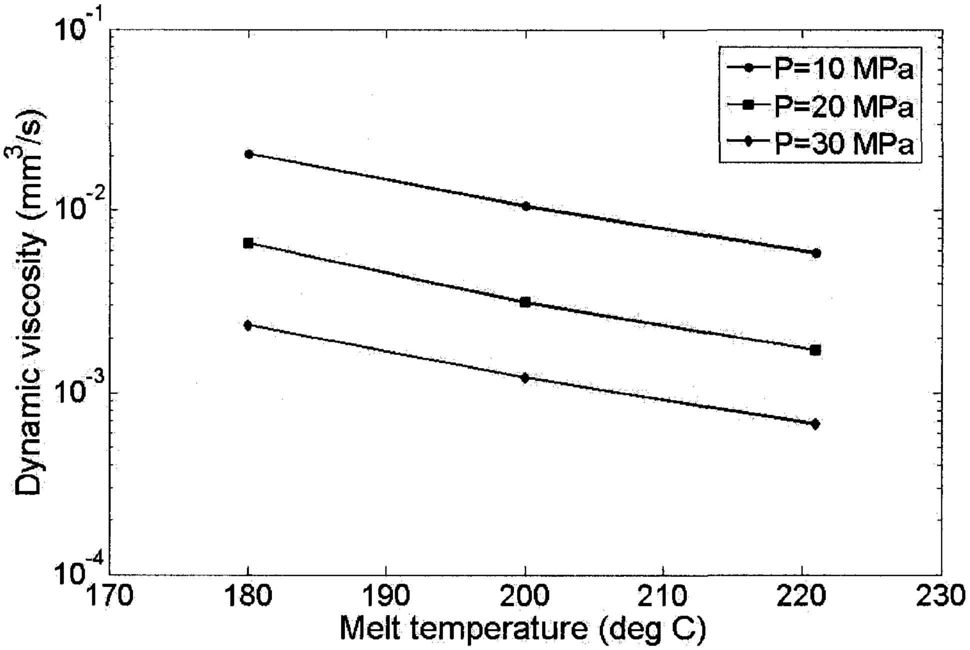

**Figure 7-10.** Calculated dynamic viscosity as a function of the melt temperature for $P_{inj}$ =10, 20, and 30 $^0$C. No slip at the boundaries. Note that the values of the velocity filed were found upon integration over the entire 3D domain.

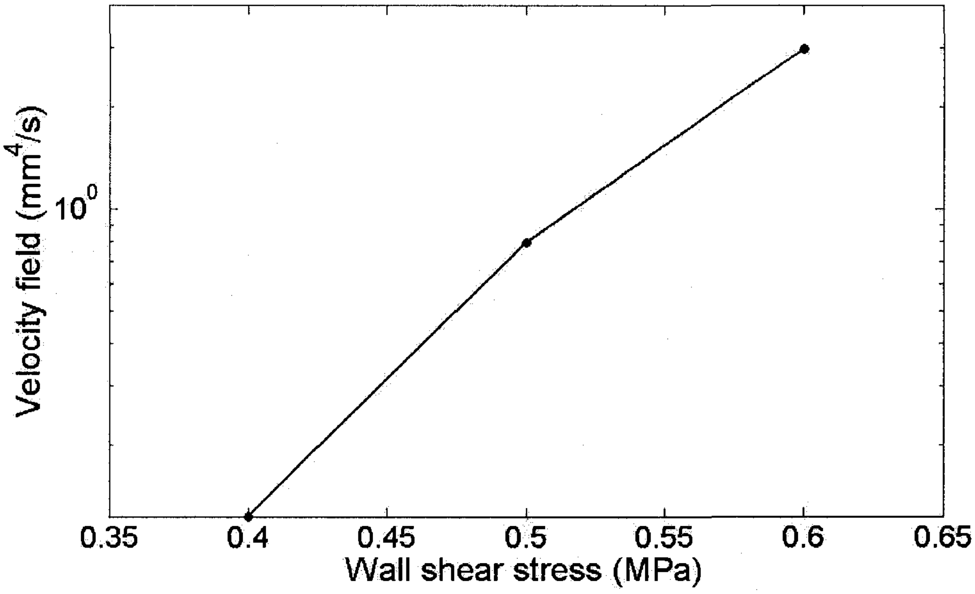

**Figure 7-11.** Calculated velocity field as a function of the wall shear stress for $T_{melt}$ =200 $^0$C. Slip at the boundaries. Note that the values of the velocity field were found upon integration over the entire 3D domain.

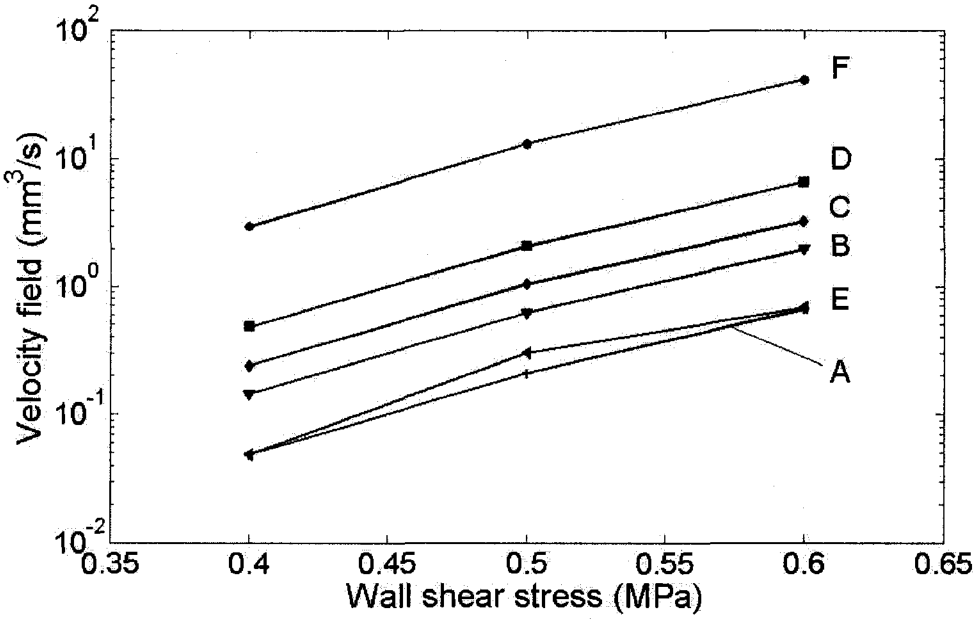

**Figure 7-12.** Calculated boundary velocity field as a function of the wall shear stress for $T_{melt}$ =200 $^0$C. Slip at the boundaries. Note that the values of the velocity filed were found upon integration over the entire 2D domains (boundaries) designated as A, B, C, D, E, and F as seen on Figure 7-6.

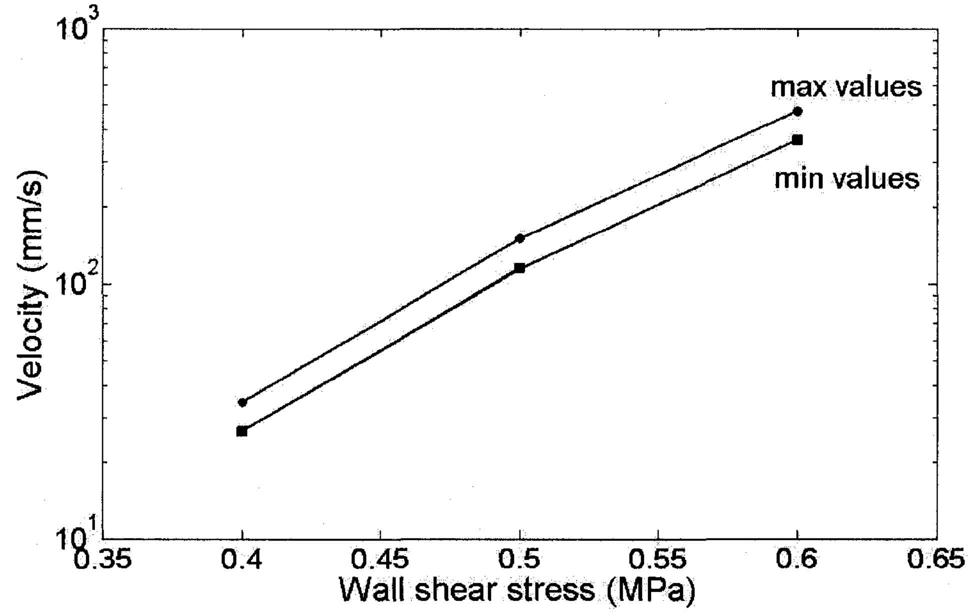

**Figure 7-13.** Calculated min/max boundary velocity as a function of the wall shear stress for $T_{melt}$ =200 $^0$C. Slip at the boundaries. Note that the values of the velocity were found upon comparison of the min/max values in the entire 2D domains (boundaries) designated as A, B, C, D, E, and F as seen on Figure 7-6.

It is important to be noted that when the critical shear stress required for an onset of a slip is higher than the local shear stress no slip occurs at the boundaries.. As seen in Figure 7-12, the velocity field distribution along the boundaries is also dependent on the value of the wall shear stress and increases with an increase of the wall stress. The values of these velocities, Figure 7-13 were found to be in the range of previously experimentally found slip velocities at micro-scale [33].

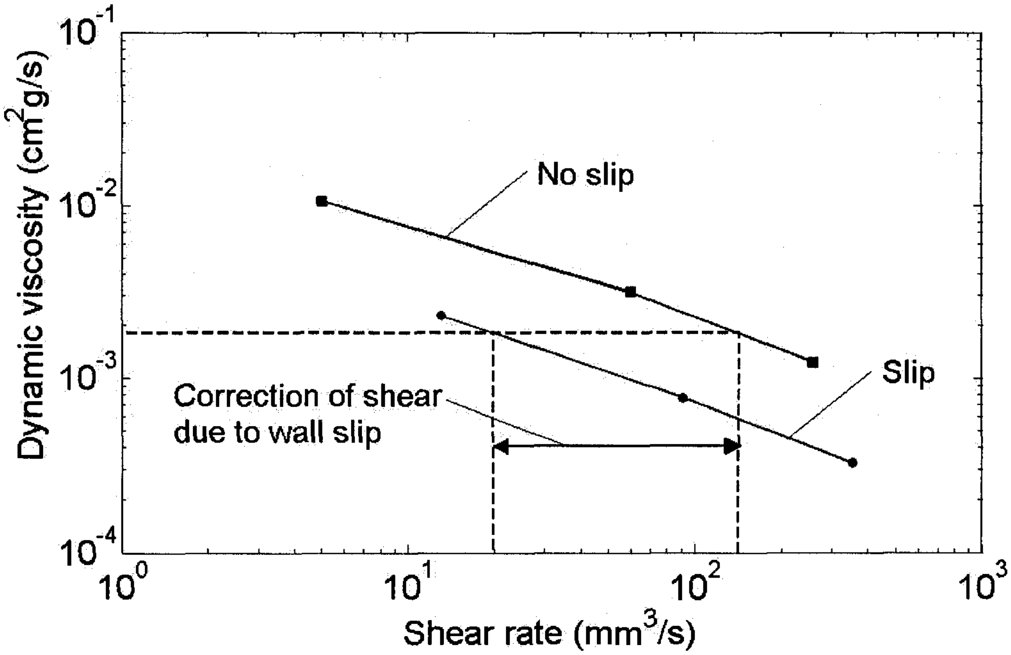

**Figure 7-14.** Calculated dynamic viscosity as a function of the shear rate for $T_{melt}$ =200 $^0$C and no slip and slip at the boundaries. Note that the values were found upon integration over the entire 3D domain.

Finally as seen in Figure 7-14, the slip condition leads to a decrease in the shear rate in the entire 3D domain. In other words there must be a correction in the shear rate which takes in account such dependence. Interestingly, experimental results [32, 33] have shown similar behavior during measurements of the viscosity as a function of the shear rate in small channels as compared with such obtained

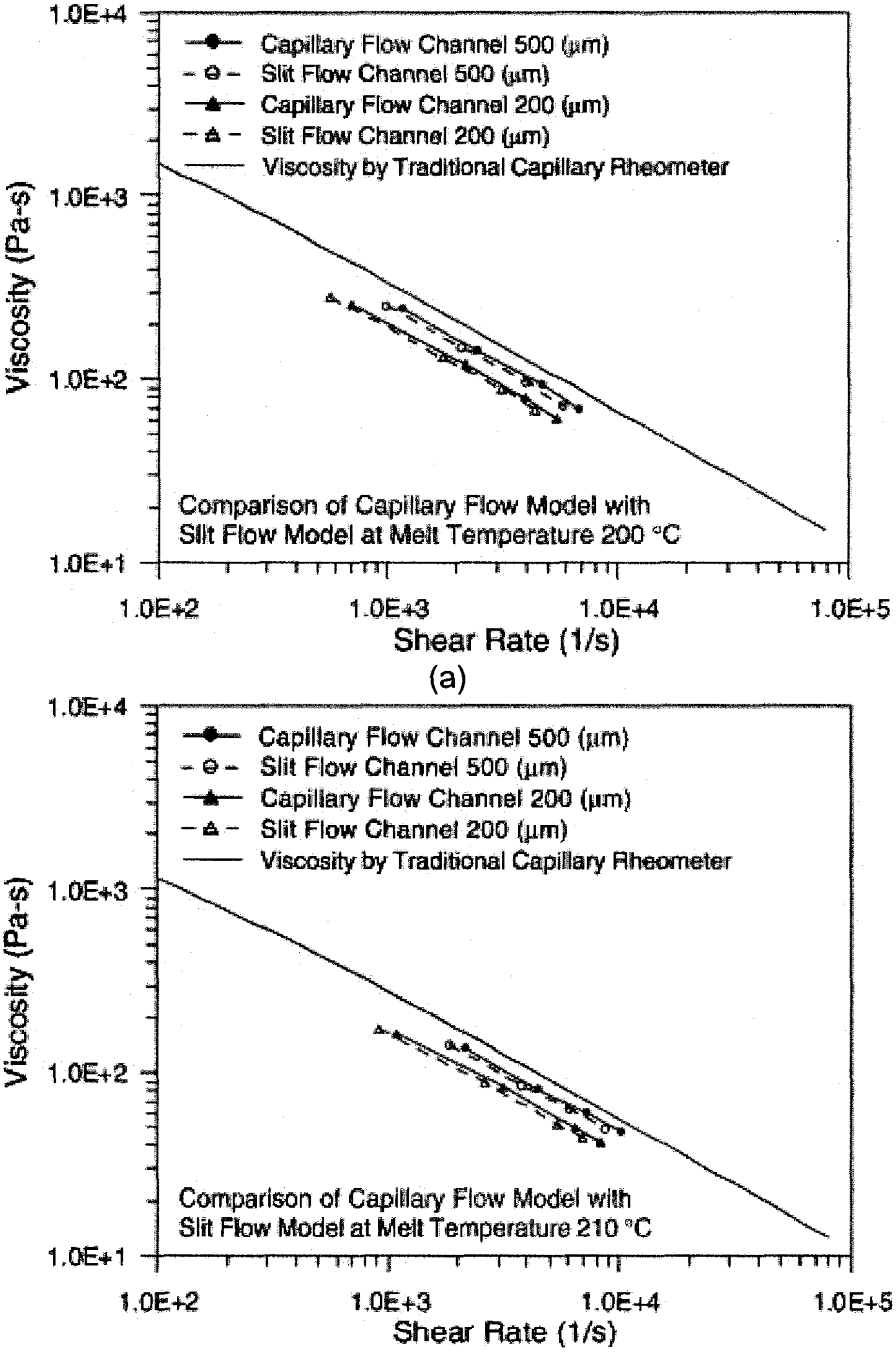

(a)

(b)

**Figure 7-15**. Comparison of melt viscosities measured at micro-scale analyzed from slit and capillary flow models for ABS (Acrylonitrile-Butadiene-Styrene-Copolymer, PA-756, CHI MEI Corporation) resin at (a) melt temperature 200 $^{0}$C, and (b) melt temperature 210 $^{0}$C. *Reprinted from [32], © 2005 with permission from Elsevier.*

by a traditional capillary rheometer as seen in Figure 7-15. The no slip condition viscosity dependence from the shear rate can be considered to be the same as that measured by the traditional rheometer. Thus the implemented model in the present numerical study was considered to represent well the expected flow behavior in micro-channels.

Results from Moldflow simulations of the isothermal flow lead to unreasonably small maximum values of the shear rate in the order ~ 20 Pa.s for all considered melt temperatures, e.g. $T_{melt}$ =180, 200, and 221 $^0$C with very high viscosity values as well. It was concluded that this is a result from the incorporation of viscous heating, inappropriate values of the thermal conductivity used in the energy equation that is coupled with the momentum equations. Predicted velocity values were also below the reasonable ones. Clearly, the output results were not logical. Simulations with mold temperatures having lower values than the temperature of the melt resulted in expected flow behavior but were not considered in this analysis since it was assumed that even though the results seemed logical they did not represent the polymer melt behavior during real flow conditions in micro-channels.

### 7.5 Summary

Three dimensional continuum based numerical analysis based on FE was implemented to investigate the polymer flow in micro-channels. An improved physical model suitable for polymer flow in micro-channels was used by incorporating Erigen-Okada's term in the expression of the shear dependent viscosity given by Cross-WLF model for polypropylene resin as well as by incorporating of wall slip conditions at the boundaries. Simulations shown that the wall slip, dependent on the melt temperature and injection pressure, has a profound effect on the shear rates of the melt in the micro-channels. This effect leads to lowering of the shear rate during slip conditions as compared with no slip conditions for the same melt viscosity. The obtained results were in good agreement with experimentally obtained ones. Simulations have also shown that the velocity filed distribution during slip is higher than that with no slip conditions. Finally, these results were compared with the output results from Moldflow simulations. The latter have shown to be very unreasonable due to the inappropriate physical model implemented in Moldflow solver. In conclusion, it is also considered that the present study can serve as a foundation for implementing COMSOL as an indispensable tool for simulating the entire molding cycle in micro-channels.

# CHAPTER 8

# CONCLUSIONS AND FUTURE RECOMMENDATIONS

*"I haven't failed, I've found 10,000 ways that don't work" - Thomas Edison*

## 8.1 Research Summary

During the present comprehensive research investigation, it was revealed that the ability to control matter deliberately and create structures by design at the nano- and micro-scale by means of injection micro-molding is a very demanding non-trivial multi-step manufacturing process requiring great levels of expertise. Throughout carefully crafted experiments it was shown that e-beam lithography and reactive ion plasma etching can be successfully utilized for the manufacture of structured silicon molds suitable for polymer replication via injection molding. It was clearly shown that the quality of the Si molds is one of the most important factors which influence the fidelity of replication at micro- and nano-scale.

It was revealed that the inductively coupled reactor of a DRIE plasma tool can be successfully utilized for plasma deposition of $C_4F_8$ film that exhibits low surface energy and excellent anti-adhesive properties. As a result, polymer nano-features with different shapes and sizes, as small as 25 nm, were successfully replicated from Cyclo Olefin Copolymer, as well as high aspect ratio submicron-sized pillars. It is believed that after optimization of the fluorocarbon deposition conditions excellent quality molds could be manufactured and subsequently used for large scale mass production of low-cost patterned polymer substrates. A new phenomena describing ground collapse of successfully replicated high aspect ratio pillars due to molecular orientation induced charge separation between the high aspect structures and the ground surface of the polymeric substrate was found. Sub-micron and nano-patterned surfaces were successfully used as substrates for the manufacture of passive optical components and such that can be used as platforms for surface plasmon-polariton generation.

In addition, static parametric stress-strain structural finite element analysis revealed that molds made out of Si can keep their structural integrity at the range of pressures and mold temperatures commonly used during polymer injection micro-molding. High principle stresses with values above $\sigma_{yield}$ were found to arise only at very high pressures which are unlikely to be used in injection micro-molding applications. Therefore, brittle failure of the Si molds with the considered geometry is not expected to occur during injection micro-molding. It was also shown that the mold temperature is the most important factor leading to total in-plane displacements in the order of several hundred nanometers which can be restrictive factor in keeping critical dimensions (CD) within limits if no mold temperature control is utilized.

Finally, non-elastic generalized Non-Newtonian governing equations describing the behavior of a polymer melt flow under isothermal conditions were considered to simulate the flow in micro-sized cavities. In this continuum based finite element scheme approach the expression for the melt viscosity was given with Cross-WLF model incorporating Eringen-Okada's term valid for micro-flows. In addition, the flow was considered in the presence of a wall slip. By means of dimensional analysis the momentum equations were simplified by removing the inertia and body forces which were considered to have negligible influence on the flow. The results were in good agreement with previously reported and obtained through experiments ones. It was shown that the slip velocity introduces a shift in the viscosity vs. shear rate dependence which must be taken into account during flow simulations.

## 8.2 Recommended Future Work

As earlier expressed in Chapter 1, the overall objective of the present study was to develop scientific understanding of the injection micro-molding process both by experimental and numerical studies, and to develop experimental protocols that enable the manufacture of structured components at nano- and micro-scale. Investigations based on those approaches and performed simultaneously, revealed that the successful manufacture of components at that scale requires scientific understanding of the underling processes physics and manufacturing techniques, and last but not least, access to high-tech equipment and sufficient mastery in tools operation. Nevertheless, upon successful completion of those studies, it is suggested that further investigation is desired in order to fully explore the manufacturing potential, which injection micro-molding holds for building devices with unique or unmet performance. It is imperative to be known, that successful numerical simulation of polymer flow behavior at micro-scale can be enabled only after determination of melt rheological behavior in micro-structured geometries. Therefore, it is envisioned that the following experimental and theoretical studies can be initiated in the future that can also serve as continuation of this work.

### 8.2.1 Future Experimental Studies

The general objective of the proposed future experimental work would be to expand micro-molding capabilities by:

i. Investigation of the tribological properties and thermal stability of plasma polymerized fluorocarbon films and their dependence on the plasma conditions.

ii. Characterization of the DRIE plasma etching and passivation processes as relevant to Si mold fabrication.

iii. Expanding the experimental capabilities to levels suitable for building of devises possessing injection micro-molded components. It is envisioned that building and subsequent testing of polymer transmission diffraction gratings and optical ring resonators is very plausible. Furthermore, SNOM imaging of gold/patterned polymeric substrates revealed intriguing wavelength dependent light transmission but did not yield to conclusive results related to the physics behind this behavior. Therefore, obtaining of the ground state spectrum of the structures, e.g. absorbance vs. wavelength would potentially elucidate if the observed phenomenon is a result from surface plasmon-polariton resonance or not. It is believed that those structures can be successfully used for planar photonic guide structures but this is yet to be shown.

iv. Building of an experimental capability suitable for analyzing rheological properties (viscosity profiles) of polymers appropriate for injection micro-molding applications.

### 8.2.2 Future Numerical Studies

During the proposed computational research approach the goal would be to improve the model described in details in Chapter 7 by incorporating packing and solidification phases of the polymer in the micro-channels. In this case, which is a truly multiphysics problem COMSOL FEM libraries can readily be employed. Such endeavor would also require implementing of several modified multyphisics application modes involving energy balance calculations. Upon implementation of this scheme the results would enable the optimization of the desired molding machine's processing conditions.

In conclusion, much was learned during the present research work while it was shown that the injection micro-molding holds tremendous potential as a top-down manufacturing process suitable for nano- and micro-fabrication. There is no doubt that any successful implementation of this manufacturing technique can only be made after careful and meticulous consideration of the many and various factors involved in such manufacture.

# CHAPTER 9

# LIST OF REFERENCES

*"When all think alike, no one is thinking very much." - Walter Lippmann*

1. Bartolini, R., et al., *Embossed hologram motion pictures for television playback.* Applied Optics, 1970. **9**(10): p. 2283-90.
2. Hannab, W.J., et al., *Holotape: A low-cost prerecorded television system using holographic storage.* Journal of the SMPTE (Society of Motion Picture and Television Engineers), 1973. **82**(11): p. 905-915.
3. Heckele, M. and Schomburg, W.K., *Review on micro molding of thermoplastic polymers.* Journal of Micromechanics and Microengineering, 2004. **14**(3): p. 1-14.
4. Ehrfeld, W., et al. *Materials for LIGA products.* 1994. Oiso, Japan: IEEE.
5. Despa, M.S., et al. *Injection molding using high aspect ratio microstructure mold inserts produced by LIGA technique.* 1998. Santa Clara, CA, USA: SPIE-Int. Soc. Opt. Eng.
6. Kandlikar, S.G. and Grande, W.J., *Evolution of microchannel flow passages-thermohydraulic performance and fabrication technology.* Heat Transfer Engineering, 2003. **24**(1): p. 3-17.
7. Yang, H., et al., *Ultra-fine machining tool/molds by LIGA technology.* Journal of Micromechanics and Microengineering, 2001. **11**(2): p. 94-99.
8. Lawes, R.A., et al., *The formation of moulds for 3D microstructures using excimer laser ablation.* Microsystem Technologies, 1996. **3**(1): p. 17-19.
9. Griffiths, S.K., *Fundamental limitations of LIGA x-ray lithography: Sidewall offset, slope and minimum feature size.* Journal of Micromechanics and Microengineering, 2004. **14**(7): p. 999-1011.

10. Mekaru, H., et al., *Microfabrication by hot embossing and injection molding at LASTI.* Microsystem Technologies, 2004. **10**(10): p. 682-8.

11. Petersen, K.E., *Silicon as a mechanical material.* Proceedings of the IEEE, 1982. **70**(5): p. 420-57.

12. Lang, W., *Silicon microstructuring technology.* Materials Science & Engineering: R: Reports, 1996. **17**(1): p. 1-55.

13. Chandrasekaran, S. and Sundararajan, S., *Effect of microfabrication processes on surface roughness parameters of silicon surfaces.* Surface and Coatings Technology, 2004. **188-189**: p. 581-587.

14. Vaed, K., et al., *An additive micromolding approach for the development of micromachined ceramic substrates for RF applications.* Journal of Microelectromechanical Systems, 2004. **13**(3): p. 514-25.

15. Sarajlic, E., et al., *Advanced plasma processing combined with trench isolation technology for fabrication and fast prototyping of high aspect ratio MEMS in standard silicon wafers.* Journal of Micromechanics and Microengineering, 2004. **14**(9): p. 70-5.

16. de Boer, M.J., et al., *Guidelines for etching silicon MEMS structures using fluorine high-density plasmas at cryogenic temperatures.* Journal of Microelectromechanical Systems, 2002. **11**(4): p. 385-401.

17. Becker, H. and Heim, U., *Polymer hot embossing with silicon master structures.* Sensors and Materials, 1999. **11**(5): p. 297-304.

18. Yongjun, Z. and Tianhong, C., *Fabrication of high-aspect-ratio polymer-based electrostatic comb drives using the hot embossing technique.* Journal of Micromechanics and Microengineering, 2003. **13**(3): p. 430-5.

19. Elders, J., et al. *DEEMO: a new technology for the fabrication of microstructures*. 1995. Amsterdam, Netherlands: IEEE.

20. Madou, M., *Fundamentals of Microfabrication, The Science of Miniaturization*. 2002, CRC Press LLC.

21. Dong-Yea, S., *Micro-spherical probes machining by EDM.* Journal of Micromechanics and Microengineering, 2005. **15**(1): p. 185-9.

22. Yeo, S.H., et al., *Magnetic field assisted micro electro-discharge machining.* Journal of Micromechanics and Microengineering, 2004. **14**(11): p. 1526-9.

23. Vogler, M.P., et al., *Microstructure-level force prediction model for micro-milling of multi-phase materials.* Transactions of the ASME. Journal of Manufacturing Science and Engineering, 2003. **125**(2): p. 202-9.

24. McFarland, A.W., et al., *Injection moulding of high aspect ratio micron-scale thickness polymeric microcantilevers.* Nanotechnology, 2004. **15**(11): p. 1628-1632.

25. Lilly, B., *Application of pulsed electrochemcial machining to micromold fabrication.* ANTEC, 2000: p. 963-967.

26. Zhang, X., et al., *Micro-stereolithography of polymeric and ceramic microstructures.* Sensors and Actuators A (Physical), 1999. **A77**(2): p. 149-56.

27. Takahashi, M., et al. *Nanoimprint of glass materials with glassy carbon mold fabricated by focused-ion-beam etching*. 2004. Osaka, Japan: The Japan Society of Applied Physics, Chiyoda-Ku, Tokyo, 102, Japan.

28. Kim, Y., et al., *Construction of injection mold with MEMS RTD sensor and MEMS heater for micro/nano molding process.* Japanese Journal of Applied Physics, Part 1: Regular Papers and Short Notes and Review Papers, 2005. **44**(5 B): p. 3591-3595.

29. Yao, D. and Kim, B., *Simulation of the filling process in micro channels for polymeric materials.* Journal of Micromechanics and Microengineering, 2002. **12**(5): p. 604-610.

30. Liyong Yu, C.G.K.L.J.L.K.W.K.M.J.M., *Experimental investigation and numerical simulation of injection molding with micro-features*. Polymer Engineering and Science, 2002. **42**(5): p. 871-888.

31. Yi-Je Juang, L.J.L.K.W.K., *Hot embossing in microfabrication. Part II: Rheological characterization and process analysis.* Polymer Engineering & Science, 2002. **42**(3): p. 551-566.

32. Chen, S.C., et al., *Preliminary study of polymer melt rheological behavior flowing through micro-channels.* International Communications in Heat and Mass Transfer, 2005. **32**(3-4): p. 501-510.

33. Chien, R.-D., et al., *Study on rheological behavior of polymer melt flowing through micro-channels considering the wall-slip effect.* Journal of Micromechanics and Microengineering, 2005. **15**(8): p. 1389-1396.

34. Ho, C.-M. and Tai, Y.-C., *MICRO-ELECTRO-MECHANICAL-SYSTEMS (MEMS) AND FLUID FLOWS.* Annual Review of Fluid Mechanics, 1998. **30**(1): p. 579-612.

35. Kim, E., et al., *Polymer microstructure formed by moulding in capillaries.* Nature, 1995. **376**(6541): p. 581-584.

36. Papautsky, I., et al., *Laminar fluid behavior in microchannels using micropolar fluid theory.* Sensors and Actuators, A: Physical, 1999. **73**(1-2): p. 101-108.

37. Molho, J.I., et al. *Fluid transport mechanisms in microfluidic devices.* 1998. Anaheim, CA, USA: ASME, Fairfield, NJ, USA.

38. Shih, J.C., et al. *Monatomic and polyatomic gas flow through uniform microchannels*. 1996. Atlanta, GA, USA: ASME.

39. Pfahler, J., et al. *Liquid transport in micron and submicron channels*. 1990. Montreux, Switzerland.

40. Tseng, F.G., et al. *Fluid filling into micro-fabricated reservoirs.* 2002. Munich: Elsevier Science B.V.

41. Dong Sung, K., et al., *Micro-channel filling flow considering surface tension effect.* Journal of Micromechanics and Microengineering, 2002. **12**(3): p. 236-46.

42. Cemal Eringen, A. and Okada, K., *A lubrication theory for fluids with microstructure.* International Journal of Engineering Science, 1995. **33**(15): p. 2297-2308.

43. Hatzikiriakos, S.G. and Dealy, J.M., *Wall slip of molten high density polyethylenes. II. Capillary rheometer studies.* Journal of Rheology, 1992. **36**(4): p. 703-741.

44. Rosenbaum, E.E. and Hatzikiriakos, S.G., *Wall slip in the capillary flow of molten polymers subject to viscous heating.* AIChE Journal, 1997. **43**(3): p. 598-608.

45. Bagley, E.B., et al., *Discontinuity in the Flow Curve of Polyethylene.* Journal of Applied Physics, 1958. **29**(1): p. 109-110.

46. Denn, M.M., *Issues in Viscoelastic Fluid Mechanics.* Annual Review of Fluid Mechanics, 1990. **22**(1): p. 13-32.

47. Leger, L., et al., *Wall slip in polymer melts.* Journal of Physics Condensed Matter, 1997. **9**(37): p. 7719-7740.

48. Black, W.B. and Graham, M.D., *Wall-slip and polymer-melt flow instability.* Physical Review Letters, 1996. **77**(5): p. 956.

49. Chen, Y.L., et al., *Shear fracture of polystyrene melts and solutions.* Rheologica Acta, 1994. **33**(4): p. 243-56.

50. Awati, K.M., et al., *Wall slip and shear stresses of polymer melts at high shear rates without pressure and viscous heating effects.* Journal of Non-Newtonian Fluid Mechanics, 2000. **89**(1-2): p. 117-131.

51. Lee, K. and Mackley, M.R., *The significance of slip in matching polyethylene processing data with numerical simulation.* Journal of Non-Newtonian Fluid Mechanics, 2000. **94**(2-3): p. 159-177.

52. Joshi, Y.M., et al., *A unified wall slip model.* Journal of Non-Newtonian Fluid Mechanics, 2000. **94**(2-3): p. 135-149.

53. Forcada, M.L. and Mate, C.M., *The Flow of Thin Viscous Liquid Films on Rotating Disks.* Journal of Colloid and Interface Science, 1993. **160**(1): p. 218-225.

54. Hasegawa, T., et al., *Anomaly of excess pressure drops of the flow through very small orifices.* Physics of Fluids, 1997. **9**(1): p. 1-3.

55. Xu, B., et al., *Study on the viscosity of the liquid flowing in microgeometry.* Journal of Micromechanics and Microengineering, 1999. **9**(4): p. 377-384.

56. Israelachvili, J.N., *Measurement of the viscosity of liquids in very thin films.* Journal of Colloid and Interface Science, 1986. **110**(1): p. 263-271.

57. Israelachvili, J.N., *Measurement of the viscosity of thin fliud films between two surfaces with and without adsorbed polymers.* Colloid and Polymer Science, 1986. **264**(12): p. 1060-1065.

58. Pozhar, L.A., *Structure and dynamics of nanofluids: Theory and simulations to calculate viscosity.* Physical Review E (Statistical Physics, Plasmas, Fluids, and Related Interdisciplinary Topics), 2000. **61**(2): p. 1432-46.

59. Schift, H., et al., *Quantitative analysis of the molding of nanostructures.* Journal of Vacuum Science and Technology B: Microelectronics and Nanometer Structures, 2000. **18**(6): p. 3564-3568.

60. Chou, S.Y., et al., *Imprint of sub-25 nm vias and trenches in polymers.* Applied Physics Letters, 1995. **67**(21): p. 3114.

61. Wang, J.J., et al., *Wafer-based nanostructure manufacturing for integrated nanooptic devices.* Journal of Lightwave Technology, 2005. **23**(2): p. 474-485.

62. Chao, C.-Y. and Guo, L.J., *Polymer microring resonators fabricated by nanoimprint technique.* Journal of Vacuum Science and Technology B: Microelectronics and Nanometer Structures, 2002. **20**(6): p. 2862-2866.

63. Huang, Y., et al., *Soft lithography replication of polymeric microring optical resonators.* Optics Express, 2003. **11**(20): p. 2452-2458.

64. Gadegaard, N., et al. *Arrays of nano-dots for cellular engineering.* 2003. Lugano, Switzerland: Elsevier.

65. Deok-Ho, K., et al. *Modulation of adhesion and growth of cardiac myocytes by surface nanotopography.* 2006. Shanghai, China: IEEE.

66. Wachenschwanz, D., et al., *Design of a manufacturable discrete track recording medium.* IEEE Transactions on Magnetics, 2005. **41**(2): p. 670-5.

67. Glinsner, T., et al., *Nanoimprint lithography enables patterned tracks for high-capacity hard disks.* Solid State Technology, 2005. **48**(3): p. 51-54.

68. Guoming, Z., et al., *Cicada wings: a stamp from nature for nanoimprint lithography.* Small, 2006. **2**(12): p. 1440-3.

69. Lee, S.-M. and Kwon, T.H., *Mass-producible replication of highly hydrophobic surfaces from plant leaves.* Nanotechnology, 2006. **17**(13): p. 3189-3196.

70. Gadegaard, N., et al., *Biomimetic polymer nanostructures by injection molding.* Macromolecular Materials and Engineering, 2003. **288**(1): p. 76-83.

71. Chou, S.Y. and Krauss, P.R., *Imprint lithography with sub-10 nm feature size and high throughput.* Microelectronic Engineering, 1997. **35**(1-4): p. 237-240.

72. Chou, S.Y., et al., *Imprint lithography with 25-nanometer resolution.* Science, 1996. **272**(5258): p. 85-87.

73. Macintyre, D. and Thoms, S., *Fabrication of high resolution features by mould injection.* Microelectronic Engineering, 1998. **41-42**: p. 211-214.

74. Schift, H., et al., *Nanostructuring of polymers and fabrication of interdigitated electrodes by hot embossing lithography.* Microelectronic Engineering, 1999. **46**(1-4): p. 121-124.

75. Mancini, D.P., et al. *Sub-80 nm contact hole patterning using step and flash imprint lithography.* 2004. Santa Clara, CA, United States: The International Society for Optical Engineering, Bellingham, United States.

76. Giboz, J., et al., *Microinjection molding of thermoplastic polymers: A review.* Journal of Micromechanics and Microengineering, 2007. **17**(6): p. 96-109.

77. Gates, B.D., et al., *Unconventional nanofabrication.* Annual Review of Materials Research, 2004. **34**: p. 339-372.

78. Gates, B.D., et al., *New approaches to nanofabrication: Molding, printing, and other techniques.* Chemical Reviews, 2005. **105**(4): p. 1171-1196.

79. Hulme, J.P., et al., *Rapid prototyping for injection moulded integrated microfluidic devices and diffractive element arrays.* Lab on a Chip, 2002. **2**(4): p. 203-6.

80. Chang, C.-H., et al., *Fabrication of sawtooth diffraction gratings using nanoimprint lithography.* Journal of Vacuum Science and Technology B: Microelectronics and Nanometer Structures, 2003. **21**(6): p. 2755-2759.

81. Wimberger-Friedl, R., *Injection Molding of Sub-µm Grating Optical Elements.* Journal of Injection Molding Technology, 2000. **4**(2): p. 78-83.

82. Hunter, W.R., et al., *Investigation of the properties of an ion-etched plane laminar holographic grating.* Applied Optics, 2001. **40**(34): p. 6157-6165.

83. Monkkonen, K., et al., *Replication of sub-micron features using amorphous thermoplastics.* Polymer Engineering and Science, 2002. **42**(7): p. 1600-1608.

84. Khanarian, G., *Optical properties of cyclic olefin copolymers.* Optical Engineering, 2001. **40**(6): p. 1024-1029.

85. Nikolova, D., et al., *Surface modification of cycloolefinic copolymers for optimization of the adhesion to metals.* Surface and Interface Analysis, 2004. **36**(8): p. 689-693.

86. Gindele, F. and Novotny, C. *Miniaturized fibre-coupled optical spectrometers with temperature compensation based on injection moulding*. 2002. Brugge, Belgium: The International Society for Optical Engineering.

87. Siitonen, S., et al., *Coupling of light from an LED into a thin light guide by diffractive gratings.* Applied Optics, 2004. **43**(30): p. 5631-6.

88. Laakkonen, P., et al. *Diffractive optics in industry and research - Novel components for optical security systems.* 2005. Warsaw, Poland: International Society for Optical Engineering, Bellingham WA, WA 98227-0010, United States.

89. Lavallee, E., et al., *Electron beam lithography of nanostructures using 2-propanol : water and 2-propanol : methyl isobutyl ketone as developers for poly-methylmethacrylate.* Journal of Vacuum Science & Technology B, 1998. **16**(3): p. 1255-1257.

90. Ayon, A.A., et al., *Influence of coil power on the etching characteristics in a high density plasma etcher.* Journal of the Electrochemical Society, 1999. **146**(7): p. 2730-2736.

91. Ayon, A.A., et al., *Characterization of a time multiplexed inductively coupled plasma etcher.* Journal of the Electrochemical Society, 1999. **146**(1): p. 339-349.

92. Ayon, A.A., et al. *Novel integrated MEMS process using fluorocarbon films deposited with a deep reactive ion etching (DRIE) tool.* 2000. Boston, MA, USA: Materials Research Society, Warrendale, PA, USA.

93. Petit, B. and Pelletier, J., *A parametric study of the etching of silicon in SF6 microwave multipolar plasmas: interpretation of etching mechanisms.* Japanese Journal of Applied Physics, Part 1 (Regular Papers &amp; Short Notes), 1987. **26**(6): p. 825-34.

94. Pelletier, J., et al., *SF6 Plasma Etching of Silicon: Evidence of Sequential Multilayer Fluorine Adsorption.* Europhysics Letters (EPL), 1987. **4**(9): p. 1049-1054.

95. Sankaran, A. and Kushner, M.J., *Fluorocarbon plasma etching and profile evolution of porous low-dielectric-constant silica.* Applied Physics Letters, 2003. **82**(12): p. 1824-1826.

96. Zhang, D. and Kushner, M.J., *Surface kinetics and plasma equipment model for Si etching by fluorocarbon plasmas.* Journal of Applied Physics, 2000. **87**(3): p. 1060-1069.

97. Standaert, T.E.F.M., et al. *High density fluorocarbon etching of silicon in an inductively coupled plasma: Mechanism of etching through a thick steady state fluorocarbon layer.* in *International workshop on basic aspects of nonequilibrium plasmas interacting with surfaces (BANPIS"97).* 1998. Shirahama, Wakayama (Japan): AVS.

98. Rooks, M.J. and Aviram, A. *Application of 4-methyl-1-acetoxycalix[6]arene resist to complementary metal--oxide--semiconductor gate processing.* in *Papers from the 43rd international conference on electron, ion, and photon beam technology and nanofabrication.* 1999. Marco Island, Florida (USA): AVS.

99. Schaper, C.D., et al., *Induced thermal stress fields for three-dimensional distortion control of Si wafer topography.* Review of Scientific Instruments, 2004. **75**(6): p. 1997-2002.

100. Yu, F., et al., *Stress analysis in silicon die under different types of mechanical loading by finite element method (FEM).* IEEE Transactions on Advanced Packaging, 2002. **25**(4): p. 522-527.

101. Rabier, J., et al., *Plastic deformation of silicon between 20 deg C and 425 deg C.* Phys. Stat. Sol, 2007. **4**(8): p. 3110-3114.

102. Kulawik, J., et al., *Determination of glass transition temperature, thermal expansion and, shrinkage of Epoxy resins.* Colloid and Polymer Science, 1989. **267**(11): p. 970-975.

103. Glavchev, I., et al., *Determination of the coefficient of thermal expansion of epoxy composites.* Polymer Testing, 2002. **21**(2): p. 177-179.

104. Rabiei, P., et al., *Polymer micro-ring filters and modulators.* Journal of Lightwave Technology, 2002. **20**(11): p. 1968-75.

105. Yanyi, H., et al., *Soft lithography replication of polymeric microring optical resonators.* Optics Express, 2003. **11**(20).

106. Fan, X., et al. *Overview of novel integrated optical ring resonator bio/chemical sensors.* 2007. San Jose, CA, United States: SPIE - International Society for Optical Engineering, Bellingham WA, WA 98227-0010, United States.

107. Srirojpinyo, C., et al. *Processing parameters affecting nanoinjection molding*. 2004. Boston, MA, United States: Nano Science and Technology Institute, Cambridge, MA 02139, United States.

108. Lee, N., et al., *Temperature dependence of anti-adhesion between a stamper with sub-micron patterns and the polymer in nano-moulding*

*processes*. Journal of Physics D: Applied Physics, 2004. **37**(12): p. 1624-1629.

109. Park, S., et al. *Anti-adhesive layers on nickel stamps for nanoimprint lithography*. in *Micro and Nano Engineering 2003*. 2004. Cambridge, United Kingdom: Elsevier.

110. Keil, M., et al., *Development and characterization of silane antisticking layers on nickel-based stamps designed for nanoimprint lithography.* Journal of Vacuum Science &amp; Technology B (Microelectronics and Nanometer Structures), 2005. **23**(2): p. 575-84.

111. Namseok, L., et al., *Self-assembled monolayer as an antiadhesion layer on a nickel nanostamper in the nanoreplication process for optoelectronic applications.* Applied Physics Letters, 2006. **88**(7): p. 73101-1.

112. Yan Xin, Z., et al., *Thermal stability of vapor phase deposited self-assembled monolayers for MEMS anti-stiction.* Journal of Micromechanics and Microengineering, 2006. **16**(11): p. 2259-64.

113. Bunning, T.J., et al., *The growth and characterization of photonic thin films.* Vacuum, 2005. **80**(1-3): p. 12-19.

114. Agraharam, S., et al., *Comparison of plasma chemistries and structure-property relationships of fluorocarbon films deposited from octafluorocyclobutane and pentafluoroethane monomers.* Journal of Vacuum Science and Technology B: Microelectronics and Nanometer Structures, 2001. **19**(2): p. 439-446.

115. Tanikella, R.V., et al., *Moisture absorption studies of fluorocarbon films deposited from pentafluoroethane and octafluorocyclobutane plasmas.* Journal of Electronic Materials, 2002. **31**(10 SPEC): p. 1096-1103.

116. Michaeli, W., et al., *Temperature stability of plasma polymerized antiadhesive coatings.* Materials Research Society Symposium - Proceedings, 1999. **544**: p. 239-244.

117. Jo, S.-B., et al., *Fabrication and surface treatment of silicon mold for polymer microarray.* Surface and Coatings Technology, 2004. **188-189**(1-3 SPECISS): p. 452-458.

118. Jaszewski, R.W., et al., *Deposition of anti-adhesive ultra-thin teflon-like films and their interaction with polymers during hot embossing.* Applied Surface Science, 1999. **143**(1): p. 301-308.

119. Gao, J.X., et al., *Antistick postpassivation of high-aspect ratio silicon molds fabricated by deep-reactive ion etching.* Journal of Microelectromechanical Systems, 2006. **15**(1): p. 84-93.

120. Yeo, L.P., et al., *Design of experiment for optimization of plasma-polymerized octafluorocyclobutane coating on very high aspect ratio silicon molds.* Langmuir, 2006. **22**(24): p. 10196-10203.

121. Marmur, A., *Thermodynamic aspects of contact angle hysteresis.* Advances in Colloid and Interface Science, 1994. **50**: p. 121-141.

122. Faibish, R.S., et al., *Contact angle study on polymer-grafted silicon wafers.* Journal of Colloid and Interface Science, 2002. **256**(2): p. 341-350.

123. Jiang, H., et al., *Plasma polymerized multilayered photonic films.* Chemistry of Materials, 2003. **15**(1): p. 340-347.

124. Beamson, G. and Briggs, D., *High resolution monochromated X-ray photoelectron spectroscopy of organic polymers: A comparison between solid state data for organic polymers and gas phase data for small molecules.* Molecular Physics, 1992. **76**(4): p. 919-936.

125. Beamson, G. and Briggs, D., *High resolution XPS of organic polymers - The Scienta ESCA300 database.* 1992: John Wiley & Sons Ltd.

126. Bunning, T.J., et al., *The growth and chemical structure of thin photonic films formed from plasma copolymerization. Part II. Effect of monomer feed location.* Polymer, 2005. **46**(19): p. 8178-84.

127. Tu, H. and Wang, J., *An XPS investigation of thermal degradation and charring processes for PVC and PVC/Cu2O systems in the condensed phase--II.* Polymer Degradation and Stability, 1996. **54**(2-3): p. 195-203.

128. Briggs, D., et al., *X-ray photoelectron spectroscopy studies of polymer surfaces. III. Flame treatment of polyethylene.* Journal of Materials Science, 1979. **14**(6): p. 1344-8.

129. Galuska, A.A. and Halverson, D.E., *Quantitative analysis of surface ethylene concentrations in ethylene-propylene polymers using XPS valence bands.* Surface and Interface Analysis, 1998. **26**(6): p. 425-432.

130. Roca-Cusachs, P., et al., *Stability of microfabricated high aspect ratio structures in poly(dimethylsiloxane).* Langmuir, 2005. **21**(12): p. 5542-5548.

131. Hui, C.Y., et al., *Constraints on microcontact printing imposed by stamp deformation.* Langmuir, 2002. **18**(4): p. 1394-1407.

132. Zhang, Y., et al., *Replica molding of high-aspect-ratio polymeric nanopillar arrays with high fidelity.* Langmuir, 2006. **22**(20): p. 8595-8601.

133. Glassmaker, N.J., et al., *Design of biomimetic fibrillar interfaces: 1. Making contact.* J. R. Soc. Interface, 2004(1): p. 23-33.

134. Wachenschwanz, D., et al., *Design of a manufacturable discrete track recording medium.* IEEE Transactions on Magnetics, 2005. **41**(2): p. 670-675.

135. Krupenkin, T.N., et al., *From rolling ball to complete wetting: The dynamic tuning of liquids on nanostructured surfaces.* Langmuir, 2004. **20**(10): p. 3824-3827.

136. Deng, X., et al., *Wideband antireflective polarizers based on integrated diffractive multilayer microstructures.* Optics Letters, 2006. **31**(3): p. 344-346.

137. Henoch, C., et al. *Turbulent drag reduction using superhydrophobic surfaces*. 2006. San Francisco, CA, United States: American Institute of Aeronautics and Astronautics Inc., Reston, VA 20191, United States.

138. Lim, J.Y., et al., *Human foetal osteoblastic cell response to polymer-demixed nanotopographic interfaces.* Journal of The Royal Society Interface, 2005. **2**(2): p. 97-108.

139. Homola, J., et al., *Surface plasmon resonance sensors: review.* Sensors and Actuators, B: Chemical, 1999. **54**(1): p. 3-15.

140. Bozhevolnyi, S.I., et al. *Surface plasmon polariton waveguiding in random surface nanostructures*. 2003. Rochester, NY, USA: Blackwell Science.

141. Melville, D.O.S. and Blaikie, R.J., *Super-resolution imaging through a planar silver layer.* Optics Express, 2005. **13**(6): p. 2127-2134.

142. Kik, P.G., et al. *Plasmon printing - A new approach to near-field lithography*. 2002. Boston, MA, United States: Materials Research Society.

143. Shao, D.B. and Chen, S.C., *Surface-plasmon-assisted nanoscale photolithography by polarized light.* Applied Physics Letters, 2005. **86**(25): p. 253107.

144. Bouhelier, A., et al., *Electromagnetic interactions in plasmonic nanoparticle arrays.* Journal of Physical Chemistry B, 2005. **109**(8): p. 3195-8.

145. Boltasseva, A., et al., *Integrated optical components utilizing long-range surface plasmon polaritons.* Journal of Lightwave Technology, 2005. **23**(1): p. 413-422.

146. Nikolajsen, T., et al., *Polymer-based surface-plasmon-polariton stripe waveguides at telecommunication wavelengths*. Applied Physics Letters, 2003. **82**(5): p. 668-70.

147. Pedersen, H.C., et al., *Integrated holographic grating chip for surface plasmon resonance sensing.* Optical Engineering, 2004. **43**(11): p. 2505-10.

148. Thirstrup, C., et al., *Diffractive optical coupling element for surface plasmon resonance sensors.* Sensors and Actuators B (Chemical), 2004. **100**(3): p. 298-308.

149. Pyo, H.-B., et al. *Multiplexed polymer surface plasmon sensor with integrated optical coupler.* 2005. Boston, MA, United States: International Society for Optical Engineering, Bellingham WA, WA 98227-0010, United States.

150. Ropers, C., et al., *Ultrafast dynamics of surface plasmon polaritons in plasmonic metamaterials.* Applied Physics B: Lasers and Optics, 2006. **84**(1-2): p. 183-189.

151. Kim, J., et al. *Near-field imaging of surface plasmon on gold nano-dots fabricated by scanning probe lithography.* 2003. Rochester, NY, USA: Blackwell Science.

152. Bouhelier, A. and Wiederrecht, G.P., *Surface plasmon rainbow jets.* Optics Letters, 2005. **30**(8): p. 884-6.

153. Lin, A., et al., *Visible to infrared photoluminescence from gold nanoparticles embedded in germano-silicate glass fiber.* Optics Express, 2007. **15**(10): p. 6374-6379.

154. Bouhelier, A., et al., *Surface plasmon characteristics of tunable photoluminescence in single gold nanorods.* Physical Review Letters, 2005. **95**(26): p. 267405-1.

155. Bozhevolnyi, S.I., et al., *Localization and Waveguiding of Surface Plasmon Polaritons in Random Nanostructures.* Physical Review Letters, 2002. **89**(18): p. 186801.

156. Bozhevolnyi, S.I., et al., *Waveguiding in Surface Plasmon Polariton Band Gap Structures*. Physical Review Letters, 2001. **86**(14): p. 3008.

157. Thirstrup, C., et al., *Diffractive optical coupling element for surface plasmon resonance sensors.* Sensors and Actuators, B: Chemical, 2004. **100**(3): p. 298-308.

158. Lahav, M., et al., *Biological sensing using transmission surface plasmon resonance spectroscopy.* Langmuir, 2004. **20**(18): p. 7365-7367.

159. Kennedy, P., *Flow analysis of injection molds.* 1995: Carl Hanser Verlag.

160. Iwamura, C., et al., *An efficient algebraic multigrid preconditioned conjugate gradient solver.* Computer Methods in Applied Mechanics and Engineering, 2003. **192**(20-21): p. 2299-2318.

161. van den Brule, B.H. and Slikkerveer, P.J., *Anisotropic conduction of heat caused by molecular orientation.* Rheologica Acta, 1990. **29**(3): p. 175-81.

162. Miyamoto, H., et al., *Rapid measurement of the thermal diffusivity of flowing polymer melts.* International Journal of Thermophysics, 1993. **14**(3): p. 585-592.

163. Davis, T.A., *A column pre-ordering strategy for the unsymmetric-pattern multifrontal method.* ACM Transactions on Mathematical Software, 2004. **30**(2): p. 165-195.

164. Davis, T.A., *Algorithm 832: UMFPACK V4.3 - An unsymmetric-pattern multifrontal method.* ACM Transactions on Mathematical Software, 2004. **30**(2): p. 196-199.

# CHAPTER 10

# VITA

*"Don't go around saying the world owes you a living; the world owes you nothing; it was here first" - Mark Twain*

Mr. Aleksandar Angelov was born to parents of Mr. Kolyu Angelov and Mrs. Elenka Angelova. The author began his undergraduate studies at the Technical University of Varna, Bulgaria in September 1995 where he obtained a Masters degree in Mechanical Engineering in 2000. Upon completion of his studies Mr. Angelov served in the Bulgarian Naval Forces as a requirement of then mandatory military service. Before joining Lehigh University in 2003, he worked as a quality engineer in a laboratory for destructive and non-destructive testing. At Lehigh University, Mr. Angelov joined the research group of Prof. John Coulter as a National Science Foundation funded research assistant to work in the area of polymer injection micro-molding. While at Lehigh, Mr. Angelov has published a number of research articles focusing on the scientific technology and development of polymer injection micro-molding.